PANJAB UNIVERSITY RESEARCH JOURNAL (SCIENCE)

VOL. 68, 2018
VOL. 69, 2019

PANJAB UNIVERSITY RESEARCH JOURNAL (SCIENCE)
VOLUME 68, 2018
VOLUME 69, 2019

The subscription of the journal may be sent in the form of a Bank Draft payable to ***The Registrar, Panjab University, Chandigarh*** and addressed to The Editor-in-Chief on the following address:

Research Journal (Science)
Old Corresponding Building,
Panjab University, Chandigarh -160 014, (India)

The manuscripts for publication or any other enquiry is also to be addressed to the Editor-in-Chief

Subscription fee:	**Inland**	**Foreign**
Annual Subscription	Rs.400/-	US$ 50
Life Membership	Rs. 3000/-	US$ 250

Printed in 2020

CONTENTS

Volume 68 (2018)

Volume 69 (2019)

Pb. Univ. Res. J (Sci.) Vol. 68, 2018, pp 1-6

SCIENTIFIC RESEARCH ON *ELAEOCARPUS GANITRUS* (RUDRAKSHA) FOR ITS MEDICINAL IMPORTANCE

Durg V. Rai*, Shiva Sharma and Manisha Rastogi
Department of Biomedical Engineering, School of Biological Engineering and Sciences, Shobhit University, NH-58, Modipuram, Meerut-250110, India.

Abstract

Rudraksha (Elaeocarpusganitrus) owes an important status both in Ayurveda as well as in Hindu mythology for its curative and spiritual benefits, respectively. Physical wearing of Rudraksha has been cited for its pharmacological actions against vast range of medical ailments including anxiety, lack of concentration, insomnia, depression, hypertension, palpitation, infertility, rheumatism and asthma. The present review aims to investigate the scientific evidences available in literature for their biochemical and compositional properties, in-vitro and in-vivo activities, as well as clinical analysis.It clearly identifies the need to carry out in-depth research in the multiple domains such as physical, pharmacological, and clinical studies in order to understand and disseminate the medical benefits of Rudraksha for the welfare of mankind. The present work sums the current state of knowledge concerning the ethno pharmacology, physical properties chemical composition, pharmacology and toxicology of E. ganitrus.

Keywords: Rudraksha, Biochemical, Physical, Mineralogical, Clinical Trials.

INTRODUCTION

Rudraksha or *Elaeocarpusganitrus* roxb. (Syn. *E. sphaericus* Gaertn; Family *Elaeocarpaceae*) fruits are popular from ancient times for their mythological, aesthetic and medicinal importance Joshi *et al.* (2014). *Elaeocarpusganitrusroxb.*trees grow to ~20 m and are found from the Gangetic plain in the foothills of the Himalayas to China, South and Southeast Asia, parts of Australia, and Guam and Hawaii.Rudraksha trees are commonly found in mountain and hilly areas of Nepal, Indonesia Javaand Sumatra. Dried *Rudrakasha* bead is obtained from the ripe fruit of *Elaeocarpus ganitrus roxb*.. Microscopic studies revealed the presence of a hard endocarp with lignified isodiametric sclereids, seeds with membranous seed coat, which enclosed a dense cellular endosperm comprising of calcium oxalate druses (Singh 2010).

Rudraksha fruits are generally categorized based upon the number of segments or grooves or popularly mukhis present over the fruit beads Tilak *et al.* (2017).

Figure 1 shows various stages related toRudraksha bead.Rudraksha beads (size ~ 25 mm) have between 1 and 21 lines (*mukhi*). Most of rudrakshas have four, five or six lines. Rudraksha beads are white, red, brown (most common) yellow, and black.

Rudraksha seeds are covered with a blue outer husk when fully ripe and are also known as blueberry beads. The blue color is not derived from pigment but is structural(Lee, 1991).

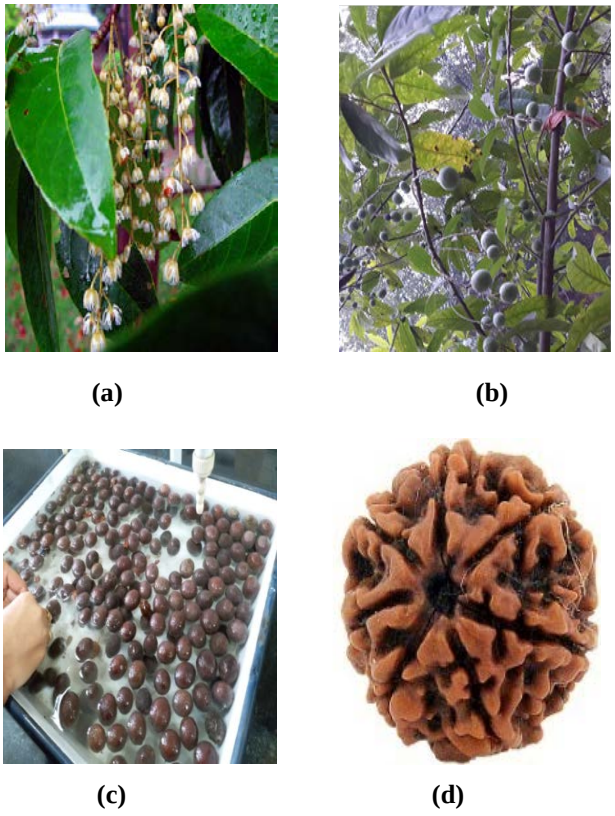

(a) **(b)** **(c)** **(d)**

Figure 1: (a) Inflorescence on Rudraksha tree, (b) Fruit on Rudraksha tree, (c) Ripen fruit and (d) Dried Rudraksha bead (six mukhi).

*Corresponding Author: durgvrai@gmail.com
MS Received: October 8, 2018, Accepted: December 21, 2018

Pharmacologically, Rudraksha beads have been reported for their therapeutic potential against several disorders like stress, anxiety, depression, palpitation, nerve pain, epilepsy, migraine, lack of concentration, asthma, hypertension, diabetes, arthritis and liver diseases Jain *et al.* (2014). Further, in our traditional system of medicine, Rudraksha beads have been reported to exert multiple pharmacological actions when applied in several forms such as physical wearing of Rudraksha rosary, oral intake of Rudraksha dipped water or Rudraksha powder. Moreover, it has also been mentioned that the specificity in their therapeutic properties differs based upon the type of grooves or Mukhis Shah *et al.* (2010); Tripathi *et al.* (2016-a); Dadhich *et al.* (2014); Sharma *et al.* (2015); Tilak *et al.* (2017); Jain *et al.* (2014); Tripathi *et al.* (2016-b).

One of the major mechanisms of action of Rudraksha beads through which it influences the systemic physiology is its electromagnetic property. It has been repeatedly mentioned in the published literature that Rudraksha beads pose inductive, resistive, dielectric, paramagnetic and diamagnetic properties due to which variable signals were emitted by different mukhiRudraksha thereby attributing positive beneficial effect on overall systemic physiology Ravishankar *et al.* (2007). However, scientific evidences regarding the electromagnetic properties of Rudraksha beads are almost nil. Single evidence regarding the bioelectric energy of Rudraksha was found where the authors reported that 108 beads Rudraksha rosary stabilized the flocculation of current applied on two medicinal plants Tripathy *et al.* (2016-a). Further, it has been hypothesized that the composition of Rudraksha beads may influence its electromagnetic property and therefore, play key role in its therapeutic benefits. Previous studies revealed presence of several bioactive phytoconstituents including alkaloids, flavonoids, tannins, steroids, triterpenoids, carbohydrates and cardiac glycosides as the major components. In-addition, other studies also reported presence of isoelaeocarpicine, elaeocapine, isoelaeocarpine and quercetin, gallic, ellagic acids and rudrakine as biomarker components in Rudraksha bead.

The current review aims to assess the available scientific evidences of Rudraksha bead with special reference to their biochemical and compositional properties, electromagnetic property, *in-vitro* and *in-vivo* activities, and clinical studies.

BIOCHEMICAL ANALYSIS

Several reports related to biochemical constituents in Rudraksha bead are availablein literature Jain *et al.* (2014). These revealed presence of glycosides, alkaloids, minerals, vitamins, steroids, flavanoid, gallic acid, ellagic acid andquercetin in Rudraksha. Hardainiyan *et al.* (2015) evaluated the ethanolic fruit extract of Rudraksha and reported the presence of alkaloids, glycosides, phenolic compounds, flavonoids, saponins, carbohydrates and fixed oils, but protein and amino acids were absent in this extract. Tripathi *et al.* (2016-c), screened the presence of phytochemical in hexane, chloroform, ethyl acetate, acetone and methanol extracts of Rudraksha. Results showed the presence of alkaloids, glycoside, phytosterols, carbohydrate, tannin, flavanoid, amino acid, saponin, and terpenoids. In another study Tripathi *et al.* (2016-d), performed spectroscopic analysis on the methanol seed extract of *E. ganitrus*. Analysis was performed using FTIR and UV-VIS for the phytochemical analysis. Results showed the presence of phenolic compound and flavanoid at 318nm and 245nm, respectively, in UV-VIS whereas in whereas FTIR spectra was obtained at the peak at 3363.97cm-1 for OH group. Das (2017),reported the presence of many significant phytochemicals like saponins, tannins, cardiac glycosides, flavanoidsand steroids in aqueous, ethanolic and methanolic extract of Rudraksha. Singh *et al.* (2016; 2018) studied the overall mechanical and compressive strength of Rudraksha bead and revealed good compressive strength in both the vertical and horizontal planes.

ELECTROMAGNETIC ANALYSIS

Electromagnetic properties in Rudrakshahave been reported by several reviewers Joshi *et al.* (2014); Jain *et al.* (2014); Arivu *et al.* (2017); Hardainiyan *et al.* (2015),where Rudraksha was mentioned as a famous electromagnetic bead helpful in curing several chronic disorders. Tripathy *et al.* (2016-b)stated the healing mechanism of Rudraksha due to its electromagnetic property. The study reported that the electromagnetic properties of Rudrakshabeads activate body's energy wheel, which in turn influences the bioelectrical properties of human body and heals various chronic diseases like blood pressure, heart rate, diabetes, gynaecological problem, neurological disorders, mental problem, insomnia and rheumatism. In another report Tripathy *et al.* (2016-a) mentioned that rotation of Rudraksha between two copper coins is an evidence of its electromagnetic property. The activity needs to be confirmed with reasoning. Further, it explains the electromagnetic and piezoelectric properties of Rudraksha and their mechanism of action in treatment. The authors stated that wearing of Rudraksha works on electromagnetism and controls bioelectric energy of human body, which in turn is responsible for mind-body coordination and its induced health benefits. Moreover, the authors reported that chanting using Rudraksha mala has its natural piezoelectric effects that would generate a charge in response to applied mechanical stress and work similar to acupressure therapy. In-addition, diamagnetic and paramagnetic characteristics of the Rudraksha further help in balancing the impaired functioning by restoring the subatomic and bioenergetics homeostasis. Prajapati *et al.* (2016)

reported the electromagnetic characteristics of Rudraksha on dracaena plant. Authors divided each plant into two zones,*i.e.*, Positive region (stem) and Negative region (plant leave). To record the parameters Cu electrodes were connected to the plant leaves and Zn electrode to plant stem. Variations in the electrical potential of the plant were observed from 1.1 to 0.8 mV without Rudraksha, which got stabilized to 0.8 mV after wearing of Rudraksha. Based upon the study outcomes, the authors reported the presence of capacitive, resistive and inductive properties in Rudraksha. Tilak *et al.* (2017), reviewed the potential benefits of physical wearing of Rudraksha due to its electromagnetic properties. Authors reported that physical wearing of Rudraksha exerted implausible power control over electromagnetic impulses brain and focus human brain on a single target. The study stated that electromagnetism of Rudraksha affects grey and white matter in brain, thereby influencing our sixth sense. Sharma *et al.* (2018) reported thequantitative electrical properties of Rudraksha bead and the possible biochemical and mineralogical components responsible for its bioelectrical property. Results of this study indicate the presence of 27 important minerals with variable electrical properties.

IN VITRO ANALYSIS

The antimicrobial, antioxidant, anti-cancerous, and immunomodulatory activities of different solvent mediated Rudraksha extracts have been studied. Chemically the extracts showed the presence of phytosterols, fats, alkaloids, flavonoids, carbohydrates, proteins and tannins (Singh 2010). Kumar *et. al.* (2014) isolated several bioactive compound from the different parts of the plant and were analysed pharmacologically. *E. ganitrus* was reported to exhibit antimicrobial, antiulcerogenic and antioxidant activity. Dharmalingam *et al.* (2017) studied antimicrobial activities of hexane, chloroform, ethylacetate and aqueous alcohol extracts of Rudraksha against gram-positive and gram-negative bacteria. The microbial load such as total bacterial count and fungal count (Enterobacteria, Escherichia coli, Salmonella species, Staphylococcus aureus and Pseudomonas aeruginosa) and antibacterial activity were measured using serial dilution method and Kirby bauer method, respectively, for selective pathogens. The study results demonstrated potent antibacterial activity of all *E. ganitrus* extract against gram-positive and gram-negative bacteria. Jayashree *et al.* (2016), evaluated the antimicrobial activities for acetone, methanol and water extracts of Rudraksha (leaf, stem, bark and Rudraksha bead) against four bacterial species (Shigellasonnei, Salmonella typhi, Staphylococcus aureus and Klebsiella pneumonia) and a fungal species (Candida albicans) using the agar well diffusion method. Results showed that plant extracts exhibited a dose-dependent inhibition of microorganisms, especially the acetone and methanol extracts of leaf and stem bark displayed maximum antibacterial activity against all the bacterial species studied. Dalei *et al.*(2016) investigated antimicrobial activity of methanol, and acetone extracts of pulp and bead of *E. ganitrus.* The extracts exhibited antimicrobial activities with zones of inhibition ranging from 9.5 mm to 21.0mm and 10.5 mm to 22 mm for methanol and acetone extracts respectively. All extracts exhibited appreciable activity against the fungal species. Tripathy *et al.* (2016-c) studied antibacterial potential of Rudraksha against two gram positive and five gram negative bacteria at three concentration (220, 330, 550 µg/Disc) through disc diffusion method. Results showed zone of inhibition in the range of 6 to 12 mm with highest zone of inhibition at 12mm for Escherichia Coli at 550 µg/Disc. These findings demonstrated antibacterial activity of *E.ganitrus*extract. Das *et al.* (2015) evaluated antioxidant activities of Rudraksha where comparable results were obtained with standard ascorbic acid. In DPPH antioxidant analysis while standard Ascorbic acid showedEC50 value at 25.53 µg/ml, methanolic extract of *E. serratus* showed EC50 at 75.47 µg/ml.

IN VIVO ANALYSIS

Barve*et al.* (2014) examined antihypertensive effect of *E. ganitrus* on male Wistar rats. To perform the analysis, powdered seeds were extracted by maceration using water in copper (E1) and glass vessel (E2) and analyzed for antihypertensive activity in cadmium chloride (1 mg/kg intraperitoneally; for a period of 15 days) induced rats. E1 was administered at dose of 5, 10, and 15 mg/kg and E2 at dose of 10, 20, and 30 mg/kg. E1 and E2 did not show any toxicity at dose of 5 g/kg in rats. It was found that 15 mg/kg of E1 and 30 mg/kg of E2 decreases the blood pressure by ~30 mmHg in hypertensive rats. Overall results showed effective antihypertensive activity using water extract of Rudraksha.

Dadhich *et al.* (2014) evaluated antidepressant effects of Rudraksha Bead extract (75% ethanol) in albino mice. Study was carried out on Group I (Untreated Control received vehicle (Distilled water)), Group II (Control (Fluoxetine) 20 mg/kg body weight) and Group III (Control (Imipramine) 15 mg/kg) administrated orally with distilled water. Group IV, V, VI and VII were administered orally with different doses (20, 40, 60 and 80 mg/kg body weight) of *E. ganitrus*fruit extract (EGFE). Antidepressant effect of EGFE was assessed by forced swim test. EGFE (20 and 40mg/kg) significantly decreased the immobility time and increased climbing and swimming time significantly. Duration of immobility of mice increased at high dose (80mg/kg) as compared to vehicle. It is concluded that while EGFE exhibited antidepressant effect at low dose, at high dose it was sedative.

Tripathy *et al.* (2016-e) investigated antidepressant activity of ethanolic extract of *E. ganitrus*at 250mg/kg dose in mice. Antidepressant activity of ethanolic extract of *E. ganitrus*was carried out using hole cross test, open field test and thiopental induced sleeping time test in swiss albino mice. The extract increased the locomotor activity of mice in open field and hole cross test significantly ($p<0.05$). The findings demonstrated that the seed extract of *E. ganitrus*have significant antidepressant activity.

Kakalij *et al.* (2017) evaluated ameliorative effect of *E. ganitrus*on gentamicin (GM)-induced nephrotoxicity in rats. *E. ganitrus*(100, 200, and 400 mg/kg body weight) was administered orally to male wistar rats. Results revealed that co- administration of *E. ganitrus*significantly reduced elevated levels of serum creatinine, BUN, uric acid and albuminuria,alongwith considerable increase in the serum albumin and urine creatinine. Furthermore, *E. ganitrus* noticeably increased serum total protein and antioxidant enzyme levels with significant alterationin phagocytic index and neutrophil adhesion assay when compared with GM treated group in a dose dependent manner. This study revealed that ethanolic extract of *E. ganitrus* had immunomodulatory and nephroprotective activity. Tripathy *et al.* (2016-c), investigated hypoglycemicactivity of methanol and water (ratio70:30) extract of *E. ganitrus* seeds in alloxan induced diabetic rats. The extract of *E.Ganitrus* seed significantly ($P<0.05$) reduced blood glucose level in alloxan induced diabetic rats after twelve hours of administration. Results supported traditional uses of *E.ganitrus* seed for the management of diabetic sores. Tripathy *et al.* (2016-c) alsoexamined antihyperglycemic effect of methanolic seed extracts of *E. ganitrus*roxb. instreptozotocin induced diabetes. The methanolic seed extract exhibited potent antidiabetic activity comparable to the standard drug glybenclamide.

Jain *et al.* (2017) screened anti-atherosclerotic ethanolic crude (70%) extract of *E.ganitrus* seed in kidney of cholesterol induced atherogenic rabbits. The ethanolic extract, when administered at a dose level of 250 mg/kg and 500 mg/kg (p.o) daily for 60 days to cholesterol-fed rabbits, rectified the altered histology by restoring the normal histology. Study concluded that the ethanolic extract of *E. ganitrus* seed may serve as a potent agent against cardiovascular diseases and resultant chronic kidney disease.

Jain *et al.* (2016) also experimentedanti-atherosclerotic activity of *E. ganitrus* extract at dose level of 250 and 500 mg/kg in New Zealand white male rabbits fed with high cholesterol diet for 120 days. The study reported significant corrections in ($p\leq0.01$, ≤0.001) disturbed lipid profile on the extract treatment in a dose-dependent manner during the 60 days of the treatment period. A significant reduction in lipid peroxidation and a considerable increase in glutathione, catalase, and superoxide dismutase levels ($p\leq0.01$, ≤0.001) were observed inthe post-treatment cholesterol-fed rabbits. The histopathological modifications such as accumulation of foam cells, atheromatous plaque formation and lumen size reduction supported the successful induction of atherosclerosis in rabbits. The*E. ganitrus* extract treated rabbits showed significant lowering of cholesterol deposition and increased lumen size when compared to cholesterol-fed group.

Bagewadi *et al.* (2015) evaluated anti-parkinsonian effect of *E. ganitrus* in rota rod and catalepsy bar tests. Assessment of oxidative stress was done by measuring the malondialdehyde (MDA) and reduced glutathione (GSH) levels in the striatal region of the brain. *E. ganitrus* (200 and 400 mg/kg, p.o.) showed significant anti-oxidative effect by causing a decrease in brain MDA levels ($p<0.001$) and a significant increase in GSH levels ($p<0.001$) that further plays a vital role in the pathophysiology of PD. Overall this study conclusively shows *E.ganitrus*has anti-oxidant and neuroprotective activity in haloperidol experimental model of PD.

CLINICAL TRIALS

Tripathi *et al.* (2016) assessed the immunomodulatory properties of *E. ganitrus* (Rudraksha). This experiment was conducted on two groups of 15 male candidates each. The Group-1 served as control without wearing the Rudraksha and Group-2 people were regularly wearing Rudraksha as necklace. Specimen blood was collected by puncturing vein of arm and morning first urine samples were collected from group-1 and group-2 for biochemical analysis. Results showed people, who were regularly wearing Rudraksha beads, were healthy and their CBC and urine tests show that their haemoglobin, RBC, DLC and TLC are in excellent condition as compared to the people who do not wear Rudraksha bead rosary. Makhija *et al.* (2015) assessed the efficacy of an ayurvedic formulation containing Rudraksha in the management of mental retardation in 15 mentally retarded children between age group of 8 months to 12 years. A combination of *Vacha, Rudraksha, Haridra andHingu*was administered twice daily for 90 days. Findings of the study revealed that treatment was highly effective over behavioural disorders, but very minimal response to treatment was noticed over mental age and social age. Also significant improvement was observed over psychological, psychomotor and biological factors.

CONCLUSION

Considering the importance of Rudraksha beads as given in our ancient Indian system of medicine against multiple disorders, it is concluded that scientific evidences regarding its pharmacological properties generated through standard in vitro, in-vivo, and clinical studies as well as its mechanism of action are highly insufficient. There is a strong need

to conduct in-depth research studies in order to prove its efficacy as cost-effective, user friendly, easily accessible, safe and holistic therapeutic approach to ameliorate adverse effects of chronic diseases.

ACKNOWLEDGEMENTS

We acknowledge the help and guidance from Mahamandeleshwar Swami Martandpuriji and also for providing traditional knowledge about Rudraksha and motivation to generate scientific evidences for Ayurvedic system of Medicine.

REFERENCES

Aruvi, I. and M. Minnady. 2017. Detailed study on *Elaeocarpusganitrus* (Rudraksha) for its medicinal importance - A review. *Int J Curr Sci*. 20(1) E: 16-30.

Bagewadi, HG.andAKA. Khan. 2015. Evaluation of anti-parkinsonian activity of *Elaeocarpusganitrus* on haloperidol induced Parkinson's disease in mice. *International Journal of Basic and Clinical Pharmacology*. 4(1): 102-106.

Barve, KH.andR. Chodankar. 2014. Does copper enhance the antihypertensive effect of *Elaeocarpusganitrus* in experimentally induced hypertensive rats? *J Ayurveda Integr Med*. 5(2): 76–79

Dadhich, A., ND.Jasuja, S. Chandra and G. Sharma. (2014). Antidepressant Effects Of Fruit Extract of *Elaeocarpusganitrus* In Force Swim Test. *IJPSR* 5(7): 2807-12.

Dalei, J. and D, Sahoo. 2016. Evaluation of antimicrobial activity and phytochemical screening of epicarp and endocarp parts of *Elaeocarpusganitrus*. *Int J Pharm Bio Sci*. 7(2): 265 – 269.

Das, P., P. Kar, S. Hasnu, S. Nath and B. Tanti. 2017. Phytochemical screening and antioxidant activity of *Elaeocarpusserratus* L. of Assam. *Journal of Pharmacognosy and Phytochemistry*. 6(4): 866-869.

Das, PK. 2015. Phytochemical Screening of Methanolic Extracts of Different Parts of Rudraksh Plant (*Elaeocarpusganitrus*). *Online Journal of Biological Sciences* 15 (3): 111-112.

Dharmalingam, V., R. Ramalingam, R. Prabhu and I. Raju. 2017. Identification of Phenolic Compounds and Study the Antimicrobial Property of *Eleaocarpusganitrus* Fruits. *International Journal of Medical and Health Sciences*.4 (2): 151-152.

Hardainiyan, S., B.C. Nandy and K. Kumar. 2015. *Elaeocarpus Ganitrus* (Rudraksha): A Reservoir Plant with their Pharmacological Effects. *Int. J. Pharm. Sci. Rev. Res.* 34(1): 55-64

Jain, P.K., P. Sharma and S.C. Joshi. 2017. Effect of *Elaeocarpus Ganitrus* Roxb. On Kidney Function of Cholesterol Fed Rabbits. *Adv.Pharmacol. Toxicol.* 18 (2): 1-9

Jain, P.K., P. Sharma and S.C. Joshi. 2016. Effect of *Elaeocarpus Ganitrus* Roxb. On Hyperlipidaemia And Liver Function of Rabbit. *EJBPS*. 3(10): 326-333.

Jain, S., K. Jatwa, V. Jain, A. Sharma and S.C. Mahajan. 2014. A Review on *Elaeocarpus Sphaericus* (Rudraksha). *Pharmatutor*. 2(7): 83-91.

Jayashree, I.M., D.H. Geetha and M. Rajeswari.(2016). Evaluation of Anti-Microbial Activity of *Elaeo carpustuberculatus* Roxb. *American-Eurasian J. Agric. and Environ. Sci*. 16 (11): 1726-1731.

Joshi, S. and P. Jain. 2014. A review on ethnomedicinal and traditional uses of *Elaeocarpusganitrus*Roxb. (Rudraksha). *Int J Pharm Bio Sci.* 5(1): 495-511.

Kakalij, R.M., C.P. Alla, R.P. Kshirsagar, B.H. Kumar and S.S. Mutha. 2014. Ameliorative effect of *Elaeocarpusganitrus*on gentamicin-induced nephrotoxicity in rats. *Indian Journal of Pharmacology.*46 (3): 298-302.

Kumar, G., K. Loganathan and K.V.B. Rao. 2014. A Review on Medicinal Properties of *Elaeocarpusganitrus* Roxb. ex G. Don. (Elaeocarpaceae). *Research J. Pharm. and Tech*. 7(10): 1184-1186.

Lee, D.W. 1991. Ultrastructural Basis and Function of Iridescent Blue Color of Fruits in Elaeocarpus. Nature 349 (6306): 260-262.

Prajapati, S., R. Kumar and S.K. Prajapati. 2016. Electronic and bioelectric properties of *Elaeocarpus Ganitrus*. Der Pharmacia Lettre. 8 (8):45-49

Makhija, D., P. Makhija and B. Patil. 2015. Clinical evaluation of an ayurvedic formulation in the management of mental retardation. *Global J Res. Med. Plants andIndigen. Med*. 4(2): 38–45.

Ravishankar, B. and V. Shykla. 2007. Indian Systems of Medicine: A Brief Profile. *Afr. J Tradit Complement Altern Med* 4(3):319-337.

Shah, G., R. Shri, A. Mann, S. Rahar and V. Panchal. (2010). Anxiolytic effects of *Elaeocarpussphaericus* fruits on the elevated plus-maze model of anxiety in mice. *Int J Pharm Tech Res.* 2(3):1781-1786.

Sharma, A., S. Joshi and N. Kumar. 2015. Antioxidant and antibacterial properties of leaves of *Elaeocarpussphaericus* Roxb. And *Pinuswallichiana*from Uttarakhand region of India. *International Journal of Green Pharmacy*. 9 (4):246-251.

Sharma, S., B. Rawat, Jayanand, D.V. Rai and M. Rastogi. 2018. Biological and Mineralogical properties of *Elaeocarpus Ganitrus* (Rudraksha). *Biochemical and Cellular Archives.*18: 1699-1703.

Singh, B., A. Chopra, M.P.S. Ishar, A. Sharma and T. Raj. 2010. Pharmacognostic and antifungal investigations of *Elaeocarpusganitrus* (Rudrakasha). Indian J Pharm Sci. 2010 Mar-Apr; 72(2): 261–265. doi: 10.4103/0250-474X.65021

Singh, A.K. and D.V. Rai. 2018.The Variation In Physical Properties Affects The Vertical Compressive Strength Of The Rudraksha-Bead (Elaeocarpus Ganitrus Roxb), *International Journal of Mechanical Engineering and Technology (IJMET),* 7(3): 267-275.

Singh, A.K., R. Kumar and D.V. Rai. 2016. Study on Engineering Properties of Rudraksha (*Elaeocarpusganitrus* Roxb.) for Design and Development of Agricultural Processing Units *International Journal of Scientific and Engineering Research*, 7(5): 105-118.

Tilak, A., S.S. Gangwar, R.N. Thakur and R. Sharma. 2017. *Elaeocarpus Ganitrus* (Rudraksha) Medicinal Use in Modern Time. *Imperial Journal of Interdisciplinary Research (IJIR)*.3(1).

Tripathy, S., A. Mida and S.R. Swain. 2016-a. *Elaeocarpusganitrus* (Rudraksha), the amazing electromagnetic bead of nature to redeem mankind from disease, sickness and medicinal problem. *World Journal of Pharmacy and Pharmaceutical Science*.5 (9): 1122-1130.

Tripathy, S., A. Midaand S.R. Swain.(2016-b).Acupressure and Magnetic Healing In relation to *Elaeocarpus Ganitrus* Seed (Rudraksha). *Am. J. Pharm Health Res.*4(8): 2321-3647.

Tripathy, S., A. Mida and S.R. Swain. 2016-c. Antimicrobial and Hypoglycemic Effects of *Elaeocarpus Ganitrus* Seed. *Imperial Journal of Interdisciplinary Research (IJIR).*1(1): 70-76.

Tripathy, S., A. Mida and S.R. Swain. 2016-d. Assessment of Phytoconstituent of Five Faced *Elaeocarpusganitrus* Beads by FTIR and UV-VIS Spectroscopic Analysis. *Imperial Journal of Interdisciplinary Research (IJIR).*2(10): 32-35.

Tripathy, S., A. Midaand S.R. Swain. 2016-e. Antidepressant and Antibacterial Activity of *Elaeocarpusganitrus* Seed (Rudrakasha) *Imperial Journal of Interdisciplinary Research (IJIR).*2(10): 305-310.

Pb. Univ. Res. J (Sci.) Vol. 68, 2018, pp 7-14

STEP-BUNCHED Si (111) TEMPLATE FOR PRODUCTION OF PLANAR PERIODIC NANOSTRUCTURES

Sunil K. Arora[1*] and Igor V. Shvets[2]

[1]*Centre for Nanoscience and Nanotechnology, Panjab University, Sector-25, Chandigarh-160014, India*

[2]*School of Physics, Trinity College, the University of Dublin, Ireland*

Abstract

We utilize dc-current annealing to exploit the electromigration induced step bunching on vicinal Si (111) surface to produce highly periodic step-bunches on Si (111). By controlling the direction of current and cooling rate across the (7x7) to (1x1) surface reconstruction transition temperature of Si (111) surfaces, we produce highly periodic step-bunched Si (111) templates with controlled periodicity ranging from 30 nm to 3 μm. Using shallow angle deposition of Fe and Co on these templates we fabricate aligned array of planar nanostructures. The planar magnetic nanowire and nanoislands arrays of Fe and Co are found to be ferromagnetic at room temperature. The template production ability combined with shallow angle deposition provide a platform to produce planar nanostructures and open up possibility of studying various fundamental aspects at nanoscale and in realizing applications. Moreover, this approach is not restricted to specific materials and template combinations which has been a major concern for many of the self-assembly techniques used earlier to realize planar nanostructures.

Keywords: Si (111) template, planar periodic nanostructures, shallow angle deposition.

INTRODUCTION

Synthesis, characterizations and applications of aligned low dimensional (0-D and 1-D) nanostructures (quantum dots, nanowires, nanorods, nanotubes and nanobelts) is an important areas of current endeavor in nanoscience and nanotechnology, as it offers a platform to test some of the intriguing science concepts and realization of new functionality for applications (Albrecht *et al*. 2000, Elnathan *et al*. 2014, Wiame *et al*. 2017). Many techniques have been developed to produce aligned nanostructures (NS), e.g. strain driven nanostructure growth during epitaxy (Stangl *et al.* 2004, Guiliani *et al*. 2018), lithography based methods (Seisyan *et al.* 2011, Assenbergh *et al*. 2018, Lei *et al*. 2007), self-assembly on surfaces (Greybush *et al*. 2017, Elacqua *et al*. 2017, Confalonieri *et al*. 2011) , and template assisted directed self-assembled growth or arrangement of nanostructures (Dikovska *et al*. 2014, Paiano *et al*. 2014). It has been shown that use of patterned catalyst/seed layer in the form of nano- or micro-structured dots/squares arrays enables one to produce site controlled arrays of vertical nanostructures of carbon nanotubes, GaAs and ZnO nanorods. Another such example is production of site controlled InAs quantum dot synthesis using a combination of nano-patterned surface and strain layer epitaxy (Maier *et al*. 2014). Many of these approaches are based on expensive lithography and thin film deposition methods.

also been used, such as nanochannel array on glass (Tonucci *et al*. 1992), radiation track-etched mica (Possin *et al*. 1970), mesoporous materials (Wu *et al*. 1994), porous silicon obtained via electrochemical etching of silicon wafer (Fan *et al*. 1999), zeolites (Enzel *et al*. 1992), and carbon nanotubes (Ajayan *et al*. 1995). Biotemplates have also been explored for the growth of nanowires and nanotubes (Gasparac *et al*. 2004). In the templates based approaches discussed above the growth nanostructures occurs along the thickness of nano-pores of the templates leading to out-of plane array of NSs. In many cases, after the growth of NS, the template is to be sacrificed. Some of the templates mentioned above cannot withstand higher temperatures during growth inhibits realization of single crystalline nanostructures, which limits the utility of the approach.

In order to exploit the electrical and optoelectronic properties of NS for applications, one requires templates on which nanostructures can be grown/arranged in planar configuration (Arora *et al*. 2012a, Jeschke *et al*. 2018, Tripathi *et al*. 2011). To realize planar nanowire arrays self-assembled templates based on vicinal substrates (a single crystal substrate having its surface cut at certain offset angle from a principal crystallographic direction) have been used in producing nanostructures using step flow, step decoration and reactive deposition epitaxy (Goldfarb *et al*. 2017, Radican et al. 2008, Akiyama *et al*. 2006). The small thickness of the nanostructures achieved using these methods (leading to superparamagnetism for magnetic NSs) and material selective nature (applicable only for certain material and substrate combinations) restricts their scope for future applications. To overcome the hurdles related to the small thickness of nanostructures, in an earlier report

we showed the production of planar magnetic nanowire arrays of Fe and Co using a shallow angle deposition method on vicinal surfaces (Arora *et al*. 2012a).

*Corresponding Author: aroras@pu.ac.in

MS Received: October 15, 2018, Accepted: December 3, 2018

In this paper we report on the preparation of step-bunched silicon templates (having parallel array of bunched steps and terraces surfaces) using dc-current annealing in UHV that produces regular array of step-bunches on vicinal silicon (111) with varying periodicity periodicity (30 nm to 3 μm). We further demonstrate the producing of highly periodic planar nanowire arrays and nanodots arrays of Fe and Co.

EXPERIMENTAL:

To produced step-bunched templates we exploit the eletromigration induced step-bunching in vicinal Si (111) (Gibbons *et al*. 2005). The vicinal Si templates used in the present study were prepared by performing a dc-current annealing under ultrahigh vacuum (UHV) conditions on n-type doped Si (111) with resistivity 1–10 Ω.cm. The 0.525-mm-thick wafers were cut into 20 x 1.5 mm2 rectangular strips with the long side along the miscut direction. The Si substrates had a miscut of 2.5 or 4 degrees along the (112) crystallographic direction. The samples were annealed at 1120^{o}C or 920^{o}C with a direct current perpendicular to the step edges, with current being either in the ascending (uphill, UH) or descending step (downhill, DH) directions. The temperature was monitored using an infra-red pyrometer. The annealed Si templates were oxidized (about 100 nm oxide thickness) using standard thermal oxidation procedure carried out at 830^{o}C for a duration of 15 hrs.

Deposition of nanostructures on step-bunched Si templates was performed using a shallow angle deposition technique (Arora *et al*. 2012a) which utilizes the geometric shadowing caused by the step-terrace structure of the template as illustrated in Figure 1. The growth was carried out at room temperature by directing the deposition flux (0.02–0.04 A ° /s) of Fe and Co onto the templates at a small angle (0.5-5^{o}) using a multi-pocket e-beam evaporator (Telemark, USA) in a UHV chamber with a base pressure of better than 5 x 10^{-10} Torr. The deposition flux was directed towards the ascending/descending step direction to either cover the step bunces completely or terraces partially by adjusting the deposition angle.

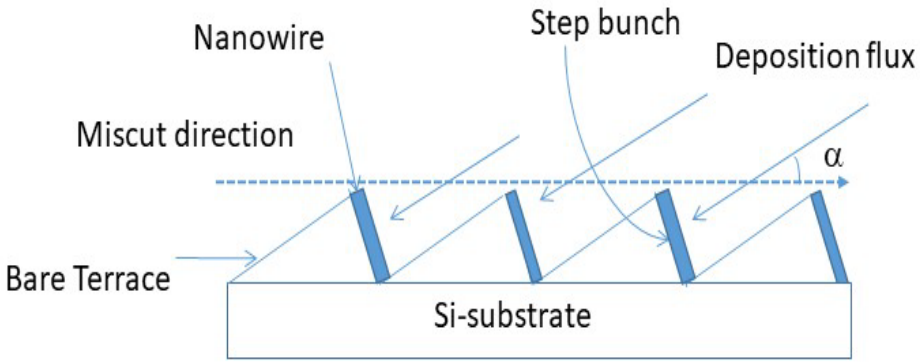

Figure 1: Deposition of nanostructures on a step-bunched template utilizing shallow angle deposition. A case of ascending step direction is illustrated in which the shallow angle produces fully or partially covered step-bunches depending on the deposition angle α.

The morphology of the templates and nanosrtcutrues deposited onto the templates characterized using an atomic force microscope (AFM, Solver Pro, NT-MDT) operated in semi-contact mode and a scanning electron microscope (SEM, Ziess Ultra). The magnetic properties of the nanostructured arrays were examined using a vibrating sample magnetometer (Quantum Design Physical Property Measurements system) with a sensitivity of 5 x 10^{-7} emu. The diamagnetic contribution from the substrate was removed from the measured data by subtracting a M–Hloop of the bare substrate. Uncertainty in the nanostructure's volume determination could be as large as 10% arising mostly from the statistical fluctuations in the terrace coverage that are related to the distribution of step-terrace periodicity of the template, whereas the thickness of the deposited material is accurate within 2%. The element specific x-ray absorption (XAS) and x-ray magnetic circular dichroism (XMCD) experiments were carried out at the ESRF's ID08 beamline.

RESULTS AND DISCUSSION:

Figure 2 shows the AFM height images and corresponding height profiles of the Si (111) step-bunched templates produced using the dc current annealing. The annealing conditions are mentioned on the corresponding figure. The resulting ordered arrays of bunches of atomic steps separated by wide (111) terraces, where the average step-edge to step-edge distance (known as the "periodicity") is on the order of a μm. It is known that at the anneal temperature (1100^{o}C in our case) the Si (111) surface adopts a (1×1) disordered phase, but below approximately 850^{o}C it reconstructs to the (7×7) reconstruction. This (7×7) reconstruction is believed to play a key role in the stabilisation of the step-bunch array (Homma *et al.* 1990, Takayanagi *et al.* 1985). The annealing at 1100^{o}C for 6 hours with current applied in the ascending step direction (uphill, UH) current and subsequent quenching to RT leads to wide step bunches with step-terrace periodicity of 3.2 μm and terrace width of 1.8 μm. One notices that the observed step-bunches are quite regular and straight. Similarly when the vicinal Si stripes are annealed with a dc current in the descending step direction (downhill, DH) current at 1100^{o}C and quenched to RT, we observe step-terrace periodicity of around 30 nm, with irregular step-bunch height and periodicity (not shown). This situation is improved if instead of quenching from 1100oC to RT, we first cool it to 920^{o}C (a temperature above (7x7) to (1x1) Si surface reconstruction transition temperature) and hold at this temperature for 4-6 hours and cool it slowly across the transition temperature. The slow cooling across the transition temperature allows greater mass flow on the surface and enable in straightening of step-bunches and widening of terraces.

Figures 2b and 2c shows the AFM images of templates obtained with cooling rates of 0.01^{o}C/sec and 10^{o}C/min leading to highly periodic step-terrace arrays. The corresponding periodicities are 1.1 um and 90 nm. One can see that the step-bunches are quite uniform as indicated by the height profiles of the images shown in figure 2 d-f. The aspect ratio (periodicity to length) of the step bunches is quite large e.g. for 90 nm periodicity template the step are straight upto 1.4 μm leading to an aspect ratio > 15.

We utilize these step-bunched periodic templates to produce nanosrtcutures by depositing materials on them by direction the deposition flux on them at a shallow angle in the uphill direction or downhill direction (Fig.1). The shadowing of the flux caused step-bunches or terraces produces partially covered terraces or step-bunches. Figure 3 shows AFM images of planar arrays of Fe stripes (micro- and nano-wires) grown on oxidized templates of two different periodicities ranging between 3.2 μm to and 110 nm. Deposition of NW arrays is realized by driving the deposition flux of Fe toward the downhill direction of the step-bunched template.

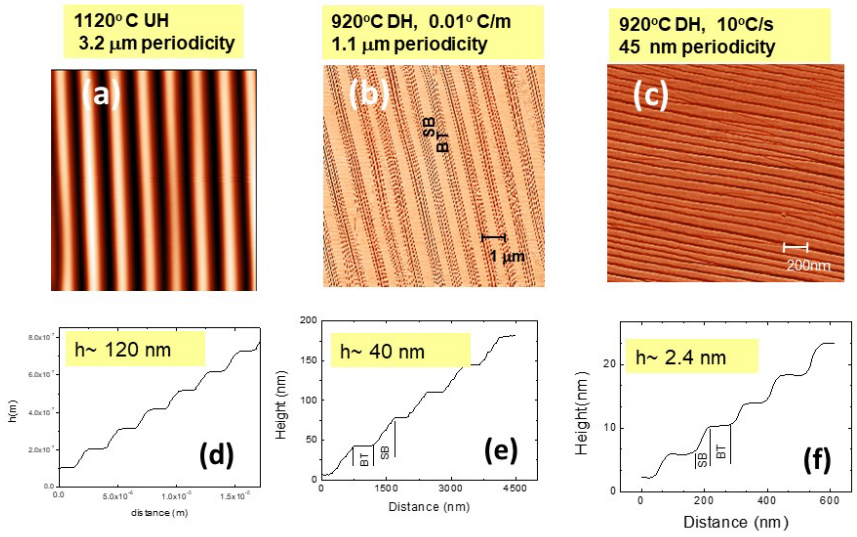

Figure 2: AFM height images of step-bunched templates obtained by annealing 4degree miscut Si (111) prepared with different annealing conditions. (a) annealed at 1120^{o}C for 12 hrs with uphill direct current and quenched to room temperature giving 3.2 μm periodicity with wide step-bunches and terraces of 1.4 and 1.8 μm widths, respectively. (b) and (c) shows the step-bunched templates obtained with downhill current and annealed at 920^{o}C for 12 hrs followed by a cooling to RT with 0.01 or 10^{o}C per minute rate giving step-terrace periodicity of 1.1 μm and 45 nm, respectively. In the lower panels figures (d-f) are shown the height profiles for the corresponding images. Height of the step-bunches obtained is also listed in the image.

It can be seen from the figure that depending on the deposition angle and miscut strength, one can change the coverage of the terraces (i.e. wire/stripe width) by modifying the extent of shadowing of the deposited Fe flux caused by the step-bunches.

Figure 1(a) shows an AFM height image and height profile of a l μm wide Fe microwire array prepared at a deposition angle of 2^o on 3.2 μm periodic template. A corresponding height profile of the image is shown in Fig. 3b the area corresponding to step-bunch, NW and bare terrace are labelled on the image. Average terrace coverage in this case is 60%. Figure 1(c) shows an AFM height image of a Fe NW array grown at a deposition angle of 1.2 degree on a 110 nm periodicity template. The reduced deposition angle produces on average 30 percent terrace coverage corresponding to an average wire width of 30 nm.

The average thickness of the Fe-NWs determined from the height profiles is 5.0 and 4.8 nm for the samples deposited on 3.2 μm and 110 nm periodicity templates. One notices that the periodic arrays of Fe are quite regular with wires remaining straight up to several μm in length for the 30 nm wire width arrays leading to a large aspect ratio (length/width ratio). The crystal structure of Fe in the NW arrays was found to be bcc, as revealed by the transmission electron microscopy investigations (images not shown). Interfaces of Fe-NWs, formed with the SiO_2 substrate and the cap layer of MgO possess a crystal structure that resembles fcc Fe-O structure. Detailed TEM characterization of the Fe-NWs and their magnetic properties determined through bulk magnetometery are described in detail in a previous article. (Arora *et al*. 2012a, Arora *et al.* 2012b).

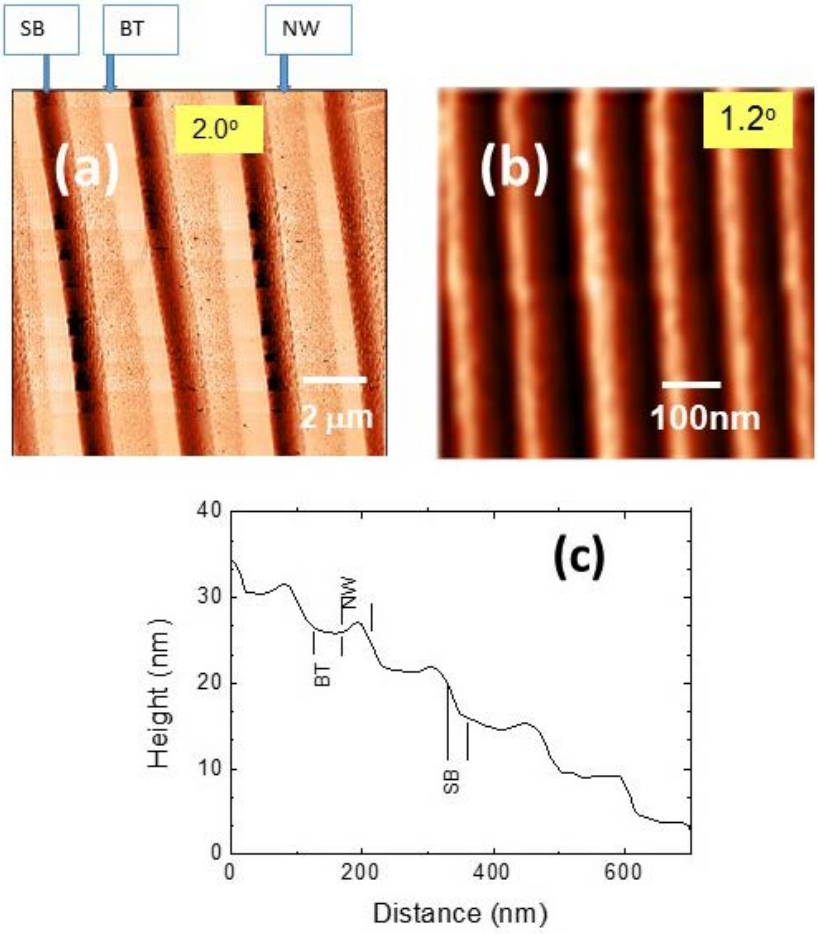

Figure 3: Shows the AFM height images of Fe stripes (micro- and nano-) deposited on a 4 degree miscut Si (111) template deposited with a downhill deposition flux of Fe (a) at 2 degree deposition angle on a 3.2 um periodicity template and (b) on 110 nm periodic template at 1.2 degree deposition angle. (c) Shows a line profile of the image shown in (b) with nanowire, bare terrace and step bunch area marked as NW, BT and SB.

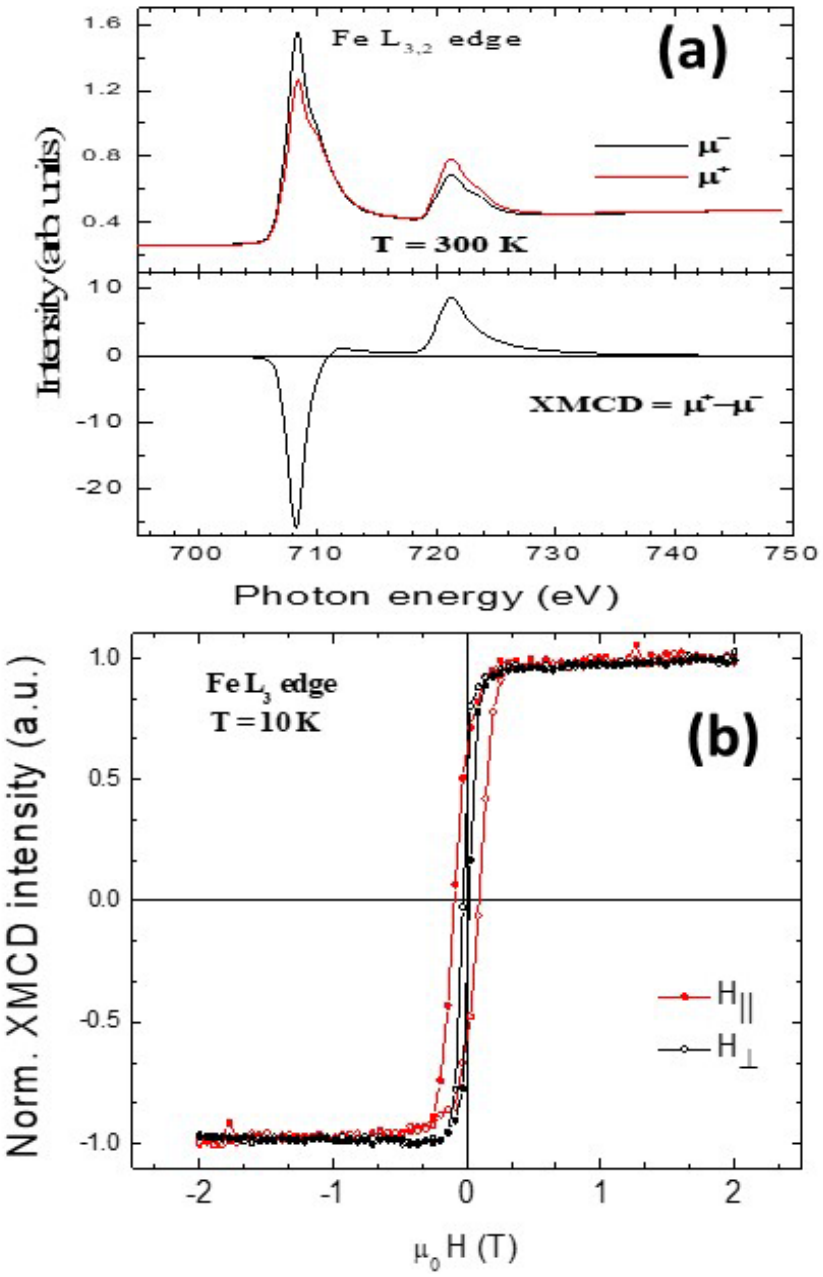

Figure 4: X-ray absorption spectra (upper panels) and corresponding XMCD spectra (lower panels) measured at 300 for the Fe L3,2 edge for a Fe NW array sample capped with 3 nm MgO with average wire width of 30 nm The spectra were recorded in the TEY mode. (b) Shows the XMXD hysteresis of the Fe NW array measured at 10 K with magnetic field parallel and perpendicular to the length of the nano wires.

Figure 4 shows the XAS spectra measured at the Fe L3,2 edge for a Fe-NW array with average wire width and thickness being 30 nm and 4.5 nm, respectively, and capped with a 3nm MgO layer. The spectra are normalized to the incident flux and pre-edge. XAS line shape is typical of metallic Fe but shows sign of oxidation, owing to the presence of oxidized interface with the cap layer of MgO and hybridization of O_{2p}-Fe_{3d}. XMCD signal (μ^+-μ^-) determined from the two XAS spectra is also shown in the lower panel. Here, μ^+ (μ^-) refers to the absorption coefficient for the photon helicity parallel (antiparallel) to the Fe 3d majority spin direction. The XMCD sum rules (Thole *et al*. 1992, Carra *et al*. 1993) were applied to extract information on the spin and orbital magnetic moments of the Fe-NW arrays both at RT (300 K), and low temperature
(10 K). The calculated values of magnetic moments at 300 (10) K are found to be; spin magnetic moment (m_s)=2.68 (3.15) μ_B/hole and orbital magnetic

moment (m_l) = 0.01 (0.04) μ_B/hole. For the evaluation of m_s and m_l, we assumed n_h (number of holes in the 3d states) 3.4 for iron, and negligible value of spin dipolar term. We also notice that the dimensionality effects that are known to enhance m_s and m_L in ultrathin Co atomic chains (Gambardella *et al*. 2002) are absent in these NW arrays of Fe due to relatively large thickness of the wires. Also shown in the figure is the hysteresis loop of Fe NW array measure at 10 K determined from the XMCD data measured with varying magnetic field applied parallel or perpendicular to the length of the nanowires. One can clearly notice that the loop measured with magnetic field parallel to the NWs shows a larger coercivity. Whereas the loop observed for the magnetic field applied perpendicular to the NW length. This suggests that magnetic anisotropy of the NW array is dominated by the shape anisotropy which keeps the magnetization in-plane with easy axis along the length of the wires (He *et al*. 2007).

We now discuss example of producing aligned nano-island chains and/arrays on step-bunched Si (111) templates. Figure 5 show SEM image of aligned nanoislands arrays of Co-produced on step-bunched templates by depositing the Coin the DH and UH directions at an elevated temperature of 200^{o}C. One notices that in case of DH deposition, because of the larger width and partial coverage of terraces, a dense array of nanoislands in the form of a stripe pattern is observed with the stripe width accommodate more than one island. This island type morphology is related to the fact that Co grows with an island type growth mode on oxidized silicon. These isolated islands form discontinuous stripe/chains of aligned nano-islands on the terraces.

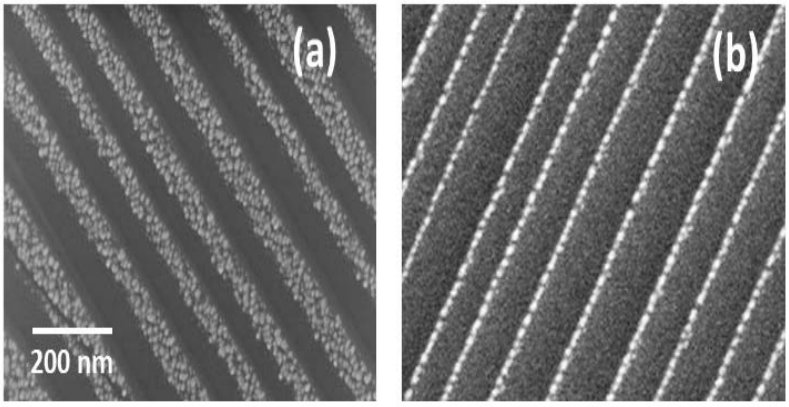

Figure 5: SEM image of the Co deposited on 110 nm periodic template deposited at 200 degrees C deposition flux direct (a) uphill and (b) downhill direction.

With increasing thickness, the density of these islands is enhanced leading to coalescence of the islands and forming a stripe of coalesced islands. Figure 5b shows an SEEM image of Co nanoislands produced with the deposition flux directed in the uphill direction leading to deposition on the step-buched facet of the template. Since its width is much smaller than the terrace, only one island of Co cover the facet, leading to an aligned array of Co islands along the length of step–buched facet. The magnetic properties of these aligned arrays depended on the density of island and their separation and thickness, determining whether they are magnetically interacting or not determines whether one observes a superparamagnetic or ferromagnetic behavior. We wish to emphasize that by selecting appropriate deposition angle and material-substrate combination, one can produce interacting nano-island of different materials. In a previous study we have grown Ag islands on stepped alumina templates and studies their plasmonic response.

CONCLUSION:

We have shown that by selecting suitable annealing condition, one can produce step-bunched Si (111) templates with controlled periodicity ranging from 30 nm to 3 μm. The templates produced are highly regular and periodic. We also showed the utility of these templates in producing planar nano-stripes (nanowires) and nano-island arrays. We demonstrated the successful production of planar magnetic nanowire and nanoislands arrays of Fe and Co respectively. The template production ability combined with shallow angle deposition provide a platform to produce planar nanostructures and open up possibility of studying various fundamental aspects ot nano-systems and exploit the knowledge for realizing applications.

ACKNOWLEDGEMENTS

This research is supported by the Science Foundation Ireland (SFI) under Contract No. 06/IN.1/I91.

REFERENCES:

Albrecht, T.T., J. Schotter, G.A. Kästle, N. Emley, T. Shibauchi, L. Krusin-Elbaum, K. Guarini, C.T. Black and M.T. Tuominen, T.P. Russell. 2000. Ultrahigh-Density Nanowire Arrays Grown in Self-Assembled Diblock Copolymer Templates *Science 290, 2126-2129*

Ajayan, P.M., O. Stephan, P. Redlich and C. Colliex. 1995. Carbon nanotubes as removable templates for metal oxide nanocomposites, nanostructures, *Nature 375, 564–567*

Akiyama, Y. and H. Sakaki, 2006. Formation of self-assembled InGaAs quantum dot arrays aligned along quasiperiodic multiatomic steps on vicinal (111) B (111) B GaAs *Appl. Phys. Lett. 89, 183108*

Arora, S.K., B.J. O'Dowd, B. Ballesteros, P. Gambardella, and I.V. Shvets. 2012a. Magnetic properties of planar nanowire arrays of Co fabricated on oxidized step-bunched silicon templates *Nanotechnology 23 235702*

Arora, S.K., B. J. O'Dowd, C. Nistor, T. Balashov, B. Ballesteros, A. Lodi Rizzini, J. J. Kavich, S. S. Dhesi, P. Gambardella and I. V. Shvets. 2012b. Structural and magnetic properties of planar nanowire arrays of Co grown on oxidized vicinal silicon (111) *templates. Journal of Applied Physics 111, 07E342*

Assenbergh, P.V., E. Meinders, J. Geraedts, D. Dodou, D. 2018. Nanostructure and Microstructure Fabrication: From Desired Properties to Suitable Processes *Small 14, 1703401*

Barriga J.S., M. Lucas, F. Radu, E. Martin, and M. Multigner. 2009. Interplay between the magnetic anisotropy contributions of cobalt nanowires *Phys. Rev. B 80 184424*

Carra, P., B. T. Thole, M. Altarelli, and X. Wang, 1993. X-ray circular dichroism and local magnetic fields *Phys. Rev. Lett. 70, 694*Confalonieri., G.A.B., V. Vega, A. Ebbing, D. Mishra., P. Szary, V. M. Prida, O. Petracic and H. Zabel. 2011. Template-assisted self-assembly of individual and clusters of magnetic nanoparticles *Nanotechnology 22 285608 (2011)*

Dikovska, A.O., M.E. Koleva, G.B. Atanasova, T.R. Stoyanchov, N.N. Nedyalkov, and P.A. Atanasov, 2014. PLD fabrication of ZnO nanostructures on metal-coated substrates. *Journal of Physics: Conference Series 514 012032*

Elacqua, E., X. Zheng, and M. Weck. 2017. Light-Mediated Reversible Assembly of Polymeric Colloids. *ACS Macro Letters 6*, 1060-1065.

Elnathan, R., M. Kwiat, F. Patolsky and N.H. Voelcker. 2014. Engineering vertically aligned semiconductor nanowire arrays for applications in the life sciences *Nano Today 9, 172-196*

Enzel, P., J.J. Zoller and T. Bein. 1992. Intrazeolite assembly and pyrolysis of polyacrylonitrile, *J. Chem. Soc. Chem. Commun. 8, 633–635*

Fan, S., M.G. Chapline, N.R. Franklin, T.W. Tombler, A.M. Cassell and H. Dai: Self-oriented regular arrays of carbon nanotubes and their field emission properties, *Science* 283, 512–514 (1999)

Furneaux, R.C., W.R. Rigby, and A.P. Davidson. 1989. The formation of controlled-porosity membranes from anodically oxidized aluminium, *Nature 337, 147–149*

Gambardella P., A. Dallmeyer, K. Maiti, M. C. Malagoli, W. Eberhardt, K. Kern, and C. Carbone. 2002. Ferromagnetism in one-dimensional monatomic metal chains *Nature 416, 301*

Gasparac, R., P. Kohli, M.O.M.L. Trofin, and C.R. Martin. 2004. Template synthesis of nano test tubes, *Nano Lett. 4, 513–516*

Gibbons, B. J., J. Noffsinger, and J. P. Pelz. 2005. Influence of Si deposition on the electro-migration induced step bunching instability on Si (111) *Surf. Sci. Lett. 575, L51-L56*

Greybush, N.J., I. Liberal, L. Malassis, J.M. Kikkawa, N. Engheta, C.B. Murray and C.R. Kagan. 2017. Plasmon Resonances in Self-Assembled Two-Dimensional Au Nanocrystal Metamolecules. *ACS Nano 11*, 2917-2927

Goldfarb, I., Y. Camus, M. Dascalu, F. Cesura, R. Chalasani, and A. Kohn, 2017. Tuning magnetic response of epitaxial iron-silicide nanoislands by controlled self-assembled growth Phys. Rev. B 96, 045415

Guiliani, J., J. Cadena and C. Monto. 2018. Template-assisted electrodeposition of Ni and Ni/Au nanowires on planar and curved substrates Nanotechnology 29 075301

He, H. and C. Chen. 2007. Effect of temperature-dependent shape anisotropy on coercivity for aligned Stoner-Wohlfarth soft ferromagnets *Phys. Rev. B 75 184424*

Homma, Y., R. McClelland and H. Hibino. 1990. DC-Resistive-Heating-Induced Step Bunching on Vicinal Si (111) *Japanese Journal of Applied Physics 29 L2254*

Jeschke, J., M. Martens, S. Hagedorn, A. Knauer, A. Mogilatenko, H. Wenzel, U. Zeimer, J. Enslin, T. Wernicke and M. Kneissl. 2018. Influence of template properties and quantum well number on stimulated emission from Al0.7Ga0.3N/Al0.8Ga0.2N quantum wells Semiconductor Science and Technology 33, 035015 Lei, Y., W. Cai, G. Wilde .2007. Highly ordered nanostructures with tunable size, shape and properties: A new way to surface nano-patterning using ultra-thin alumina masks Progress in *Materials Science 52, 465-539*

Maier, S., K. Berschneider, T. Steinl, A. Forchel, S. Höfling1, C. Schneider and M. Kamp. 2014. Site-controlled InAs/GaAs quantum dots emitting at telecommunication wavelength *Semiconductor Science and Technology, 29, 052001* Seisyan, R.P. 2011. Nanolithography in microelectronics: A review Technical Physics 56, 1061

Paiano, I.P., P. Prete, E. Speiser, N. Lovergine, W. Richter, L. Tapfer and A.M. Mancini. 2007. GaAs nanowires grown by Au-catalyst-assisted MOVPE using tertiarybutylarsine as group-V precursor *Journal of Crystal Growth,298 620-624*

Possin, G.E., 1970. A method for forming very small diameter wires, *Rev. Sci. Instrum. 41, 772–774*

Radican, K., N. Berdunov, and I.V. Shvets. 2008. Studies of the periodic faceting of epitaxial molybdenum oxide grown on Mo (110) Phys. Rev. B 77 085417

Stangl, J., V.Holý, and G. Bauer. 2004. Structural properties of self-organized semiconductor nanostructures Reviews of Modern Physics 76, 725-783

Takayanagi, K. 1985. Structural analysis of Si (111) - 7×7 by UHV-transmission electron diffraction and microscopy *Journal of Vacuum Science & Technology A: Vacuum, Surfaces, and Films 3, 1502*

Thole, B.T., P. Carra, F. Sette, and G. van der Laan. 1992. X-ray circular dichroism as a probe of orbital magnetization *Phys. Rev. Lett. 68, 1943*

Tonucci, R.J., B.L. Justus, A.J. Campillo, and C.E. Ford. 1992. Nanochannel array glass, *Science 258, 783–787 (1992)*

Tripathi, J.K., M. Garbrecht, Claudia G. Sztrum-Vartash, Eran Rabani, Wayne D. Kaplan, and I. Goldfarb.2011. Coverage-dependent self-organized ordering of Co- and Ti-silicide nanoislands along step-bunch edges of vicinal Si (111) Phys. Rev. B 83, 165409

Wiame, F. 2017 Strategies for the growth of large-scale self-organized structures *Thin Solid Films 642, 258-275*

Wu, C., T. Bein: Conducting polyaniline filaments in a mesoporous channel host, Science 264, 1757–1759 (1994)

Pb. Univ. Res. J (Sci.) Vol. 68, 2018, pp 15-24

FORMULATING MODEL INDEPENDENT YUKAWA MATRICES

Rohit Verma*
Department of Applied Sciences, Chitkara University - Himachal Pradesh, Pinjore-Barotiwala, Himachal Pradesh – 174 103, India

Abstract

We extract vital clues towards the formulation of Yukawa matrices Y_q (q = u,d) in a model independent way. The available quark mixing data unequivocally suggests that the corresponding Yukawa matrices must have a natural structure, *i.e.*, $Y_{11} < Y_{12,21} < \sim Y_{13,31} < Y_{22} < Y_{23,32} < Y_{33}$, with $Y_{22} << Y_{33}$, especially when $Y_{13,31}$ off-diagonal elements in these are $\sim \sqrt{m_u m_t}$ for the up type and $\sim \sqrt{m_d m_s}$ for the down type Yukawa matrices, respectively. Such strongly hierarchical Yukawa structures not only provide a natural explanation for $|V_{us}| \cong |V_{cd}|$, $|V_{cb}| \cong |V_{ts}|$, and $|V_{ub}/V_{cb}| < |V_{td}/V_{ts}|$, but are also in excellent agreement with the observed quark mixing and CP-violation data up to 1σ C.L.

Keywords: Standard model, Yukawa matrices, Quark mixing, CP violation

INTRODUCTION

In the Standard Model (SM), the weak charged current quark interactions are given as

$$-L_{cc} = \frac{g}{\sqrt{2}} \overline{(u \quad c \quad t)}_L \gamma^\mu V \begin{pmatrix} d \\ s \\ b \end{pmatrix}_L \left(W_\mu^+\right) + h.c. \quad (1)$$

The Cabibbo-Kobayashi-Maskawa (CKM) matrix (Cabibbo 1963; Kobayashi and Maskawa, 1973) or the quark mixing matrix, V, measures the non-trivial mismatch between the flavor and mass eigenstates of quarks such that

$$U_L^{u\dagger} Y_u Y_u^\dagger U_R^u = Diag(m_u^2,\, m_c^2,\, m_t^2),$$

$$U_L^{d\dagger} Y_d Y_d^\dagger U_R^d = Diag(m_d^2,\, m_s^2,\, m_b^2) \quad (2)$$

where Y_u and Y_d denote the Yukawa matrices for the up-type and down-type quarks, respectively. The elements of $V = U_L^{u\dagger} U_L^d$ are thereby related to the quark mass ratios and non-trivial phase differences between Y_u and Y_d. Unfortunately, the matrices Y_u and Y_d are not constrained by the SM gauge symmetry and hence are arbitrary 3 × 3 complex matrices involving 36 free parameters, way large as compared to the ten physical observables, *viz.*, the six quark masses, three mixing angles and a CP-violating phase. In the absence of flavor-changing right-handed currents, one can always redefine the right-handed quark fields such that the resulting quark mass matrices are Hermitian (Liu and Zhou, 2013), in general, thereby reducing the free parameters in these to 18. As a result, one does not lose generality in restricting the analysis to Hermitian matrices Y_u and Y_d.

Interestingly, the quark masses as well as the elements of V, observe a hierarchical pattern, *viz.*, $m_1 \ll m_2 \ll m_3$ and (V_{ub}, V_{td}) < (V_{cb}, V_{ts}) < (V_{us}, V_{cd}) < (V_{ud}, V_{cs}, V_{tb}). It is natural to expect this hierarchy to be embedded within the Yukawa matrices. In particular, one may start in the "u-diagonal" basis, wherein $Y_u = Y_u^{Diag} = Diag\{m_u, m_c, m_t\}$ is real diagonal and the CKM matrix V diagonalizes Y_d such that

$$Y_d = V Y_d^{Diag} V^\dagger = \begin{pmatrix} e_d & a_d e^{i\alpha_d} & f_d e^{i\delta_d} \\ a_d e^{-i\alpha_d} & d_d & b_d e^{i\beta_d} \\ f_d e^{-i\alpha\delta_d} & b_d e^{-i\beta_d} & c_d \end{pmatrix} \quad (3)$$

From the current experimental data and the unitarity of V, the magnitudes of all the nine CKM matrix elements have now been determined to a reasonably high degree of accuracy (Olive *et al*. 2014; Ahuja *et al*. 2007, 2012):

$$|V| \sim \begin{pmatrix} V_{ud} & V_{us} & V_{ub} \\ V_{cd} & V_{cs} & V_{cb} \\ V_{td} & V_{ts} & V_{tb} \end{pmatrix} = \begin{pmatrix} 0.97427 \pm 0.00014 & 0.22536 \pm 0.00061 & 0.00355 \pm 0.00015 \\ 0.22522 \pm 0.00061 & 0.97343 \pm 0.00015 & 0.0414 \pm 0.0012 \\ 0.00886^{+0.00033}_{-0.00032} & 0.0405^{+0.0011}_{-0.0012} & 0.99914 \pm 0.00005 \end{pmatrix} \quad (4)$$

*Corresponding Author: rohitverma@live.com
MS Received: October 11, 2018, Accepted: December 24, 2018

The above observation indicates

$$|V_{us}| \cong |V_{cd}|, |V_{cb}| \cong |V_{ts}|,$$

$$|V_{ub}/V_{cb}| < |V_{td}/V_{ts}|. \quad (5)$$

As a result, one expects (for $q = u, d$)

$$e_q < a_q < \sim f_q < d_q < b_q < c_q \quad (6)$$

with $d_q << c_q$ both in the u- and d-diagonal basis. Such mass matrices are also referred to as natural mass matrices (Peccei and Wang, 1996; Verma, 2013a).

For example, an order estimate for the general structure of the mass matrix Y_d, in the u-diagonal representation, can be made using m_d = 2.9 MeV, m_s = 55 MeV and m_b = 2.9 GeV (Xing *et al*., 2012) along with the mean values of above CKM elements:

$$|Y_d| = \begin{pmatrix} 0.0055 & 0.0131 & 0.0107 \\ 0.0131 & 0.0572 & 0.1215 \\ 0.0107 & 0.1215 & 2.8948 \end{pmatrix} GeV \quad (7)$$

Interestingly, it seems that the observed strong hierarchy among the quark masses and CKM elements gets naturally translated onto the structure of the corresponding Yukawa (or quark mass) matrices, predicting certain very simple yet compelling relations between the elements of the CKM matrix and the quark mass ratios (Fritzsch, 1979; Fritzsch and Xing, 2003; Xing and Zhang, 2004; Hall and Rain 1993; Ramond *et al*. 1993; Barbieri *et al*., 1999; Roberts *et al*. 2001; Kim *et al*. 2004; Branco *et al*. 2007):

$$V_{us} = \sqrt{\frac{m_d}{m_s}} e^{-i\phi_1} - \sqrt{\frac{m_u}{m_s}},$$

$$\left|\frac{V_{ub}}{V_{cb}}\right| = \sqrt{\frac{m_u}{m_c}}, \left|\frac{V_{td}}{V_{ts}}\right| = \sqrt{\frac{m_d}{m_c}}. \quad (8)$$

The above relations not only provide vital clues (Dimopoulos *et al*., 1992; Froggatt and Nielsen 1979; Desai and Roy, 1998) towards the formulation of the quark mass matrices, but also facilitate in understanding the possible underlying symmetries (Grimus *et al*., 2004; Feruglio, 2015; Emmanuel-Costa and Simões, 2012; Ma, 2004; Lavoura and Kuhbock, 2008). However, it was observed (Roberts *et al*. 2001; Kim *et al*. 2004; Branco and Rebelo, 2007; Chiu, 2000) that these relations are only approximate and do not account for the observed flavor mixing data. Consequently, one must look for the next leading order corrections to the above relations in agreement with for the observed flavor mixings. One possible way to obtain such relations is through texture zero ansatz for fermion mass matrices (Fritzsch, 1979; Weinberg, 1977; Fritzsch, 1978; Verma *et al*., 2010; Gupta *et al*., 2009; Mahajan *et al*., 2010; Verma *et al*., 2009; Verma, 2013b; Verma, 2014a; Verma, 2014b; Fakay *et al*., 2013; Ahuja *et al*., 2009], wherein a texture zero corresponds to a matrix entry that is sufficiently suppressed as compared to its neighboring ones.

In this paper, we attempt to extract vital clues towards the formulation of Yukawa matrices from a model independent prospective using the available data on quark masses and flavor mixing matrix. Particularly, in section I, we attempt to translate the observed hierarchies in the CKM matrix onto the corresponding Yukawa matrices so that the latter exhibit a natural structure. In the section II, we make use of the facility of weak basis transformations to further simplify the Yukawa structures. In section III, we consider the natural Yukawa matrices as a starting point, and using the freedom of weak basis transformations, we obtain the empirical relations for the various CKM parameters by retaining next to leading order terms and assuming that the phases to be factorizable in these matrices. Using the inputs and constraints from section IV, in section V, we show that such natural Yukawa structures offer a convincing explanation for the observed quark mixing and CP violation data up to a level of 1σ C.L. Finally, we also investigate the conditions under which such viable natural structures for Yukawa matrices may be realized in model building.

NATURAL MASS MATRICES

To this end, we consider the Wolfenstein parametrization for V (Wolfenstein, 1983),

$$\begin{pmatrix} 1-\lambda^2/2 & \lambda & A\lambda^3(\rho - i\eta) \\ -\lambda & 1-\lambda^2/2 & A\lambda^2 \\ A\lambda^3(1-\rho-i\eta) & -A\lambda^2 & 1 \end{pmatrix} \quad (9)$$

where λ = 0.22, A = 0:82, ρ = 0:13 and η = 0.345. One may rewrite the above matrix in the approximate form as

$$V = \begin{pmatrix} 1 & \lambda & 0.3\lambda^3 \\ -\lambda & 1 & 0.8\lambda^2 \\ 0.6 & -0.8\lambda^2 & 1 \end{pmatrix} \quad (10)$$

As a result, in the u-diagonal representation, we attempt to translate the observed hierarchy among the quark masses and V on to the mass matrix Y_d using $Y_d = VY_d^{Diag}V^\dagger$, *e.g.*,

$$Y_d \sim \begin{pmatrix} m_d & \lambda m_s & 0.3\lambda^3 m_b \\ -\lambda m_s & m_s & 0.8\lambda^2 m_b \\ 0.3\lambda^3 m_b & -0.8\lambda^2 m_b & m_b \end{pmatrix}, \quad (11)$$

Using $\lambda \sim \sqrt{m_d/m_s}$, one obtains

$$Y_d \sim \begin{pmatrix} m_d & \sqrt{m_d m_s} & 0.3\Omega\sqrt{m_d m_b} \\ -\sqrt{m_d m_s} & m_s & 0.8\Omega\sqrt{m_d m_b} \\ 0.3\Omega\sqrt{m_d m_b} & -0.8\Omega\sqrt{m_d m_b} & m_b \end{pmatrix}, \quad (12)$$

where $\Omega = \lambda^2\sqrt{m_b/m_s} \sim 0.35$, so that

$$Y_d \sim \begin{pmatrix} m_d & \sqrt{m_d m_s} & 0.1\sqrt{m_d m_b} \\ -\sqrt{m_d m_s} & m_s & 0.3\sqrt{m_d m_b} \\ 0.1\sqrt{m_d m_b} & -0.3\sqrt{m_d m_b} & m_b \end{pmatrix}, \quad (13)$$

Interestingly, the above mass matrix has a natural structure (Peccei and Wang 1996), i.e., $Y_{11} < Y_{12,21} < \sim Y_{13,31} < Y_{22} < Y_{23,32} < Y_{33}$, with $Y_{22} << Y_{33}$, which is a consequence of the observed hierarchies in the quark masses and the CKM matrix as discussed before. Furthermore, the above structure is model independent and should provide the starting point towards the formulation of Yukawa matrices as well as provide important clues to the possible underlying symmetries responsible for the same (Grimus *et al*. 2004; Feruglio, 2015; Emmanuel-Coata and Simões 2012; Ma 2004; Lavoura and Kuhbock, 2008). It is, therefore, desirable to investigate the exact structure for the Yukawa matrices that accounts for the current precision data on quark mixing and CP violation. This obviously requires additional next to leading order corrections for Eqs. (8).

WEAK BASIS TRANSFORMATIONS

In the recent decade, considerable work has been done in investigating which sets of texture zeros result only from the choice of a given basis and when these textures imply restrictions on fermion mass matrices. Starting with a basis wherein Y_u = Diag(m_u, m_c, m_t) and Y_d is general Hermitian, one always has the freedom to apply an overall unitary transformation W (Branco *et al*. 2009, Fritzsch and Xing, 1997) on both quark mass matrices, viz., $Y_u \to M_u = W^\dagger Y_u W$ and $Y_d \to M_d = W^\dagger Y_d W$. Such unitary transformations, also called the Weak Basis Transformations (WBTs), only change the mass matrices and not the associated charged current. As a result, the two sets of quark mass matrices (Y_u, Y_d) and (M_u, M_d), related by W, essentially have the same physical content.

The WBTs also allow to create texture zeros or weak basis zeros (WBZs) at certain positions in these matrices. As a result, the zeros arising from such transformations have no physical content. More importantly, in the WBT approach, it is observed (Branco *et al*., 2000) that the maximum number of WBZs are restricted to three for Hermitian quark mass matrices. Branco *et. al*. (2000), Xing and Zhang (2004) and Fritzsch and Xing (1997) have discussed that there exists more than one possibility of WBT parametrization with zeros at different positions in the quark mass matrices, *viz.*, for (B-Type) WBZs given by Branco *et al*. (2000), one obtains

$$M_u = \begin{pmatrix} 0 & a_u & 0 \\ a_u^* & d_u & b_u \\ 0 & b_u^* & c_u \end{pmatrix}, \; M_d = \begin{pmatrix} 0 & a_d & f_d \\ a_d^* & d_b & b_d \\ f_d^* & b_d^* & c_d \end{pmatrix}. \quad (14)$$

or vice versa for M_u and M_d. Whereas for (FX-Type) WBZs given by Fritzsch (1997), one obtains

$$M_u = \begin{pmatrix} 0 & a_u & 0 \\ a_u^* & d_u & b_u \\ 0 & b_u^* & c_u \end{pmatrix}, \quad M_d = \begin{pmatrix} e_d & a_d & 0 \\ a_d^* & d_d & b_d \\ 0 & b_d^* & c_d \end{pmatrix}. \quad (15)$$

or vice versa for M_u and M_d.

Interestingly, it turns out (Verma, 2013a; Sharma *et al*., 2015) that the e_q elements in (FX-Type) WBZ matrices are physically redundant in reproducing the quark mixing data implying that these matrices essentially have the same physical content as the Fritzsch-like texture four zero Hermitian mass matrices. Recently, adopting the (FX-Type) WBZ mass matrices, Sharma *et al*. (2015) claimed that the Fritzsch-like texture four zero mass matrices are the only viable possibility for quarks. These mass matrices, however, do not observe a natural structure as expected for Yukawa matrices.

In addition, using this approach, one is not able to study the implications of the (13) and (31) elements in the mass matrices for the mixing data. In fact, most of

the studies (Sharma *et al*. 2015; Emmanuel-Costa and Simões, 2009; Giraldo 2012; Ludl and Grimus, 2015; Ludl and Grimus, 2014) involving mass matrices with nonvanishing (13) and (31) elements have relied on numerical calculations. This calls for a thorough investigation based on the (B-Type) WBZ mass matrices. Furthermore, it is difficult to carry out an analytical investigation of various phenomenologically allowed texture zero possibilities, for viability, since each of these has to be diagonalized on a case to case basis. It therefore becomes desirable to formulate a mechanism which allows for such a study.

NEXT TO LEADING ORDER CALCULATION

Motivated by the above discussion, it is natural to expect the following structure for the Hermitian Yukawa matrices, up to a leading order, e.g.,

$$M_q = \begin{pmatrix} e_q & a_q e^{i\alpha_q} & f_q e^{i\delta_q} \\ a_q e^{-i\alpha_q} & d_q & b_q e^{i\beta_q} \\ f_q e^{-i\delta_q} & b_q e^{-i\beta_q} & c_q \end{pmatrix} \sim \begin{pmatrix} m_1 & \sqrt{m_1 m_2}\, e^{i\alpha_q} & \sqrt{m_1 m_2}\, e^{i\delta_q} \\ \sqrt{m_1 m_2}\, e^{-i\alpha_q} & m_2 & \sqrt{m_1 m_2}\, e^{i\beta_q} \\ \sqrt{m_1 m_2}\, e^{-i\delta_q} & \sqrt{m_1 m_2}\, e^{-i\beta_q} & m_3 \end{pmatrix}, \tag{16}$$

Furthermore, a characteristic nature of (B-Type) WBZ matrices is that $e_q = 0$ in these. Assuming the 4 phases to be factorizable in M_q, so that $\delta_q = \alpha_q + \beta_q$, one can diagonalize M_q using three successive rotations in the 13, 23 and 12 generations leading to the following CKM matrix up to next to leading order terms, where $\phi_1 = \alpha_u - \alpha_d$ and $\phi_2 = \beta_u - \beta_d$:

$$\begin{aligned} M_q^{Diag} &= \begin{pmatrix} -\kappa_q m_1 & 0 & 0 \\ 0 & \kappa_q m_2 & 0 \\ 0 & 0 & m_3 \end{pmatrix} \\ &= \begin{pmatrix} 1 & -s_{12}^q & 0 \\ s_{12}^q & 1 & 0 \\ 0 & 0 & 1 \end{pmatrix} \begin{pmatrix} 1 & 0 & 0 \\ 0 & 1 & -s_{23}^q \\ 0 & s_{23}^q & 1 \end{pmatrix} \begin{pmatrix} 1 & 0 & -s_{13}^q \\ 0 & 1 & 0 \\ s_{13}^q & 0 & 1 \end{pmatrix} \begin{pmatrix} e^{-i\alpha_q} & 0 & 0 \\ 0 & 1 & 0 \\ 0 & 0 & e^{i\beta_q} \end{pmatrix} \times \\ & M^q \times \begin{pmatrix} e^{i\alpha_q} & 0 & 0 \\ 0 & 1 & 0 \\ 0 & 0 & e^{-i\beta_q} \end{pmatrix} \begin{pmatrix} 1 & 0 & s_{13}^q \\ 0 & 1 & 0 \\ -s_{13}^q & 0 & 1 \end{pmatrix} \begin{pmatrix} 1 & 0 & 0 \\ 0 & 1 & s_{23}^q \\ 0 & -s_{23}^q & 1 \end{pmatrix} \begin{pmatrix} 1 & s_{12}^q & 0 \\ -s_{12}^q & 1 & 0 \\ 0 & 0 & 1 \end{pmatrix}, \end{aligned} \tag{17}$$

$$V \cong \begin{pmatrix} \left(e^{-i\phi_1} + s_{12}^u s_{12}^d\right) & \left(s_{12}^d e^{-i\phi_1} + s_{12}^u\right) & \left(s_{13}^d e^{-i\phi_1} - s_{13}^u e^{i\phi_2}\right) - s_{12}^u V_{cb} \\ \left(s_{12}^u e^{-i\phi_1} + s_{12}^d\right) & \left(s_{12}^u s_{12}^d e^{-i\phi_1} + 1 + s_{23}^u s_{23}^d e^{i\phi_2}\right) & \left(s_{23}^d - s_{23}^u e^{i\phi_2}\right) \\ \left(s_{13}^u e^{-i\phi_1} - s_{13}^d e^{i\phi_2}\right) - s_{12}^d V_{ts} & \left(s_{23}^u - s_{23}^d e^{i\phi_2}\right) & \left(s_{23}^u s_{23}^d + e^{i\phi_2}\right) \end{pmatrix} \tag{18}$$

with $\kappa_q = \pm 1$. For strongly hierarchical M_q, one obtains the following next to leading order relations among the mass matrix elements and the rotation angles:

$$\begin{aligned} e_q &= 0 = -\kappa_q m_1 + \kappa_q m_2 \left(s_{12}^q\right)^2, \\ d_q &= \kappa_q m_2 + m_3 \left(s_{23}^q\right)^2, \\ f_q &= m_3 s_{13}^q . \end{aligned} \tag{19}$$

and

$$\begin{aligned} a_q &= \kappa_q m_2 s_{12}^q + m_3 s_{13}^q s_{23}^q, \\ b_q &= m_3 s_{23}^q, \\ c_q &= m_3 . \end{aligned} \tag{20}$$

where e_q, d_q and f_q are free parameters along with ϕ_1 and ϕ_2. Solving Eqs. (19) and using $f_q = \varepsilon_q \sqrt{m_1 m_3}$, where $\varepsilon_q < 1$, one obtains

$$s_{12}^q = \sqrt{\frac{m_1}{m_2}},\ s_{13}^q = \varepsilon_q \sqrt{\frac{m_1}{m_3}},\ s_{23}^q = \sqrt{\frac{d_q - \kappa_q m_2}{m_3}}, \tag{21}$$

These are substituted in Eqs. (20) to obtain the other matrix elements a_q, b_q and c_q in M_q. As a result, using Eq. (18) and Eq. (21), it is trivial to obtain the following general relations for the off-diagonal CKM matrix elements and the Jarlskog's CP invariant parameter $J_{CP} = Im(V_{ub}^* V_{cs}^* V_{cb} V_{us})$ (Jarlskog, 1985a; 1985b):

$$V_{us} = \sqrt{\frac{m_d}{m_s}} e^{-i\phi_1} - \sqrt{\frac{m_u}{m_c}}, \tag{22}$$

$$V_{cd} = \sqrt{\frac{m_u}{m_c}} e^{-i\phi_1} - \sqrt{\frac{m_d}{m_s}}, \tag{23}$$

$$V_{cb} = \sqrt{\frac{d_d - \kappa_d m_s}{m_b}} - \sqrt{\frac{d_u - \kappa_u m_c}{m_t}}\, e^{i\phi_2}, \quad (24)$$

$$V_{ts} = \sqrt{\frac{d_u - \kappa_u m_c}{m_t}} - \sqrt{\frac{d_d - \kappa_d m_s}{m_b}}\, e^{i\phi_2}, \quad (25)$$

$$V_{ub} = \varepsilon_d \sqrt{\frac{m_d}{m_b}}\, e^{-i\phi_1} - \varepsilon_u \sqrt{\frac{m_u}{m_t}}\, e^{i\phi_2} - \sqrt{\frac{m_u}{m_c}}\, V_{cb}, \quad (26)$$

$$V_{td} = -\varepsilon_u \sqrt{\frac{m_u}{m_t}}\, e^{-i\phi_1} - \varepsilon_d \sqrt{\frac{m_d}{m_b}}\, e^{i\phi_2} - \sqrt{\frac{m_d}{m_s}}\, V_{ts}, \quad (27)$$

$$J_{CP} = (s_{12}^u s_{12}^d |V_{cb}|^2 - s_{13}^u s_{23}^u s_{12}^d - s_{12}^u s_{13}^d s_{23}^d)\, Sin\ \phi_1 - (s_{23}^u s_{12}^d s_{13}^d + s_{13}^u s_{12}^u s_{23}^d)\, Sin\ \phi_2 + (s_{12}^u s_{23}^u s_{13}^d + s_{13}^u s_{12}^d s_{23}^d)\, Sin\left(\phi_1 + \phi_2\right). \quad (28)$$

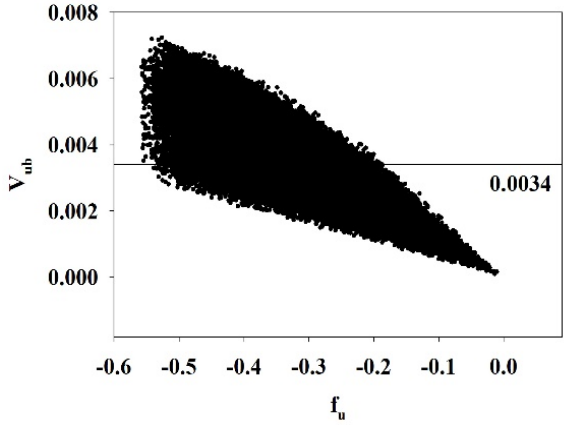

Fig. 1: Plot emphasizing the implications of non-vanishing fu for V_{ub}.

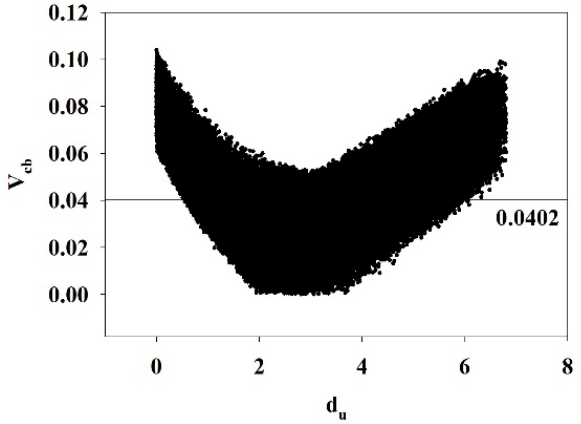

Fig. 2: Plot depicting du = 0 is not allowed by V_{cb} measurements.

Interestingly, one observes that starting with the (FX-Type) WBZ matrices, it should never be possible to obtain strongly hierarchical Yukawa matrices since $f_u = f_d = 0$ imply $|V_{ub}/V_{cb}| = \sqrt{m_u/m_c}$, which is not able to account for the observed values of this ratio. This indicates that perhaps one requires $f_q \neq 0$ to translate the observed strong hierarchy among the quark masses and mixing angles on to the corresponding Yukawa matrices. We prove this point in the discussions below. Eq. (24) for V_{cb} provides yet another important clue towards the formulation of such Yukawa matrices viz. $d_u = 0$ is not allowed by the current CKM data since $\sqrt{(d_d - \kappa_d m_s)/m_b} - \sqrt{m_c/m_t}$ is always > 0.04 even when $d_d = 0$.

INPUTS AND CONSTRAINTS

We use the following quark masses at M_Z (Olive *et al*., 2014; Xing *et al*., 2012) as inputs for calculations. In addition, the mixing angles are constrained using the best fit PDG data for CKM matrix (Olive *et al*., 2014; Ahuja *et al*., 2007), *viz*., V_{us} = 0.2247 – 0.2260, V_{ub} = 0.0034 – 0.0037, V_{cb} = 0.0402 – 0.0426 along with Sin2β = 0.663 – 0.701.

$$\begin{aligned} m_u &= 1.38\,^{+\,0.42}_{-\,0.41}\, MeV, \\ m_d &= 2.82 \pm 0.48\, MeV, \\ m_s &= 57\,^{+\,18}_{-\,12}\, MeV, \\ m_c &= 0.638^{+0.043}_{-0.084}\ MeV, \\ m_b &= 2.86^{+0.16}_{-0.06}\, GeV, \\ m_t &= 172.1 \pm 1.2\, GeV, \\ m_u/m_d &= 0.38 - 0.58, \\ m_d &= 17 - 22. \end{aligned} \quad (29)$$

The non-trivial phases differences, ϕ_1 and ϕ_2, are allowed free variations between 0^o – 360^o.

PRECISION TESTS

Noting that there exist two possibilities for M_u and M_d in the (B-Type) approach, we categorize them as Type-I and Type-II possibilities, respectively. Type-I has $f_d \propto \varepsilon_d = 0$ and $f_u \neq 0$, while Type-II has $f_u \propto \varepsilon_u = 0$ and $f_d \neq 0$.

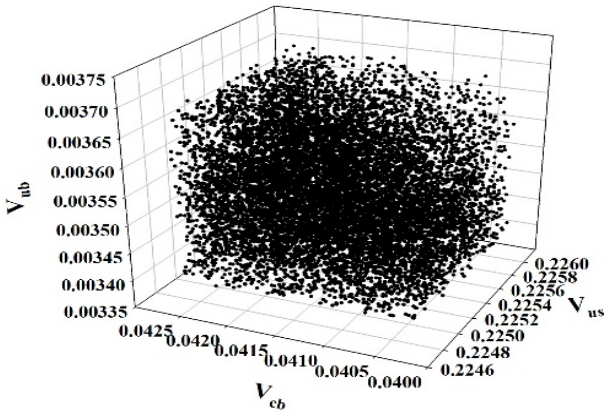

Fig. 3: Predictions for the three flavor mixing angles.

a. Type-I (f_d = 0)

Using the above inputs and constraints, and choosing κ_u = -1, κ_d = -1 along with d_d = 0, we obtain the following viable structures for the Yukawa matrices, which not only observe a natural structure, but are also in excellent agreement with the current data up to 1σ C.L., *i.e.*,

$$\begin{pmatrix} 0 & (-0.093)-(-0.066) & (-0.42)-(-0.19) \\ (-0.093)-(-0.066) & 2.3-6.3 & 22.4-32.7 \\ (-0.42)-(-0.19) & 22.4-32.7 & 170-173 \end{pmatrix} GeV, \quad (30)$$

$$\begin{pmatrix} 0 & (-0.015)-(-0.010) & 0 \\ (-0.015)-(-0.010) & 0 & 0.35-0.47 \\ 0 & 0.35-0.47 & 2.8-3.0 \end{pmatrix} GeV, \quad (31)$$

where ϕ_1 = 60° – 120° and ϕ_2 = 0° – 360°. In Fig.1, we emphasize the importance of non-vanishing f_u for V_{ub} and observe that $f_u \sim \sqrt{m_u m_t}$ is able to account for the observed Vub up to 1σ C.L. Fig. 2 confirms our previous observation that d_u = 0 is not possible for any physical M_u. In particular, we plot the predictions of the above Yukawa matrices for the three mixing angles along with the three angles of unitarity triangle, *viz.*, α, β and γ (Olive *et al*. 2014), *e.g.*,

$$\beta = \arg\left(-\frac{V_{cd}V_{cb}^*}{V_{td}V_{tb}^*}\right) \quad (32)$$

etc. in Fig. 3 and Fig. 4, respectively. In addition, one obtains J_{CP} = (2.8 – 3.4) x 10^{-5} also in good agreement with data (Olive *et al*. 2014).

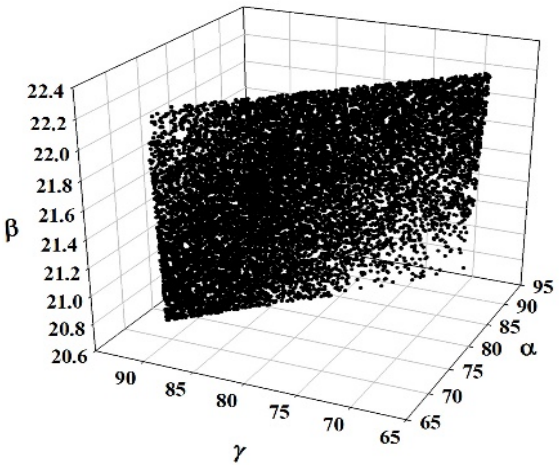

FIG. 4: Predictions for the three angles of the unitarity triangle in degrees.

b. Type-II (f_u = 0)

For the above inputs and constraints, and choosing κ_u = -1, κ_d = -1 along with d_d = 0, we obtain the following viable structures for the Yukawa matrices which are also in good agreement with the current data up to 1σ C.L. as well as display the expected structural hierarchy among the quark mass matrix elements, *i.e.*, $e_q < a_q <\sim f_q < d_q < b_q < c_q$ with $d_q << c_q$ in agreement with Eq. (16), *i.e.*,

$$M_u' = \begin{pmatrix} 0 & (-0.035)-(-0.022) & 0 \\ (-0.035)-(-0.022) & 1.1-5.5 & 17.4-32.2 \\ 0 & 17.4-32.2 & 170-173 \end{pmatrix} GeV, \quad (33)$$

$$M_d' = \begin{pmatrix} 0 & (-0.015)-(-0.010) & 0.003-0.007 \\ (-0.015)-(-0.010) & 0 & 0.35-0.47 \\ 0.003-0.007 & 0.35-0.47 & 2.8-3.0 \end{pmatrix} GeV, \quad (34)$$

where ϕ_1 = 60° - 110° and ϕ_2 = 340° - 350°. In Fig. 5, we emphasize the importance of non-vanishing f_d for V_{ub} and observe that $f_d \sim \sqrt{m_d m_s}$ accounts for the observed V_{ub} up to 1σ C.L. This is understandable from Eq. (26) since the down type quark masses are less hierarchical than the corresponding masses for the up-type quarks. The predictions for the three mixing angles and the three angles of the unitarity triangle remain the same as in the previous case, leading to scatter plots like the ones in Fig. 3 and Fig. 4, respectively, along with J_{CP} = (2.82 – 3.44) x 10^{-5}.

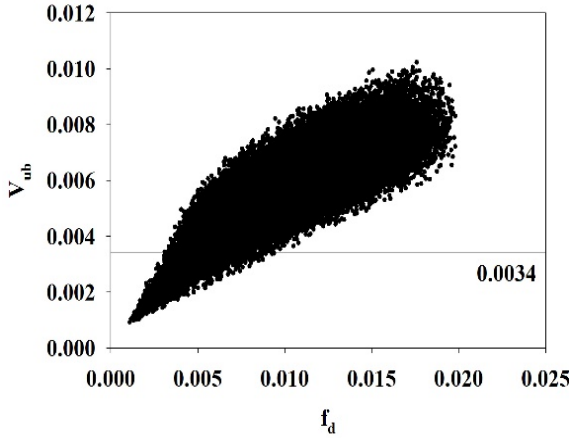

Fig. 5: Plot emphasizing the implications of nonvanishing f_d for V_{ub}.

CONCLUSIONS

Assuming factorizable phases in Hermitian Yukawa matrices obtained through weak basis transformations (Branco *et al*. 2000), we attempt to extract vital clues towards the formulation of these matrices using the available data on quark masses and CKM parameters in a model independent way. It is observed that one requires $f_u \sim \sqrt{m_u m_t}$ or $f_d \sim \sqrt{m_d m_s} \sim a_d$ to realize the strong mass hierarchy in the Yukawa matrices, which are also in agreement with the concept of natural mass matrices (Peccei and Wang 1996; Verma 2013), *i.e.*, $a_q <\sim f_q < d_q < b_q < c_q$, with $d_q << c_q$. The CKM data seems to forbid $d_u = 0$ in the up-type Yukawa matrix. We also derive the most general empirical relations for the vital CKM parameters which offer a natural description for $|V_{us}| \cong |V_{cd}|$, $|V_{cb}| \cong |V_{ts}|$, and $|V_{ub}/V_{cb}| < |V_{td}/V_{ts}|$. Given the generality of these results, it should be interesting to see if and $|V_{ub}|/|V_{cb}|$ and $|V_{td}|/|V_{ts}|$ can be used as a probe of specific mass matrix ansatzes in future B-physics experiments.

ACKNOWLEDGMENTS

The author is thankful to Vice-Chancellor, Chitkara University, for providing the necessary facilities to work.

REFERENCES

Ahuja, G., M. Gupta, S. Kumar, and M. Randhawa. 2007. Implications of unitarity and precision measurements on CKM matrix elements. Phys. Lett. B 647, 394-399.

Ahuja, G., M. Gupta, M. Randhawa, and R. Verma. 2009. Texture specific mass matrices with Dirac neutrinos and their implications. Phys. Rev. D 79, 093006.

Ahuja, G., R. Verma, P. Fakay, P. S. Gill, and M. Gupta. 2012. Revisiting the possibility of new physics in the $K - \bar{K}$ and $B_d - \bar{B}_d$ systems. Mod. Phys. Lett. A 27, 1250125.

Barbieri, R., L. J. Hall, and A. Romanino. 1999. Precise tests of a quark mass texture. Nucl. Phys. B 551, 93-101.

Branco, G. C., D. Emmanuel-Costa, and R. González Felipe. 2000. Texture zeros and weak basis transformations. Phys. Lett. B 477, 147-155.

Branco, G. C., M. N. Rebelo, and J. I. Silva-Marcos. 2007. Yukawa textures, new physics, and nondecoupling. Phys. Rev. D 76, 033008.

Branco, G. C., D. Emmanuel-Costa, R. González Felipe, and H. Serôdio. 2009. Weak basis transformations and texture zeros in the leptonic sector. Phys. Lett. B 670, 340-349.

Cabibbo., N. 1963. Unitary symmetry and leptonic decays. Phys. Rev. Lett. 10, 531-533.

Chiu, S.-H., T.-K. Kuo, and G.-H. Wu. 2000. Hermitian quark mass matrices with four texture zeros. Phys. Rev. D 62, 053014.

Desai, B. R., and D. P. Roy. 1998. Pattern of texture zeros in quark mass matrices with a divergent top-Yukawa coupling at the GUT scale. Phys. Rev. D 58, 113007.

Dimopoulos, S., L. J. Hall, and S. Raby. 1992. Predictive Framework for Fermion Masses in Supersymmetric Theories. Phys. Rev. Lett. 68, 1984-1987.

Emmanuel-Costa, D., and C. Simoes. 2009. Reconstruction of quark mass matrices with weak basis texture zeroes from experimental input. Phys. Rev. D 79, 073006.

Emmanuel-Costa, D., and C. Simões. 2012. Nearest-neighbor-interactions from a minimal discrete flavor symmetry within SU (5) grand unification. Phys. Rev. D 85, 016003.

Fakay, P., S. Sharma, R. Verma, G. Ahuja, and M. Gupta. 2013. Implications of θ_{13} on Fritzsch-like lepton mass matrices. Phys. Lett. B 720, 366-372.

Feruglio, F., 2015. Pieces of the flavour puzzle arXiv:1503.04071 [hep-ph].

Fritzsch, H. 1978. Weak-interaction mixing in the six-quark theory, Phys. Lett. B 73, 317-322.

Fritzsch, H., 1979. Quark masses and flavor mixing. Nucl. Phys. B 155, 189-207.

Fritzsch, H., and Z. Xing. 1997. Flavor symmetries and the description of flavor mixing. Phys. Lett. B 413, 396-404.

Fritzsch, H., and Z.-Z. Xing. 2003. Four-zero texture of Hermitian quark mass matrices and current experimental tests. Physics Letters B 555, 63-70.

Froggatt, C. D., and H. B. Nielsen. 1979. Hierarchy of quark masses, cabibbo angles and *CP* violation. Nucl. Phys. B 147, 277-298.

Giraldo, Y., 2012. Texture zeros and weak basis transformations in the quark sector of the standard model. Phys. Rev. D 86, 093021.

Grimus, W., A. S. Joshipura, L. Lavoura, and M. Tanimoto. 2004. Symmetry realization of texture zeros. Eur. Phys. J. C 36, 227-232.

Gupta, M., G. Ahuja, and R. Verma. 2009. Implications of precision measurements on texture specific fermion mass matrices, Int. J. Mod. Phys. A 24S1, 3462-3468.

Hall, L. J., and A. Rain. 1993. On the generality of certain predictions for quark mixing. Physics Letters B 315, 164-169.

Jarlskog, C., 1985. Commutator of the Quark Mass Matrices in the Standard Electroweak Model and a Measure of Maximal CP Nonconservation, Phys. Rev. Lett. 55, 1039-1042; Erratum Phys. Rev. Lett. 58, 1698 (1987).

Jarlskog, C., 1985. A basis commutator of the quark mass matrices in the standard electroweak model and a measure of maximal cp nonconservation. Z. Phys. C 29, 491-497.

Kim, H. D., S. Raby, and L. Schradin. 2004. Quark mass textures and sin 2 beta Phys. Rev. D 69, 092002.

Kobayashi, M., and T. Maskawa. 1973. *CP*-violation in the renormalizable theory of weak interaction. Prog. Theor. Phys. 49, 652-657.

Lavoura, L., and H. Kühböck. 2008. A_4 model for the quark mass matrices. Eur. Phys. J. C 55, 303-308.

Liu, X.-W., and S. Zhou. 2013. Texture Zeros for Dirac Neutrinos and Current Experimental Tests. Int. J. Mod. Phys. A 28, 1350040.

Ludl, P. O., and W. Grimus. 2014. A complete survey of texture zeros in the lepton mass matrices. *Journal of High Energy Physics* 07, 090. [Erratum: JHEP10,126(2014)].

Ludl, P. O., and W. Grimus. 2015. A complete survey of texture zeros in general and symmetric quark mass matrices. Phys. Lett. B 744, 38-42.

Ma, E., in Summer Institute 2004 (SI 2004) UCRHEP-T379 (Sep 2004)

Mahajan, N., R. Verma, and M. Gupta. 2010. Investigating non-Fritzsch like texture specific quark mass matrices. Int. J. Mod. Phys. A 25, 2037-2048.

Olive, K. *et al*. (Particle Data Group). 2014. Review of particle physics. Chin. Phys. C 38, 090001.

Peccei, R. D., and K. Wang. 1996. Natural mass matrices. Phys. Rev. D 53, 2712-2723.

Ramond, P., R. G. Roberts, and G. G. Ross. 1993. Stitching the Yukawa quilt. Nucl. Phys. B 406, 19-42.

Roberts, R., A. Romanino, G. Ross, and L. Velasco-Sevilla. 2001. Precision test of a Fermion mass texture. Nucl. Phys. B 615, 358-384.

Sharma, S., P. Fakay, G. Ahuja, and M. Gupta. 2015. Finding a unique texture for quark mass matrices. Phys. Rev. D 91, 053004.

Verma, R., G. Ahuja, and M. Gupta. 2009. Implications of CP asymmetry parameter sin2β on structural features of texture specific mass matrices. Phys. Lett. B 681, 330.

Verma, R., G. Ahuja, N. Mahajan, M. Gupta, and M. Randhawa, Exploring the parameter space of texture four-zero quark mass matrices. 2010. J. Phys. G 37, 075020.

Verma, R. 2013a. Lower bound on neutrino mass and possible CP violation in neutrino oscillations. J. Phys. G 40, 125003.

Verma, R., 2013b. Lower bound on neutrino mass and possible CP violation in neutrino oscillations. Phys. Rev. D 88, 111301.

Verma, R., 2014a. Generic lepton mass matrices and neutrino oscillations. Phys. Rev. D 89, 053007.

Verma, R., 2014b. Lepton textures and neutrino oscillations. Int. J. Mod. Phys. A 29, 1444009.

Wolfenstein, L., 1983. Parametrization of the Kobayashi-Maskawa Matrix. Phys. Rev. Lett. 51, 1945-1947.

Weinberg, S. 1977. The problem of mass, Transactions of the New York Academy of Sciences 38, 185-201.

Xing, Z.-Z., and H. Zhang. 2004. Complete parameter space of quark mass matrices with four texture zeros, J. Phys. G 30, 129-136.

Xing, Z., H. Zhang, and S. Zhou. 2012. Impacts of the Higgs mass on vacuum stability, running fermion masses, and two-body Higgs decays. Phys. Rev. D 86, 013013.

Pb. Univ. Res. J (Sci.) Vol. 68, 2018, pp 25-33

QUASI-FISSION IN HEAVY-ION INDUCED FUSION-FISSION REACTIONS

KAVITA CHAUHAN* AND HARDEV SINGH
Department of Physics, Kurukshetra University, Kurukshetra-136119, India

Abstract

Fusion-fission dynamics is considered as one of the important aspects of study in heavy ion induced reactions. Quasi-fission (QF) represents the splitting of compound nuclei before the full equilibration in all degrees of freedom is achieved. This process being the main hindrance to complete fusion is considered as the main challenge in synthesis of super heavy elements (SHE). The main signature of QF process in relatively broader fragment mass distributions than expected from complete fusion-fission (FF) reactions. The dependence of onset and probability of QF on various reaction variables, such as, N/Z of colliding nuclei, product of charges of projectile and target, deformation of the projectile and/or target, energy brought in by the projectile etc. is not yet understood. This article describes the general behavior and its dependence on different reaction variables.

Key words: Heavy-ions, fusion-fission reaction dynamics, quasi-fission

INTRODUCTION

Fission is a unique process where large scale rearrangement of protons and neutrons takes place inside a nucleus. Nuclear fission was discovered in 1939 by Hahn and Strassman (1939a, 1939b) in the reaction of uranium target with the neutrons. Meitner and Frisch (1939) were the first to propose a theoretical interpretation based on a model of nuclear liquid drop and suggested the word ”fission” in analogy with the biological cell division process. They figured out that just as a drop of vibrating liquid could split into two drops, nucleus might divide itself into two smaller nuclei. They worked out the energy that would be released in such a process is approximately 200 MeV on the basis of electric repulsion energy between the fragments from their atomic numbers and mass defect. Also, Frisch (1939) confirmed the energy of the fragments by measuring the pulses from a U-lined ionization chamber and a Raα + Be source of neutrons.

Bohr and Wheeler (1939) later, explained the properties of fission using a model that included a charged liquid drop with surface tension. Further, the importance of dissipation in the nuclear fission process was pointed out by Kramers (1940). Even though nuclear fission was discovered a long time ago, it continues to be a challenging topic experimentally as well as theoretically. Fission is a distinctive phenomenon like fusion involving a dramatic rearrangement of nuclear matter. Fission process study offers a thorough knowledge of the issue of nuclear dynamics. Nuclear dissipation does not allow the system to alter the shape rapidly during the fission decay process and thus introduces a time delay in the system’s evolution.

The present work (Sections I-VII) addresses some of the attention-grabbing findings within the fusion-fission (FF) studies and also the significance of dynamics within the fission process.

HEAVY ION INDUCED FUSION-FISSION REACTIONS

Nuclear reaction deals with the phenomena that occur when two nuclei are brought into contact such that the nuclear force that holds the protons and neutrons together within one nucleus, is felt by the other nucleus. If the two interacting nuclei are heavier than helium, generally, the reaction is termed as heavy ion reaction. The study of heavy-ion collisions has been carried out for the last few decades to obtain the information about the reaction dynamics on a wide energy domain. The advancement of heavy ion accelerators offer sufficient amount of energy to overcome the electrostatic repulsion between projectile and target. A wide range of available heavy ion beams have opened up a tremendous opportunity to investigate the area of heavy ion reactions and have shown a variety of phenomena of significant interest to study nuclear reaction and structure physics. When projectile and the target approach each other, a short range nuclear attractive force and a long range Coulomb repulsion come into the picture. During the collision process, there are drastic changes in the shape, N/Z ratio and internal excitation energy of interacting nuclei. These reactions at moderate excitation energies, exhibit a wide range of reaction mechanisms ranging from direct reactions to perfectly equilibrated compound nuclear reactions, depending on the degree of equilibration in different degrees of freedom. As the relaxation times for various degrees of freedom are different, the nature of the nuclear

*Corresponding Author: rajputkavita59@gmail.com
MS Received: November 12, 2018, Accepted: December 21, 2018

reaction will depend on the interaction time between the colliding nuclei. Hence, the sticking time or the interaction time after collision is one of the principal aspects that decides the future of projectile-target system. For a very short interaction time (10^{-23} - 10^{-21}s), peripheral reactions are favoured, leading to quasi-elastic processes. With increase in interaction time, overlapping of the colliding nuclei also increases, which leads to large mass transfer in which the di-nuclear system leads to deep-inelastic processes. However, in the compound nucleus (CN) reactions, the sharing of projectile energy and momentum among the nucleons of target nucleus takes place and thermodynamic equilibrium is established. The time scale for such reactions is in the range of 10^{-18} to 10^{-16} s. The CN so formed may deexcite through light particle evaporation like neutrons, light charged particles or gamma rays and ends up as a stable or long-lived evaporation residue (ER). If relatively higher fissility CN is produced at larger excitation energy, it undergoes binary fission. However, in some cases, the composite system may re-separate and breaks up in fission like events much before completing the full rotation, due to the short sticking time (10^{-21} - 10^{-18}s) and this decay channel is referred as Quasi-fission (QF). Fig. 1 displays different processes depending on interaction time in such reactions. The dynamics of colliding nuclei in terms of potential energy curve is shown in Fig. 2. It is clear from this figure that when the projectile collides with the target, it forms a composite system. If the projectile energy exceeds the fusion barrier, the composite structure overcomes the barrier and can lose some of the relative energy through nuclear friction to get trapped in the potential pocket and eventually lead to formation of fully equilibrated CN, which further decays by fission or evaporation of particles. But if the projectile energy is less than fusion barrier, composite system so formed splits into fission like products before formation of CN. This phenomenon

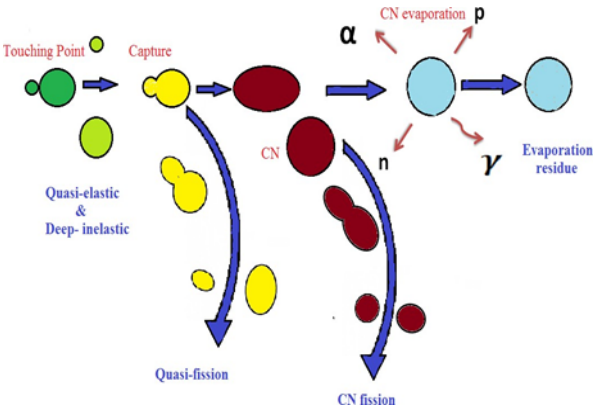

Fig. 1: Classification of heavy ion induced reaction based on the interaction time during the collision.

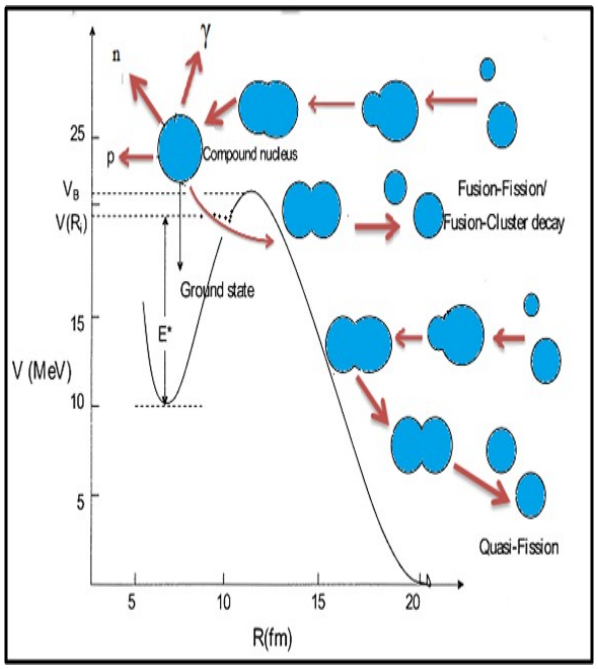

Fig. 2: The variation of potential energy curve as a function of distance (R).

is known as "non-compound nucleus (NCN) processes (quasi-fission, fast fission etc.)". Experimentally, it has been observed that based upon the angular momentum (L), excitation energy (E^*) and "mass asymmetry of the entrance channel (α)" etc, the composite system so produced as a result of heavy ion collision could either form an equilibrated CN or the projectile is captured by the target for relatively shorter period of time and re-separates much before the evolution of final equilibrated CN.

Fast fission

Fast fission **(**Grégoire, Ngô, and Remaud 1982)is a phenomenon which has intermediate properties between deep inelastic and CN reactions. It is a capture process like CN formation but here, the adiabatic potential no longer has a fission barrier (B_f) due to the larger value of angular momentum, i.e, $L > L_{Bf}$, where L_{Bf} being the fission barrier dependent angular momentum. The triaxial shape di-nuclear composite system so formed become unstable and hinders the formation of CN due to extremely small fission barrier which is close to zero. Consequently, the system re-separates much before the formation of CN and fission occur without full equilibration. Hence, this reaction process could occur at higher bombarding energies plus for systems with larger fissility and small fission barrier. A fast fission is further favourable, if the configuration accomplished during the capture phase is between the saddle point and the scission region **(**Grégoire, Ngô, and Remaud 1982).

Pre-equilibrium fission

Ramamurthy and Kapoor (1985) have suggested the concept of pre-equilibrium fission (PEF), where, the interacting system reached the unconditional fission saddle point and mass equilibrium is achieved, but the composite nucleus breaks prior to complete equilibration in shape or 'K-distribution'. This is because "the height of the fission barrier (B_f) is not sufficient to keep the system long enough to equilibrate fully in K-degree of freedom". The fission events re-separate before the characteristic K equilibration time $\tau_K \sim 10^{-20}$ s and therefore have a narrow K distribution around K=0 reaction plane. Here, K represents the projection of total angular momentum on the fission asymmetry axis (Kailas, 1997). The PEF process is therefore a new mode of fission arising as a result of anomalously high fission fragment anisotropies and the final "K-distribution" is presumed to be very narrow, nearly equivalent to composite system's initial value, whereas, the system that survive fission for a time longer than τ_K, results in the formation of equilibrated CN. Hence, the "K-distribution" is wider and is affected by the transition state.

Quasi-fission

Quasi-fission (QF) is a process resulting from relatively faster breakup of partially fused composite system that has some resembling FF events, such as, complete relaxation of relative kinetic energy along with a substantial transfer of mass within the two fragments. It is basically the fast fission with heavier systems. QF process lies halfway between the deep-inelastic collision and the CN reactions in terms of reaction time range. Existence of fast fission can be a preclude at low and medium excitation energy range used for the SHEs production. Fig. 3 schematically illustrates the difference in FF and QF. The PEF is described by unequilibrated K distribution exhibiting more fragments in beam direction as compared to perpendicular direction with no significant change in fusion-fission mass distribution (FFMD) as with mass degree of freedom being equilibrated further, the system would pass over a mass symmetric unconditional fission barrier (Ghosh *et al*., 2009). This results in larger angular anisotropy but it does not influence production of the evaporation residues. In QF, the dinuclear composite enters the fission valley during the descent from saddle-to-scission point. In this way, composite system splits into fragments before attaining the complete mass equilibrium and have strong mass-angle correlation, consequently inhibiting the evaporation residue production probability and the heavy elements production cross-section (Banerjee *et al*., 2009).

FACTORS INFLUENCING COMPETITION BETWEEN FF AND QF

Sticking time

The sticking time is one of the significant factors that determines the future of the projectile and target system after collision. The sticking time is anticipated to be associated with the probability of fusion forming a compact CN (P_{CN}). The probability of QF (P_{QF} = 1- P_{CN}) would be expected to be smaller for longer sticking times and hence more favourable to SHEs synthesis (Hinde *et al*., 2018). The two nuclei that collide always approach one another in the direction of beam and rotate after contact with angular velocities. Measurement of the angle of rotation thus helps in the estimation of the sticking period. In the case of fission following fusion, the target- projectile system stick jointly for extended period (10^{-18} - 10^{-16} sec) and generally complete several rotations. Thus equilibrium is attained in all degrees of freedom, which leads to the formation of CN. If the interaction time is short ($\sim 10^{-20}$ sec), system splits into fragments prior to a complete rotation. Therefore, a strong mass- angle correlation is anticipated and full mass equilibrium may not be achieved. This asymmetric feature in mass angle distribution provides first hand information on the dynamical time scales, representing a dominant QF component in the reactions (Prasad *et al*., 2016). Hinde *et al*. (2018) discussed the concept of average sticking time concluded from the measurements of the QF characteristics which is considered to be relevant for SHEs synthesis.

Charge product (Z_1Z_2)

Charge Product Z_1Z_2 (Z_1, Z_2 being the projectile and target atomic numbers, respectively) is an important factor having a decisive role in the dynamical evolution of trajectories of "heavy ion induced reactions". In 1980s, the theoretical models predicted that QF is expected to occur for heavier systems having $Z_1Z_2 \geq 1600$ (Blocki, Feldmeier and Swiatecki, 1986). But onset of QF was reported in many asymmetric reactions in the $\sim$ 200 mass region around barrier energies, the charge product (Z_1Z_2) considerably lower than 1600. The presence of QF was reported for systems having Z_1Z_2= 711 for ^{30} Si + 186W (Berriman *et al*. 2013), 888 for ^{24}Mg + ^{186}W (Prasad *et al*., 2010), and around 1000 for ^{30}Si + 180Hf and ^{34}S + ^{168}Er (Radiei et al., 2008; Shamlath *et al*., 2017) reactions. However, the relative percentage of the contribution of QF in these reactions is still not clearly understood.

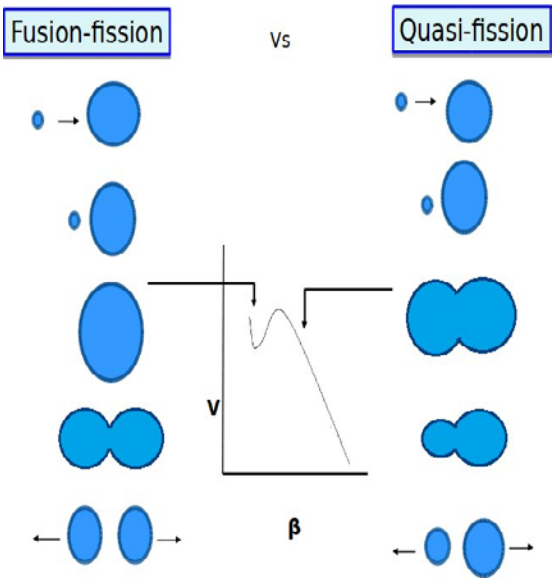

Fig. 3: Illustration of the difference in fusion fission (FF) and Quasi fission (QF) processes.

Entrance channel mass asymmetry

Entrance channel mass asymmetry is another significant quantity in terms of understanding the saddle point behaviour and its stability w.r.t the "Businaro Gallone mass asymmetry (α_{BG})". For a given projectile target combinations, the fusion path followed by the dinuclear complex is affected by the relative value of "entrance channel mass asymmetry w.r.t the critical Businaro-Gallone mass asymmetry". The entrance channel mass asymmetry (α) is defined as follows:

$$\alpha = \frac{A_{tar} - A_{proj}}{A_{tar} + A_{proj}} \quad (1)$$

where A_{tar} and A_{proj} are atomic masses of target and projectile, respectively. α_{BG} is given as

$\alpha_{BG} = 0$ when $X < X_{BG}$ and

$$\alpha_{BG} = a\sqrt{\frac{X - X_{BG}}{(X - X_{BG}) + b}} \text{ when } X > X_B; \quad (2)$$

where $X_{BG} = 0.396$, a = 1.12 and b = 0.24. Here, X is the fissility of CN and is given by

$$X = \frac{Z^2/A}{(Z^2/A)_{crit}} \quad (3)$$

$$(Z^2/A)_{crit} = 50.883\left[1 - 1.7826\left(\frac{(A-2Z)}{A}\right)^2\right] \quad (4)$$

where, Z is the atomic number and A is mass number of the CN.

For the system with $\alpha < \alpha_{BG}$, mass transfer takes place from target to projectile nucleus giving rise to dinuclear system, which reseparates before equilibrating in all degrees of freedom and favour more asymmetric shapes leading to QF. On the other hand, for $\alpha > \alpha_{BG}$, the direction of mass drift is preferentially in reverse order leading to formation of CN (Pant *et al.*, 1996). Here, equilibration is attained in all degrees of freedom and thus, the identity of the entrance channel is totally lost. Later, depending on the available angular momentum and excitation energy, it undergoes decay via either fission or particle evaporation (Choudhury and Thomas, 2011).

Orientation of projectile-target system

The projectile-target system's orientation during collision also plays a important role in determining the exit channel reaction mechanism. There is a strong competition between QF and FF in the reactions involving deformed nuclei and it has important implications for understanding and predicting production cross-section for SHEs. Hinde *et al.* (1995), proposed the occurrence of orientation-dependent QF in ground state deformed target nuclei. According to this model, for reactions having energy less than the Coulomb barrier only the contact of the projectile with the flattened side of the prolate target will lead to the compact dinuclear system, whereas, for lower barrier there will be a chances of tip-to-tip collision of deformed target nuclei, leading to formation of an elongated dinuclear system. Consequently, the former configuration would lead to fission following fusion and the latter to QF (Hinde et al., 1995; Banerjee et al. 2011). Fig. 4 shows the schematic diagram of the collision at axial and equatorial position of the deformed target nucleus. "Only deformation-aligned collisions lead to contact or capture at beam energies E $<V_B$. For E $>V_B$, capture also occurs for more compact equatorial configurations on account of small distance of closest approach (R_{Min})". So, capture seems to be feasible also for more compact equatorial configurations, giving longer sticking times, anticipated to correlate with larger P_{CN} (Hinde et al., 2017).

Neutron to proton (N/Z) ratio

The fission dynamics for different isotopes of a given element, the effect of neutron excess and contributions coming from near scission configurations are some other factors/processes affecting the FF events. It is therefore of considerable interest to study the fission properties of heavy nuclei by populating different isotopes of CN using appropriate reaction channels and compare the experimental observable to look for any possible anomaly.

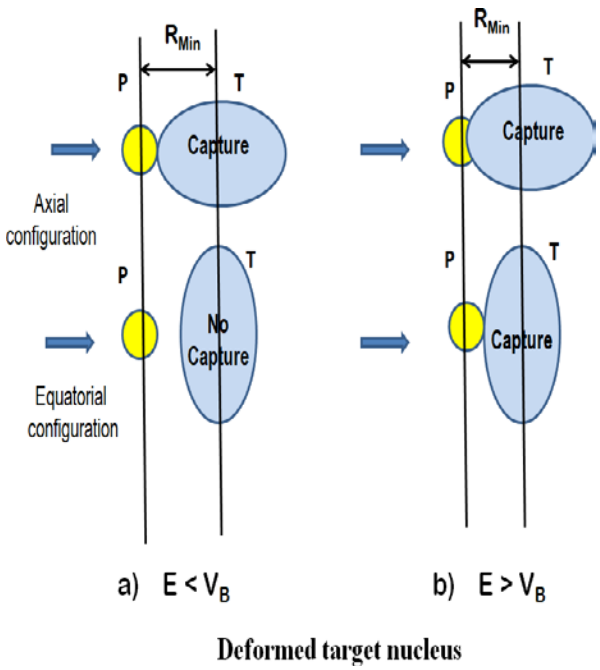

Fig. 4: Schematic of axial and equatorial collision configurations [24].

NEW ASYMMETRIC MODE IN MEDIUM MASS REGION

β-Delayed fission is a crucial source for understanding low-energy fission properties of exotic nuclei having unusual neutron to proton ratio (N/Z). Recently asymmetric mass distribution observed in β-Delayed fission of ^{180}Tl in pioneering experiment was carried out by Andreyev *et al.* (2010). Prasad *et al.* (2015) also observed asymmetric fission in the β-Delayed fission of neutron-deficient ^{180}Hg nuclei.

PROBES TO STUDY THE FUSION-FISSION REACTION DYNAMICS

To explain the underlying mechanism of the FF processes, experimental probes, like, neutron multiplicity, fission fragment mass distribution, fission fragment angular distribution and evaporation residue cross-sections are used. All the above mentioned probes are discussed in the following subsections.

Mass-energy correlations

The mass and total kinetic energy (TKE) distribution provides valuable information about the mass splitting process from the saddle to scission path. The correlation study between TKE and fragment mass is very crucial to explore reaction mechanism of the FF process and to look into the effect of shell closure in the nuclei. Distribution of fragments mass is normally decided at the transition state from saddle to scission and through the shape of scission configuration, the TKE released in fission could be determined. It is noticed experimentally, that the fragment mass distribution is symmetric in shape and peaked around M_{CN} /2 where, M_{CN} is the mass of CN. Moreover, smooth variation of

fragment mass width with energy of the CN is observed (Lestone, 1993). For QF, the mass distribution may still be peaked around M_{CN} /2, but larger width of the mass distribution is a distinct feature of the said process. With the change in the excitation energy, if the QF component in the reaction increases, the mass width will further increase. For better understanding the nature of QF process, variation of fission fragment mass widths with excitation energy have been studied by different groups (Warda *et al*., 2012; Prasad *et al*., 2015; Nishio *et al*. 2015) all over the world for varying target projectile combinations at energies around as well as above the barrier.

Fission fragment angular distribution

The fission fragment angular distributions (FFAD) explained for composite systems with fission barrier (B_f) heights comparable to their intrinsic temperatures, have unraveled many aspects of FF dynamics. The statistical model failed to reproduce the experimental data on fragment angular anisotropy due to onset of the non equilibrium processes, in particular QF, “fast fission” and “pre-equilibrium fission” etc. The compound and non-compound nucleus fission can be distinguished using the distribution of “K degree of freedom”. The fast fission process takes place for composite system with B_f = 0, QF for composite systems with B_f shapes more compact than the entrance channel contact configuration and PEQ occurs in a time comparable to the characteristic relaxation time in “K degree of freedom” when B_f become comparable to the temperature of composite system. The fission fragment angular anisotropy is defined as the ratio of fission yield at 0^o (180^o) to 90^o. In accordance to the standard transition state model (TSM) (Vandebosch and Huizenga, 1973), the angular distribution is characterized by the angular anisotropy (A) as:

$$A = 1 + \frac{\langle l^2 \rangle}{4K_0^2} \qquad (5)$$

where, $< l^2 >$ the mean square angular momentum of the fissioning system. K^2 represents the variance of K-distribution,

$$K_0^2 = T\frac{I_{eff}}{h^2} \qquad (6)$$

where, T is the ‘saddle point temperature’ of the nucleus and I_{eff} being the effective moment of inertia.

For light charged particle induced reactions, anisotropy was observed to be consistent with TSM estimation. However, the angular anisotropy values are found to be larger than those of TSM estimation in large number of reactions using actinide nuclei.

Evaporation residue measurements

Evaporation Residue (ER) provides a clear cut signature of CN formation and is a useful probe for studying both the statistical and dynamical aspects of FF reactions. They are formed following a few nucleon emission from the CN. By measuring the ER cross-sections, one can study the signature of viscous nature of the fission process. ER cross-sections may be referred to as the product of capture cross-section, CN formation probability and its survival against fission (Blocki, Feldmeier and Swiatecki, 1986). Experimentally, the capture cross-section ($\sigma_{capture}$) is defined as the sum of CN-fission ($\sigma_{CN-fission}$), the QF (σ_{QF}), and ER (σ_{ER}) cross-sections as,

$$\sigma capture = \sigma_{CN-fission} + \sigma_{QF} + \sigma_{ER} \quad (7)$$

The cross-section for SHE formation via ER can be mathematically represented as:

$$\sigma ER = \sigma_{capture} \, . \, P_{CN} \, . \, P_{survival} \quad (8)$$

where P_{CN} is usually defined as the probability of CN formed by complete fusion of the dinuclear system. It is the most challenging and least accepted factor that influences cross-sections of heavy element formation. $P_{survival}$ is the survival probability of the CN against fission. For SHEs synthesis, currently the challenge is to understand the QF process that influence P_{CN} process. Several groups (Sharma *et al.*, 2017) have recently conducted a systematic study of ER cross-section measurement, in order to investigate the interplay between fusion and QF in different reactions.

Neutron multiplicity measurements

Measurement of pre-scission neutron multiplicities in FF reactions due to heavy ions provides significant information on the energy dissipation mechanism in FF dynamics. During the fission process, many neutrons are also emitted, both before and after the scission. The neutrons emitted prior to fission are called the pre-scission neutrons. They are likely to carry the signature of the dynamics of the process and therefore can be used as an independent experimental probe, similar to fragment angular anisotropy. For the QF process, the multiplicity of neutrons is lower than the multiplicity of neutrons in the fusion-fission process. Neutron multiplicity study by several groups (Ramachandaran *et al.*, 2006; Mahajan *et al.*, 2018) have shown that the measured values of pre-scission neutron multiplicities are substantially much larger than the standard statistical model estimation. The lower value of average neutron yield per fission of certain nuclei may be used to indicate the presence of QF in the reaction under study.

Light particle measurements

In fusion-fission, the light charged particles (proton and α) and giant dipole resonance (GDR) γ ray emission takes place continuously during CN formation phase, pre saddle, saddle to scission, scission and fission fragment acceleration stage. The measurement of charged particles can be used to understand the fission dynamics and it is also possible to estimate the time scale of fusion fission process after comparing the yield with model predictions. GDR γ rays measurement provide useful information to study the viscosity of saddle to scission motion. Measurements of the fission time scale are performed by determining multiplicities of GDR γ-ray spectra (Lestone, 1993; Shaw *et al*., 2000) as well as charged particles spectra (proton and alpha) [Ramachandaran, 2006; Gupta *et al*., 2011; Lestone, 1993), to calculate the strength of nuclear dissipation. Recently, Kapoor *et al*. (2017), reported the Pre- and post-scission α-particle multiplicities measurements for the reaction $^{16}O + {}^{194}Pt$ and compared the result with JAONNE2 statistical code to extract the fission time scale. They found that the fission time of the order of 50 - 60 x 10^{-21} s is required to reproduce the neutron and α particle multiplicities.

QF AND SYNTHESIS OF SUPER-HEAVY ELEMENTS

One of the important topics of present nuclear physics research is the production of Super heavy Elements (SHEs) by choosing the appropriate projectile-target combinations. Understanding the dynamics of heavy ion interaction processes is very crucial, as it can provide vital information about the hindrances in the synthesis of SHEs. The impact of nuclear dissipation on the path to scission is extremely important, as such data hold exclusive information on fission dynamics, such as fission time scale, the interaction between collective and single-particle degrees of freedom and the degree of equilibration on the path to fission (Andreyev, Nishio and Schmidt, 2017). QF is a dynamic process between deep-inelastic collisions and complete fusion that divides the fused system into binary fragments without forming a CN. It is a major opponent to CN formation and thus, reduces the probability of formation of SHEs in the fusion of heavy nuclei. The present challenge, therefore, is the quest for the initial conditions that would favour SHEs production. The effect of deformation and orientation on QF process were reported by different groups (Ramachandran, 2006; Mein et al. 1997; Hinde *et al*. 1996) in reactions involving actinide targets. It was also reported by Chizov *et al*. (2003), that effect of shell closure in fission dynamics plays an important

role in the CN's survival probability with deformed targets/projectiles. The attempts are made by different groups to find appropriate projectile-target combinations which would give better SHEs production yield at reasonably low excitation energies.

ASYMMETRIC MASS DISTRIBUTIONS IN FISSION

Asymmetric mass distributions proved to be one of the fission process's most constant puzzles. Moreover, in relatively low-energy fission of actinides, mass distribution asymmetry is widely known and has been intensively investigated for many years. In particular, asymmetric shape was explained theoretically by considering the fragment shell properties (Meitner, 1950; Möller *et al*., 2001; Oganessian, 2007). However, subject got more attention after the recent experimental discovery of asymmetric fission in β-delayed fission of ^{180}Tl [Andreyov *et al*., 2010; Andreyev *et al*., 2014; Elseviers *et al*., 2013). Fig. 5 shows the resulting spectrum of fragment mass and TKE distribution (Andreyev *et al*., 2010). Mass distribution is obviously asymmetric, with A_H =100 and A_L=80 being the most likely heavy and light masses. This experiment was followed by several theoretical works (Andreev et al., 2013; Warda et al., 2012) claiming that shell structure apart from fragment configuration can sometimes play a crucial part in shaping the outcome of fission. The

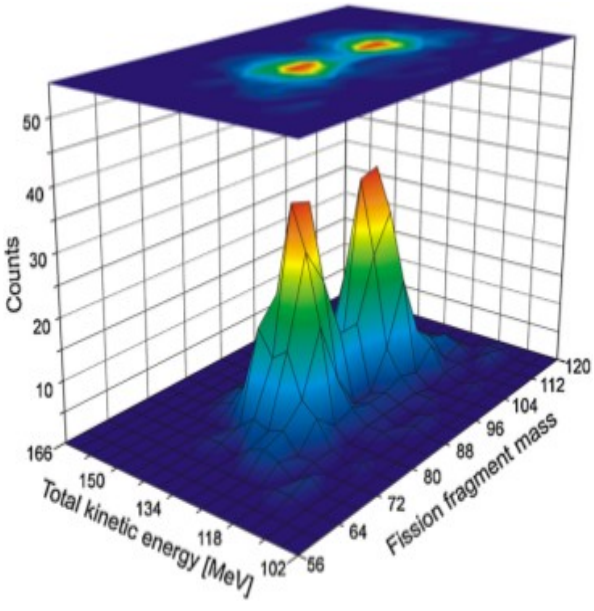

Fig. 5: Mass-energy contours from fission of ^{180}Hg [Kailas, 1997].

new experiments were later carried out to measure the mass distributions for the fissioning nuclei in the Hg - Po region. Nishio *et al*. (2015), measured fission fragment mass distributions from ^{190}Hg and ^{180}Hg formed in ^{36}Ar + ^{154}Sm and ^{36}Ar + ^{144}Sm fusion reactions, respectively.

The mass asymmetry for ^{180}Hg, appears to agree well with the result of low-energy β-Delayed fission of ^{180}Tl. For ^{190}Hg, the mass-asymmetry was observed to be having almost the same value as for ^{180}Hg. In recent years, several groups around the globe have carried out experim ents on fragments mass distributions in medium mass region in order to understand and quantify the factors that influence the onset and existence of QF in fusion-fission reactions (Prasad *et al*., 2015; Lin *et al*., 2012; Williams *et al*., 2013; Hirose *et al*. 2017).

SUMMARY

Exploring the dynamics of heavy-ion induced fusion-fission reactions is one of the key areas of research in nuclear physics. Recent work shows the enhanced efforts (both experimentally and theoretically) at understanding the presence and nature of QF process. Various experimental investigations by different research groups have attempted to characterize and quantify QF using fragment mass distribution as probe. Broadened mass width and mass-angle or mass-energy correlations could be a strong indicator of the deviation of reaction mechanism from compound nucleus formation. Despite so much efforts by researchers in the field, basic nature and its dependence on reaction variables is yet to be fully understood and this certainly demands more experimental data which can help to define a model predicting the nature of QF in such reactions.

REFERENCES

Andreyev, A. N. and J. Elseviers, *et al.* 2010. New type of asymmetric fission in proton-rich nuclei. Phys. Rev. Lett. 105: 252502.

Andreev, A. V., G. G. Adamian, N. V. Antonenko and A. N. Andreyev. 2013. Isospin dependence of mass-distribution shape of fission fragments of Hg isotopes. Phys. Rev. C 88: 047604.

Andreyev, A. N., M. Huyse and P. Van Duppen. 2014. Beta-Delayed Fission: A rare decay mode as probe for phenomena near and beyond the fission barrier. Nuclear Physics News 24: 14-18.

Andreyev, A. N., K Nishio and K-H Schmidt. 2017. Nuclear fission: a review of experimental advances and phenomenology. Rep. Prog. Phys., 81: 016301.

Banerjee, K. and T. K. Ghosh, *et al*. 2011. Evidence of quasifission in the ^{16}O ^{238}U reaction at sub-barrier energies. Phys. Rev. C 83: 024605.

Banerjee, K. and T. K. Ghosh, *et al*. 2016. Fission dynamics study in ^{243}Am and ^{254}Fm. Phys. Rev. C 93: 064602.

Berriman, A. C. and D. J. Hinde, *et al*. 2013. Unexpected inhibition of fusion in nucleus–nucleus collisions . Nature 413: 144-147.

Blocki, J.P., H. Feldmeier and W.J. Swiatecki. 1986. Dynamical hindrance to compound-nucleus formation in heavy-ion reactions. Nucl. Phys. A 459: 145-172.

Bohr, N. and J. A. Wheeler. (1939) The Mechanism of Nuclear Fission. Phys. Rev. 56: 426-450.

Chizhov, Yu. and M. G. Itkis, *et al*. 2003. Unexpected entrance-channel effect in the fission of 216Ra*. Phys. Rev. C 67: 011603(R).

Choudhury, R. K. and R. G. Thomas. 2011. Non-equilibrium processes in Heavy-ion induced Fission Reactions. J. Phys.: Conf. Ser. 282: 012004 and references therein.

Elseviers, J. and A. N. Andreyev *et al. 2013*. β-delayed fission of ^{180}Tl. Phys. Rev. C 88: 044321.

Frisch, O. R. 1939. Physical Evidence for the Division of Heavy Nuclei under Neutron Bombardment. Nature 143: 276.

Ghosh, T. K. and K. Banerjee *et al*. 2009. Sharp change-over from compound nuclear fission to quasifission. Phys. Rev. C 79: 054607.

Grégoire, C., C. Ngô and B. Remaud. 1982. Fast fission phenomenon, deep inelastic reactions and compound nucleus formation described within a dynamical macroscopic model. Nucl. Phys. A, 383: 392-420 and references therein.

Gupta, Y. K. and D. C. Biswas, *et al*. 2011. Systematics of pre- and near-scission α-particle multiplicities in heavy-ion-induced fusion-fission reactions. Phys. Rev. C 84, 031603(R).

Hahn, O. and F. Strassmann. 1939a. Über den Nachweis und das Verhalten der bei der Bestrahlung des Urans mittels Neutronen entstehenden Erdalkalimetalle. Naturwissenschaften 27: 11–15.

Hahn, O. and F. Strassmann. 1939b. Nachweis der Entstehung aktiver Bariumisotope aus Uran und Thorium durch Neutronenbestrahlung; Nachweis weiterer aktiver Bruchstücke bei der Uranspaltung. Naturwissenschaften 27: 89-95.

Hinde, D. J. and M. Dasgupta, *et al*. 1995. Fusion-Fission versus Quasifission: Effect of Nuclear Orientation. Phys. Rev. Lett. 74: 1295-1298.

Hinde, D. J., M. Dasgupta, J. R. Leigh, J. C. Mein, C. R. Morton, J. O. Newton and H. Timmers. 1996. Conclusive evidence for the influence of nuclear orientation on quasifission. Phys. Rev. C 53: 1290-1300.

Hinde, D.J. and M. Dasgupta, *et al*. 2017. Quasifission Dynamics in the Formation of Superheavy Elements. EPJ Web Conf. E3S Web of Conferences 163: 00023.

Hinde, D. J. 2018. Fusion and quasifission in superheavy element synthesis. Nucl Phys. News 28: 13-19.

Hinde, D. J. and D. Y. Jeung, *et al*. 2018. Sub-barrier quasifission in heavy element formation reactions with deformed actinide target nuclei. Phys. Rev. C 97: 024616.

Hirose, K. and K. Nishio, *et al*. 2017. Role of multichance fission in the description of fission-fragment mass distributions at high energies. Phys. Rev. Lett. 119, 222501.

Kailas, S. 1997. Heavy-ion induced fission at near-barrier energies. Phys. Rep. 284: 381-416.

Kapoor, K. and S. Verma, *et al*. 2017. Fission time scale from pre-scission neutron and α multiplicities in the ^{16}O + ^{194}Pt reaction. Phys. Rev. C 96: 054605.

Kramers, H. A. 1940. Brownian motion in a field of force and the diffusion model of chemical reactions. Physica 7: 284-304.

Lestone, J. P. 1993. Determination of the time evolution of fission from particle emission. Phys. Rev. Lett. 70, 2245-2248.

Lestone, J. P. and J.R. Leigh, *et al*. 1993. Pre-scission charged-particle multiplicities following the reactions ^{164,167,170}Er + ^{28}Si. Nucl. Phys. A 559: 277-316.

Lin, C. J., R. du Rietz, D. J. Hinde, M. Dasgupta, R. G. Thomas, M. L. Brown, M. Evers, L. R. Gasques and M. D. Rodriguez. 2012. Systematic behavior of mass distributions in ^{48}Ti-induced fission at near-barrier energies. Phys. Rev. C 85: 014611. *Erratum* 2017. Phys. Rev. C 96: 029901.

Mahajan, R. and B. R. Behera, *et al*. 2018. Systematic study of ^{192,202,206,210}Po compound nuclei using neutron multiplicity as a probe. Phys. Rev. C 98, 034601.

Mein, J. C., D. J. Hinde, M. Dasgupta, J. R. Leigh, J. O. Newton and H. Timmers. 1997. Precise fission fragment anisotropies for the ^{12}C+^{232}Th reaction: Supporting the nuclear orientation dependence of quasifission. Phys. Rev. C 55: R995-R998.

Meitner, L. and O. R. Frisch. 1939. Disintegration of Uranium by Neutrons: a New Type of Nuclear Reaction. Nature 143: 239-240.

Meitner., L. 1950. Fission and nuclear shell model. Nature 65: 561.

Möller, P., D. G. Madland, A. J. Sierk and A. Iwamoto. 2001. Nuclear fission modes and fragment mass asymmetries in a five-dimensional deformation space. Nature 409: 785-790.

Nishio, K. and A. N. Andreyev, *et al*. 2015. Excitation energy dependence of fragment-mass distributions from fission of ^{180,190}Hg formed in fusion reactions of ^{36}Ar + ^{144,154}Sm. *Physics Letters B* 748: 89-94.

Oganessian, Y. 2007. Heaviest nuclei from ^{48}Ca-induced reactions. Journal of Physics G: Nuclear and Particle Physics, 34:R165.

Pant, L. M., A. Saxena, R. K. Choudhury and D. M. Nadkarni. 1996. Mass dependence of fragment anisotropy in the fission of ^{11}B+^{237}Np and ^{16}O+^{209}Bi systems. Phys. Rev. C 54: 2037-2040.

Prasad, E. and K. M. Varier, *et al*. 2010. Conclusive evidence of quasifission in reactions forming the ^{210}Rn compound nucleus. Phys. Rev. C 81: 054608.

Prasad, E. and D. J. Hinde, *et al.* 2015. Observation of mass-asymmetric fission of mercury nuclei in heavy ion fusion. Phys. Rev. C 91: 064605.

Prasad, E. and A. Wakhle, *et al*. 2016. Exploring quasifission characteristics for ^{34}S+^{232}Th forming ^{266}Sg. Phys. Rev. C 93: 024607.

Rafiei, R. and R. G. Thomas, *et al*. 2008. Strong evidence for quasifission in asymmetric reactions forming ^{202}Po. Phys. Rev. C 77: 024606.

Ramachandran, K. and A. Chatterjee, *et al*. 2006. Fission time scale from prescission neutron, proton, and α particle multiplicities in 28Si+175Lu. Phys. Rev. C 73: 064609.

Ramamurthy, V. S. and S. S. Kapoor. 1985. Interpretation of Fission-Fragment Angular Distributions in Heavy-Ion Fusion Reactions. Phys. Rev. Lett. 54: 178-181.

Shamlath, A. and E. Prasad, *et al*. 2017. Fusion and quasifission studies in reactions forming Rn via evaporation residue measurements. Phys. Rev. C 95: 034610.

Sharma, P. and B. R. Behera, *et al*. 2017. Evaporation residue cross-section measurements for ^{48}Ti-induced reactions. Phys. Rev. C 96, 034613 and references therein.

Shaw, N. P. and I. Diószegi, *et al*. 2000. Nuclear viscosity of hot rotating ^{240}Cf. Phys. Rev. C 61: 044612.

Vandenbosch, R. and J. R. Huizenga. 1973. Nuclear fission, Academic Press.

Warda, M., A. Staszczak and W. Nazarewicz. 2012. Fission modes of mercury isotopes. Phys. Rev. C 86: 024601.

Williams, E. and D. J. Hinde, *et al*. 2013. Evolution of signatures of quasifission in reactions forming curium. Phys. Rev. C 88: 034611.

Pb. Univ. Res. J (Sci.) Vol. 69, 2019, pp 1-12

DEVELOPMENT OF DISPOSABLE PIPETTE EXTRACTION METHOD FOR THE PRECONCENTRATION OF PHTHALATES AND ITS APPLICATION TO SYNTHETIC AND SPIKED REAL SAMPLES

Deepika Sardana[1], Priyanka Narula[1], Varinder Kaur[1*] and Raghubir Singh[2]

[1] *Department of Chemistry, Panjab University, Chandigarh, 160014, India*

[2] *Department of Chemistry, DAV College, Sector 10, Chandigarh, 160011, India*

Abstract

In this paper, a new method is standardized for the quantification of some endocrine disrupting phthalates using disposable pipette extraction (DPX) tips in conjunction with high performance liquid chromatography - diode array detection (HPLC-DAD). In this method phthalates were loaded into DPX tip via 'draw and eject' cycles followed by air aspiration, which established a very rapid adsorption-desorption equilibrium of phthalates between solution and sorbent. The desorbed mixture of phthalates was injected manually in the injection port of HPLC-DAD system for quantification. The limit of detection and limit of quantification for the method were found in the range 0.10-4.90 ng mL^{-1} and 0.33-16.3 µg mL^{-1}, respectively. In addition, the developed method was used for the determination of various phthalates from spiked samples such as water samples, soil samples and commercially available lens cleaning solution. The recoveries of spiked samples were found approximately 80%.

Keywords: Disposable pipette extraction, phthalates, di-ethylphthalate, di-*n*-propylphthalate, benzyl-*n*-butylphthalate, di-*n*-butylphthalate, HPLC-DAD.

INTRODUCTION

Disposable pipette extraction (DPX) tip is a modified solid phase extraction (SPE) cartridge used to get rapid and low-volume solid phase extraction of analytes from a variety of matrices (Brewer, 2003). DPX claims to be an environmental friendly, simple and effective sample preparation technique for the extraction of analytes (Lamber, 2009). It consists of a modified standard pipette tip (1 or 5 mL capacity) loaded with loosely confined stationary phase and offers following advantages over conventional methods; 1) It can be attached to a syringe for manual use and hence, easy to handle for loading a sample on solid sorbent. 2) The dynamic mixing of solid and liquid phase during 'draw and eject' cycles directly exposes the analytes to sorbent surface resulting in efficient sorption. 3) It is economical to use and does not require accessories like low pressure chamber in SPE, interface in solid phase microextraction (SPME) etc. 4) It is simple in operation, uses variety of sorbents and has ability to automate the extraction for rapid sample preparation method. 5) Moreover, it requires less sorbent, less solvent, provides faster extraction and can be considered as greener technique. Recently, DPX has been used in the determination of pesticides from various real samples (Ziang, 2012; Guan, 2010; Ellison, 2009), drugs and their metabolites (Ellison, 2009; Schroeder, 2008), explosives (Guan, 2014) palladium (Jaison, 2012), neurotransmitters (Oliveira, 2019), human blood components (Fernandes, 2018), fungicides (Aguiar Junior, 2019), and pollutants (Turazzi, 2019). To our best knowledge, no report is available on the analysis of phthalic acid esters using DPX as a sample preparation tool.

Phthalic acid esters (PAEs), commonly referred to as phthalates, are industrial chemicals that are mainly used as industrial solvents and lubricants, as additives in textile industry and pesticides, and also in personal care products like deodorants, lotions, perfumes and other cosmetics to retain their color and fragrance (Koch, 2003). They are widely used in food packaging materials, toys and polyvinylchloride plastics (PVCs). Some of the phthalates have been identified as endocrine disrupting chemicals (EDCs) and hormonal active agents (HAAs) whose exposure may result in the disruption of hormonal activity resulting in carcinogenic and teratogenic effects (Ghisari, 2009; Kavlock, 2002; Welshons 2003; Thompson, 2004; Hauser, 2005). Phthalates are postulated to produce endocrine-disrupting effects in many species, where foetal exposure to these compounds is found to induce developmental and reproductive toxicity.

Their entry into the environment occurs directly from the production of tons of plastic materials and via emissions from polymeric materials. Since phthalates do not form stable bonds with plastic, they migrate in food when come in contact with oil or other fat containing foods. Therefore, they are easily released into the environment, especially, water resources (Serodio, 2006). In order to assess the health risk from exposure to phthalates, a simple, quick, efficient and reliable method is required for the determination of phthalates in the environmental samples.

Several sample preparation methods have been developed for phthalates in the past such as liquid - liquid extraction (LLE) (Soresen, 2006), micro-extraction by packed sorbents (MEPS) (Prieto 2010), solid phase microextraction (SPME) (Li, 2004), cloud point extraction (CPE) (Ling, 2007), solid phase extraction (Stiles, 2007), microwave assisted extraction (Bartolome, 2005), liquid phase microextraction (Yao, 2008) and stir bar sorptive

*Corresponding Author: var_ka04@pu.ac.in

MS Received: November 12, 2019, Accepted: December 20, 2019

extraction (SBSE) (Prieto, 2008). It is well known that classical liquid-liquid extraction technique is laborious, time consuming, utilizes plenty of harmful solvents, and associated with loss of analytes etc, therefore, it has been replaced by solid phase extraction techniques. The use of disposable pipette extraction is found to be better in some respects over some commonly used sample preparation techniques like SPE, SPME and SBSE. Amongst these, SPE suffers due to involvement of large sample volume and cartridge choking problems (Li, 2012). On the other hand, SPME suffers due to less stability of fibers, expensiveness and cross-contamination problems (Guan, 2010). Similarly, SBSE suffers from requirement of excessive amount of sorbent as well as time consuming desorption step. Besides, the technique has not been widely accepted as could be anticipated, due to the limited number of coating materials commercially available and the difficulty of full automation (Lehotay, 2013). Comparatively, DPX is cost effective, less solvent consuming, free from choking problems, free from damage, does not require any accessories (like interface in SPME and vacuum chamber in SPE), and can be used with a syringe or autopipette. DPX tips can be re-used several times and moreover, all the operations in this experiment were done on single DPX tip. In addition, its handling is very easy and loss of analytes is almost negligible. Most of these methods involved GC/MS or GC/FID as quantification technique. In the present method, disposable pipette extraction has been used with HPLC-DAD system for the determination of some phthalates for the first time. Herein, di-ethylphthalate (DEP), di-*n*-propylphthalate (DPP), di-*n*-butylphthalate (DBP), and butyl-*n*-benzylphthalate (BBP) have been chosen as analytes as they produce reproductive and developmental toxicity. The developed method has been applied for the determination of phthalates from spiked samples.

MATERIALS AND METHOD

Reagents and materials handling

All reagents namely di-ethylphthalate (Merck, USA), di-*n*-propylphthalate (Acros Organics, Germany), benzyl-*n*-butylphthalate (Acros Organics, Germany), and di-*n*-butylphthalate (CDH, India) were of analytical grade. Acetonitrile (Sigma Aldrich, USA), methanol (Merck, USA), isopropyl alcohol (Merck, USA) were of HPLC grade and water was triple distilled in the lab using water distillation unit. All the solvents were filtered through Nylon-6,6 membrane filter and degassed by sonication before use. Stock solutions of 1000 µg mL^{-1} of each phthalate were prepared by dissolving 0.01 g of each phthalate in 10 mL methanol. All samples prepared were then allowed to pass through nylon membrane filter of 0.22 µm pore size. The stock solutions of each phthalate were diluted to 100 µg mL^{-1} and were subjected to UV-Vis spectrophotometric analysis to select λ_{max} for detection in HPLC-DAD system. In order to avoid the contact of reagents and solvents with plasticizers, special care was taken during the handling of plastic materials. Because of the ubiquity of plasticizers and the tendency of residues to persist, all glasswares were cleaned prior to the analysis according to the recommendations specified in U.S. EPA Method 506 (Munch, 1995).

Instrumentation

Reverse phase disposable pipette extraction tips (DPX tips) equipped with 30 mg of C18 material (90 µm particle size) and 1 mL capacity were bought from Gerstel (Germany). The equipment consisted of a plastic syringe to which DPX tip was attached. Sonication was done with Wensor Digital Ultrasonic Cleaner (LMUC-2A) having ultrasonic wattage of 50 W and ultrasonic frequency of 40 ± 3 KHz. HPLC analysis was carried out with a Waters HPLC system equipped with Waters 515 pump, pump control module II PC2 and waters 2996 UV-Vis photodiode array detector. All the separations were obtained using Ascentis C18, 5 µm, column of dimensions 4.6 mm × 250 mm bought from Supelco analytical, USA. Maximum wavelength of absorption for each phthalate was selected by recording UV spectrum on a JASCO V-530 UV-Vis spectrophotometer.

DPX-HPLC-DAD procedure

Stock standard solutions (0.50-5.00 µg mL^{-1}) of each phthalate i.e. di-ethylphthalate (DEP), di-*n*-propylphthalate (DPP), benzyl-*n*-butylphthalate (BBP) and di-*n*-butylphthalate (DBP) were prepared in methanol. For preconcentration, DPX tip was attached to a syringe and preconditioned with 2 mL of methanol. Then, sample was loaded inside the tip by upright movement of plunger of the attached syringe. The sample and sorbent were mixed together by passing air to expose the sorbent surface for the effective sorption of analytes. After the sorption of sample on C18 material filled in the tip, solution was discharged (dispensed) by the downward movement of plunger. This ‘draw and eject’ process was repeated 25 times to complete the equilibration. The sorbent loaded with phthalates was washed by 1 mL of acetonitrile for the elution of phthalates by repeating ‘draw and eject’ process for 10 times and the eluted sample was directly injected into

the injection loop of HPLC system. The contents were separated at C18 column using acetonitrile-water (70:30, v/v) as mobile phase and detected at 225 nm. DPX tip was then washed with 2 mL of acetonitrile. Washing was repeated for 5 cycles to wash the sorbent thoroughly, rinsed with methanol and reused. The synthetic and spiked samples were also analysed following the same procedure.

Optimization of DPX procedure

Number of cycles: In order to obtain the maximum sorption of analytes, all the phthalates were analysed for different 'draw and eject' cycles. The cycles were varied from 5 to 30 for the sorption of phthalates. For this operation, a known concentration (5 µg mL^{-1}) of each phthalate was taken and treated with DPX tip as the mechanism discussed above. Each phthalate solution was loaded in the DPX tip by drawing the sample for 5 times followed by its elution for 10 times. The procedure was continued for 10, 15, 20, 25, and 30 drawing cycles until equilibrium was achieved. Similarly, number of cycles was also optimized for the elution of phthalates by fixing the drawing cycles to 25 and varying the elution cycles for 5, 10, 15, and 20 times.

Choice of solvent: To optimize solvents for maximum sorption and elution of phthalates, methanol, ethanol, acetonitrile and dichloromethane were tried for a known concentration of phthalates (5 µg mL^{-1}).

OPTIMIZATION OF CHROMATOGRAPHIC CONDITIONS

Phthalates were separated at C18 column and chromatographic conditions such as mobile phase composition, flow rate and wavelength were varied to get the best resolution of phthalate peaks and maximum sensitivity of the method.

Mobile phase

Mobile phase was varied for different ratios of acetonitrile-water. Initially, a mixture containing known concentration (5 µg mL^{-1}) of each phthalate in methanol was treated under optimized conditions of DPX (25 drawing cycles and 10 elution cycles) and eluted sample of phthalates in acetonitrile was injected in the injection port of HPLC-DAD system. The contents were separated on C18 column using 90:10 (v/v), acetonitrile: water as mobile phase. Then, acetonitrile content was decreased and water was increased in the mobile phase at a difference of 5% to get the best resolution. Therefore, the mobile phase composition was varied from 90:10 (v/v) to 60:40 (v/v) for acetonitrile-water.

Flow rate

The flow rate was varied from 0.5 to 1 mL min^{-1} with an increment of 0.1 mL min^{-1} in order to get best resolution of peaks. The operations were carried out for the known concentration (5 µg mL^{-1}) of phthalates as per the procedure discussed above.

Detection wavelength

Further, detection wavelength was optimized to get the maximum sensitivity for phthalates. As the detection system is diode array, therefore, chromatograms were checked for best peak separation and peak shape at the wavelengths ranging between 210 nm to 300 nm.

Sample preparation of synthetic samples and spiked real samples (tap water, bottled water, soil samples and lens cleaning solution)

For synthetic samples, known concentrations of different phthalates (varying from 0.5 to 5 µg mL^{-1}) were mixed and the total volume was made to 10 mL. The samples were quantified using optimized procedure given above. The developed analytical method was also applied for the analysis of soil samples, tap water, lens cleaning solution and mineral water commercialized in plastic bottles to check the presence of phthalates. Firstly, real samples (tap water, bottled mineral water and lens cleaning solution) were treated with DPX and analysed by the optimized procedure discussed above without any further treatment. Then, 5mL of each of the real samples was spiked with mixture of all the four (DEP, DPP, DBP, BBP) phthalates of known concentrations and the volume was made to 10 mL. These were analysed following the same procedure mentioned above.

Soil samples were collected from the University campus and 1 g of soil sample was added with 5 mL of water. The contents were stirred and filtered over membrane filter for three times to remove the soil particles completely. The sample was filtered with syringe filter and used for DPX-HPLC-DAD without any other pretreatment. Similarly, 1 g of soil was spiked with different concentrations of mixture of phthalates and preconcentrated following the same procedure discussed before.

RESULTS AND DISCUSSION

Working of DPX

In the present method, DPX tips filled with C18 material have been used for the sorption of phthalates. An illustration showing the DPX tips is given in Fig. 1 (I). DPX operates via 'draw and eject' cycles for loading and desorbing a sample and involves following steps shown in Fig 1 (II-IV).

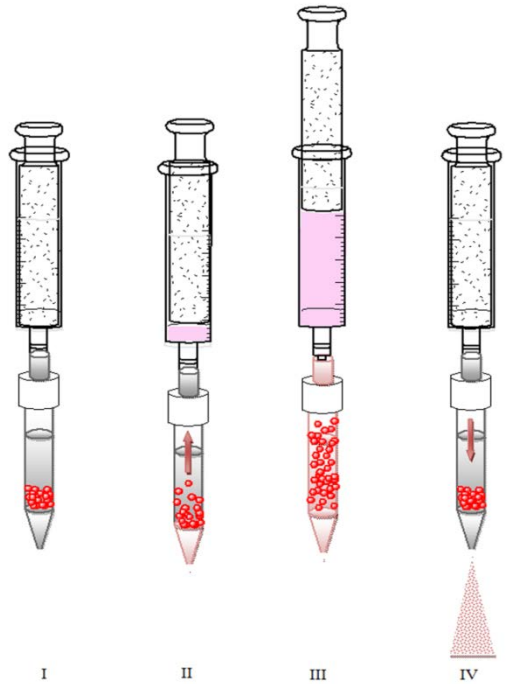

Figure 1: Working of DPX tips; (I) Commercially available DPX tip (II) Loading of sample (III) Agitation of sample (IV) Elution of sample.

Loading of sample: In this step, sample is loaded in the tip by 'draw and eject' cycles *i.e.* upright and downward movement of plunger. During this step, phthalates come in direct contact with the solid surface.

Agitation of the sample: In this step, sample is aspirated by air for thorough mixing and to get maximum contact between solid phase and the phthalate solution. The mobility of the stationary phase particles enables rapid mixing and equilibration with the sample solution during aspiration and leads to efficient and rapid sorption of phthalates.

Elution of analytes: The analyte is then removed from solid phase by drawing a small volume of solvent (1 mL acetonitrile in present method) into pipette tip and agitating as before. The resulting analyte solution is then expelled from the tip and is analyzed by suitable method.

In the present method, phthalates were loaded into DPX tips filled with C18 sorbent from different matrices and eluted with acetonitrile. When phthalates were allowed to interact with the stationary phase, several types of interactions are possible for adsorption and partition. Here, we have chosen C18 (octadecylsilyl) sorbent due to its greater hydrophobicity. Phthalates show retention on C18 material mainly due to non-polar interactions. Another parameter which decides the equilibration of phthalates on to sorbent is number of 'draw and eject' cycles. When the number of 'draw and eject' cycles was less, the adsorption of phthalates was less whereas an increase in adsorption was observed with the increase in number of cycles. The adsorption became almost constant after 25 cycles for all the phthalates i.e. DPP, DBP, DBB and DEP attained equilibrium thereafter (Fig. 2). Therefore, twenty five cycles were optimized for the complete adsorption of phthalates. The elution of samples was found independent of the cycles as it remained same for 10, 15 and 20 cycles. Therefore, we chose 10 cycles for the elution of samples. The elution of phthalates was found better in acetonitrile as compared to methanol, ethanol and dichloromethane; therefore, it was chosen as eluting solvent for the present analysis. The method discussed above provides extraction of phthalates in less time with less solvent and high extraction efficiency.

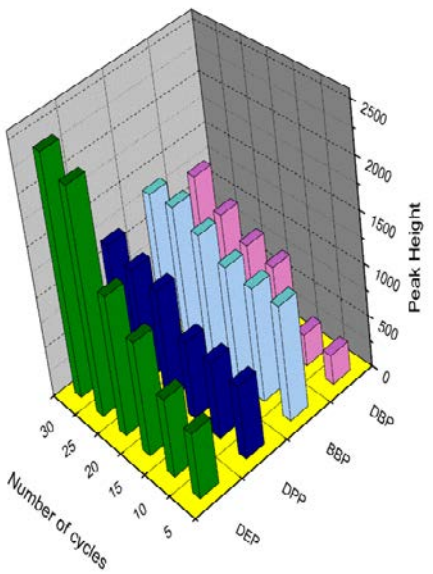

Figure 2: Variation in sorption of phthalates with the increase in 'draw and eject' cycles.

ANALYSIS OF PHTHALATES USING DPX

After the optimization of DPX parameters, separation and detection methods were standardized using HPLC-DAD system. UV-Vis spectrum (Fig. 3) revealed maxima at 225 nm along with a weak absorption band at 280 nm for all the phthalates in acetonitrile. Therefore, 225 nm was selected for detection of phthalates in HPLC-DAD system to get higher sensitivity. The separation and peak shapes of phthalates depend upon the time for which the phthalates remained in contact with the sorbent due to the nature of interactions involved. The retention of phthalates increased in the column with the increase in the alkyl chain. Therefore, DEP, DPP, BBP and DBP were observed at a retention time of 5.5 min, 9.1 min, 14.4 min, and 16.9 min, respectively (Fig. 3 Insert). Variation of solvent polarity indicated best separation in 70:30 acetonitrile: water (v/v) at a flow rate of 1 mL min^{-1} as below this flow rate, broadening of peaks was observed in the chromatogram. The separation was not tried at flow rates above 1 mL min^{-1} to avoid the increase in column pressure. The optimized conditions for resolving mixture of phthalates were 70:30 acetonitrile: water (v/v) as mobile phase at a flow rate of 1 mL min^{-1} and detection at 225 nm.

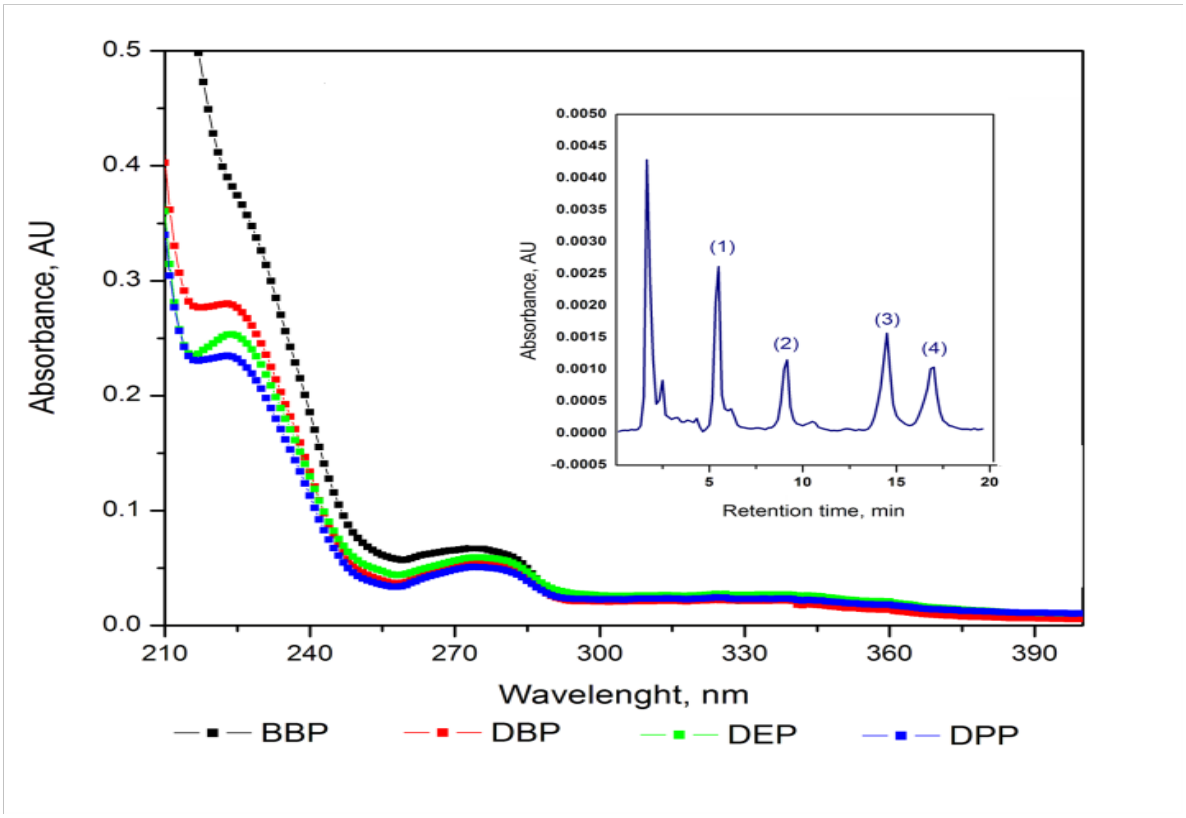

Figure 3: UV-Vis spectra of BBP, DBP, DEP and DPP [Inset: Chromatogram of mixture of phthalates (each having 3 µg mL-1) resolved at 225 nm using acetonitrile: water in 70:30 (v/v) ratio, (where peak 1 corresponds to DEP, 2 - DPP, 3 - BBP, 4 – DBP].

Validation parameters

Different parameters like selectivity, sensitivity, linearity, recovery, precision (intra-day/inter-day), accuracy , carryover and analyte stability were evaluated for the validation of the developed method. The results for all the parameters are given in Table 1.

Table 1 : Validation parameters for phthalates.

Validation parameter	**DEP**	**DPP**	**BBP**	**DBP**
Limit of detection (ng mL^{-1}); S/N =3	0.90	4.0	0.10	4.9
Limit of quantification (µg mL^{-1}); S/N =10	3.00	13.3	0.33	16.3
Regression equation (calculated from area of the peaks)	43041.7 x - 12843.7	11794.6 x + 8288.1	12303.0 x + 85.97	10897.42 x + 5823.7
Regression coefficient	0.9982	0.9945	0.9856	0.9918
Inter-assay precision in retention time (% RSD)	1.320	1.473	0.111	0.189
Intra-assay precision in retention time (% RSD)	0.048	0.0109	0.800	0.070
Inter-assay precision in adsorption of phthalates (% RSD)	2.06	2.79	2.95	2.40
Intra-assay precision in adsorption of phthalates (% RSD)	1.48	1.56	2.50	1.59

The linearity of method was studied by recording chromatograms for different concentrations of phthalates (0.5 to 15 µg mL^{-1}). It was demonstrated by calculating the regression line by least squares method ($y = mx$ +c) from the area of each peak and expressed by coefficient of determination (r^2). The reproducibility, precision and accuracy of the phthalate solutions were also determined from inter-day and intra-day determinations. Intra-assay precision was measured by using three replicates of a mixture containing 5 µg mL^{-1} of each phthalate in the same day. Inter-assay precision was evaluated for three replicates analyzed on separate days (n = 3) for the same concentration. The precision was calculated as percent of relative standard deviation and accuracy was calculated as percent of target concentration. The intra- and intra-day precision ranged from 1-3% and 3% respectively, which means the method is reliable and can be used. All the parameters showed acceptable values according to accepted Protocols.

Application to the real and synthetic samples

The method was applied to synthetic and spiked samples. Validation of this method was checked by spiking different concentrations of four phthalates into tap water, bottled water and lens cleaning solution without any pretreatment and chromatograms obtained are shown in Fig 4. The proposed analytical method has been applied to the analysis of different lens cleaning solutions commercialized in plastic bottles to check the presence of these phthalates and determine their concentrations, Hence lens cleaning solution was also used to study the matrix effect.

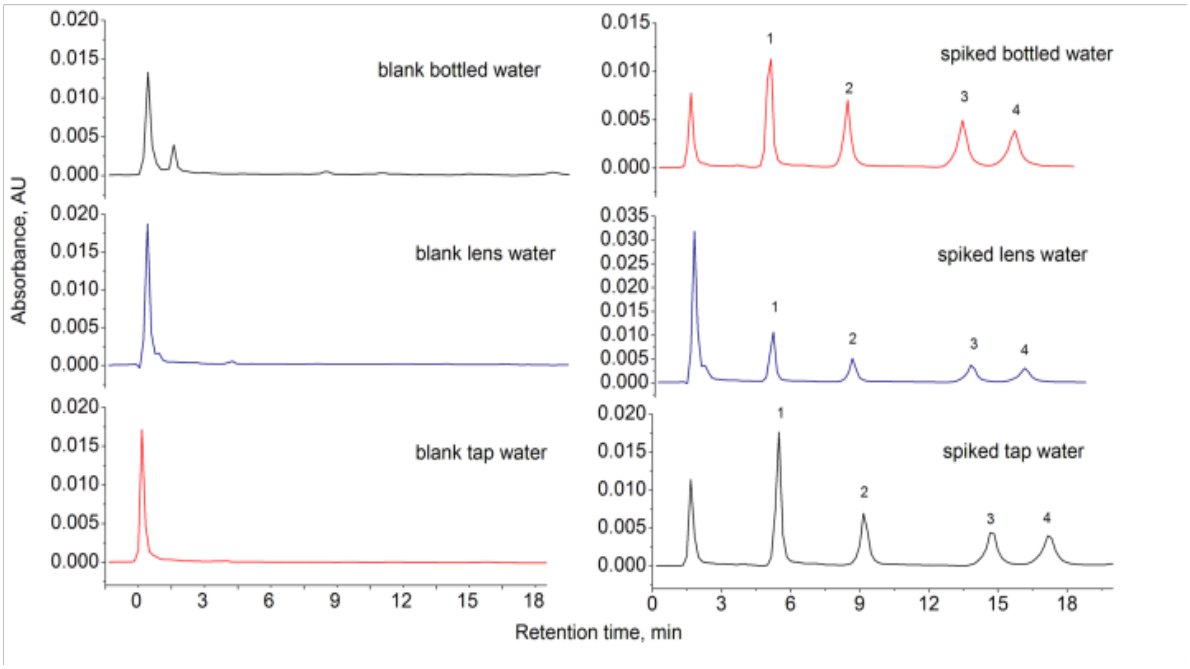

Figure 4: Chromatograms showing separation of phthalates in spiked samples with peaks labeled as 1- DEP, 2- DPP, 3- BBP, 4- DBP, resolved at 225 nm using acetonitrile:water in 70:30 (v/v) ratio as mobile phase concentration at a flow rate of 1 mL min^{-1}.

Results for the recovery of synthetic and spiked samples are summarized in Table 2, which revealed around 80% recovery for the spiked samples. Additionally, different concentrations of phthalates were spiked in a soil sample to check the matrix effects. It is clearly observed in the chromatograms of real and spiked samples that interferences due to matrix are negligible. Moreover, the chemicals like Hydranate (hydroxyalkylphosphonate), poloxamine, Dymed (polyaminopropyl biguanide), edetate disodium, sodium borate, sodium chloride and boric acid present in the lens solution did not show any significant change in the chromatograms. The comparison of peak area, peak height and retention time of spiked samples remained same as quantified from the synthetic samples.

Comparison with existing methods

The developed method is less sensitive than some of the reported methods utilizing sophisticated analytical instrumentation for quantification such as GC-MS and GC-FID (Zafra-Gomez, 2008; Fatoki, 2002; Casajuana, 2004; Li, 2008; Hadjmohammado, 2012; Lu, 2011). The reason for comparatively less sensitivity may be attributed to different modes of analysis as well as very less amount of sorbent filled in the DPX tip. However, there is scope to improve the values of LOD using more sensitive quantification methods or by loading more amount of sorbent in the DPX tip. The method can also be improved using some selective and high surface area sorbents with high analyte loading capacity. Despite of less sensitivity of developed method, it is comparable and even better to some of the reported methods (Carlo, 2008; Zhao, 2008; Shen, 2007; Liang, 2010). The present method is sensitive than the methods involving molecularly imprinted polymers used with GC-RD and GC-MS (He, 2010; Yan 2012). In case of solid phase micro extraction of phthalates, GC-MS is mainly used for quantification except one report where HPLC-DAD system is used for the analysis (Chafer-Pericas, 2008). The present method is even more efficient than the SPME-HPLC-DAD (LOD for DBP = 1 µg L^{-1}), which revealed that DPX can be a better sample preparation method in terms of sensitivity and cost as compared to SPME. The method is also better than other HPLC-UV/DAD methods like microdialysis enrichment (LOD for DEP and DBP = 0.44 and 0.40 µg L^{-1}) (Jen, 2006), continuous flow microextraction (LOD for DEP and DBP = 1 and 5 µg L^{-1}) (Liang, 2008) and using monolith (LOD for DBP = 2.7 µg L^{-1}) (Su, 2010) as solid sorbent. It also provides better quantification results using a simple and economic quantification method i.e. HPLC-DAD relative to the expensive GC/MS or GC/FID. Overall, the developed method is better in terms of sensitivity and other parameters as compared to methods reported in literature.

Table 2: Quantification of synthetic and spiked samples.

Phthalate	Sample	Amount Spiked (amount calculated) (µg in 10 mL of solution)	Recovery (%)	Amount in original solution (ng mL^{-1}) calculated from original solution
DEP	(i) Synthetic sample	(a) 7.0 (6.0) (b) 2.25 (1.91)	(a) 87.50 (b) 84.88	-
	(ii) Tap water	8.50 (7.42)	87.29	NIL
	(iii) Bottled water	7.00 (5.90)	84.20	390
	(iv) Lens cleansing solution	6.00 (4.67)	77.83	350
DPP	(i) Synthetic sample	(a) 1.50 (1.21) (b) 5.00 (4.20)	(a) 80.66 (b) 84.00	-
	(ii) Tap water	15.00 (13.36)	89.06	NIL
	(iii) Bottled water	8.00 (7.01)	87.60	838
	(iv) Lens cleansing solution	10.00 (8.61)	86.10	790
BBP	(i) Synthetic sample	(a) 0.80 (0.58) (b) 5.00 (3.63)	(a) 72.5 (b) 72.5	-
	(ii) Tap water	13.00 (11.31)	87.00	NIL
	(iii) Bottled water	13.50 (12.25)	87.5	49.6
	(iv) Lens cleansing solution	10.00 (8.39)	83.90	70
DBP	(i) Synthetic sample	(a) 1.50 (1.10) (b) 4.00 (3.29)	(a) 73.33 (b) 82.25	-
	(ii) Tap water	13.00 (10.78)	82.92	NIL
	(iii) Bottled water	12.00 (10.57)	88.08	18.8
	(iv) Lens cleansing solution	9.00 (7.33)	81.44	NIL

CONCLUSION

The studies showed that developed DPX method for the determination of phthalates has good sensitivity. The use of C18 sorbent and optimization of DPX conditions provided quantitative recovery of phthalates. This sample preparation method is robust and fast, and provides an easy separation of phthalates in less than 30 minutes. It alleviates the tedious nature of sample preparation. It has ability for automation and makes the extraction rapid so that number of samples can be processed in a short time providing high throughput analysis. So, it proves to be a cost effective, simpler and faster technique as compared to previously reported techniques. Thus, the reported method appears very promising for application to other complex environmental, geological and biological samples.

ACKNOWLEDGEMENTS

The authors are thankful to CSIR, New Delhi for providing financial support (No. 01(2698)/12/EMR-II dated 03-10-2012)

REFERENCES

Aguiar Junior, C.A.S., A.L.R. dos Santos, and A.M. de Faria. 2019. Disposable pipette extraction using a selective sorbent for carbendazim residues in orange juice. Food Chem., 125756(1-8).

Bartolome, L., E. Cortazar, J. C. Raposo, A. Usobiaga, O. Zuloaga, N. Etxebarria, and L. A. Fernandez. 2005. Simultaneous microwave-assisted extraction of polycyclic aromatic hydrocarbons, polychlorinated biphenyls, phthalate esters and nonylphenols in sediments. J. Chromatogr. A, 1068: 229-236.

Brewer, W.E. 2003. Disposable pipette extraction. U.S. Pat., 6566145B2.

Carlo, M.D., A. Pepe, G. Sacchetti, D. Compagnone, D. Mastrocola, and A. Cichelli. 2008. Food Chem., Determination of phthalate esters in wine using solid-phase extraction and gas chromatography–mass spectrometry 111: 771-777.

Casajuana, N. and S.J. Lacorte. 2004. New methodology for the determination of phthalate esters, bisphenol A, bisphenol A diglycidyl ether, and nonylphenol in commercial whole milk samples. J. Agr. Food Chem., 52: 3702-3707.

Chafer-Pericas, C., P. Campins-Falco, and M. C. Prieto-Blanco. 2008. Automatic in-tube SPME and fast liquid chromatography: A cost-effective method for the estimation of dibuthyl and di-2-ethylhexyl phthalates in environmental water samples. Anal Chim Acta, 610: 268-273.

Ellison, S.T., W.E. Brewer, and S.L. Morgan. 2009. Comprehensive analysis of drugs of abuse in urine using disposable pipette extraction. J. Anal. Toxicol., 33: 356-365.

Fatoki, O.S. and A. Noma. 2002. Solid phase extraction method for selective determination of phthalate esters in the aquatic environment. Water Air Soil Poll., 140: 85-98.

Fernandes, A.R., P.S. de Souza, A.E. de Oliveira, and A.R. Chaves. 2018. A New Method for the Determination of Creatinine in Urine Samples Based on Disposable Pipette Extraction. J. Braz. Chem. Soc., 29:695-700.

Ghisari, M. and E. Jorgensen. 2009. Effects of plasticizers and their mixtures on estrogen receptor and thyroid hormone functions. Toxicol letters, 189: 67-77.

Guan, H. and K. Stewart. 2014. Determination of explosives in water using disposable pipette extraction and high performance liquid chromatography. Analyt. Lett., 47: 1434-1447.

Guan, H., W.E. Brewer, S.T. Garris, and S.L. Morgan. 2010. Disposable pipette extraction for the analysis of pesticides in fruit and vegetables using gas chromatography/mass spectrometry. J. Chromatogr. A, 1217: 1867-1874.

Guan, H., W.E. Brewer, S.T. Garris, C. Craft, and S.L. Morgan. 2010. Multiresidue analysis of pesticides in fruits and vegetables using disposable pipette extraction (DPX) and micro-luke method. J. Agric. Food Chem., 58: 5973-5981.

Hadjmohammado, M.R. and E. Ranjbari. 2012. Utilization of homogeneous liquid–liquid extraction followed by HPLC-UV as a sensitive method for the extraction and determination of phthalate esters in environmental water samples. Int. J. Environ. Anal Chem., 94: 1312-1324.

Hauser, R. and A. M. Calafat. 2005. Phthalates and human health. Occup. Environ. Med., 62: 806-818.

He, J., R. Lv, J. Zhu, and K. Lu. 2010. Selective solid-phase extraction of dibutyl phthalate from soybean milk using molecular imprinted polymers. Anal Chim Acta, 661: 215-221.

Jaison P.G., P. Kumar, V.M. Telmore, and S.K. Aggarwal. 2012. Electrospray ionisation mass spectrometric studies for the determination of palladium after pre
-concentration by dispersal
extraction. Rapid Commun. Mass Spectrum, 26: 1971-1979.

Jen J.F. and T.C. Liu. 2006. Determination of phthalate esters from food-contacted materials by on-line microdialysis and liquid chromatography. J. Chromatogr A, 1130: 28-33.

Kavlock, R., K. Boekelheide, R. Chapin, M. Cunningham, E. Faustman, P. Foster, M. Golub, R. Henderson, I. Hinberg, R. Little, J. Seed, K. Shea, S. Tabacova, P. Williams, and T. Zacharewski. 2002. NTP Center for the Evaluation of Risks to Human Reproduction:phthalates expert panel report on the reproductive and developmentaltoxicity of di-n-butyl phthalate. Reprod. Toxicol., 16: 489–527.

Koch, H.M., L.M. Gonzalez-Reche, and J. Angerer., 2003. On-line cleanup by multidimensional LC-ESI-MS/MS for high throughput quantification of primary and secondary phthalate metabolites in human urine. J. Chromatogr. B, 784: 169-182.

Lamber, S. 2009. Disposable Pipette tip Extraction - Leaner, Greener Sample Preparation. Chromatogr. Tod., 2: 12-14.

Lehotay, S.J., K. Mastovska, A.R. Lightfield, A. Nunez, T. Dutko, C. Ng, and L. Bluhm. 2013. Rapid analysis of aminoglycoside antibiotics in bovine tissues using disposable pipette extraction and ultrahigh performance liquid chromatography–tandem mass spectrometry. J. Chroma. A, 13:103-112.

Li, J., Y. Cai, Y. Shi, S. Mou, and G. Jiang. 2008. Analysis of phthalates via HPLC-UV in environmental water samples after concentration by solid-phase extraction using ionic liquid mixed hemimicelles. Talanta, 74: 498-504.

Li, X. J., Z. R. Zeng, Y. Chen, and Y. Xu. 2004. Determination of phthalate acid esters plasticizers in plastic by ultrasonic solvent extraction combined with solid-phase microextraction using calix [4] arene fiber. Talanta, 63: 1013-1019.

Li, Z., Y. Li, X. Liu, X. Li, L. Zhou, and C. Pan. 2012. Multiresidue analysis of 58 pesticides in bean products by disposable pipet extraction (DPX) cleanup and gas chromatography–mass spectrometry determination. Journal of agricultural and food chemistry. J. Agric. Food Chem., 60: 4788-4798.

Liang, P., L. Zhang, L. Peng, Q. Li, and E. Zhao. 2010. Determination of Phthalate Esters in Soil Samples by Microwave Assisted Extraction and High Performance Liquid Chromatography. Toxicol. Bull. Environ. Contam., 85: 147-151.

Liang, P., Q. Li, J. Xu, and D. Du. 2008. LC determination of phthalate esters in water samples using continuous-flow microextraction. Chromatography, 68: 393-397.

Ling, W., J. Gui-bin, C. Ya-qi, H. Bin, W. Ya-wei, and S. Da-zhong. 2007. Cloud point extraction coupled with HPLC-UV for the determination of phthalate esters in environmental water samples. J Environ Sci. 19: 874-878.

Lu, L., Y. Hashi, Z.H. Wang, Y. Ma, and J.M. Lin. 2011. Determination of phthalate esters in physiological saline solution by monolithic silica spin column extraction method. J. Pharm. Anal., 1: 92-99.

Munch, J.W., U.S. 1995. In: EPA and NERL Method 506 revision 1.1, Cincinnati, Ohio 1995, 45268.

Oliveira, I.G. de Carvalho, C. Marchioni, and M.E.C. Queiroz. 2019. Determination of anandamide in cerebrospinal fluid samples by disposable pipette extraction and ultra-high performance liquid chromatography tandem mass spectrometry. J. Chromatogr. B, 1130–1131:121809 (1-7).

Prieto, A., O. Telleira, N. Etxebarria, L.A. Fernández, A. Usobiaga, and O. Zuloaga. 2008. Simultaneous preconcentration of a wide variety of organic pollutants in

water samples: Comparison of stir bar sorptive extraction and membrane-assisted solvent extraction. J. Chromatogr. A, 1214: 1-10.

Prieto, S., Schrader, S., and M. Moedar, 2010, Determination of organic priority pollutants and emerging compounds in wastewater and snow samples using multiresidue protocols on the basis of microextraction by packed sorbents coupled to large volume injection gas chromatography–mass spectrometry analysis. J. Chromatogr. A, 1217: 6002-6011.

Schroeder, J., L. Marinetti, R. Smith, W. Brewer, B. Clelland, and S. Morgan. 2008. The analysis of Δ-9-tetrahydrocannabinol and metabolite in whole blood and 11-nor-Δ-9-tetrahydrocannabinol-9-carboxylic acid in urine using disposable pipette extraction with confirmation and quantification by gas chromatography-mass spectrometry. J. Anal. Toxicol., 32: 659-666.

Serodio, P. and J.M.F. Nogueira. 2006. Considerations on ultra-trace analysis of phthalates in drinking water. Water Res., 40: 2572-2582.

Shen, H.Y., H.L. Jiang, H.L. Mao, G. Pan, L. Zhou, and Y.F. Cao. 2007. Simultaneous determination of seven phthalates and four parabens in cosmetic products using HPLC-DAD and GC-MS methods. J. Sep. Sci., 30: 48-54.

Soresen, L.K. 2006. Determination of phthalates in milk and milk products by liquid chromatography/tandem mass spectrometry. Rapid Commun. Mass Sp., 20: 1135-1143.

Stiles, R., I. Yang, R.L. Lippincott, E. Murphy, and B. Buckley. 2007. Potential sources of background contaminants in solid phase extraction and microextraction. J. Sep. Sci. 30: 1029-1036.

Su, R., X. Zhao, Z. Li, Q. Jia, P. Liu, and J. Jia. 2010. Poly(methacrylic acid-co-ethylene glycol dimethacrylate) monolith micro extraction coupled with high performance liquid chromatography for the determination of phthalate esters in cosmetics. Anal Chim Acta, 676: 103-108.

Thompson, C.J., S.M. Ross, and K.W. Gaido. 2004. Di (n-butyl) phthalate impairs cholesterol transport and steroidogenesis in the fetal rat testis through a rapid and reversible mechanism. Endocrinol., 145: 1227-1237.

Turazzi F.C., L. Mores, E. Carasek, J. Merib, and G.M. de Oliveira Barraa. 2019. A rapid and environmentally friendly analytical method based on conductive polymer as extraction phase for disposable pipette extraction for the determination of hormones and polycyclic aromatic hydrocarbons in river water samples using high-performance liquid chromatography/diode array detection. J. Environ. Chem. Eng., 7: 103156(1-8).

Welshons, W.V., K.A. Thayer, B.M. Judy, J.A. Taylor, E.M. Curran, and F.S. Saal. 2003. Large effects from small exposures. I. Mechanisms for endocrine-disrupting chemicals with estrogenic activity. Environ. Health Perspect., 111: 994-1006.

Yao, J., H. Xu, L. Lv, D. Song, Y. Cui, and T. Zhang. 2008. A novel liquid-phase microextraction method combined with high performance liquid chromatography for analysis of phthalate esters in landfill leachates. Anal. Chim. Acta, 616, 42: 42-48.

Yan, H., X. Cheng, and G. Yang. 2012. Dummy molecularly imprinted solid-phase extraction for selective determination of five phthalate esters in plastic bottled functional beverages. J. Agr. Food Chem., 60: 5524-5531.

Zafra-Gomez,,A., O. Ballesteros, A. Navalon, and J.L.Vilchez, 2008. Determination of some endocrine disrupter chemicals in urban wastewater samples using liquid chromatography - mass spectrometry. Microchem. J., 88:87-94.

Zhao, R.S., X. Wang, J.P. Peng, and J.M. Lin. 2008. Investigation of feasibility of bamboo charcoal as solid-phase extraction adsorbent for the enrichment and determination of four phthalate esters in environmental water samples. J. Chromatogr. A, 1183: 15-20.

Ziang, L., L. Yanjie, L. Xiaochen, L. Xuesheng, L. Zhou, and P. Canping. 2012. Multiresidue analysis of 58 pesticides in bean products by disposable pipet extraction (DPX) cleanup and gas chromatography–mass spectrometry determination. J. Agric. Food Chem., 60: 4788-4798.

Pb. Univ. Res. J (Sci.) Vol. 69, 2019, pp 13-22

THROMBOLYTICS: AN OVERVIEW

Prakash Kumar Sinha[1], Eshu Singhal Sinha[1], Jagdeep Kaur[1*]
[1]*Department of Biotechnology, Panjab University, Chandigarh,160014, India*

Abstract

Thrombolytic enzymes dissolve blood clots and are of considerable interest in clinical research. This is because the incidence of thrombotic disorders including myocardial infarction, deep venous thrombosis and ischemic stroke is increasing worldwide. These medical problems are caused by the presence of blood clots in blood vessels. The un-lysed thrombi inside blood vessels cause severe health problems, and if untreated may even lead to death. Therefore, the dissolution of blood clots is inevitable. With the discovery of plasminogen activators which are considered efficient thrombolytic agents, therapeutic area for thrombosis has advanced. But being non-specific for plasminogen whether present in clot or general bloodstream, many of these enzymes may cause systemic hemorrhage. Over the time, different thrombolytics and their mutant derivatives based on improved stability, plasma clearance, safety, efficacy with enhanced fibrin specificity and cost effectiveness were discovered. This review discusses different thrombolytic enzymes which are most extensively used against thrombosis.

Keywords: Thrombolytic, cardiovascular diseases, streptokinase, tissue- plasminogen activator, plasminogen.

INTRODUCTION

Cardiovascular diseases (CVDs) cause 31% of all global deaths (17.9 million people), higher than any other causes. 85% of these deaths take place in low and middle income countries, and occur equally in men and women. Out of the 17 million deaths, an estimated 7.3 million deaths occur due to coronary heart disease and 6.2 million deaths are due to strokes, which are mainly caused by thrombus formation upon blood vessel injury (WHO report 2011). There are three reasons for thrombus formation: difference in the vasculature of blood vessels, decrease in blood flow and increase in the propensity of blood coagulation (Virchow's triad) (Bagot and Arya, 2008). Upon vascular injury, sympathetic nervous system secretes prostaglandins, serotonin and epinephrine which act on smooth muscle fibers of blood vessels and cause their contraction leading to reduction in diameter of blood vessels, which restricts blood flow to ruptured area (Wilson *et al.,* 2005). When vessels are injured, platelets aggregate at the site of injury and bind to exposed collagen to form a plug that can stop minor bleeding. Platelet aggregation stimulates coagulation pathway which eventually ends in the formation of a fibrin clot. Platelet aggregation provides the surface for the assembly and activation of coagulation complexes and generation of thrombin. Thrombin converts fibrinogen (a glycoprotein of 340 kDa) to fibrin and the fibrin strands thus generated bind aggregated platelets (Riddel Jr. *et al.,* 2007). Thrombin binds to the central domain of fibrinogen and releases fibrinopeptides and factor XIIIa, and catalyzes cross linking of fibrin peptides (Weisel and Litvinov, 2017).

Once the bleeding is arrested and the injured vessel is repaired, regulatory processes limit the growth of the thrombus. Finally, the clot is dissolved by the action of fibrinolytic system (Riddel Jr. *et al.,* 2007). Thus, a balance between thrombus formation and thrombolysis regulates hemostasis. Rarely, this physiological balance is disturbed and blood clot formation leads to blockage of blood flow and is accompanied by unavailability of oxygen to affected tissue leading to ischemia. Full or partial restriction of blood flow to cardiac muscle results in shortness of breath, angina, cardiac arrhythmia and myocardial infarction which may even lead to death. In rare cases blood clot formed in distal parts of body gets dislodged and then trapped in the brain's narrow arteries. This deprives the brain of necessary oxygen resulting in brain cell death in the affected area (Ali *et al.*, 2014). An effective therapy is rapid clot dissolution to minimize tissue damage. Therefore, thrombolytic treatment is given clinically to renovate the function of clot affected tissue.

Classical therapy for thrombosis involves administration of warfarin and heparin, both of which act as anticoagulants. Warfarin inhibits vitamin K-dependent coagulation factors and heparin blocks factor-X activation and thrombin formation (Kotb, 2014). Alternatively, in classical therapy antiplatelet drugs are administered to inhibit blood vessel blocking due to increase in thrombus size. These antiplatelet drugs inhibit either platelet aggregation or platelet activation. Surgeries are also performed for the removal of massive blood vessel occlusion by thrombi. Nowadays, fibrinolytic enzymes produced by microorganisms and other organisms are being used to degrade pre-existing thrombi (Adivitiya and Khasa, 2017) because of their direct dissolving action on fibrin with less side effects (Kotb, 2014). The thrombolytic/ fibrinolytic system involves dissolution of fibrin cl ots by the non-specific serine protease, plasmin (PN), which plays a pivotal role in degradation of thrombi. Plasmin degrades insoluble fibrin meshwork and thus restores the vascular patency via dissolution of blood clots (Chapin and Hajjar, 2015).

*Corresponding Author: jagsekhon@pu.ac.in
MS Received: November 13, 2019, Accepted: December 19, 2019

HUMAN PLASMINOGEN (PROFIBRINOLYSIN)

The major component of fibrinolysis system is plasminogen (PG). PG is a 92 kDa protein synthesized mainly in liver as a single polypeptide chain of 810 amino acids with 19 residues as leader sequences. The mature protein consists of 791 amino acids including 48 cysteines which form 24 disulphide bonds. The plasma concentration of PG is 2.2 µM (Leipnitz *et al.*, 1988). PG activators (PAs) urokinase-plasminogen activator (u-PA) and tissue-plasminogen activator (t-PA) are naturally found in human body. These PAs catalyze cleavage of Arg 561-Val 562 scissile peptide bond of PG and convert it to its active form, PN. PN thus generated, cleaves the fibrin network of the clot (Figure 1). A cardinal feature of physiological fibrinolysis is achieved by therapeutic administration of PAs and targeted generation of PN activity at the surface of clot (fibrin selectivity) (Marder and Sherry, 1988).

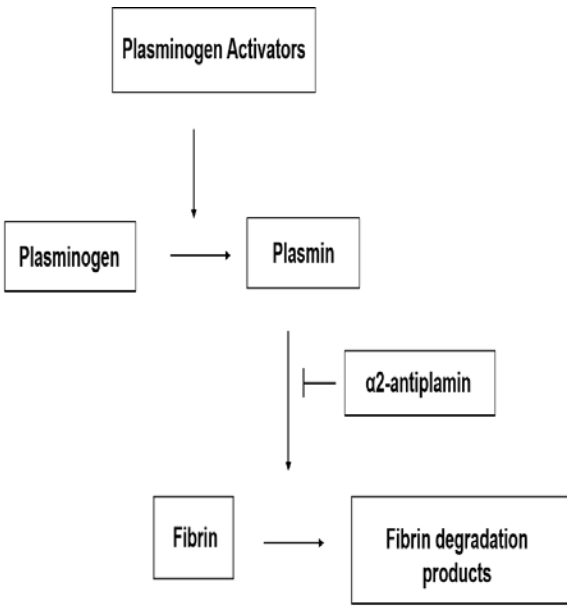

Figure 1: Schematic representation of fibrinolysis.

Upon injury, plasminogen activators (tissue plasminogen activator, urokinase, Streptokinase, Staphylokinase, etc.) catalyze cleavage of plasminogen into plasmin which acts on fibrin of clot to generate fibrin degradation products (FDPs). Fibrinolysis is regulated by α_2-antiplasmin, an inhibitor of plasmin.

PG consists of seven distinct domains *viz*. N-terminal pre-activation peptide followed by five structurally homologous kringle domains and a serine-protease like catalytic domain (Joshi *et al.*, 2012). These kringles have the affinity for lysine, and through these kringles, PN binds with fibrin present inside clot (Adivitiya and Khasa, 2017). The native form of PG is also known as Glu-PG as its N-terminal has glutamic acid (Wallén and Wiman, 1972) and exists in closed conformation, while its truncated form Lys78–PG, exists in an open conformation (Collen and De Maeyer, 1975). PG is reported to exist in two variants, which differ in their extent of glycosylation (Cole and Castellino, 1984). Type I of PG is glycosylated at Asn 289 and at Thr 346, while Type II form of PG has glycosylation at only one position, Thr 346 (Hayes and F. J. Castellino, 1979; Hayes and J. F. Castellino, 1979). Later on, a site for O-linked glycosylation was also discovered in variant II at Ser 248 (Pirie-Shepherd *et al.*, 1997). Variant I is more readily activated by the PAs compared to variant II. However, this difference is abrogated in the presence of fibrin. PG also gets phosphorylated at Ser 578 (Castellino and Ploplis, 2005).

PLASMIN

PN, the active form of the zymogen PG is a serine protease, having broad substrate specificity. However, it cannot directly activate PG via proteolytic cleavage of PG (Summaria *et al.*, 1967). Activation of single chain PG after cleavage at scissile peptide bond (Arg 561-Val 652) generates PN that is stabilized by two disulphide bonds. PN consists of a heavy chain (A-chain) of 58 kDa, linked to a short light chain (B-chain/ catalytic domain) of 26 kDa by two disulphide bonds (Robbins *et al.*, 1967). PN plays a crucial physiological function to dissolve fibrin blood clots. Apart from fibrinolysis, PN also degrades other coagulation factors including factor V, VIII, IX, XI, XII, insulin and growth hormones (Kunamneni *et al.*, 2007). Other functions of PN include activation of collagenases (Davis *et al.*, 2001), some mediators of the complement system and weakening the wall of the Graafian follicles thus helping in ovulation (Yoshimura *et al.*, 1992). Additionally, it cleaves fibrin, fibronectin, thrombospondin, laminin, and von Willebrand factor (Yoshimura *et al.*, 1992).

PG ACTIVATORS

The activation of PG by PAs is the central event in the fibrinolytic cascade. PAs can be broadly divided into two categories:

Indirect/ non-physiological PAs: These activators are of bacterial origin and do not possess any enzymatic activity of their own. They form complexes with PG or PN and these complexes then act as PAs. Indirect PG activators include Staphylokinase (SAK), *Streptococcus uberis* PG activator (SUPA) and Streptokinase (SK). Being bacterial in origin, the non-physiological PAs are immunogenic in nature.

Direct/ physiological PAs: These are "intrinsic" PAs and show high degree of substrate specificity. They activate PG by direct cleavage of the Arg 561- Val 562 scissile peptide bond. These activators include tPA and uPA and their mutated or protein engineered derivatives.

Indirect/ non-physiological PG activators:

Streptokinase: Streptokinase (SK) is a single chain extracellular protein produced by some species of hemolytic *Streptococci*. It has a molecular weight of ~47 kDa and is composed of 414 amino-acids. SK lacks carbohydrates and lipids (Castellino and Powell, 1981) and is also free from cystines, cysteines and phosphate (De Renzo *et al.*, 1967). It is a flexible multi-domain protein (Damaschun *et al.*, 1992) which is composed of three domains (α, β and γ) having independent stability (Dahiya *et al.*, 2005). These domains behave as single cooperative units. SK is classified as an α+β protein having 17% α-helix, 28% β-sheet, 21% β-turn and 34% random coil. It does not have any proteolytic or esterase activity of its own (Dahiya *et al.*, 2005).

The fibrinolytic activity of SK originates from its ability to activate plasma PG. SK is a fibrin-independent activator of PG/PN (*Reed et al., 1999*). It acts as a protein cofactor to PG or PN, with which it combines in equimolar ratio and modulates the wide-spectrum non-specificity of protease PN into that of a specific PG activator (Davidson *et al.*, 1990). This step can be generated by two pathways (Figure 2).

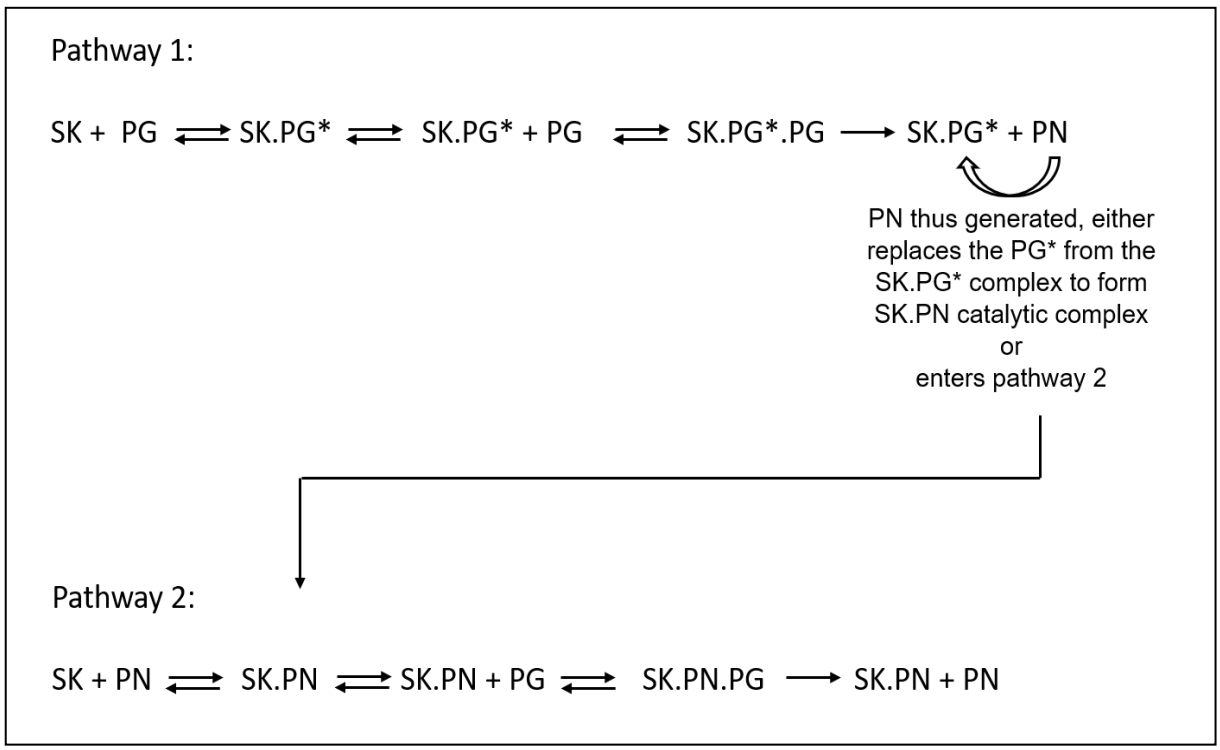

Figure 2: Schematic representation of mechanisms of plasminogen activation by Streptokinase. In pathway 1, SK forms a 1:1 molar complex with PG (SK.PG*) that binds free PG as a substrate, forming a ternary complex (SK.PG*.PG). PN is generated from the ternary complex due to intermolecular proteolytic cleavage of PG. PN thus generated, either binds free SK or replaces the PG* from the SK.PG* complex to form SK.PN catalytic complex. In pathway 2, SK forms an equimolar high affinity complex with PN (SK.PN) that binds free PG as a substrate to form SK.PN.PG, from which free PN is generated. [SK, Streptokinase; PG, Plasminogen; PN, Plasmin].

Pathway 1: In this pathway, SK first forms a 1:1 molar complex with PG (SK.PG), which then undergoes conformational transition without any proteolytic cleavage to form a transition complex, SK.PG* that possesses an active site in the zymogen (Summaria *et al.*, 1982). This SK.PG* binds free PG as a substrate, forming the ternary complex (SK.PG*.PG), from which PN is produced due to intermolecular proteolytic cleavage of PG. The PN generated by SK.PG* either binds free SK or replaces the PG* from the SK.PG* complex to form SK.PN catalytic complex. The exchange of product PN with PG* occurs due to ~11,000 fold higher affinity of PN for SK in comparison to PG (Covarsi *et al.*, 1978).

Pathway 2: SK first forms an equimolar high affinity complex with PN. The tightly bound SK.PN complex now initiates the direct proteolytic catalytic cycle, binding free PG in the substrate mode to form SK.PN.PG, from which free PN is generated (Boxrud and Bock, 2004).

The clot lysis capacity of SK is comparable to different forms of tPA (Cassels *et al.*, 1987). Furthermore, SK is cost effective when compared to tPA (Baker Jr., 2002). Hence, SK has been used in the clinical treatment of acute myocardial infarction following coronary thrombosis and has served as a thrombolytic agent for more than five decades. It indirectly causes the activation of PG to its active form PN (Murray *et al.*, 2010).

Staphylokinase: Staphylokinase (SAK), a single domain protein of ~15.5 kDa is produced by *Staphylococcus aureus*. It forms a 1:1 stoichiometric complex with PN and the complex then acts on human PG, thus converting it to human PN (Hui *et al.*, 2012). In circulating plasma, SAK does not induce systemic

PN generation as SAK-PN complex is rapidly neutralized by α_2-antiplasmin in absence of fibrin (Bokarewa *et al.*, 2006). However, fibrin bound PN complexed to SAK is relatively resistant to get inactivated by α_2-antiplasmin allowing preferential PG activation on fibrin surface (Bokarewa *et al.*, 2006). SAK has 160 fold higher affinity for PN as compared to PG (Sakharov *et al.*, 1996). Crystal structure of SAK in complex with catalytic domain of PN (Parry *et al.*, 1998) reveals that contacts of catalytic domain of PN with SAK are similar to those made by the α-domain of SK, thereby suggesting strong structural-functional homology of SAK with the isolated α-domain of SK (Parry *et al.*, 1998; Wang *et al.*, 1998).

***Streptococcus uberis* PA:** *Streptococcus uberis* PA (SUPA) was isolated from *Streptococcus uberis*, causative agent for bovine mastitis (Zhang *et al.*, 2012). SUPA has a two-domain structure (~29 kDa), an intermediate between the one-domain structure of SAK (~16 kDa) and the three-domain structure of SK (~47 kDa) (Zhang *et al.*, 2012). SUPA is capable of induction of virgin enzyme activity in bovine PG (even in the absence of a γ-equivalent domain), though, C-terminal β-domain of SUPA cannot activate human PG but forms an activator complex with human PN (Zhang *et al.*, 2012). Thus, SUPA shows activation kinetics similar to SK, but exhibits SAK-like susceptibility to α_2-antiplasmin (Johnsen *et al.*, 2000) and its mechanism of action is also intermediate between SK and SAK (Sazonova *et al.*, 2001).

BACTERIAL PATHOGENESIS AND THE FIBRINOLYTIC SYSTEM

Tissue damage by bacterial proteases initiates the bacterial invasion in host body. It includes degradation of host tissue barriers formed by extracellular matrices and basement membranes. Tissue degradation and penetration requires lysis of collagen fibrins, elastin, fibronectin, and proteoglycans through interaction with proteinase-dependent cascade systems. The fibrinolytic system offers a potential proteolytic system that is being exploited by pathogenic bacteria and involves PG activation to PN (Parry *et al.*, 2000). Being a non-specific protease, PN can degrade various extracellular matrices and membranes (Lahteenmaki *et al.*, 2001). This enhances bacterial invasiveness into secondary infection sites within the host body (Lahteenmaki *et al.*, 2001). Several pathogenic bacteria, such as *Streptococcus* and *Staphylococcus*, produce PAs that are either secreted or surface-bound proteins, which bind PN to their surface and it exploits the inactivation by α2-antiplasmin inhibitor (Lahteenmaki, Kuusela and Korhonen, 2001). The bound PN can activate metalloproteinases and collagenases, thereby aiding in migration through tissues and probably contribute to invasiveness of bacteria (Boyle and Lottenberg, 1997). This property has been exploited in clinical medicine where SK has been used as a thrombolytic drug (Banerjee *et al.*, 2004). SK and SAK are co-factors that form 1:1 complexes with PG and PN, leading to changes in conformation and specificity of PG. Their PG activation mechanisms are different. SK-PG complex is enzymatically active, whereas SAK-PG is inactive in nature and requires the conversion of PG to PN. Another important difference is that SAK primarily activates fibrin-bound PG (Parry *et al.*, 2000).

Direct/ physiological PAs

Urokinase PG activator: Urokinase PA (uPA) is a 54 kDa serine protease, synthesized by the kidneys. uPA is present in several other physiological locations, such as bloodstream and the extracellular matrix. It exists in two forms of molecular weight ~31 and 54 kDa, the smaller one being the proteolytic product of the larger form (Ellis *et al.*, 1987). The 54 kDa single-chain uPA contains 411 amino acids and has a four-domain structure including an epidermal growth factor domain, a kringle domain, a connecting peptide and the protease domain. The sessile peptide bond that converts inactive single chain uPA to the active two-chain form is situated between Lys 158 and Ile 159. The two chains thus generated are held together by a disulfide bond. The molecular mechanism of activation of HPG by uPA involves cleavage of the scissile peptide bond in PG (Arg 561-Val 562), forming PN, which then auto-catalytically cleaves the Lys 76-Lys 77 peptide bond in PN heavy chain, yielding Lys78 PN (Crippa, 2007).

Tissue-plasminogen activator: Tissue-plasminogen activator (tPA) is a chymotrypsin family serine protease central to fibrinolysis (Collen and Lijnen, 1995). *In vivo*, tPA activates PG in the presence of fibrin, as both tPA as well as substrate PG are adsorbed to fibrin surface sites, which leads to increased localized PN generation, while preventing systemic activation of PG (Collen and Lijnen, 1995). The mature tPA contains 527 amino acids and is organized by eight disulphide bonds into five distinct

structural domains: a finger domain (Ser 1-His 44), an epidermal growth factor-like domain (Ser 50-Asp 87), two kringle domains (Cys 92-Cys 173 and Cys 180-Cys 261) and the C-terminal catalytic domain (Ser 262-Pro 527) (Pennica *et al.*, 1983). tPA is secreted as a single chain protein. However, upon cleavage at the Arg275-Ile276 sessile peptide bond by plasmin, two-chain tPA is generated. Interestingly, single chain tPA is not a zymogen and in the presence of fibrin, it is almost as active as two chain tPA (Rijken, Hoylaerts and Collen, 1982). In the absence of fibrin, tPA is a very inefficient activator of PG. However, in the presence of fibrin; the activation of HPG by tPA is greatly (100-1000 fold) enhanced (Hoylaerts *et al.*, 1982). The binding of tPA to fibrin is mediated through lysine binding site present inside kringle 2 and finger domains of tPA (Gething *et al.*, 1988). In circulating blood α2-antiplasmin inactivates plasmin, but administered therapeutic doses of tPA (or any other PAs) by clinicians are sufficient for enough plasmin formation to surpass α2-antiplasmin mediated inhibition of plasmin.

SPECIES SPECIFICITY OF DIFFERENT PA$_S$

SK shows considerable species specificity for PG activation i.e. SK isolated from different species consistently showed the ability to activate PG from that species but not necessarily from other species (Parry et al., 2000). In contrast to therse bacterial PG activators, the animals PG activators viz uPA and tPA activate a broad spectrum of animal PGs, indicating that these protein-protein interactions between different animal PGs and animal Pas are conserved, which might be due to a process of mutual co-evolution of interaction partners (Sasajima et al., 2000; Giuliani and Tomasi, 2002).

RECOMBINANT AND MUTATED DERIVAT--IVES OF DIFFERENT PA$_S$

Anistreplase (Anisoylated PG SK activator complex): Anisoylated PG SK activator complex (APSAC) is an equimolar complex of bacterial SK and human lys-PG (131 kDa). Active site of Lys-PG is being acylated via using reversible acylating agent, which gets hydrolysed inside plasma (Munger and Forrence, 1990). Acylation imparts catalytic inactivation and protects the complex from plasmin inhibitors. Hence, it has a better half-life and improved specificity when compared with SK alone (Munger and Forrence, 1990).

Pro-urokinase (pro-uPA): Pro-uPA is unglycosylated form of recombinant pro-uPA (411 amino acids), expressed and isolated from *E. coli*. It was found to be safe and effective as tPA during acute myocardial infarction treatment (Bar *et al.*, 1997).

Reteplase: Reteplase is un-glycosylated, truncated derivative (del Val^4-Glu^{175}) of tPA, *i.e*. devoid of finger, epidermal growth factor and kringle 1 domains of tPA (Figure 3). It is cheaper to produce reteplase than full length tPA. Kringle 1 domain of tPA plays a role in its rapid clearance inside the liver, so reteplase has an increased half-life. However, the overall activity of this truncated derivative is 4 fold lower than tPA (Adivitiya and Khasa, 2017). Reteplase is clinically approved thrombolytic agent and is sold with brand name Retavase.

Tenecteplase: Tenecteplase (TNK-tPA) is another protein engineered form of tPA that was patented by Gennova Inc in 1997. It has three mutations: (i) replacement of glutamine at position 117 with asparagine that resulted in prolonged half-life through the removal of high mannose-type side chain, (ii) replacement of threonine 103 with asparagine resulting in generation of a new glycosylation site that further increased its half-life through enlargement of the molecule, and (iii) substitution of tetra-alanine at positions 296–299 (Figure 3) that enhanced fibrin specificity and also the resistance of tPA to PAI-1 (Ali *et al.*, 2014; Collen *et al*., 1994; Refino et al. 1993 and Smalling *et al*., 1996). Thus, tenecteplase has increased half-life and lesser systemic effects than alteplase (Smalling *et al*., 1996 and Keyt *et al.*, 1994). However, there is hardly any catalytic enhancement over tPA when clot lysis activity was compared (Keyt *et al.*, 1994).

Amediplase: Amediplase is a hybrid PA which comprises of kringle 2 domain of tPA and catalytic domain of uPA (Figure 3). It has a higher plasma half-life and less fibrin specificity. Notably, it has a better thrombolytic ability when compared to Tenecteplase and uPA (Rijken *et al.*, 2004; Guimarães *et al.*, 2006).

Desmoteplase: Desmoteplase was isolated from the saliva of the vampire bat *Desmodus rotundus*. It is composed of a finger domain, EGF domain and a kringle domain which is similar to kringle 1 of tPA (Figure 3). Its activity is highly fibrin dependent, i.e. in presence of fibrin its clot dissolving activity gets enhanced >10000 fold (Bringmann *et al.*, 1995). This molecule can be inhibited by lysine analogue tranexamic acid, which can be used to control bleeding complications upon administration (Niego *et al.*, 2008).

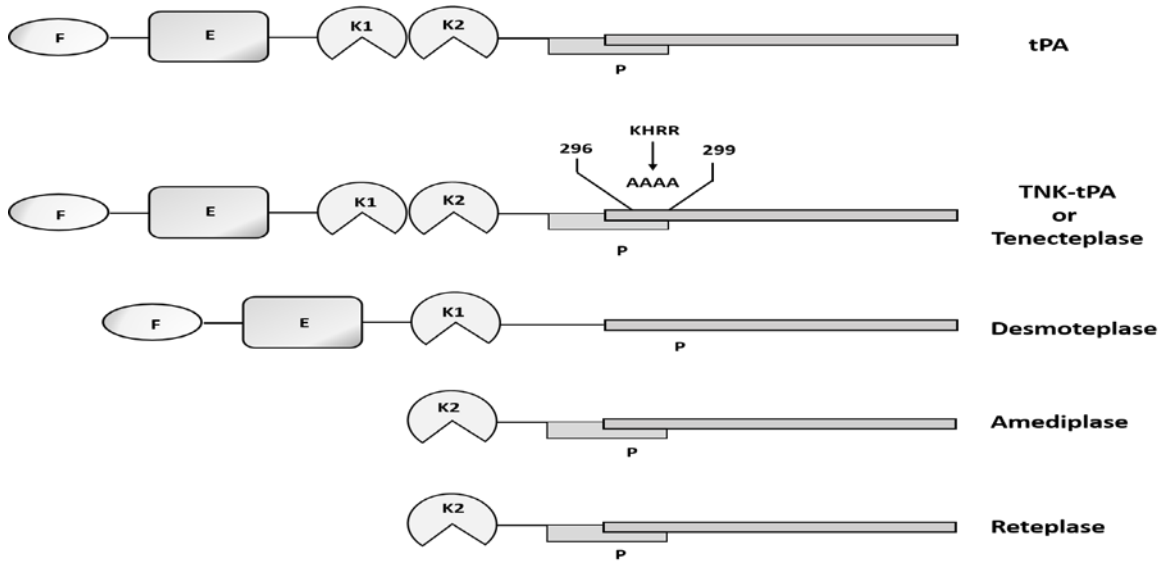

Figure 3: Recombinant and mutated derivatives of tPA (tissue plasminogen activator). Mature tPA is composed of 527 amino acids that are organized by eight disulphide bonds into five domains: a finger (F) domain (Ser 1-His 44), an epidermal growth factor-like E-domain (Ser 50-Asp 87), two kringle domains i.e. K1 and K2 (Cys 92-Cys 173 and Cys 180-Cys 261), and a C-terminal catalytic domain (Ser 262-Pro 527). Full length tPA is used as a thrombolytic agent with brand name Alteplase. Tenecteplase is another recombinant tPA with augmented half-life and fibrin specificity that are attained by tetra-alanine substitution at positions 296–299 by KHRR. Desmoteplase is similar to tPA but devoid of kringle 2 and plasmin-sensitive cleavage site. Amediplase has kringle 2 domain of tPA and catalytic domain of uPA. Reteplase is un-glycosylated, truncated derivative of tPA that is devoid of finger, epidermal growth factor and kringle 1 domains of tPA.

CONCLUSION

Thrombolytic enzymes are required to treat clinical manifestations that occur due to thrombosis in vasculature. These thrombolytic/ fibrinolytic enzymes are generally PAs. Among various thrombolytic agents, tPA and its derivatives are drugs of choice for the clinicians in developed nations but SK remains the choice of clot dissolving drugs in developing country due to its cost effectiveness. Before administration of thrombolytic drugs, focus is given to their efficacy, immunogenicity, half-life, plasma clearance and also to the cost of treatment. PAs from bacterial origin e.g. SK and SAK are immunogenic in nature. However, the cost of SK is much lesser than tPA. Furthermore, being unable to distinguish between plasminogen present in bloodstream and one bound to thrombi, many PAs can lead to systemic hemorrhage. Hence, there is a need of constant development like finding other source of PA and making fusion protein of PAs from different sources to increase their specificity and stability. Moreover, with the help of recombinant DNA technology and protein engineering, manufacturing cost of thrombolytic enzymes can further be decreased.

ACKNOWLEDGEMENTS

This work was supported by the Senior Research Associate fellowship awarded to Prakash Kumar Sinha by Council of Scientific and Industrial Research, India.

Conflict of Interest: The authors declare that they have no conflict of interest.

Declaration of Originality: This article has not been published elsewhere and it has not been simultaneously submitted for publication elsewhere.

REFERENCES:

Adivitiya and Y. P. Khasa. 2017. The evolution of recombinant thrombolytics: Current status and future directions. Bioengineered, 8: 331-358.

Ali, M. R., M. S. Hossain, M. A. Islam, M. S. Arman, G. S.. Raju, P. Dasgupta, and T. F. Noshin. 2014. Aspect of thrombolytic therapy: A review. Scientific World Journal, 2014: 586510-586517.

Bagot, C. N. and R. Arya. 2008. Virchow and his triad: A question of attribution. British Journal of Haematology, 143: 180-190.

Baker Jr., W. F. 2002. Thrombolytic therapy. Clin Appl Thromb Hemost, 8: 291-314.

Banerjee, A., Y. Chisti and U. C. Banerjee. 2004. Streptokinase: a clinically useful thrombolytic agent. Biotechnol Adv, 22: 287–307.

Bar, F. W., J. Meyer, F. Vermeer, R. Michels, B. Charbonnier, K. Haerten, M. Spiecker, C. Macaya, M. Hanssen, M. Heras, J. P. Boland, M. C. Morice, F. G. Dunn, R. Uebis, C. Hamm, O. Ayzenberg, G. Strupp, A. J. Withagen, W. Klein, J. Windeler, G. Hopkins, H. Barth, and M. J. von Fisenne. 1997. Comparison of saruplase and alteplase in acute myocardial infarction. SESAM Study Group. The Study in Europe with Saruplase and Alteplase in Myocardial Infarction. The American journal of cardiology, 79: 727-732.

Bokarewa, M. I., T. Jin, and A. Tarkowski. 2006. *Staphylococcus aureus*: Staphylokinase. Int J Biochem Cell Biol, 38: 504–509.

Boxrud, P. D. and P. E. Bock. 2004. Coupling of conformational and proteolytic activation in the kinetic mechanism of plasminogen activation by streptokinase. Journal of Biological Chemistry, 279: 36642–36649.

Boyle, M. D. and R. Lottenberg. 1997. Plasminogen activation by invasive human pathogens. Thromb Haemost, 77: 1–10.

Bringmann, P., D. Gruber, A. Liese, L. Toschi, J. Kratzschmar, W. D. Schleuning, and P. Donner. 1995. Structural features mediating fibrin selectivity of vampire bat plasminogen activators. Journal of Biological Chemistry, 270: 25596-25603.

Cassels, R., R. Fears and R. A. G. Smith. 1987. The interaction of streptokinase -plasminogen activator complex, tissue-type plasminogen activator, urokinase and their acylated derivatives with fibrin and cyanogen bromide digest of fibrinogen. Biochem. J., 247: 395-400.

Castellino, F. J. and V. A. Ploplis. 2005. Structure and function of the plasminogen/plasmin system. Thrombosis and Haemostasis, 93: 647-654.

Castellino, F. J. and J. R. Powell. 1981. Human plasminogen. Methods Enzymol., 80: 365–378.

Chapin, J. C. and K. A. Hajjar. 2015. Fibrinolysis and the control of blood coagulation. Blood Reviews, 29: 17-24.

Cole, K. R. and F. J. Castellino. 1984. The binding of antifibrinolytic amino acids to kringle-4-containing fragments of plasminogen. Archives of Biochemistry and Biophysics, 229: 568-575.

Collen, D. and H. R. Lijnen. 1995. Molecular basis of fibrinolysis, as relevant for thrombolytic therapy. Thromb Haemost,74: 167–171.

Collen, D. and L. D. Maeyer. 1975. Molecular biology of human plasminogen. I. Physicochemical properties and microheterogeneity. Thromb Diath Haemorrh, 34: 396-402.

Collen D, J. M. Stassen, T. Yasuda, C. Refino, N. Paoni, B. Keyt, T. Roskams, J. L. Guerrero, H. R. Lijnen and H. K. Gold. 1994. Comparative thrombolytic properties of tissue-type plasminogen activator and of a plasminogen activator inhibitor-1-resistant glycosylation variant, in a combined arterial and venous thrombosis model in the dog. Thromb Haemost, 72:98–104.

Covarsi, A., A. Gonzalo, J. Sarrias, and M. Carrera. 1978. Berger's disease: study of 12 cases. Rev Clin Esp, 148: 69-72.

Crippa, M. P. 2007. Urokinase-type plasminogen activator. International Journal of Biochemistry and Cell Biology, 39: 690-694.

Dahiya, M., G. Rajamohan, and K. L. Dikshit. 2005. Enhanced plasminogen activation by staphylokinase in the presence of streptokinase beta/betagamma domains: plasminogen kringles play a role. FEBS Letter, 579: 1565–1572.

Damaschun, G., H. Damaschun, K. Gast, D. Gerlach, R. Misselwitz, H. Welfle, and D. Zirwer. 1992. Streptokinase is a flexible multi-domain protein. Eur Biophys J, 20: 355–361.

Davidson, D. J., D. L. Higgins, and F. J. Castellino. 1990. Plasminogen activator activities of equimolar complexes of streptokinase with variant recombinant plasminogens. Biochemistry, 29: 3585-3590.

Davis, G. E., K. A. Pintar Allen, R. Salazar, and S. A. Maxwell. 2001. Matrix metalloproteinase-1 and -9 activation by plasmin regulates a novel endothelial cell-mediated mechanism of collagen gel contraction and capillary tube regression in three-dimensional collagen matrices. J Cell Sci, 114: 917-930.

Ellis, V., M. F. Scully, and V. V. Kakkar. 1987. Plasminogen activation by single-chain urokinase in functional isolation. Kinetic study. Journal of Biological Chemistry, 262: 14998-5003.

Gething, M. J., B. Adler, J. A. Boose, R. D. Gerard, E. L. Madison, D. McGookey, R. S. Meidell, L. M. Roman, and J. Sambrook. 1988. Variants of human tissue-type plasminogen activator that lack specific structural domains of the heavy chain. EMBO J, 7: 2731–2740.

Giuliani, A. and M. Tomasi. 2002. Recurrence quantification analysis reveals interaction partners in paramyxoviridae envelope glycoproteins. Proteins, 46: 171-176.

Guimarães, H. C. Ana, M. M. Barrett-Bergshoef, M. Criscuoli, S. Evangelista, and D. C. Rijken. 2006. Fibrinolytic efficacy of amediplase, tenecteplase and scu-PA in different external plasma clot lysis models. Thrombosis and Haemostasis, 96: 325-330.

Hayes, M. L. and F. J. Castellino. 1979. Carbohydrate of the human plasminogen variants. II. Structure of the asparagine-linked oligosaccharide unit. Journal of Biological Chemistry, 254: 8772–8776.

Hayes, M. L. and F. J. Castellino. 1979. Carbohydrate of the human plasminogen variants. I. Carbohydrate composition, glycopeptide isolation, and characterization. Journal of Biological Chemistry, 254: 8768–8771.

Hoylaerts, M., D. C. Rijken, H. R. Lijnen, and D. Collen. 1982. Kinetics of the activation of plasminogen by human tissue plasminogen activator. Role of fibrin. Journal of Biological Chemistry, 257: 2912–2919.

Hui, J., Y. Dai, Y. Bian, H. Li, X. Cui, X. Yu, S. You, and F. Hu. 2012. Construction of novel bifunctional chimeric proteins possessing antitumor and thrombolytic activities. J Microbiol Biotechnol, 22: 894–901.

Johnsen, L. B., L. K. Rasmussen, T. E. Petersen, M. Etzerodt, and S. N. Fedosov. 2000. Kinetic and structural characterization of a two-domain streptokinase: dissection of domain functionality. Biochemistry, 39: 6440–6448.

Joshi, K. K., J. S. Nanda, P. Kumar, and G. Sahni. 2012. Substrate kringle-mediated catalysis by the streptokinase-plasmin activator complex: critical contribution of kringle-4 revealed by the mutagenesis approaches. Biochim Biophys Acta, 1824: 326–333.

Keyt, B. A., N. F. Paoni, C. J. Refino, L. Berleau, H. Nguyen, A. Chow, J. Lai, L. Peña, C. Pater, J. Ogez, T. Etcheverry, D. Botstein, and W. F. Bennett. 1994. A faster-acting and more potent form of tissue plasminogen activator. Proceedings of the National Academy of Sciences of the United States of America, 91: 3670–3674.

Kotb, E. 2014. The biotechnological potential of fibrinolytic enzymes in the dissolution of endogenous blood thrombi. Biotechnology Progress, 30: 656-672.

Kunamneni, A., T. T. A. Abdelghani and P. Ellaiah 2007. Streptokinase-The drug of choice for thrombolytic therapy. Journal of Thrombosis and Thrombolysis, 23: 9-23.

Lahteenmaki, K., M. Kukkonen, and T. K. Korhonen. 2001. The Pla surface protease/adhesin of *Yersinia pestis* mediates bacterial invasion into human endothelial cells. FEBS Lett, 504: 69–72.

Lahteenmaki, K., P. Kuusela, and T. K. Korhonen. 2001. Bacterial plasminogen activators and receptors. FEMS Microbiol Rev, 25: 531–552.

Leipnitz, G., C. Miyashita, M. Heiden, G. V. Blohn, M. Köhler, and E. Wenzel. 1988. Reference values and variability of plasminogen in healthy blood donors and its relation to parameters of the fibrinolytic system. Pathophysiology of Haemostasis and Thrombosis, 18: 61-68.

Marder, V. J. and S. Sherry. 1988. Thrombolytic Therapy: Current Status. New England Journal of Medicine, 318: 1512-1520.

Munger, M. A. and E. A. Forrence. 1990. Anistreplase: A new thrombolytic for the treatment of acute myocardial infarction. Clinical Pharmacy, 9: 530-540.

Murray, V., B. Norrving, P. A. Sandercock, A. Terent, J. M. Wardlaw, and P. Wester. 2010. The molecular basis of thrombolysis and its clinical application in stroke. J Intern Med, 267: 191–208.

Niego, Be'eri, A. Horvath, P. B. Coughlin, M. K. Pugsley, and R. L. Medcalf. 2008. Desmoteplase-mediated plasminogen activation and clot lysis are inhibited by the lysine analogue tranexamic acid. Blood Coagulation and Fibrinolysis, 19: 322-324.

Parry, M. A., C. Fernandez-Catalan, A. Bergner, R. Huber, K. P. Hopfner, B. Schlott, K. H. Guhrs, and W. Bode. 1998. The ternary microplasmin-staphylokinase-microplasmin complex is a proteinase-cofactor-substrate complex in action. Nat Struct Biol, 5: 917-923.

Parry, M. A., X. C. Zhang, and I. Bode. 2000. Molecular mechanisms of plasminogen activation: bacterial cofactors provide clues. Trends Biochem Sci, 25: 53-59.

Pennica, D., W. E. Holmes, W. J. Kohr, R. N. Harkins, G. A. Vehar, C. A. Ward, W. F. Bennett, E. Yelverton, P. H. Seeburg, H. L. Heyneker, D. V Goeddel, and D. Collen. 1983. Cloning and expression of human tissue-type plasminogen activator cDNA in E. coli. Nature, 301: 214-221.

Pirie-Shepherd, S. R., R. D. Stevens, N. L. Andon, J. J. Enghild, and S. V. Pizzo. 1997. Evidence for a novel O-linked sialylated trisaccharide on Ser-248 of human plasminogen 2. Journal of Biological Chemistry, 272: 7408–7411.

Reed, G. L., A. K. Houng, L. Liu, B. Parhami-Seren, L. H. Matsueda, S. Wang, and L. Hedstrom. 1999. A catalytic switch and the conversion of streptokinase to a fibrin-targeted plasminogen activator. Proc Natl Acad Sci U S A, 96: 8879–8883.

Refino, C. J., N. F. Paoni, B. A. Keyt, C. S. Pater, J. M. Badillo, F. M. Wurm, J. Ogez and W. F. Bennett. 1993. A variant of t-PA (T103N, KHRR 296–299 AAAA) that, by bolus, has increased potency and decreased systemic activation of plasminogen. Thromb Haemost, 70:313–319.

Renzo, E. C. De., P. K. Siiteri, B. L. Hutchings, and P. H. Bell. 1967. Preparation and certain properties of highly purified streptokinase. Journal of Biological Chemistry, 242: 533–542.

Riddel Jr., J. P., B. E. Aouizerat, C. Miaskowski, and D. P. Lillicrap. 2007. Theories of blood coagulation. J Pediatr Oncol Nurs, 24: 123–131.

Rijken, D. C., M. M. Barrett-Bergshoeff, A. F. H. Jie, M. Criscuoli, and D. V. Sakharov. 2004. Clot penetration and fibrin binding of amediplase, a chimeric plasminogen activator (K2tu-PA). Thrombosis and Haemostasis, 91: 52-60.

Rijken, D. C., M. Hoylaerts, and D. Collen. 1982. Fibrinolytic properties of one-chain and two-chain human extrinsic (tissue-type) plasminogen activator. Journal of Biological Chemistry, 257: 2920-2925.

Robbins, K. C., L. Summaria, B. Hsieh, and R. J. Shah. 1967. The peptide chains of human plasmin. Mechanism of activation of human plasminogen to plasmin. Journal of Biological Chemistry, 242: 2333–2342.

Sakharov, D. V, H. R. Lijnen, and D.C. Rijken. 1996. Interactions between staphylokinase, plasmin(ogen), and fibrin. Staphylokinase discriminates between free plasminogen and plasminogen bound to partially degraded fibrin. Journal of Biological Chemistry, 271: 27912–27918.

Sasajima, T., Y. Takano, Y. Hiraishi, K. Goh, M. Inaba, N. Azuma, Y. Sasajima, K. Yamazaki, and H. Yamamoto. 2000. High accumulation of plasminogen and tissue plasminogen activator at the flow surface of mural fibrin in the human arterial system. J Vasc Surg, 32: 374–382.

Sazonova, I. Y., A. K. Houng, S. A. Chowdhry, B. R. Robinson, L. Hedstrom, and G. L. Reed. 2001. The mechanism of a bacterial plasminogen activator intermediate between streptokinase and staphylokinase. Journal of Biological Chemistry, 276: 12609-12613.

Smalling, R. W. 1996. Molecular biology of plasminogen activators: what are the clinical implications of drug design? Am J Cardiol, 78:2–7.

Summaria, L., R. C. Wohl, I. G. Boreisha, and K. C. Robbins. 1982. A virgin enzyme derived from human plasminogen. Specific cleavage of the arginyl-560-valyl peptide bond in the diisopropoxyphosphinyl virgin enzyme by plasminogen activators. Biochemistry, 21: 2056-2059.

Summaria, L., B. Hsieh, and K. C. Robbins. 1967. The specific mechanism of activation of human plasminogen to plasmin. Journal of Biological Chemistry, 242: 4279-4283.

Wallén, P., and B. Wiman. 1972. Characterization of human plasminogen II. Separation and partial characterization of different molecular forms of human plasminogen. BBA - Protein Structure, 257: 122-134.

Wang, X., X. Lin, J. A. Loy, J. Tang, and X. C. Zhang. 1998. Crystal structure of the catalytic domain of human plasmin complexed with streptokinase. Science, 281: 1662–1665.

Weisel, J. W. and R. I. Litvinov. 2017. Fibrin formation, structure and properties. Sub-Cellular Biochemistry, 82: 405-456.

Wilson, S. M., H. S. Mason, L. C. Ng, S. Montague, L. Johnston, N. Nicholson, S. Mansfield, and J. R. Hume. 2005. Role of basal extracellular Ca2+ entry during 5-HT-induced vasoconstriction of canine pulmonary arteries. British journal of pharmacology, 144: 252–264.

World Health Organization. 2011. Global atlas on cardiovascular disease prevention and control. https://apps.who.int/iris/handle/10665/44701.

Yoshimura, Y., Y. Nakamura, T. Oda, M. Ando, Y. Ubukata, N. Koyama, M. Karube, and H. Yamada. 1992. Effects of prolactin on ovarian plasmin generation in the process of ovulation. Biol Reprod, 46: 322–327.

Zhang, Y., I. P. Gladysheva, A. K. Houng, and G. L. Reed. 2012. *Streptococcus uberis* Plasminogen Activator (SUPA) Activates Human Plasminogen through Novel Species-specific and Fibrin-targeted Mechanisms. Journal of Biological Chemistry, 287: 19171-19176.

Pb. Univ. Res. J (Sci.) Vol. 69, 2019, pp 23-34

REMOVAL OF CHROMIUM FROM AQUEOUS SOLUTIONS USING MODIFIED WATER HYACINTH IN A FIXED BED COLUMN

BALJINDER SINGH

Department of Biotechnology, Panjab University, Chandigarh, 160014, India

Abstract

This paper investigates the removal of Cr (VI) on water hyacinth via column studies. The performance of the study is described through the breakthrough curves concept under relevant operating conditions such as column bed depths (1.5 and 2 cm) and influent metal concentrations (50, 75, and 100 ppm) at constant flow rate (0.5ml/min). The Cr (VI) uptake mechanism is particularly bed depth and concentration-dependant, favoring higher bed depth and lower influent metal concentration. The surface chemical functional groups of biomass identified by FTIR were amino, carboxyl, hydroxyl, and carbonyl groups, which may be involved in the biosorption of heavy metals. Adams–Bohart model and Thomas model kinetic models were applied to study the column performance. The adsorption data fitted in Langmuir and Freundlich isotherm models. The results illustrate that water hyacinth could be utilized effectively for the removal of Cr (VI) ions from aqueous solution as a low cost adsorbent.

Keywords: Modified water hyacinth powder, fixed bed column, Cr (VI) removal.

INTRODUCTION

Pollution by heavy metals, due to their toxic nature and other adverse effects is a major issue in environmental science. This is due to anthropogenic activities and fast industrialization, which has lead to major environmental concern (Singh et al., 2016). The elimination of toxic heavy metal ions from wastewater has been commonly studied in recent years, because they may be toxic to organisms including humans (Sekhon and Singh, 2013). Cr (VI) occurs in nature mainly in three oxidation states as Cr(II), Cr(III) and Cr(VI), of which only the latter two of which are stable (Garcia-Reyes and Rangel-Mendez, 2010). Cr (VI) occurs mainly in the form of chromate $CrO4^{-2}$ and dichromate $CrO7^{-2}$ ions and is known to be highly mobile, and highly toxic and hazardous with as compared to Cr (III). Cr (VI) is toxic to most of the organisms at concentrations higher than 0.02 ppm (Garcia-Reyes and Rangel-Mendez 2010). It is highly carcinogenic to animals and is most frequently encountered in raw wastewater discharged from industries, such as electroplating, leather tanning, steel fabrication, wood preservations, textile metaling, paint, and pigments, and petroleum refining processes (Gupta and Babu, 2009). The permissible levels of Cr (VI) in drinking water, industrial wastewater and inland surface water according to WHO (world health organization) are 0.05, 0.25 and 0.1 mg/L, respectively. Increase in concentration of Cr (VI) may cause cancer of lungs and nasal sinuses. Acute poisoning of Cr (VI) causes headache, sickness and vomiting, dizziness, chest pain, tightness of the chest, dry cough and shortness of breath, rapid respiration, cyanosis and extreme weakness. Increase in toxicity of heavy metals has led to an increase in research activities on various strategies that can be used to clean up the environment (Sharma and Singh, 2013). Rapidly used methods for removal of heavy metals from industrial effluents includes solvent extraction, ion-exchange, membrane separation, and reverse osmosis. Pakade et al. (2019) recently reviewed some of the major adsorbents used for Cr(VI) elimination from aqueous solution. Several research studies have demonstrated adsorption of Cr (VI) on agro-waste materials (Cherdchoo et al., 2019; Khan et al., 2016; Mohan et al., 2019; Mitra and Das, 2019; Nasseh et al., 2017; Rane et al., 2019; Singh et al., 2009; Venugopal and Mohanty, 2011; Ullah et al., 2013). Several studies have proven that live water hyacinth can be used for phytoremediation and recovery of heavy metals (Rezania et al. 2015; Saha et al. 2017). But only few studies related to ability of dried water hyacinth biomass to adsorb heavy metals from aqueous effluents has been reported in literature.

The water hyacinth plant is rapidly infesting various aquatic ecosystems in many countries. It clogs waterways thereby limiting boating, fishing and almost all other water activities impossible moreover it degrades water quality by blocking photosynthesis, which diminishes oxygen levels in the water.

The objective of this study is to assess the performance and breakthrough curve characteristics of the water hyacinth for the removal of Cr (VI) from aqueous solution via fixed-bed system. The various parameters such as influent metal concentration and column bed depth were examined using a laboratory scale fixed-bed column. The adsorption mechanism of Cr (VI) onto the water hyacinth was analyzed using Adams–Bohart

*Corresponding Author: sbaljinder@pu.ac.in

MS Received: November 19, 2019, Accepted: December 24, 2019

model and Thomas model kinetic models for the purpose of describing the column's dynamic behaviour.

MATERIAL AND METHODS

Preparation of water hyacinth powder (WHP) and Cr (VI) stock solution

The water hyacinth was collected from a local pond situated near Chandigarh, India. It was washed with deionized water and chopped into small pieces. Pieces were sun dried for 2 days, and crushed, then sieved to desired mesh size of 2.5mm. This powder was stored in glass bottle at room temperature. Prior to use water hyacinth powder was modified by treating with sulphuric acid (0.007 M) solution for 6 hrs to enhance the adsorption property of adsorbent. The resulting mixture of water hyacinth powder and sulphuric acid was stirred well for 1 h. The resulting mixture was washed with distilled water until pH 7 was attained. It was filtered and oven dried at 65˚C for 24 h to remove the moisture. The final treated adsorbent was stored at room temperature.

The stock solution of 500 mg/L of Cr (VI) was prepared by dissolving an required weight of pure potassium dichromate salt in the desired volume of de-ionized water.

Fixed-bed column adsorption and desorption studies

A laboratory-scale glass column (a length of 30 cm and internal diameter of 2.0 cm) were used for fixed bed column studies. The column was supported and plugged with glass wool to ensure uniform liquid distribution as support at the bottom of column to avoid WHP being washed away. Column was packed with 2.0 and 2.2 g of WHP to obtain a bed depth of 1.5 and 2.0 cm, keeping flow rate and influent Cr (VI) concentration constant. Cr (VI) solution of known concentrations (50,75 and 100 mg/L) at natural pH (6.7) was flowed through the column at a desired flow rate of 500µl/min. Effluent samples were collected at regular time intervals to determine the metal ion concentration in the effluent solutions. Metal concentration in effluent was determined by AAS (flame–atomic adsorption spectrophotometer) GBC AVANTA GF 5000 Model, to find out adsorption capacity of water hyacinth. The flow to the column was continued until there was no further adsorption.

Fourier transform infrared analysis

FTIR spectroscopy was used to identify the chemical groups present in water hyacinth powder. Two mg of given water hyacinth powder were mixed with 98 mg of dry powdered potassium bromide **(**KBr) and finely grounded. The material was used for preparing pellets by applying pressure of 10,000-15,000 psi. The samples were examined using IR- Affinity-1, Shimadzu spectrophotometer high resolution (≤ 0.001 cm^{-1}). FTIR spectra of water hyacinth indicated the presence of hydroxyl, carboxyl, carbonyl, amino and nitro groups which are important sorption sites for chromium.

Column data analysis

To determine the response of sorption column, time for breakthrough appearance and the shape of the breakthrough curve were important factors (Sharma and Singh 2013). The column was analyzed for the adsorption of Cr (VI) at various concentrations i.e 50 mg/L, 75 mg/L, and 100 mg/L. Bed depth was kept 1.5 and 2 cm for each concentration. Various calculations related to column data was done as described by Sharma and Singh (2013).

Adsorption isotherm

The metal uptake by the biosorbent was calculated using the formula-

$$Q = V(C_i - C_f)/m \quad (1)$$

where; Q = Metal uptake (ml of metal/g biosorbent);

V = the liquid sample volume (ml);

C_i = the initial concentration of the metal in the solution (mg/l);

C_f = the final concentration of the metal in the solution (mg/l);

m = the amount of the added biosorbent on the dry basis (mg).

The empirical models *viz.,* Freundlich (1906) and Langmuir (1916) for single solute system and modified Langmuir for multiple situations were employed to describe the biosorption equilibria of the test plant.

Freundlich equation: $q_e = K_F C_e^{1/n}$ (2)

Langmuir equation: $\frac{q_{max} K_L C_e}{1+K_L C_e}$ (3)

where; q_e = metal ions adsorbed per unit weight of adsorbent at equilibrium (mg/g);

q_{max} = maximum possible amount of metal ions adsorbed per unit of weight of adsorbents (mg/g);

K_L = constant related to the affinity of binding sites for metal ions (L/mg);

C_e = equilibrium (residual) concentration (mg/L);

K_F = Freundlich characteristic constant of the system, incorporating parameters affecting the adsorption process, such as adsorption capacity;

n = Freundlich characteristic constant of the system, incorporating parameters such as effect of concentration on the adsorption capacity and represents the adsorption intensity (dimensionless).

RESULTS AND DISCUSSION

Effect of influent concentration on removal efficiency

The adsorption efficiency of column were evaluated and presented in Tables 1 and 2 for various parameters at bed depth of 2.0 cm and 1.5 cm, respectively. Analysis from Figure 1a and 1b showed that the increase in initial concentration of Cr (VI) ions results in decrease in % adsorption of the metal ions. However, uptake capacity of metal ions increased with increase in initial concentration Cr (VI) ions. This is due to more availability of Cr (VI) ions in solution. Also higher initial metal ion concentration offers higher energy to overcome all mass transfer resistances and results in increased probability of the metal ions towards active sites of the WHP column. The maximum adsorption of Cr (VI) ions was 68.5mg/L at 75 mg/L influent concentration of Cr (VI) ions with 2 cm bed depth of WHP column.

Parameters in fixed-bed column for Nickel adsorption by WHP:

Table 1: Calculations of various parameters using bed depth of 2 cm.

C_o mgL^{-1}	C_{eff} mgL^{-1}	V_{eff} (ml)	Q (mL min^{-1})	t_{total} (min)	Z (cm)	Time (C_{ad} max) (min)	(C_{ad} max) mgL^{-1}	m_{total} (mg)	q_{total} (mg)	q_{eq} (mg g^{-1})	Y (%)
50	26	35	0.777	45	2.0	33.6	34	1.74	0.887	0.443	48
75	46	33	0.731	42	2.0	25.2	52	2.27	1.170	0.585	52
100	50	30	0.697	43	2.0	30.8	55	2.99	1.180	0.590	49

Table 2: Calculations of various parameters using a bed depth of 1.5 cm.

C_o mgL^{-1}	C_{eff} mgL^{-1}	V_{eff} (ml)	Q (mL min^{-1})	t_{total} (min)	Z (cm)	Time (C_{ad} max) (min)	(C_{ad} max) mgL^{-1}	m_{total} (mg)	q_{total} (mg)	q_{eq} (mg g^{-1})	Y (%)
50	41	42	0.686	61	1.5	52	17	2.098	0.250	0.125	11.9
75	55	39	0.619	63	1.5	52	32	2.971	1.030	0.515	35.3
100	82	26.3	0.567	64	1.5	40	33	3.628	0.748	0.374	20.6

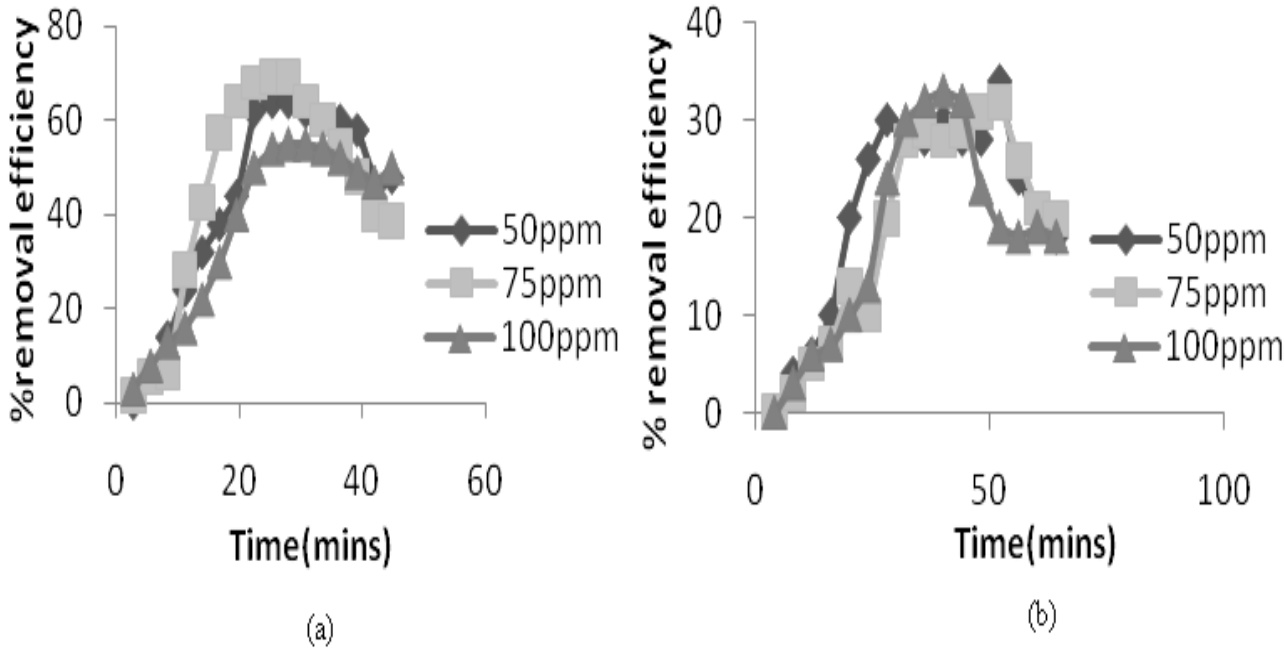

Figure 1: Effect of contact time on total Cr removal (a) by RSP (Bed depth 2 cm) (b) by RSP (Bed depth 1.5 cm).

Effect of contact time and bed depth on removal efficiency

Figure 1a and 1b showed removal efficiency of Cr (VI) ions at a constant bed depth of 2.0 cm and 1.5 cm respectively. It was found that as time increases, removal efficiency of column increases (Chen et al., 2012). This is due to availability of more binding sites for adsorption of metal ions (Gupta and Babu, 2009). The sorption column data were evaluated and presented in Table 3 and 4. The increase in Cr (VI) uptake capacity of WHP was observed as the bed depth increased with the highest bed capacity. It could be because of more contact time than surface area. Moreover, WHP mass at higher bed depth would provide a larger surface area and more cations fixations towards the active binding site for the occurrence of the adsorption process leading to an increase in the volume of treated effluent. These results revealed that the bed depth of 2 cm provided optimum % removal efficiency.

FT-IR analysis

FT-IR analysis of the biomass was carried out. The FTIR spectra of unloaded and metal loaded water hyacinth biomass were shown in supplementary figures. The absorption band characterisation including alkyl and CHO group peaks were assigned ranging between 2921 and 2851 cm^{-1}, COO^- of the carboxylate groups appeared at 1544 cm^{-1}, the band located at 1233, 1383 cm^{-1} represented COO^- anions whereas those located at 738 cm^{-1} was assigned SO_3^- groups.

Furthermore, the peaks located at 1039 and 1056 cm^{-1} were indicative of organic phosphate groups and P–O of the ($C–PO_2^{-3}$) moiety, respectively. The IR spectra of the loaded biomass varied with the metal ion. The IR spectra revealed a stretching of band appearing at 1035, 1060, and 1105 cm^{-1} which was attributed to the interaction of sorbed metal ion with phosphate groups. Additionally, shifting of bands observed at 3031 and 3173 cm^{-1} to after biosorption could be due to the involvement of alkyl and CHO group.

Table 3: Calculation of percentage (%) removal efficiency $[= (C_0 - C_t)/C_0] \times 100$ using bed depth of 2.0 cm.

	C_0=50 mgL^{-1}		C_0=75 mgL^{-1}		C_0=100 mgL^{-1}	
Time (min)	C_t (mgL^{-1})	Removal efficiency (%)	C_t (mgL^{-1})	Removal efficiency (%)	C_t (mgL^{-1})	Removal efficiency (%)
2.8	50	0	74	1.3	97	3
5.6	47	6	71	5.3	92	8
8.4	43	14	63	6	87	13
11.2	38	24	54	28	84	16
14.0	34	32	43	42.6	78	22
16.8	31	38	32	57.3	70	30
19.6	28	44	27	64	60	40
22.4	19	62	24	68	50	50
25.4	18	64	23	69.3	46	54
28.0	18	64	23	69.3	45	55
30.8	17	62	27	64	45	55
33.6	16	60	30	60	46	54
36.4	20	60	34	54.6	48	52
39.2	21	58	39	48	51	49
42.0	27	46	45	40	53	47
44.8	26	48	46	38.6	50	50

Table 3: Calculation of percentage (%) removal efficiency $[= (C_0 - C_t)/C_0] \times 100$ using bed depth of 1.5 cm.

Time (min)	C_0=50 mgL^{-1}		C_0=75 mgL^{-1}		C_0=100 mgL^{-1}	
	C_t (mgL^{-1})	Removal efficiency (%)	C_t (mgL^{-1})	Removal efficiency (%)	C_t (mgL^{-1})	Removal efficiency (%)
4	50	0	75	0	100	0
8	48	4	73	2	97	3
12	47	6	70	5	94	6
16	45	10	68	7	93	7
20	40	20	62	13	90	10
24	37	26	65	10	87	13
28	35	30	55	20	76	24
32	34	28	47	28	70	30
36	34	28	46	29	68	32
40	35	30	47	28	67	33
44	34	28	46	29	68	32
48	34	28	44	31	77	23
52	33	34	43	32	81	19
56	38	24	49	26	82	18
60	40	20	54	21	81	19
64	41	18	55	20	82	18

Breakthrough curve modeling

To predict breakthrough curve for the effluent, a successful design of column adsorption process is required (Oguz and Ersoy 2010). Several simple mathematical models are studied at laboratory scale to analyse the dyanamic behavior of the column for industrial scale. Adams–Bohart, and Thomas were used to predict the dynamic behavior of the column.

Adams–Bohart model

Bohart and Adams (1920) recognized a basic equation, which describes the relationship between C_t/C_0 and t in a continuous system. This model imagines that equilibrium is not immediate. It is used for relating the initial part of the breakthrough curve.

This is expressed as

$$Ln(C_t/C_0) = k_{AB}C_0t - k_{AB}N_0(Z/U_0) \quad (4)$$

where C_0 and C_t are the influent and effluent concentration (mg/L),k_{AB} is the kinetic constant (L/mg/min), N_0 is the saturation concentration (mg/L), Z is the bed depth of the fix-bed column(cm) and U_0 is the superficial velocity (cm/min) defined as the ratio of the volumetric flow rate Q (cm^3/min) to the cross-sectional area of the bed A (cm^2), k_{AB} and N_0 can be calculated from the linear plot of $\ln(C_t/C_0)$ against time (Figure 2a and 2b). As shown in Table 1a and b, values of k_{AB} decreased with increase of influent Ni (II) ions concentration from 50 to 100 mg/L, but increased with increasing bed depth from 1.5 to 2.0 cm. N_0 (saturation concentration) also increases with increase in bed depth but decreases with increase in influent concentration of metal ions. It was analyzed that the overall system kinetics was dominated by external mass transfer in initial part of adsorption in the column.

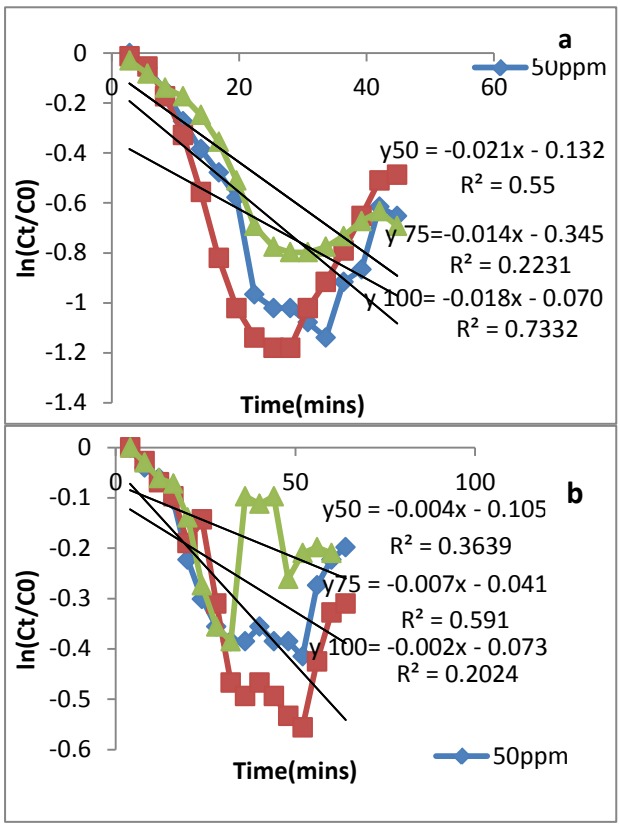

Figure 2: Adam-bohart model curve for (a) bed depth 2.0 cm (b) bed depth 1.5 cm.

Thomas model

Thomas model (Thomas 1944) studied plug flow behavior of column. This is mainly used to explain the performance theory of the adsorption process in fixed-bed column. The linearized form of this model can be described as:

$$Ln[(C_0/C_t) - 1] = k_{Th}m - k_{th}C_0t \quad (5)$$

where k_{Th} is the Thomas model constant (mL/min/mg), q_0 is the adsorption capacity (mg/g), and t stands for total flow time (min). The values of k_{Th} and q_0 can be determined from the linear plot of $Ln[(C_o/C_t)-1]$ against t (Figures 3a and 3b).

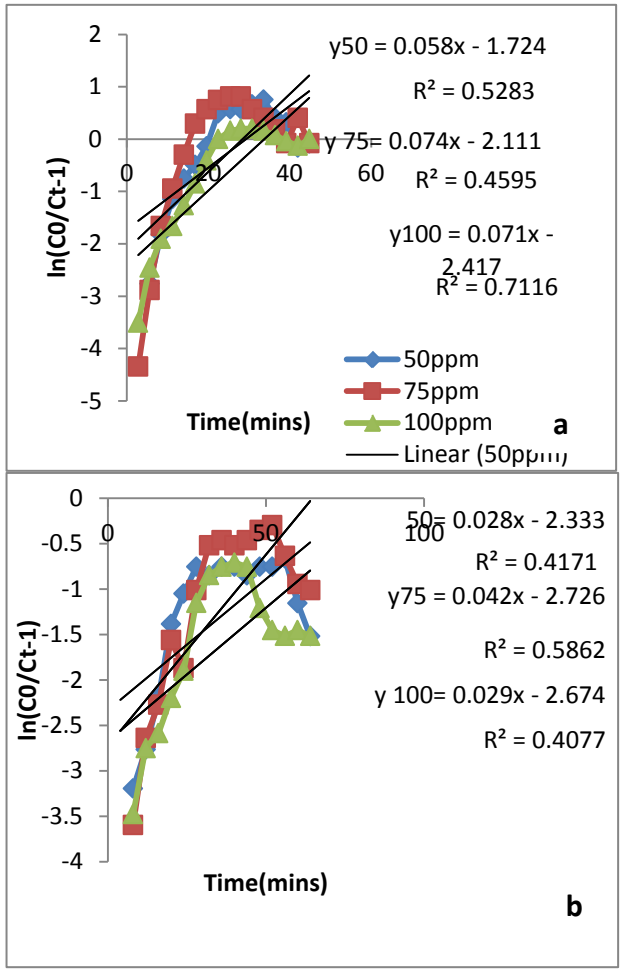

Figure 3: Thomas model curve for (a) bed depth 2.0 cm (b) bed depth 1.5 cm.

The relative constants and coefficients were obtained using linear regression analysis according to Eq. (5) and the results were presented in Table 5a and b. Thomas model was suitable for adsorption process, which indicated that the external and internal diffusions were not the limiting step (Sharma and Singh, 2013; Chen et al., 2012). Value of k_{Th} decreases with increase in influent concentration and bed depth. It was recognized to the driving force for adsorption in the concentration difference. Therefore it was found that adsorption capacity of metal ions on WHP column increased with lower the flow rate, influent concentration and bed depth.

Adsorption isotherm

The results obtained for determining the applicability of Langmuir model and Fruendlich's model to the observations recorded in the present study are presented in Figure 4a to 4c. A perusal of these figures reveals that Freundlich model is more suitable for describing the biosorption of metal ions by water hyacinth biomass in the studies concern ranges. Much better correlation coefficients 0.995 and were obtained using Freundlich isotherm model as compare to 0.982 using Langmuir isotherm model. The Langmuir isotherm model (Langmuir, 1916) predicts the formation of adsorbed solute monolayer with no side interactions between the adsorbed ions. It also assumes that the interactions taken place by absorption of one ion per binding site and also that the sorbent surface is homogenous containing only one type of binding site. On the other hand, the Fruendlich's model (Fruendlich, 1906) assumes the existence of multilayered structure and heterogenity of the adsorption sites on biomass.

Table 5: Parameters of Adam-Bohart and Thomas model under different conditions using (a) Fig. 1a (bed depth is 2 cm) (b) Fig. 1b (bed depth is 1.5 cm), respectively.

A. Adam-Bohart model

C_o(mg/L)	Q(ml/min)	Z(cm)	K_{AB} (L/mg/min)	N_o (mg/L)
(i)				
50 mgL^{-1}	0.777	2	4.2×10^{-4}	0.151×10^{3}
75 mgL^{-1}	0.731	2	1.8×10^{-4}	0.350×10^{3}
100 mgL^{-1}	0.697	2	1.8×10^{-4}	0.067×10^{3}
(ii)				
50 mgL^{-1}	0.686	1.5	8×10^{-5}	3.11×10^{2}
75 mgL^{-1}	0.619	1.5	9.3×10^{-5}	0.9×10^{2}
100 mgL^{-1}	0.567	1.5	2×10^{-5}	6.5×10^{2}

B. Thomas model

C_o(mg/L)	Q(mL/min)	Z(cm)	k_{Th}(mL/min mg^{-1})	q_o(mg/g)
(i)				
50 mgL^{-1}	0.777	2	3.4×10^{-2}	2.650
75 mgL^{-1}	0.731	2	2.8×10^{-2}	0.965
100 mgL^{-1}	0.697	2	2.4×10^{-2}	1.000
(ii)				
50 mgL^{-1}	0.686	1.5	4.6×10^{-2}	0.206
75 mgL^{-1}	0.619	1.5	3.6×10^{-2}	0.358
100 mgL^{-1}	0.567	1.5	2.6×10^{-2}	0.316

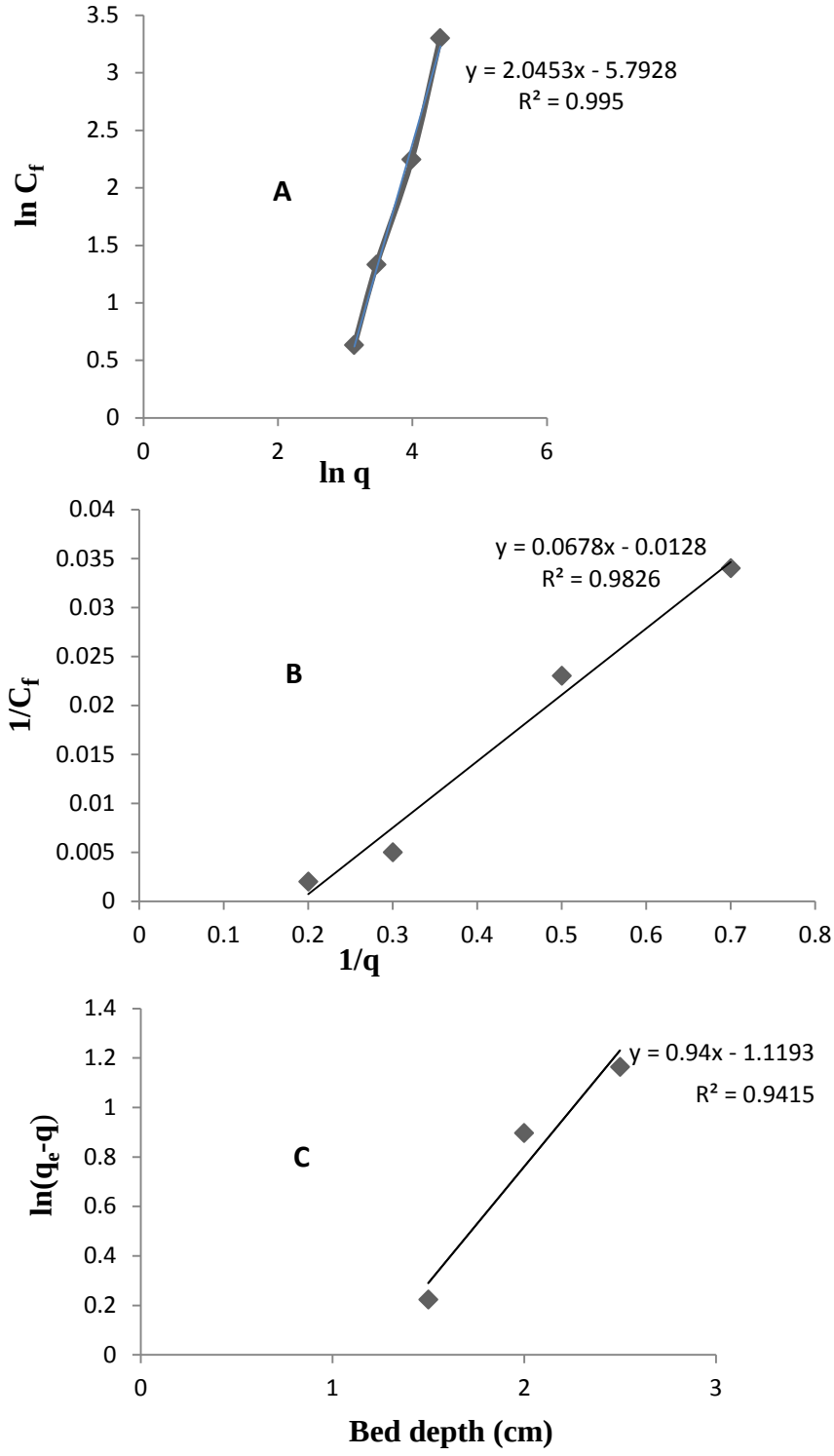

Figure 4: Adsorption isotherm for 2.0 cm bed depth with 75 ppm Cr concentration (A) Freundlich Isotherm, (B) Langmuir's isotherm, (C) Pseudo first order kinetics for 1.5, 2.0 and 2.5 cm bed depth.

CONCLUSION

This study identified modified water hyacinth as an effective and promising adsorbent to be applied for the elimination of Cr (VI) ions from aqueous solution. Uptake of Cr (VI) through a fixed-bed column was dependent on the bed depth, influent Cr (VI) concentration and contact time. Adsorption capacity was decreased with increasing the influent Concentration but increased with increasing bed depth and contact time. Column sorption process was found to perform better at lower influent Cr (VI) concentration, and higher bed depth. The adsorption capacity of hexavalent Cr (VI) onto WHP was strongly dependent on the initial metal concentration.

ACKNOWLEDGEMENTS

The authors thank the Chairperson, Department of Biotechnology, Panjab University, for providing necessary facilities.

SUPPLEMENTARY FIGURES

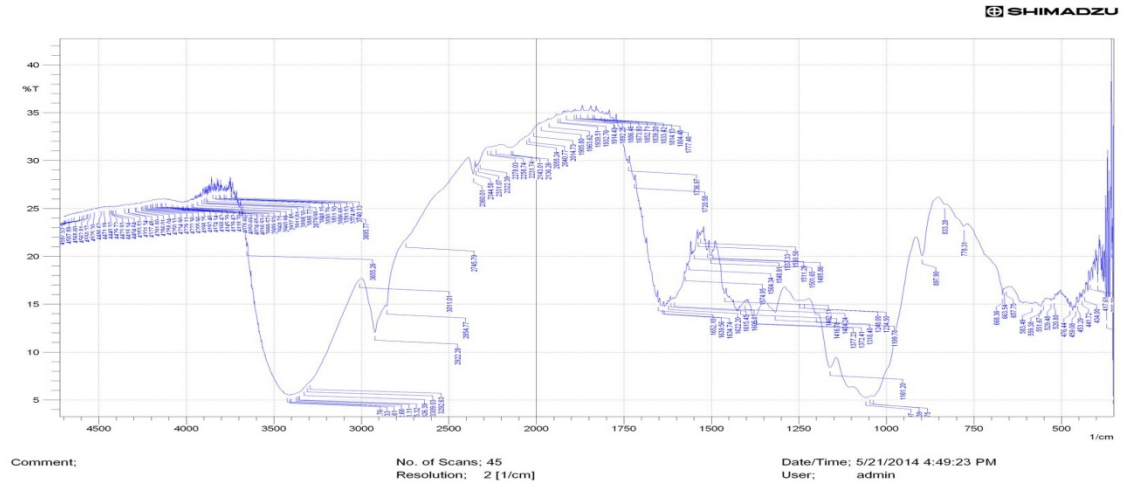

Figure 1: FTIR of metal unloaded water hyacinth biomass.

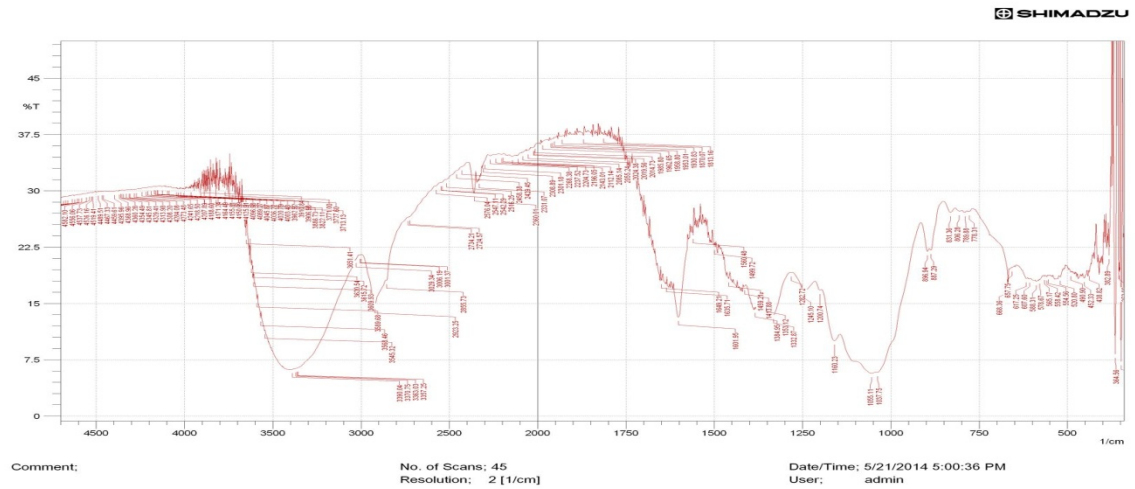

Figure 2: FTIR of metal loaded water hyacinth biomass.

REFERENCES

Bohart, G.S. and E.Q. Adam 1920. Some aspects of the behaviour of charcoal with respects to chlorine. J. Am. Chem. Soc., 42:523-529.

Chen, S., Q. Yue, B. Gao, Q. Li, X. Xu and K. Fu, 2012. Adsorption of hexavalent chromium from aqueous solution by modified corn stalk: a fixed-bed column study. Bioresour. Technol., 113: 114–120

Cherdchoo, W., S. Nithettham and J. Charoenpanich, 2019. Removal of Cr(VI) from synthetic wastewater by adsorption onto coffee ground and mixed waste tea. Chemosphere, 221:758767.

Freundlich, H.M.F. 1906. Uber die adsorption in lasungen (J). J. Phys. Chem., 57:385

Garcia-Reyes, R.B. and J.R. Rangel-Mendez, 2010. Adsorption kinetics of chromium(III) ions on agro-waste materials. Bioresour. Technol., 101:8099–8108.

Gupta, S. and B.V. Babu, 2009. Removal of toxic metal Cr(VI) from aqueous solutions using sawdust as adsorbent: equilibrium, kinetics, and regeneration studies. Chem. Eng. J., 150: 352–365.

Khan, T., M. Isa, M. Ul Mustafa, H. Yeek Chia, L. Baloo, Abd Binti, T. Manan and M. Saeed, 2016. Cr (vi) adsorption from aqueous solution by an agricultural waste based carbon. RSC Adv., 6: 56365–56374.

Langmuir, I. 1916. The constitution and fundamental properties of solids and liquids. part i. solids. J. Am. Chem. Soc., 38(11):2221-2295.

Mitra, T. and S.K. Das, 2019. Cr(VI) removal from aqueous solution using Psidium guajava leaves as green adsorbent: column studies. Appl. Water Sci., 9: 153.

Mohan, G. V. K., A. N. Babu and K. K. K. Ravindhranath, 2019. Removal of chromium (VI) from water using adsorbent derived from spent coffee grounds, Int. J. Environ. Sci. Technol.,16: 101–112.

Nasseh, N., L. Taghavi, B. Barikbin and A. R. Hari-Mood, 2017. The removal of Cr(VI) from aqueous solution by almond green hull waste material: kinetic and equilibrium studies, J. Water Reuse Desalin., 7:449–460.

Oguz, E. and M. Ersoy, 2010. Removal of Cu^{2+} from aqueous solution by adsorption in a fixed bed column and neural network modeling. Chem. Eng. J., 164(1): 56–62.

Pakade, V.E., N.T. Tavengwa and L.M. Madikizela, 2019. Recent advances in hexavalent chromium removal from aqueous solutions by adsorptive methods. : RSC Adv., 9: 26142- 26164.

Rane, N. M., S. V. Admane and R. S. Sapkal, 2019. Adsorption of hexavalent chromium from wastewater by using sweetlime and lemon peel powder by batch studies, Waste Manag. Resour. Effic., 1207–1220.

Rezania, S., M. Ponraj, A. Talaiekhozani, S.E. Mohamad, M.F.M. Din, S.M. Taib, F. Sabbagh and F.M. Sairan, 2015. Perspectives of phytoremediation using water hyacinth for removal of heavy metals, organic and inorganic pollutants in wastewater. J. Environ. Manag., 163: 125–133.

Saha, P., O. Shinde and S. Sarkar, 2017. Phytoremediation of industrial mines wastewater using water hyacinth. Intern J phytoremediation, 19(1): 87–96.

Sekhon, G.S. and B. Singh, 2013. Estimation of heavy metals in the groundwater of Patiala district of Punjab, India. Earth Resour., 1: 1–4.

Sharma, R. and B. Singh, 2013. Removal of Ni (II) ions from aqueous solutions using modified rice straw in a fixed bed column. Bioresour. Techno., l 146: 519-524.

Singh, B., V. Thakur, G. Bhatia, D. Verma and K. Singh, 2016. Eco-friendly and cost-effective use of rice straw in the form of fixed bed column to remove water pollutants. J. Bioremediat Biodegrad., 7: 374.

Singh, K.K., H.S. Hasan, M. Talat, V.K. Singh and S.K. Gangwar, 2009. Removal of Cr(VI) from aqueous solutions using wheat bran. Chem Eng J., 151: 113–121.

Thomas, H.C. 1944. Heterogeneous ion exchange in a flowing system. J. Am. Chem. Soc., 66:1466–1664.

Ullah, I., R. Nadeem, M Iqbal and Q. Manzoor, 2013. Biosorption of chromium onto native and immobilized sugarcane bagasse waste biomass. Ecol. Eng., 60: 99-107.

Venugopal, V. and K. Mohanty, 2011. Biosorptive uptake of Cr(VI) from aqueous solutions by *Parthenium hysterophorus* weed: Equilibrium, kinetics and thermodynamic studies. Chem Eng J., 174: 151-158.

Pb. Univ. Res. J (Sci.) Vol. 69, 2019, pp 35-40

DIET AND DIABETES - INSEPARABLE RELATIONSHIP

Kawaljit Kaur[1*], Sargun Singh[2] and Angad Singh[3]
[1]**Mata Sahib Kaur Girls College, Talwandi Sabo (Bathinda)*
[2]*Government Medical College, Amritsar (Panjab)*
[3]*Himachal Dental College, Sundernagar*

Abstract

Glucose is an instant source of energy for our body. It is derived from the food stuff we eat and comes in the blood. Blood glucose has to be at a certain level as per recommendations of American Diabetic Association for human beings to function optimally. In a normal person, excess blood glucose is transferred to the body tissues with the help of a hormone called insulin. Sometimes due to non-availability or deficiency of insulin or due to other reasons the blood glucose does not remain controlled and leads to various complications in the body. In some cases it can lead to even death. Under such conditions, it becomes very important to control the blood glucose level by taking proper and controlled diet along with adoption of other changes in daily life style.

Keywords: Diabetes, Diet, Energy, Food, Insulin

INTRODUCTION

The instant source of energy for our body is glucose that comes from the food we eat. Glucose directly comes from its primary source carbohydrates. If the latter is not available, then it is formed either from glycogen stored in the liver for this purpose by means of glycogenolysis or other food stuffs like fats and carbohydrates by means of gluconeogenesis. If glucose supply to brain is interrupted for a short span, major complications may arise and the person may go in coma. In nut shell, glucose is very important for our survival. But it should be present in the blood in some fixed range, not more not less. If it is in lesser amount, it leads to hypoglycemia and if in more amount, it causes the state of hyperglycemia and neither of these is good for the body. The amount of glucose in the blood is controlled by the hormone insulin which is produced by the gland, pancreas. In most of the cases both of these states i.e. hypoglycemia and hyperglycemia are linked to diabetes.

Diabetes mellitus, commonly referred to as Diabetes, is a chronic disorder. When body produces very little or no insulin, one needs daily insulin injection to maintain the blood glucose level. This is called as type 1 diabetes. The other one, called as type 2 diabetes occurs when the pancreas does not secrete enough insulin or when the cells of the body become resistant to insulin. In either case, the blood sugar cannot get into the cells for storage, which may cause serious complications that can lead to disability and premature death, for example, cardiovascular disease, peripheral vascular disease, nephropathy, and changes to the retina and blindness, which impose significant medical and economic burdens. Genetic family history and environmental influences seem to be the most important factors responsible for the development of this condition. Type 2 diabetes accounts for 90% to 95% of all diabetes cases (Centre for Disease Control and Prevention, 2017; Kastorini and Panagiotakos, 2010; Thomas *et al*. 2006; Scott, 1990).

The worldwide burden of type 2 diabetes has increased rapidly in tandem with increase in obesity coupled with changes in life style. Globally, an estimated 422 million adults are living with diabetes, according to the latest data from the World Health Organization (WHO, 2016). The number is projected to almost double by 2030 (Wild *et al*., 2004). India has more diabetics than any other country in the world. According to the International Diabetes Foundation (Gale, 2010), the country has now been surpassed to the top spot by China (BBC, March 25th, 2010).

Obesity is seen as one of the major contributing factors to the development of insulin resistance in approximately 90% of the individuals with type 2 diabetes. However, what's alarming is the fact that India is home to 62 million diabetics and the number is estimated to be 100 million by 2030. The global figures on diabetes, released by the International Diabetes Federation, has raised a serious alarm for India by saying that nearly 52% of Indians aren't aware that they are suffering from high blood sugar (Sinha, 2012).

In most cases, achieving ideal body weight is associated with the restoration of normal blood sugar level. Hence dietary modifications and treatment are fundamental to the successful management of the diabetes whatever the type be. Other than type 1 and type 2 diabetes, there is pre-diabetes when blood sugar is high, but not high enough to be type 2 diabetes and gestational diabetes where high blood sugar affects the pregnant women. The amount and type of food consumed is a fundamental

*Corresponding Author: virk.khokhar@yahoo.com
MS Received: December 27, 2017, Accepted: November 21, 2019

determinant of human health. With the number of people suffering from diabetes on the rise globally (WHO, 2016), it is imperative to develop preventative measures involving intervention of diet and lifestyle, which would greatly reduce the risk of developing diabetes other than medication (Sami *et al.*, 2017; Lindstrom *et al.*, 2006). There are different prescribed diets across continents and countries (Ajala *et al.*, 2013). Medical nutrition therapy is an integral component of diabetes management and of diabetes self-management education (American Diabetes Association, 2004)

WHY GLUCOSE IS IMPORTANT?

Like most other tissues, brain metabolism depends primarily on glucose for fuel under most circumstances. There is no reservoir of glucose. A limited amount of glucose can be derived from glycogen stored in astrocytes, but it is consumed within minutes. For constant working, the brain is dependent on a continual supply of glucose diffusing from the blood into the interstitial tissue within the central nervous system and into the neurons themselves. In mammalian brain, neurons have the maximum demand of energy (Howarth *et al.*, 2012). In humans, the brain accounts for ~2% of the body weight, but it consumes ~20% of glucose-derived energy making it the main consumer of glucose (Erbsloh *et al.*, 1958).The energy consumed is utilized to provide the precursors for the synthesis of neurotransmitters. Disruption of pathways of glucose delivery and metabolism leads to debilitating brain diseases.

If the amount of glucose supplied by the blood falls, the brain is one of the first organs to be affected. In most people, when the glucose falls below 65 mg/dl, slight reduction of mental efficiency can be observed. Impairment of action and judgment usually becomes obvious below 40 mg/dl. Seizures may occur as the glucose falls further. Similarly, as blood glucose level falls below 10 mg/dl, most neurons become electrically silent and nonfunctional, resulting in coma. Coma can occur at glucose levels in the range of 2.3–2.7 mmol/l (41–49 mg/dl) as well as at lower glucose levels (Ben-Ami *et al.*, 1999). These brain defects are collectively referred to as neuroglycopenia. If the blood sugar level falls too low, the liver converts stored glycogen into glucose and releases it into the bloodstream to prevent the person going into a diabetic coma for a short period of time. A subject with a consistent range between100–126 mg/dl is considered slightly hyperglycemic, while above126 mg/dl is generally held to have diabetes (American Diabetes Association 2019 a).

Brief or mild hypoglycemia produces no lasting effects on the brain, though it can temporarily alter brain responses to additional hypoglycemia. Prolonged, severe hypoglycemia can produce lasting damage of a wide range. This can include impairment of cognitive function, motor control, or even consciousness. Deficits in learning and memory have been shown to be a direct consequence of this severe hypoglycemia-induced hippocampal neuronal damage (Suh *et al.*, 2003, 2005; Auer, 2004). The likelihood of permanent brain damage from any given instance of severe hypoglycemia is difficult to estimate, and depends on a multitude of factors such as age, recent blood and brain glucose experience, concurrent problems such as hypoxia, and availability of alternative fuels. Significant hypoglycemia appears to increase the risk of cardiovascular disease (Goto, 2013).

Similarly, temporary hyperglycemia is often benign and asymptomatic. Blood glucose level can rise well above the normal and cause pathological and functional changes for significant periods without producing any permanent effects or symptoms. During this asymptomatic period, an abnormality in carbohydrate metabolism can occur which can be tested by measuring plasma glucose (American Diabetes Association, 2004). However, chronic hyperglycemia at above normal levels can leads to glucose toxicity and produces a very wide variety of serious complications over a period of years, including kidney damage, neurological damage, cardiovascular damage, damage to the retina or damage to feet and legs and may lead to fall in neutrophils (Kawahito *et al.*, 2009). Diabetic neuropathy may be a result of long-term hyperglycemia. Impairment of growth and susceptibility to certain infection can occur as a result of chronic hyperglycemia (American Diabetes Association, 2014).

In untreated hyperglycemia, a condition called ketoacidosis may develop because decreased insulin levels increase the activity of hormone sensitive lipase (Kraemer and Shen, 2002). The degradation of triacylglycerides by hormone-sensitive lipase produces free fatty acids that are eventually converted to acetyl-CoA by beta-oxidation. Ketoacidosis, also called as diabetic ketoacidosis is a life-threatening condition which requires immediate treatment. Symptoms include: shortness of breath, breath that smells fruity (such as pear drops), nausea and vomiting, and very dry mouth. Chronic hyperglycemia injures the heart in patients without a history of heart disease or diabetes and is strongly associated with heart attacks and death in subjects with no coronary heart disease or history of heart failure (News Medical Life Sciences, 2012).

DIET AND DIABETES

DIET FOR DIABETES

There is no single dietary pattern that is best for all people with all types of diabetes like type 1 or type 2 or gestational diabetes. For overweight and obese people with type 2 diabetes, any weight-loss diet that the person will adhere to and achieve weight loss is effective (Grams and Garvey, 2015). Since carbohydrate is the macronutrient that raises blood glucose levels most significantly, the important issue is regarding how low in carbohydrates the diet should be? Likewise, people with diabetes may be encouraged to reduce their intake of carbohydrates that have a high glycemic index, although this is also controversial because in cases of hypoglycemia, they are advised to have food or drink that can raise blood glucose quickly (McDougall, 2006).

A study by the Diabetes Prevention Program Research Group (Knowler et al., 2002) concluded that lifestyle intervention resulted in 39% lower incidence of diabetes than another group using only metformin, an interventive medication for people who are at risk of diabetes. Diet is individualized depending on age, weight, gender, health condition, and occupation etc. The dietary pattern emphasizes a consumption of foods high in unsaturated fatty acids, and encourages daily consumption of fruits, vegetables, low fat dairy products and whole grains, low consumption of fish, poultry, tree nuts, legumes, very less consumption of red meat (Barnard *et al*., 2005; American Diabetes Association, 2004, 2010).

Fruits, vegetables, and other plant foods tend to be rich in antioxidants and other phytochemicals. Antioxidants consumed in food inhibit damaging reactions within the human body and have a beneficial effect upon health. By reducing free-radical damage, antioxidants reduce inflammation, promote cardiac health, and reduce the risk of neurodegenerative diseases like Alzheimer's and Parkinson's disease. Fruit and vegetable consumption has been associated with decreased incidence of and mortality from a variety of health outcomes including obesity, hypertension, and cardiovascular diseases in epidemiological studies (He *et al*., 2004; Hung *et al*., 2004; Joshipura *et al*., 1999).

A typical healthy diet that is high in fiber, with a variety of fruit and vegetables, and low in both sugar and fat, especially saturated fat is recommended. Diets that are high in fiber may be able to help in the management of diabetes. Soluble fiber delays glucose absorption from the small intestine and thus may help prevent the spike in blood glucose levels that follow a meal or snack. Fibers promote good bowl health, prevent from certain types of cancers and play significant role in controlling diabetes. Fibers don't require insulin to digest. It is accepted that viscous and gel-forming properties of soluble dietary fibers inhibit macronutrient absorption, reduce postprandial glucose response, and beneficially influence certain blood lipids (Martin and Andreas, 2008). According to InterAct Consortium (2015), in a recent study conducted by researchers at the Imperial College London, those who had the highest intake of fiber (more than 26 grams a day) had an 18 percent lower risk of developing type 2 diabetes than those with the lowest intake (less than 19 grams a day). Antioxidants lie in the fibers. It is not soluble dietary fibers, but mainly the consumption of insoluble cereal fibers and whole grains that is consistently associated with reduced risk of type 2 diabetes in large prospective cohort studies (Schulze *et al*., 2007; de Munter *et al*., 2007). Vegetarian (Kahleova *et al*., 2011) and low-glycemic index (Ben-Avraham *et al*., 2009) diets are recommended to help reduce the use of diabetic medication.

There is no standard meal plan or eating pattern that works universally for all diabetic people (American Diabetes Association, 2014). In order to be effective, nutrition therapy should be individualized for each patient/client based on his or her individual health goals; personal and cultural preferences (Kattlemann *et al*., 2009; Mian and Brauer, 2009). In a major change, the American Diabetes Association (2019a,b) in their position statement now states "research indicates that low carbohydrate eating plans may result in improved glycemia and have the potential to reduce anti-hyperglycemic medications for individuals with type 2 diabetes". Further, low carbohydrate diets are not recommended for pregnant and lactating women, those who have or are at risk for disordered eating, and those with renal diseases (American Diabetes Association, 2019 b).

Although it is clear that carbohydrates do have different glycemic responses, the data reveal no clear trend in outcome benefits. If there are long-term effects on glycemia and lipids, these effects appear to be modest. Moreover, the number of studies is limited, and the design and implementation of several of these studies are subject to criticism. Effective lifestyle modifications including counseling on weight loss, adoption of a healthy dietary pattern like the Mediterranean diet, together with physical activity are the cornerstone in the prevention of type-2 diabetes.

CONCLUSION

For many individuals with diabetes, the most challenging part is to determine what to eat? According to American Diabetes Association, there is not a "one-size-fits-all" eating pattern for individuals with diabetes. Ideally, the individual with diabetes should be referred to a registered dietician. Individualized meal planning

should focus on personal preferences, needs, and goals rather than focusing on any specific macronutrient distribution. An intensive lifestyle intervention can reduce the incidence of any type of diabetes.

REFERENCES

Ajala, O., P. English and J. Pinkney. 2013. Systematic review and meta-analysis of different dietary approaches to the management of type 2 diabetes. Am. J. Clin. Nutr, 97: 505–516.

American Diabetes Association. 2004. Nutrition Principles and Recommendations in Diabetes. Diabetes Care, 27(Supplement 1): S36-S36.

American Diabetes Association. 2010. Standards of medical care in diabetes--2010.Diabetes Care, 33 (Supplement 1):S11-S61.

American Diabetes Association. 2014. Standards of medical care in diabetes - 2014. Diabetes Care. 37(Suppl. 1):S14–S80

American Diabetes Association. 2019 (a). Classification and Diagnosis of Diabetes: Standards of Medical Care in Diabetes. Diabetes Care. 42 (Supplement 1): S13-S28.

American Diabetes Association. 2019 (b). Low Carb Diet in 2019 American Diabetes Association Standards of Care. Diabetes Care. 42 Supplement 1:S46–S60.

Auer, R.N. 2004. Hypoglycemic brain damage. Metab. Brain Dis., 19(3-4):169-175.

Barnard, N.D., A.R. Scialli, G. Turner-McGrievy, A.J. Lanou and J. Glass. 2005. The effects of a low-fat, plant-based dietary intervention on body weight, metabolism, and insulin sensitivity. Am. J. Med., 118(9):991-997.

BBC News. March 25, 2010. "China faces 'diabetes epidemic', research suggests". Available on: http://news.bbc.co.uk/2/hi/asiapacific/8587032.stm.

Ben-Ami, H., P. Nagachandran, A. Mendelson and Y. Edoute. 1999. Drug-induced hypoglycemic coma in 102 diabetic patients. Arch. Intern. Med., 159 (3):281-284.

Ben-Avraham, S., I. Harman-Boehm, D. Schwarzfuchs and I. Shai. 2009. Dietary strategies for patients with type 2 diabetes in the era of multi-approaches; review and results from the Dietary Intervention Randomized Controlled Trial (DIRECT). Diabetes Res. Clin. Pract., 86 (Supplement 1):S41-S48.

Centers for Disease Control and Prevention (CDC). 2017. National Diabetes Statistics Report, 2017; Estimates of Diabetes and its Burden in the United States, Atlanta, GA: U.S. Department of Health and Human Services, Centers for Disease Control and Prevention. Available on: https://www.cdc.gov/diabetes/pdfs/data/statistics/national-diabetes-statistics-report.pdf.

De Munter, J.S., F.B. Hu, D. Spiegelman, M. Franz and R.M. van Dam. 2007. Whole grain, bran, and germ intake and risk of type 2 diabetes: a prospective cohort study and systematic review. PLoS Med., 4: e261.

Erbsloh, F., A. Bernsmeier and H. Hillesheim. 1958. The glucose consumption of the brain & its dependence on the liver. Arch Psychiatr Nervenkr Z Gesamte Neurol Psychiatr, 196 (6): 611-626.

Gale, J. November 7, 2010. India's Diabetes Epidemic Cuts Down Millions Who Escape Poverty". Available on: https://www.bloomberg.com/news/articles/2010-11-07/india-s-deadly-diabetes-scourge-cuts-down-millions-rising-to-middle-class.

Goto, A. 2013. Severe hypoglycaemia and cardiovascular disease: systematic review and meta-analysis with bias analysis. BMJ, 347: f4533.

Grams, J. and W.T. Garvey. 2015. Weight Loss and the Prevention and Treatment of Type 2 Diabetes Using Lifestyle Therapy, Pharmacotherapy, and Bariatric Surgery: Mechanisms of Action. Current Obesity Reports, 4 (2): 287–302.

He, K., F.B. Hu, G.A. Colditz, J.E. Manson, W.C. Willett and S. Liu. 2004. Changes in intake of fruits and vegetables in relation to risk of obesity and weight gain among middle-aged women. Int. J. Obes. Relat. Metab. Disord, 28(12):1569-1574.

Howarth, C., P. Gleeson and D. Attwell. 2012. Updated energy budgets for neural computation in the neocortex and cerebellum. J. Cereb. Blood. Flow. Metab., 32(7):1222-1232.

Hung, H.C., K.J. Joshipura, R. Jiang, F.B. Hu, D. Hunter, S.A. Smith-Warner, G.A. Colditz, B. Rosner, D. Spiegelman and W.C. Willett. 2004. Fruit and vegetable intake and risk of major chronic disease. J. Natl. Cancer Inst. 96:1577–1584.

InterAct Consortium. 2015. Dietary fiber and incidence of type 2 diabetes in eight European countries: the EPIC-InterAct Study and a meta-analysis of prospective studies. Diabetologia, 58(7):1394-1408.

Joshipura, K.J., A. Ascherio, J.E. Manson, M.J. Stampfer, E.B. Rimm, F.E. Speizer, C.H. Hennekens, D. Spiegelman and W.C. Willett. 1999. Fruit and vegetable intake in relation to risk of ischemic stroke. JAMA, 282 (13):1233–1239.

Kahleova H., M. Matoulek, H. Malinska, O. Oliyarnik, L. Kazdova, T. Neskudla, A. Skoch, M. Hajek, M. Hill, M. Kahle and T. Pelikanova. 2011. Vegetarian diet improves insulin resistance and oxidative stress markers more than conventional diet in subjects with Type 2 diabetes. Diabet. Med., 28(5):549-559.

Kastorini, C.M. and B.D. Panagiotakos. 2010. Mediterranean diet and diabetes prevention: Myth or fact? World J. Diabetes, 1:65-67.

Kattelmann, K.K., K. Conti and C. Ren. 2009. The medicine wheel nutrition intervention: a diabetes education study with the Cheyenne River Sioux Tribe. J. Am. Diet. Assoc., 109:1532–1539.

Kawahito, S., H. Kitahata, and S. Oshita. 2009. Problems associated with glucose toxicity: Role of hyperglycemia-induced oxidative stress. World J. Gastroenterol., 15(33): 4137–4142.

Knowler W.C., E. Barrett-Connor, S. E. Fowler, R. F. Hamman, J. M. Lachin, E. A. Walker and D. M. Nathan. 2002. Diabetes Prevention Program Research Group. Reduction in the incidence of type 2 diabetes with lifestyle intervention or metformin. N. Engl. J. Med., 346(6):393-403.

Kraemer, F.B. and W.J. Shen. 2002. Hormone-sensitive lipase control of intracellular tri-(di-) acylglycerol and cholesteryl ester hydrolysis. The Journal of Lipid Research, 43:1585-1594.

Lindström, J., P. Ilanne-Parikka, M. Peltonen, S. Aunola, J. G. Eriksson, K. Hemiö, H. Hämäläinen, P. Härkönen, S. Keinänen-Kiukaanniemi, M. Laakso, A. Louheranta, M. Mannelin, M. Paturi, J. Sundvall, T.T. Valle, M. Uusitupa and J.F. Tuomilehto. 2006. Sustained reduction in the incidence of type 2 diabetes by lifestyle intervention: follow-up of the Finnish Diabetes Prevention Study. Lancet, 368 (9548):1673-1679.

Martin W. and P. Andreas. 2008. Metabolic effects of dietary and prevention of diabetes. Journal of Nutrition, 138: 439-442.

Mc Dougall J. 2006. Glycemic Index – Not Ready for Prime Time, The McDougall Newsletter, 2006: 5(7):1-5.

Mian, S.I. and P.M. Brauer. 2009. Dietary education tools for South Asians with diabetes. Can J Diet. Pract. Res., 70:28–35.

News Medical Life Sciences. 2012. Chronic hyperglycemia may lead to cardiac damage. Journal of the American College of Cardiology. Available at: www.news medical.net/news/ 20120203/Chronic-hyperglycemia-may-lead-to-cardiac-damage.aspx.

Sami, W., T. Ansari, N.S. Butt and M.R.A. Hamid. 2017. Effect of diet on type 2 diabetes mellitus: A review. Int. J. Health Sci. (Qassim), 11(2): 65–71.

Schulze, M.B., M. Schulz, C. Heidemann, A. Schienkiewitz, K. Hoffmann and H. Boeing. 2007. Fiber and Magnesium Intake and Incidence of Type 2 Diabetes: A Prospective Study and Meta-analysis. Arch. Intern. Med., 167:956–965.

Scott, F.W. 1990. Cow milk and insulin-dependent diabetes mellitus: Is there a relationship? Am J. Clin. Nutr., 51:489-491.

Sinha, K. 2012. 44 lakh Indians don't know they are diabetic. Available on: https://timesofindia. indiatimes.com/india/44-lakh-Indians-dont-know-they-are diabetic/articleshow/17274366. cms.

Suh, S.W., K. Aoyama, Y. Matsumori, J. Liu and R.A. Swanson. 2005. Pyruvate administered after severe hypoglycemia reduces neuronal death and cognitive impairment. Diabetes, 54(5):1452-1458.

Suh, S.W., K. Aoyama, Y. Chen, P. Garnier, Y. Matsumori, E. Gum, J. Liu and R.A. Swanson. 2003. Hypoglycemic neuronal death and cognitive impairment are prevented by poly (ADP-ribose) polymerase inhibitors administered after hypoglycemia. J. Neurosci., 23(33):10681-10690.

Thomas, D.E., E.J. Elliott and G.A. Naughton. 2006. Exercise for type 2 diabetes mellitus. Cochrane Database Syst. Rev., 3:CD002968.

Wild S., G. Roglic, A. Green, R. Sicree and H. King. 2004. Global prevalence of diabetes: Estimates for the year 2000 and projections for 2030. Diabetes Care. 27 (5): 1047–1053.

World Health Organization (WHO). 2016. Global Report on Diabetes. Geneva. Available on: https://www.who.int/diabetes/global-report/en/.

Pb. Univ. Res. J (Sci.) Vol. 68,2018, pp 41-44

SYMPTOMATIC BENIGN MIGRATORY GLOSSITIS WITH FISSURED TONGUE – A RARE CASE REPORT

Leena Verma*, Sidhi Passi and Jyoti Gupta
Department of Pedodontics and Periodonticss, HSJIDS, Panjab University, Chandigarh

Abstract

Benign migratory glossitis is an inflammatory lesion with a prevalence of 2.5% in adults and less than 1% in children. It appears as multifocal, erythematous irregular patches, which are surrounded by a white elevated keratotic band present on dorsal surface of the tongue and which recurs on different locations on tongue. This change in posture on the tongue gives rise to the usage of the term 'migratory' This article presents a rare case report of symptomatic geographic tongue (GT) along with fissured tongue in a 10 year old girl with a history of unknown allergic reactions, who reported to the clinics with a painful erosion on the tongue. Symptomatic GT is a rare occurrence in pediatric dentistry though asymptomatic GT is comparatively common. In this case, symptomatic GT case was managed with the application of Topical Lignocaine gel. This case report discusses the details of the aforementioned patient and various treatment options in symptomatic GT, which is a rare occurrence in pediatric patients.

Keywords: Benign migratory glossitis, Fissured tongue, Allergy

INTRODUCTION

Benign migratory glossitis (BMG) is also known as geographic tongue, erythema migrans, and wandering rash of tongue (Pinto *et al*., 2014). It is benign in nature and appears as a red and white lesion. It is more commonly seen in adults as compared to children and appears on the dorsal surface or lateral borders of the tongue (Shulman, 2005). It clinically presents as multifocal, erythematous irregular patches on the tongue with the loss of filiform papilla and is surrounded by a slightly elevated keratotic band or line. The white border consists of regenerating filiform papillae mixed with keratin and neutrophils. Due to loss of papillae, the surface appears ulcerated (Shulman, 2005). These patches are well defined and show a variation in size. Pattern and location of these lesions change with time, hence the term benign migratory glossitis is used. The reason for the migration can be attributed to the loss of epithelium at one site and proliferation at another site. Fissuring in the tongue is characterized by grooves of varying depth seen on the dorsal surface of the tooth (Prinz, 1927).

This article discusses a case report of a 10 year old female child having symptomatic benign migratory glossitis with fissured tongue which is a rare occurrence.

CASE REPORT

A 10-year-old female reported to the pedodontic clinic with her parents/guardians with the chief complaint of a painful erosion on the tongue. She had mild discomfort along with burning sensation, which increased on consumption of spicy food and acidic beverages. Patient's past medical history revealed that she had history of allergic reactions. On intraoral examination, we found a red patch on right posterolateral dorsal surface of tongue surrounded by white graying margin (Figure 1). There was loss of papillae in this area which was causing irritation to the patient. The characteristic feature of GT includes periods of exacerbation and remission, so it was noticed that after 15 days of the first dental visit, the lesion disappeared from right posterolateral dorsal surface of tongue and reappeared on the right anterolateral dorsal surface of the tongue.

The lesion healed without residual scar formation (Figure 2). The patient had no painful symptoms, no taste loss, but only mild irritation on the affected area. A large and deep central fissure was seen separating the dorsal surface of the tongue into two halves (Figure 3).

Her parents and siblings were orally examined, but no such lesions were evident in them. Based on history and clinical examination of the patient diagnosis of Geographic Tongue along with fissured tongue was made which include characteristic migratory pattern, chronic nature and patient history of allergic reactions.

As the patient complained of mild irritation, so she was advised to use 0.12% Chlorhexidine gluconate mouthwash two times a day to reduce the discomfort of the patient. Only symptomatic treatment with topical Lignocaine gel was advised as the symptoms used to resolve on their own. Proper cleaning of the fissured tongue was also demonstrated to the patient. Patient was kept on a bimonthly recall.

Ideally a biopsy specimen should be obtained from a site, which includes keratotic margins and atrophic area, but due to the lack of patient cooperation, it could not be done.

*Corresponding Author: leenagulati32@gmail.com
MS Received: July13, 2018, Accepted: December 20,2019

FIGURE 1: A red patch on right posterolateral dorsal surface of tongue surrounded by white greying margin on first visit of patient

FIGURE 2: Previous lesion resolved, new lesion developing on right anterolateral dorsal surface of the tongue (fresh site) after 15 days

FIGURE 3: A large and deep central fissure seen separating the dorsal surface of the tongue into two halves

DISCUSSION

Geographic tongue (GT) also known as benign migratory glossitis and erythema migrans is a descriptive term applied to a map like appearance of the tongue which occurs as a result of irregular patches occurring along its surface. This condition has a familial predisposition and shows a polygenic mode of inheritance. Conditions producing stress on the body such as allergies like asthma, hormonal disturbances, nutritional deficiencies, psychological disturbances and local irritants cause geographic tongue. There are

also strong associations with diseases like psoriasis and juvenile diabetes (Flores *et al*., 2013).

In the present case, an allergic reaction can be linked to the etiology of GT. This finding was similar to studies done by Barton *et al*. (1982) and Mehta *et al.* (2017), where also GT patients were associated with having unknown etiology. The rate of occurrence of GT in normal population is between 1.0 and 2.5% and is less common in children than in adults (Goswami *et al*. 2012). Redman (1970) reported a 1% prevalence of GT in schoolchildren, with an equal rate of occurrence in both sexes (Redman 1970). However, Rezaei *et al*. (2015) reported higher prevalence rate of GT 8.94% among in boys as compared to 6.78% among girls from schools of Kermanshah, Iran.

Rahamimoff and Muhsam (1957) observed a 14% prevalence of migratory glossitis in 5000 children aged 2 years old and younger. Kleinman and colleagues (1994) reported a prevalence of geographic tongue of 0.6% in 39,206 children aged 5 to 17 years.

The association between fissured tongue and BMG supports a genetic basis for the development of the condition. The fissures may act as stagnation areas on the tongue surface in which glossitis may begin.

In the present case allergic reaction can be linked to the etiology of GT. A study was done by Marks and Cranzy (1984) on atopic patients having a history of asthma or rhinitis They found a 50% prevalence of BMG in these patients and concluded that they may have a similar pathogenesis. Barton and associates (1982) concluded with about 95% of BMG patients are associated with different types of allergies. Another case report presented by Gosawami *et al.* (2012), reported symptomatic geographic tongue with fissured tongue with a history of asthma (Goswami 2012). In our case also the patient had history of allergies, so this could be the etiology of BMG as reported in various studies.

A routine oral examination in paediatric patients can prove to be beneficial for diagnosis of GT. This condition results due to loss of papillae on the particular area of the tongue referred to as denuded areas, which may persist for more than one month.

GT causes symptoms in children which require proper management and treatment The dentist should take a detailed medical history with emphasis on allergies. Most GT paediatric patients do not require any treatment but patients presenting with painful symptoms require a supportive and symptomatic management which includes balanced diet, acetaminophen for systemic pain relief, topical LA for local relief.

It is common to find BMG as a painless ulcer on the dorsum of the tongue but symptomatic BMG is a rare occurrence. Exfoliative cytology can be helpful in ruling out candidiasis.

In Symptomatic lesions, topical prednisolone is administered. However, treatment with cyclosporine (Abe *et al*., 2007) and with topical and systemic antihistamines (Assimakopulos *et al*., 2002) has been reported. Patients are encouraged to brush the dorsum of the tongue to remove debris which can act as an irritant. The patients are counselled that the lesions are benign and they may disappear, reappear and even change the location. Periodic follow up is required in these cases.

It is concluded that in this kind of disease the patient should pay more attention to his oral hygiene and nutrition, and it should be mandatory for the professional to alert the patient concerning maintaining oral hygiene cares and reassure him about the benign nature of this pathology.

REFERENCES

Abe, M., Y. Sogabe, H. Syuto TIshibuchi and Y. Yokohama, et al. 2007. Successful treatment with cyclosporine administration for persistent benign migratory glossitis J. Dermatol 34(5):340-343

Assimakopulos, D., G. Patrikakos, C. Fotika and E. Moses. 2002. Benign migratory glossitis or geographic tongue. An enigmatic oral lesion Am J Med 113(9):751-755

Barton, D.H., S.K. Spiker and T.J. Crovella. 1982. Benign migratory glossitis and allergy. Pediatr Dent 4:249-250

Flores, I.L., S. Santos, A.R. Coletta, P.A. Vargas and M.A. Lopes. 2013. Widespread red oral lesions J. American Dent. Assoc, 144(11) :1257-1260

Goswami, M., A. Verma and M. Verma. 2012. Benign migratory glossitis with fissured tongue. J. Indian Soc Pedod Prev Dent 30:173-75

Kleinman, D.V., P.A. Swango, and J.J. Pindborg. 1994. Epidemology of oral mucosal lesions in United States children. Community Dent Oral Epidemiol 22 :243-253

Marks, R. and D. Czarny. 1984. Geographic tongue: Sensitivity to the environment. Oral Surg 58:156-159

Mehta, V. 2017. Benign Migratory Glossitis : Report of a rare case with Review of literature. J. Dent Health Oral Disoder Ther 6(4):1-3

Pinto, A., C.M. Haberland and S. Baker. 2014. Paediatric soft tissue oral lesions. Dent Clin North Am .58:437-53

Prinz, H. 1927. Wandering rash of the tongue (geographic tongue). Dent Cosmos 69: 272-275.

Rahamimoff, P., H.V. Muhsam. 1957. Some observations of 1,246 cases of geographic tongue. Am J Dis Child 93; 519-525.

Redman, R.S. 1970. Prevalence of geographic tongue, fissured tongue, median rhomboid glossitis and hairy tongue among 3, 611 Minnesota school children Oral Surg 30:390-395

Rezaei F., M. Safarzadeh, H. Mozafari and P. Tavakoli. 2015. Prevalence of Geographic Tongue and Related Predisposing Factors in 7-18 Year-Old Students in Kermanshah, Iran 2014. Global Journal of Health Science; 7(5): 91-95.

Shulman, J.D. 2005. Prevalence of oral mucosal lesions in children and youth in USA. Int J Paediatr Dent. 15(2): 89-97.

Pb. Univ. Res. J (Sci.) Vol. 69, 2019, pp 45-62

EFFECT OF β-CYCLODEXTRIN ON THE BEHAVIOUR OF THERMOPHYSICAL AND SPECTROSCOPIC PROPERTIES OF MIXTURES OF (α, ω-ALKANEDIOLS + PYRROLIDIN-2-ONE)

Ganga Ram Chaudhary*, Avneet Kaur and Navneet Kaur
Department of Chemistry & Centre of Advanced Studies in Chemistry, Panjab University, Chandigarh - 160014, India

Abstract

The thermodynamic parameters, viz., excess molar volume (V^E) and ultrasonic speed (u), transport parameter viscosity (η) and spectroscopic parameters, viz., IR, ^{1}H, ^{13}C NMR have been measured for the liquid mixtures of α,ω-alkanediols and pyrrolidin-2-one in the presence of β-cyclodextrin over the whole composition range. The partial molar quantities, excess isentropic compressibility (K_S^E), deviation in isentropic compressibilities (ΔK_S), deviation in ultrasonic velocity (u^D), viscosity deviation ($\Delta\eta$), deviation in Gibbs energies of activation for viscous flow (g(x)) and excess NMR chemical shift (δ^E) have also been estimated and analyzed. Results have clearly shown that that position of hydroxyl groups of α,ω-alkanediols showed noticeable change in the thermophysical properties for the mixtures. Furthermore, the effect of addition of β-cyclodextrin caused significant changes, due to the difference in the fitting of α,ω-alkanediols in the hydrophobic cavity of cyclodextrin. It is inferred that 1,5-PTD has more affinity for the hydrophobic cavity of β-CD. Whereas, the dispersion forces are more prevalent on addition of β-CD in 1, 3-PPD + PY system. These results have been found to be in excellent concurrence with NMR and FT-IR studies. However, for 1,2-ED and 1,3-PPD, dispersion forces due to dissociation of self-associated PY and diols are predominant. The spectroscopic measurements confirm that the interaction between unlike molecules take place through hydroxyl group of α,ω-alkanediols and carbonyl group of pyrrolidin-2-one.

Keywords: Thermophysical, *β*-Cyclodextrin, (PY + Alkanediols), Spectroscopic.

INTRODUCTION

The thermophysical properties of liquid mixtures containing polar and self-associated components exhibit significant deviation from ideality, arising not only from the difference in size and shape, but also from possible hydrogen-bonding interaction between unlike molecules. By the suitable selection of the components in the mixtures, we can obtain an appreciable correlation between thermodynamic and spectroscopic measurements and hence the contributions to non-ideal behavior of liquid mixture can be evaluated (Bansal *et al*., 2014, Mehta *et al*., 2007, Santos *et al*., 2017, Kaur *et al*., 2019)

Due to the presence of two chemically active hydroxyl groups, alkanediols are the simplest structural units for polyhydroxy compounds. Alkanediols are chemically very similar to alcohols and the presence of the additional hydroxyl group in the diol molecule turns the position of the two-hydroxyl groups very important for the hydrophobic/hydrophilic hydration (Ali *et al*., 2005, Chaudhary *et al*., 2013, Panda *et al*., 2017, Das *et al*., 2004, Kaur *et al*., 2019). In addition, their two chemically reactive hydroxyl groups make the alkanediols important Alkanediols have been used in variety of practical and theoretical applications. (Malandain *et al*., 1996, Mehta *et al*., 2006). 1,2-Ethanediol (1,2-ED), 1,3-propanediol (1,3-PPD), and 1,5-pentanediols (1,5-PTD) are clear colorless, slightly syrupy liquids at room temperature.

1,2-ED is the simplest alkanediol. The molecule is small and can form hydrogen-bonded networks similar in nature to those of water but considerably different in the details of the structure. 1,2-ED possesses a high cohesive energy, a fairly high dielectric constant and is a very good solvent for micellization or liquid crystal formation. It is one of the major products of the chemical industry. 1,2-ED lowers the freezing point of water. Its ease of handling makes it perfect antifreeze that is used, for example, in motor vehicles, solar energy units, heat pumps, water heating systems, solar energy systems, and industrial cooling systems. It is also a commercially important raw material for the manufacture of polyester fibers. Other uses of 1,2-ED are as an ingredient in photography-film developing, hydraulic brake fluids and inks used in stamp pads, ballpoint pens and print shops(Ruiz *et al*., 2001, Jerie *et al*., 2004, Grzybowski *et al*., 2015, Katrinak *et al*., 2012). 1,3-PPD is used to absorb extra water and maintain moisture in certain medicines, cosmetics and food products. It is also used as a heat-transfer fluid in uses, where leakage might lead to food contact, such as in coolants for dairy refrigeration equipment. It is also used as a solvent in food colours and flavours, antifreeze in breweries and establishments, and an additive to latex paint to provide freeze-thaw stability (Luster *et al*., 2002, Verevkin *et al*., 2007).

*Corresponding Author: grc22@pu.ac.in
MS Received: November 6, 2019, Accepted: December 19, 2019

It is also used to create artificial smoke or fog used in fire-fighting training and in theatrical productions. 1,5-PTD (Quan *et al*., 2004) shows activity against virus, bacteria, and fungi. It is also effective against dermatitis and is also used as preservative for shampoo and hand creams.

A perusal of the literature shows that the behavior of aqueous solution alkanediols has been extensively studied through the measurements of various thermophysical properties, while the studies on alkanediols in non-aqueous media, particularly in amides are scarce. The alkanediols, in particular, are interesting because their structures result in different isomers with (i) a possibility of change in the relative –OH positions along the alkyl chain and (ii) the presence of terminal hydrophobic alkyl units. Therefore, information about physicochemical properties of alkanediols in non-aqueous solvents (amides) is therefore necessary for understanding of the system itself.

Amides are very interesting compounds as they possess donor-acceptor -CONH- peptide bond which displays the property of self-association by the H-bond. In particular, cyclic amides (lactams) offer great interest because they are related to structural problems in molecular biology. Cyclic amides in general are high density, high boiling point, and high polarity solvents. They are completely miscible over the entire composition range with water. The cyclic amides (lactams) are very interesting compounds as they have carbon and nitrogen of a peptide bond linked by a ring composed of methylene groups. Owing to its donor-acceptor properties, it can interact with other amide molecules via hydrogen bond. In this way, lactam provides small molecular models for the amide group in peptides, polypeptides and protiens. Self–association (Walmsley *et al*., 1976) of lactams also serves as a base in nucleic amides. Of particular interest is the compound γ-butyrolactam (n = 5), pyrrolidin-2-one (PY), which is a highly polar, non-aqueous solvent.

The general aim has been to use the composition dependence of the excess quantities as a means of understanding the nature of the molecular scale processes within the mixtures of alkanediols in non-aqueous media and the effect of addition of additive on such mixtures. The major emphases have been given to produce thermodynamic and related data of mixtures of alkanediols and amides in order to gain insight into the structural and interactional behavior of these mixtures. The effects of addition of β-cyclodextrin on the behavior of alkanediol-amide liquid mixtures have also been investigated in detail.

Cyclomalto-oligosaccharides (cyclodextrin, CDs) are cyclic oligosaccharides containing from 6 to 12 α-(1,4)-linked glycopyranose units. CDs can interact, in solution with various organic compounds to form inclusion compounds that have technological, pharmaceutical, and biological applications (Schonbeck *et al*. 2019.). They have a toroidal or hollow, truncated cone shape with a nonpolar, hydrophobic inside and two hydrophilic rims, formed by the primary (narrower rim) and secondary (wider rim) –OH groups (figure 1) (He etal.,2019).

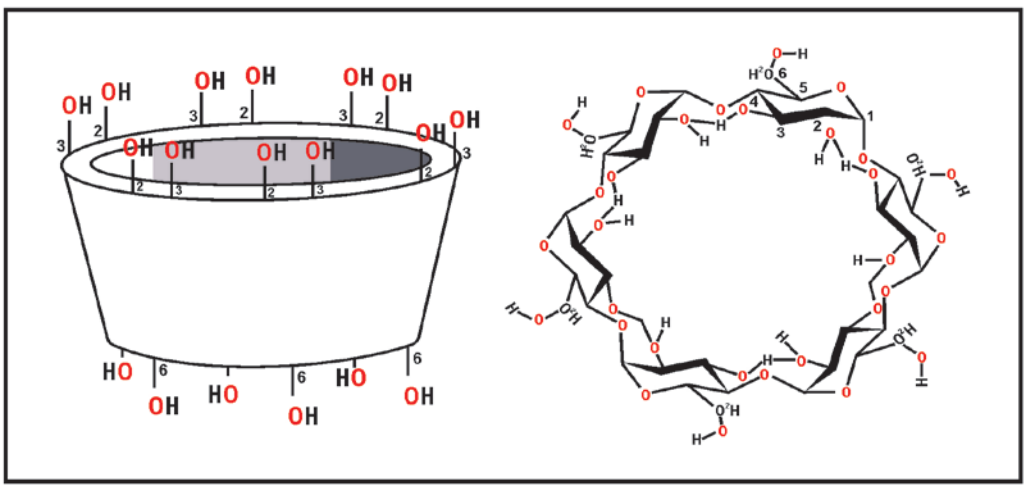

Figure1: Structure of Cyclodextrin (CD).

The most common CD is *β*-cyclodextrin (*β*-CD) containing glycopyranose units. The shape of *β*-CD is often described as a truncated hollow cone. *β*-CD forms stable inclusion complexes with a wide variety of inorganic and organic guest molecules in aqueous solution, (Han *et al*., 2018) a property that makes them important in applied areas, such as analytical and pharmaceutical chemistry (Li *et al*., 1992). CDs can be used to advantage in the production of pharmaceuticals, pesticides, foodstuffs, and toilet

articles, the (micro-encapsulated) active and aromatic substances enclosed within them are protected from the effects of light and atmosphere and can be easily handled and stored in powder form. Substances, which are not very soluble in water, become more soluble in the presence of CDs, creams and emulsions can be stabilized, and the growth and yield of grain harvests can be increased.

The main aim of the present work is to measure new data and obtain information about structural and interactional studies for the effect on thermophysical and spectroscopic properties in the presence of β-cyclodextrin in the mixtures of α, ω-alkanediols + amides. The results have been compared with aqueous based systems of diols and analyzed.

MATERIALS AND PROCEDURE

Materials: The chemicals used in the present work are listed in Table 1 along with their sources and grades. All the alkanediols used in this experiment are stored using molecular sieves to adsorb any trace amounts of water present. The Molar masses (M), boiling points (T_b), melting points (T_m), experimental densities ($\rho^{expt.}$), literature densities ($\rho^{lit.}$), critical temperatures (T_c), critical pressures (P_c), critical volumes (V_c), refractive indices (n_D), vapour pressures (P), ultrasonic velocities (u), isobaric thermal expansivities (α_p) and molar isobaric heat capacities (C_p) for the pure substances at 308.15 K have been summarized in Table 2.

Table 1: Sources and grades of chemicals.

Chemicals	Sources	Grades
1,2-Ethanediol	Fluka AG (Buchs)	purum > 99.5% (GC)
1,3-Propanediol	Fluka AG (Buchs)	purum > 99.0% (GC)
1,4- Butanediol	Merck (India)	purum > 99.0% (GC)
1,5-Pentanediol	Fluka AG (Buchs)	purum > 96.0% (GC)
Pyrrolidin-2-one	Fluka AG (Buchs)	purum > 99.0% (GC)
β -Cyclodextrin	Fluka AG (Buchs)	purum > 99.0% (HPLC)

Methods: The clear solutions of of binary mixtures of (α, ω-alkanediols + pyrrolidin-2-one) in presence of cyclodextrin were made afresh by weighing the components using a Mettler Toledo balance with an accuracy of $\pm 1.10^{-4}$ g. The temperature dependent thermophysical parameters, i.e., density ρ and ultrasonic sound velocity u, measurements of binary mixtures of α, ω-alkanediols + pyrrolidin-2-one over various composition range were carried out using Anton Paar DSA 5000 densimeter and ultrasonic sound velocity analyzer. The desired temperature has been controlled by in-built thermostat with precision better than $\pm 1 \times 10^{-3}$ K. The repeatability in digits for density and ultrasonic sound velocity measurements were $g.cm^{-3}$ and $m.s^{-1}$, respectively. The ambiguities in density and ultrasonic sound velocity measurements are presumed to be less than $g.cm^{-3}$ and $m.s^{-1}$, respectively.

Refractive index (n_D) measurements have been carried out using an Abbemat 500 Automatic refractometer with precision of $\pm 2 \times 10^{-5}$ and resolution of 1×10^{-6}. Refractometer was calibrated by measuring n_D values of high purity distilled water. A bubble-free sample was introduced in refractometer and measured using temperature controlled in-built thermostat with resolution 0.01 K and precision of 0.03 K. Viscosity measurements are made using a modified form of a Ubbelohde viscometer placed in a water thermostat, the temperature of which is controlled to 308.15±0.01K.

MEASUREMENTS OF SPECTROSCOPIC PARAMETERS

FT-NMR Spectroscopy: ^{1}H and ^{13}C NMR spectra have been recorded using a JEOL AL FT NMR spectrometer operating at 300 MHz. The chemical shift, δ for all the pure liquids and liquid mixtures have been observed in the presence of $CDCl_3$ used as an external solvent.

FT-IR Spectroscopy: Perkin Elmer (RX1) FT-IR spectrometer in the frequency range (4400-350) cm^{-1} is used to record the FT-IR spectra. AgCl plates are used to determine the wave number, ν for all the pure liquids and liquid mixtures for all the FT-IR measurements.

Table 2: Molar masses (M), boiling points (T_b), melting points (T_m), experimental densities ($\rho^{expt.}$), literature densities (ρ^{lit}), critical temperatures (T_c), critical pressures (P_c), critical volumes (V_c), refractive indices (n_D), vapour pressures (P), ultrasonic velocities (u), isobaric thermal expansivities (α_p) and molar isobaric heat capacities (C_p) for the pure substances at 308.15 *K*.

Component	M (g mol^{-1})	T_b (K)	T_m (K)	$\rho^{expt.}$ (kg m^3)	ρ^{lit} (kg m^3)	T_c (K)	P_c (MPa)	V_c (10^3 m^{3}mol^{-1})	n_D -	P (MPa)	u (ms^{-1})	α_p (10^4 K^{-1})	C_p (JK^{-1}mol^{-1})
1,2-ED	62.0	470.4	260.5	1102.9	1102.5[a]	630.9	75.95	47.60	1.431[a,f]	0.01[g]	1633.36	6.7[g]	149.7[e,f]
1,3-PPD	76.1	487.6	246.4	1042.7	1043.7[b]	639.90	59.49	61.42	1.438[b,f]	1.30[g]	1604.47	7.0[g]	176.4[e,f]
1,5-PTD	104.1	515.6	515.6	974.3	974.3[c]	649.37	41.46	83.46	1.448[f]	1.33[g]	1566.12	11.2[g]	233.2[e,f]
Pyrrolidin-2-one	85.1	518.0	298.0	1097.1	1099.1[d]	568.55	55.40	62.07	1.484[f]	1.30[g]	1599.97	-	169.4[f]

[a] Tasheirkezos (1989)
[b] George (2003)
[c] Riddick (1986)
[d] Houyelos (1996)
[e] Piekarski (2005)
[f] At 298.15K
[g] derived from density [(Riddick(1986), George (2003), Tasheirkezos (1989)]

RESULTS AND DISCUSSION

Excess molar volume (V^E), ultrasonic speed (u) and viscosity (η) data have been determined and tabulated in Table 3, 4 and 5, respectively, for (α,ω-alkanediols in β-cyclodextrin + pyrrolidin-2-one).

The V^E values are graphically presented in Figure 2. The V^E values are positive for all the mixtures except for 1,5-PTD + (β-CD + PY), for which it shows S-shaped behavior. Variation in V^E with successive addition of methylene group in these systems show a decreasing pattern as: 1,2-ED > 1,3-PPD > 1,5-PTD. This may be due to the fact that with increase in hydrophobicity, the possibility of fitting of diols in the hydrophobic cavity of β-CD increases. Data have been fitted in following equation:

$$Y^E = X(1 - X)\sum_i A_i(2X - 1) \quad (1)$$

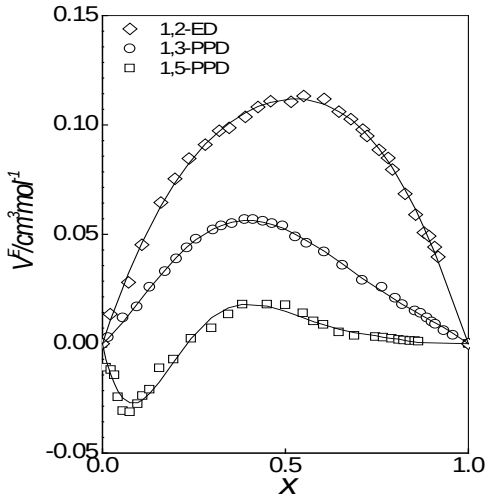

Figure 2: Excess molar volume V^E values for X α,ω-alkanediols + (*1-X*) (β-CD + PY).

Table 3: Excess molar volume (V^E) values for X α,ω-alkanediols + (*1-X*) (β-CD + PY) at 308.15 *K*.

X	V^E ($cm^3.mol^{-1}$)	X	V^E ($cm^3.mol^{-1}$)	X	V^E ($cm^3.mol^{-1}$)
1,2-ED		1,3-PPD		1,5-PTD	
0.0220	0.014	0.0160	0.003	0.0104	-0.011
0.0715	0.028	0.0551	0.012	0.0227	-0.012
0.1079	0.045	0.0938	0.017	0.0319	-0.014
0.1593	0.065	0.1289	0.026	0.0419	-0.024
0.1979	0.075	0.1707	0.033	0.0555	-0.031
0.2361	0.085	0.2027	0.039	0.0751	-0.031
0.2815	0.091	0.2314	0.044	0.0956	-0.027
0.3185	0.097	0.2564	0.048	0.1097	-0.024
0.3456	0.099	0.3021	0.052	0.1290	-0.021
0.3895	0.104	0.3245	0.054	0.1562	-0.011
0.4247	0.108	0.3546	0.055	0.1944	-0.007
0.4589	0.111	0.3887	0.057	0.2429	0.003
0.5146	0.111	0.4110	0.057	0.2979	0.007
0.5498	0.113	0.4385	0.056	0.3442	0.013
0.6065	0.112	0.4641	0.055	0.3825	0.018
0.6468	0.106	0.4924	0.054	0.4501	0.018
0.6780	0.103	0.5270	0.049	0.4996	0.018
0.7111	0.098	0.5585	0.046	0.5487	0.014
0.7236	0.095	0.6052	0.042	0.5771	0.010
0.7559	0.088	0.6551	0.036	0.6030	0.009
0.7806	0.085	0.7099	0.029	0.6458	0.005
0.7924	0.080	0.7632	0.026	0.6890	0.004
0.8275	0.068	0.7999	0.021	0.7457	0.003
0.8556	0.059	0.8201	0.018	0.7681	0.003
0.8788	0.051	0.8544	0.015	0.7897	0.002
0.8929	0.049	0.8700	0.014	0.8094	0.002
0.9076	0.044	0.8864	0.012	0.8240	0.002
0.9181	0.040	0.8996	0.010	0.8396	0.001

Table 4: Ultrasonic speeds (u) values for X α,ω-alkanediols + (1-X) (β-CD + PY) at 308.15 K.

X	u (m.s^{-1})	X	u (m.s^{-1})	X	u (m.s^{-1})
1,2-ED		1,3-PPD		1,5-PTD	
0	1608.45	0	1608.45	0	1608.45
0.0293	1608.89	0.0249	1608.5	0.0551	1598.61
0.0529	1609.33	0.062	1608.59	0.1259	1593.6
0.1171	1609.91	0.1059	1608.71	0.2136	1589.39
0.2149	1610.79	0.2004	1608.89	0.3048	1586.19
0.3220	1611.51	0.3152	1609.07	0.4162	1582.98
0.4040	1612.39	0.4165	1609.18	0.5006	1580.78
0.4986	1613.41	0.5076	1609.22	0.6154	1577.77
0.5965	1615.01	0.5988	1609.18	0.6998	1575.98
0.6943	1617.05	0.7203	1608.92	0.8078	1572.97
0.8024	1620.11	0.8115	1608.41	0.9192	1569.77
0.9036	1624.62	0.8925	1607.45	0.9732	1567.56
0.9576	1628.41	0.9431	1606.37		

Table 5: Viscosity (η) values for X α,ω-alkanediols + (1-X) (β-CD + PY) at 308.15 K.

X	η ($mPa\ s$)	X	η ($mPa\ s$)	X	η ($mPa\ s$)
1,2-ED		1,3-PPD		1,5-PTD	
0	9.756	0	9.756	0	9.756
0.0293	9.812	0.0249	9.938	0.0551	11.955
0.0529	9.855	0.0620	10.448	0.1259	14.322
0.1171	9.957	0.1059	11.031	0.2136	17.635
0.2149	10.074	0.2004	12.342	0.3048	21.186
0.3220	10.190	0.3152	14.235	0.4162	25.920
0.4040	10.263	0.4165	15.983	0.5006	29.234
0.4986	10.351	0.5076	17.585	0.6154	34.678
0.5965	10.452	0.5988	19.188	0.6998	39.175
0.6943	10.569	0.7203	21.373	0.8078	46.129
0.8024	10.744	0.8115	23.048	0.9192	55.412
0.9036	10.962	0.8925	24.577	0.9732	60.894
0.9576	11.152	0.9431	25.451		

Where Y_E is excess molar volume. The standard deviation of the fit and the values of the coefficients A_i for each system are included in Table 6.The effect of β-CD in (α,ω values of alkanediols + PY) mixtures has been analyzed by comparing excess molar volume V^E of α,ω-alkanediols + (β-CD + PY) with (α,ω-alkanediols + PY) (Figure 3) (Mehta *et al*., 2008). It has been found that the addition of β-CD in the successive addition of the -CH_2 group in the series of α,ω-alkanediols in PY affected differently. In 1,2-ED system, there negligible change in V^E value. However, on addition of β-CD, the volumetric behavior of 1,3-PPD and 1,5-PTD systems are significantly different from their parent systems. Volume loss for 1,5-PTD in (β-CD + PY), particularly at lower diol concentration region, infers that 1,5-PTD is fitting in the hydrophobic cavity of β-CD resulting in formation of inclusion complex (Scheme 1) in a way that V^E is drastically affected. Whereas, the dispersion forces are more prevalent on addition of β-CD in 1,3-PPD + PY system (Chaudhary *et al*., 2013).

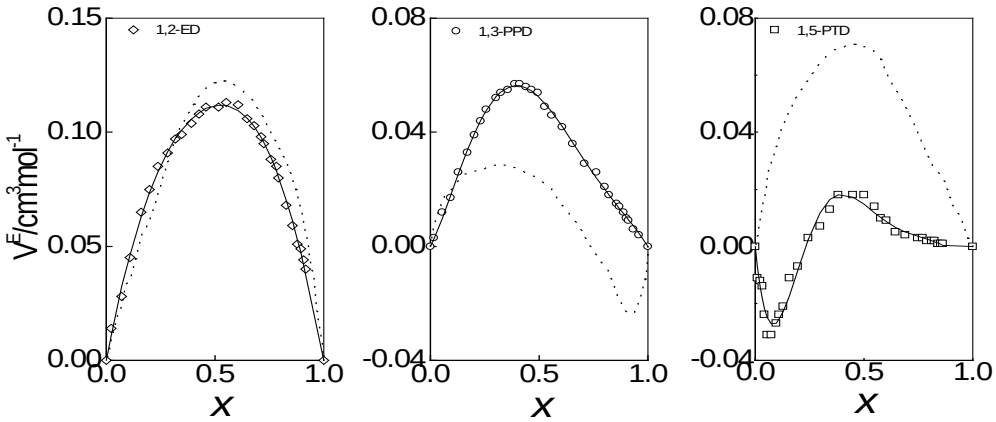

Figure 3: Comparison of excess molar volumes for *X* α,ω-alkanediols + (*1-X*) (*β*-CD + PY).

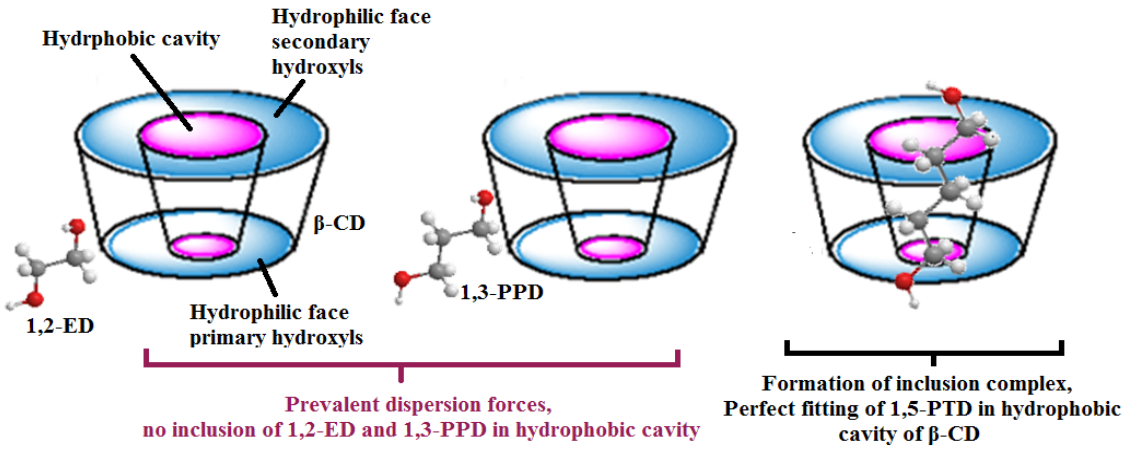

Scheme 1: Possible interaction of α,ω-alkanediols with *β*-CD.

The ultrasonic speeds *u* (m.s^{-1}) for the α,ω-alkanediols in (*β*-CD + PY) have been graphically depicted in Figure 4. *u* values show increase over entire composition range with the addition of diol for 1, 2-ED in (*β*-CD + PY), similar to 1,2-ED + PY system. *u* values for 1, 3-PPD in (*β*-CD + PY) are nearly constant in the lower diol region and at higher diol concentration show decrease. For 1, 5-PTD in (*β*-CD + PY), *u* values decrease with the addition of diols over the whole composition range. The hydrophilicity order for α,ω-alkanediols follows order: 1,2-ED > 1,3-PPD> 1,5-PTD. With increase in diol concentration, 1,2-ED with close vicinity of OH groups packs better due to greater hydrophilicity and provide a medium for sound wave to travel fast as compared to 1,3-PPD and 1,5-PPD. The deviations in isentropic compressibilities ΔK_S were also calculated by using following equations:

$$K_s = -V^{-1}\left(\frac{\partial V}{\partial P}\right)S = (\rho u^2)^{-1} = \frac{[\sum x_i V_i + V^E]}{(u^2 \sum x_i K_{s,i})} = \frac{V}{Mu^2} \qquad (2)$$

$$\Delta K_s = K_s - \sum_i X_i k_{s,i} \qquad (3)$$

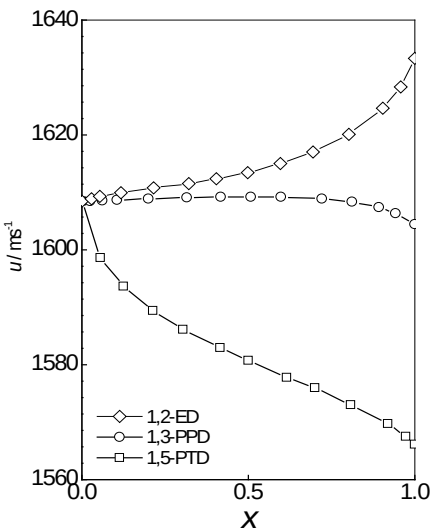

Figure 4: Ultrasonic speeds *u* values for *X* $\alpha,\omega-$alkanediols + (*1-X*) (β -CD + PY).

Figure 5 shows the variation of ΔK_S for the mixtures of α,ω-alkanediols with (β-CD + PY). The ΔK_S values are positive for 1,2-ED system and may be due to breaking of self-associated 1,2-ED molecules in the mixture. ΔK_S values are negative for 1,3-PPD over the entire composition range. However, it shows both positive and negative behavior for 1,5-PTD system. Equation (1) was again utilized for fitting of ΔK_S data. The coefficients and the standard errors are also included in Table 6. The partial molar excess volumes V_i^E and partial deviation in isentropic compressibility $\Delta K_{S,i}$ were calculated from following equations:

$$V_i^E = V^E + (1 - X_i)(\frac{\partial V^E}{\partial x_i}) \quad (4)$$

$$\Delta K_{s,i} = \Delta k_s + (1 - X_i)(\frac{\partial k_s}{\partial x_i}) \quad (5)$$

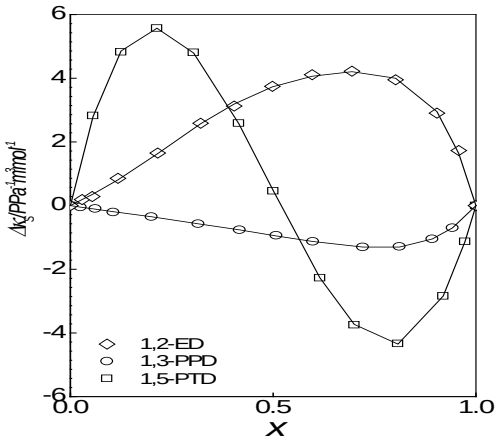

Figure 5: Deviation in isentropic compressibility values ΔK_S for *X* α,ω-alkanediols + (*1-X*) (β-CD + PY).

Table 6: Least-square coefficients of equation (1) and standard deviation σ of *X* α,ω-alkanediols + (*1-X*) (CD + PY).

(β-CD+PY)		A_0	A_1	A_2	A_3	A_4	σ	X^E (x=0.5)
1,2-ED	$V^E / cm^3 \cdot mol^{-1}$	0.447	0.036	0.099	-0.039	-0.051	0.002	0.111
	$\Delta\kappa_{S,i} / PPa^{-1} \cdot m^3 \cdot mol^{-1}$	14.95	9.02	3.19	11.14	8.57	0.06	3.70
	$\Delta\eta / mPa \cdot s$	-0.691	-1.195	-0.216	-0.874	-0.726	0.005	-0.175
	$g(x) / J \cdot mol^{-1}$	-25	-267	-29	-198	-160	1	-10
	$\delta^E / 10^{-6}$ ($^1H - OH$)	0.195	0.040	-0.041	-0.193	0.098	0.002	0.049
	$\delta^E / 10^{-6}$ ($^1H - NH$)	-0.109	-0.094	0.092	-0.135	-0.040	0.002	-0.027
	$\delta^E / 10^{-6}$ ($^{13}C - CO$)	0.734	0.195	0.091	-0.805	0.540	0.007	0.182
1,3-PPD	$V^E / cm^3 \cdot mol^{-1}$	0.209	-0.147	-0.064	0.133	-0.014	0.001	0.051
	$\Delta\kappa_{S,i} / PPa^{-1} \cdot m^3 \cdot mol^{-1}$	-3.72	-3.98	-3.55	-2.81	-1.56	0.01	-0.92
	$\Delta\eta / mPa \cdot s$	5.535	3.150	-1.673	1.886	1.273	0.035	1.373
	$g(x) / J \cdot mol^{-1}$	870	56	-333	435	-30	8	215
	$\delta^E / 10^{-6}$ ($^1H - OH$)	-0.066	0.009	-0.010	0.082	-0.016	0.002	-0.017
	$\delta^E / 10^{-6}$ ($^1H - NH$)	0.139	-0.067	0.030	0.020	0.002	0.001	0.035
	$\delta^E / 10^{-6}$ ($^{13}C - CO$)	0.820	-0.217	-0.384	-0.457	1.117	0.010	0.204
1,5-PTD	$V^E / cm^3 \cdot mol^{-1}$	0.059	-0.117	-0.050	0.462	-0.438	0.003	0.015
	$\Delta\kappa_{S,i} / PPa^{-1} \cdot m^3 \cdot mol^{-1}$	1.94	-50.82	4.45	-2.60	1.66	0.02	0.46
	$\Delta\eta / mPa \cdot s$	17.43	-6.062	-11.208	-2.469	5.922	0.113	4.349
	$g(x) / J \cdot mol^{-1}$	1799	-5130	-168	-579	1859	18	447
	$\delta^E / 10^{-6}$ ($^1H - OH$)	-0.327	0.254	0.202	-0.050	-0.182	0.002	-0.082
	$\delta^E / 10^{-6}$ ($^1H - NH$)	0.353	-0.083	-0.199	0.143	0.224	0.001	0.087
	$\delta^E / 10^{-6}$ ($^{13}C - CO$)	0.795	-0.658	-0.001	-0.525	1.087	0.008	0.190

The variation of V_i^E and $\Delta K_{S,i}$ as a function of mole fraction of diol is shown graphically in Figure 6 and 7.In the dilute solvent region, both V_i^E and $\Delta K_{S,i}$ show a significant increase from a negative value for 1,5-PTD to a positive value of 1,2-ED. Negative values of partial molar quantities in the case of 1,5-PTD may be taken as a sign of fitting of 1,5-PTD molecule in the hydrophobic cavity of *β*-CD (as the 1,5-PTD has longest methylene chain among all measured diols). The estimated values of V_i^E and $\Delta K_{S,i}$ at infinite dilution are listed in Table7.

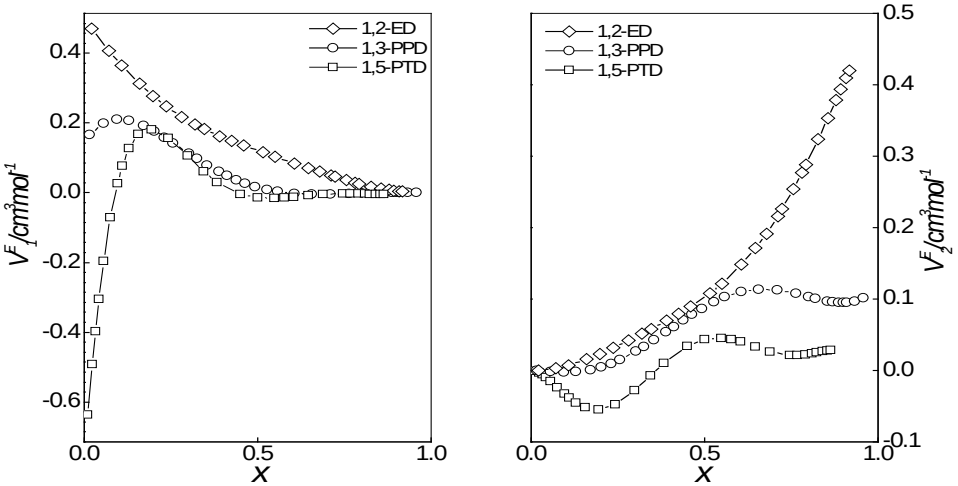

Figure 6: Partial molar excess volumes V_1^E and V_2^E *for X α,ω-* alkanediols + (*1- X*) (*β*-CD + PY)

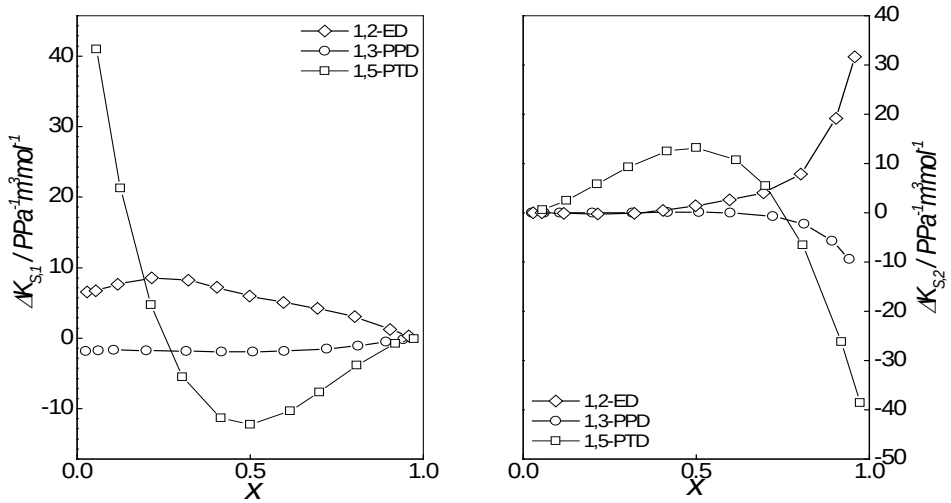

Figure 7: Partial deviation in isentropic compressibility K_1^E and K_2^E *for X α,ω-* alkanediols + (*1- X*) (*β*-CD + PY)

Table 7: Excess partial molar volumes $V_i^{E,\infty}$ and excess partial molar isentropic compressibilities $K_{s,i}^{E,\infty}$ of *X α,ω-* alkanediols + (*1-X)* PY at infinite dilution at 308.15 *K*.

PY	$V_1^{E,\infty}$ ($cm^3\,mol^{-1}$)	$V_2^{E,\infty}$ ($cm^3\,mol^{-1}$)	$\Delta\kappa_{S,1}^{\infty}$ ($PPa^{-1}\,m^3\,mol^{-1}$)	$\Delta\kappa_{S,2}^{\infty}$ ($PPa^{-1}\,m^3\,mol^{-1}$)
1,2-ED	0.538	0.550	6.19	42.25
1,3-PPD	0.145	0.108	1.96	-13.74
1,5-PTD	-0.690	0.055	55.92	-45.66

From Table 7, it can be seen that $V_i^{E,\infty}$ and $K_{s,i}^{E,\infty}$ values are more negative for 1,5-PTD in comparison to other isomers indicating that hydrogen bonding and affinity of fitting between 1,5-PTD and β-CD +PY are greater than the other isomers. However for 1,3-PPD and 1,2-ED systems dispersion forces due to dissociation of self-associated PY and diols are predominant. The viscosity η (*mPa.s*) for the mixtures of α,ω-alkanediols in (β-CD + PY) has plotted in Figure 8. Viscosity deviation $\Delta\eta$ {calculated using the equation (6)} are shown in Figure 8. The viscosity η ((*mPa.s*)) for the mixtures of α,ω-alkanediols in (β-CD + PY) has plotted in Figure 7. Viscosity deviation $\Delta\eta$ are calculated using following equation and the variation has been shown in Figure 7.

$$\Delta\eta = \eta - \exp(\sum X_i \ln \eta_i^*) \qquad (6)$$

With the successive addition of methylene group, an increase in $\Delta\eta$ values is observed in the order as 1,2-ED < 1,3-PPD < 1,5-PTD. $\Delta\eta$ values are positive for the mixtures of 1,5-PTD and 1,3-PPD with β-CD + PY over the entire composition range. Whereas, $\Delta\eta$ values are negative throughout the composition range for 1,2-ED + (β-CD + PY). The results obtained from viscosity measurement are in good agreement with the measured V^E values. The negative $\Delta\eta$ values increases in the order 1, 2-ED < 1, 3-PPD < 1, 5-PTD. Large negative $\Delta\eta$ values for 1,2-ED and 1,3-PPD systems show that dispersion forces are predominant because of dissociation of PY dimer/trimer and diols. Positive $\Delta\eta$ values may be ascribed to an increase in specific interactions and to a decrease in dispersion forces.

A comparative analysis of $\Delta\eta$ values of α,ω-alkanediols + (β-CD + PY) with its parent system i.e. α,ω-alkanediols + PY (Mehta *et al.*, 2008) depicts (Figure 9) that viscosity behavior is significantly different for 1,5-PTD, which on addition of β-CD shows a transition in Δη values from large negative values to large positive values. This can be explained on the basis of fitting of 1,5-PTD in the hydrophobic cavity of β-CD (as the 1,5-PTD has longest methylene chain among all measured diols). The possibility of fitting decreases from 1,5-PTD to 1,2-ED.

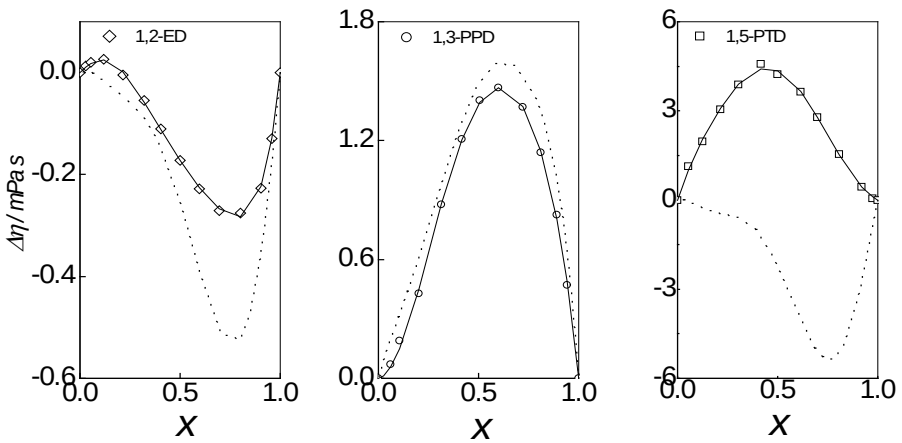

Figure 8: Viscosity η and viscosity deviation $\Delta\eta$ for *X* α,ω-alkanediols + (*1- X*) (β-CD + PY).

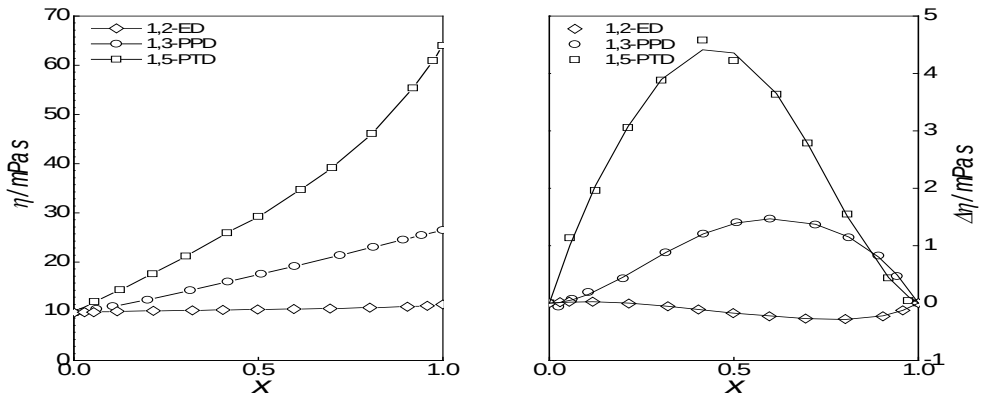

Figure 9: Comparison of viscosity deviation $\Delta\eta$ for *X* α,ω-alkanediols + (*1- X*) (β-CD + PY).

Deviations in Gibbs energies of activation for viscous flow g(x) values were also obtained using the following equation:

$$g(x) = RT[ln\,\eta V - \left(\sum X_i \ln\,\eta_i^* V_i^*\right)] \quad (7)$$

Figure 10 depicts the graphical representation of g(x) values and its values decrease from 1,3-PPD + PY to 1,5-PTD. The g(x) values are negative for 1,2-ED, positive for 1,3-PTD and both negative and positive for 1,5PTD. By comparing g(x) values of α,ω-alkanediols + (*β*-CD + PY) with α,ω-alkanediols + PY, it has been found that the addition of *β*-CD in 1,5-PTD + PY, particularly at lower diol concentration region, shows increase in g(x) values from large negative values to large positive values.

The positive g(x) values 1,5-PTD in β-CD + PY, infer that 1,5-PTD is fitting in the hydrophobic cavity of *β*-CD at the lower diol mole fraction region. Both $\Delta\eta$ and g(x) values were fitted to the equation (1) and parameters are listed in Table 6. IR data of α,ω-alkanediols + (*β*-CD + PY) show that shift in wave number ν appears for hydroxyl groups of α,ω-alkanediols and >CO group of PY, indicating that the interactions are taking place through both –OH and >CO groups. The wave number ν values at maximum absorbance of –OH and >CO stretching frequencies for mixtures of diols in PY are listed in Table 8 and 9.

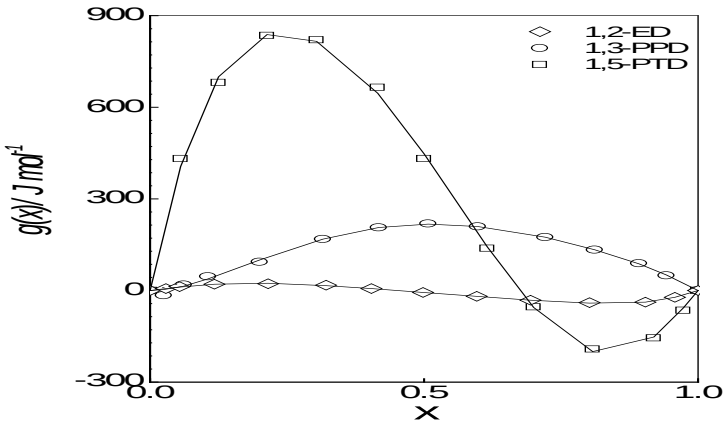

Figure 10: Deviation in Gibbs free energies of activation for viscous flow g(x) for *X* α,ω-alkanediols + (*1- X*) (*β*-CD + PY).

Table 8: Wave number ν values at maximum absorbance of –OH groups for *X* α,ω-alkanediols + (*1- X*) (*β*-CD + PY).

X	*v* (cm^{-1})	*X*	*v* (cm^{-1})	*X*	*v* (cm^{-1})
1,2-ED		1,3-PPD		1,5-PTD	
0.0293	3252.3	0.0249	3355.1	0.0551	3245.0
0.0529	3256.7	0.0620	3266.3	0.1259	3254.7
0.1171	3263.4	0.1059	3377.0	0.2136	3260.8
0.2149	3275.1	0.2004	3365.9	0.3048	3278.1
0.3220	3288.3	0.3152	3374.1	0.4162	3297.0
0.4040	3310.0	0.4165	3379.2	0.5006	3324.8
0.4986	3329.8	0.5076	3358.0	0.6154	3326.6
0.5965	3338.1	0.5988	3341.7	0.6998	3335.0
0.6943	3341.4	0.7203	3345.6	0.8078	3332.9
0.8024	3339.0	0.8115	3353.1	0.9192	3338.1
0.9036	3343.1	0.8925	3371.2	0.9732	3338.2
0.9576	3344.5	0.9431	3389.1	1.0000	3338.1
1.0000	3350.9	1.0000	3391.0		

Table 9: Wave number ν values at maximum absorbance of >CO groups for *X* α,ω-alkanediols + (*1- X*) (*β*-CD + PY).

X	ν (cm^{-1})	X	ν (cm^{-1})	X	ν (cm^{-1})
1,2-ED		1,3-PPD		1,5-PTD	
0.0293	1697.1	0.0249	1677.0	0.0551	1693.0
0.0529	1693.1	0.0620	1676.1	0.1259	1691.5
0.1171	1692.1	0.1059	1673.8	0.2136	1688.1
0.2149	1687.1	0.2004	1675.5	0.3048	1689.8
0.3220	1683.0	0.3152	1673.1	0.4162	1687.7
0.4040	1679.8	0.4165	1669.0	0.5006	1688.0
0.4986	1676.5	0.5076	1667.8	0.6154	1687.3
0.5965	1673.8	0.5988	1668.5	0.6998	1690.1
0.6943	1673.0	0.7203	1666.2	0.8078	1684.4
0.8024	1672.4	0.8115	1667.0	0.9192	1684.5
0.9036	1671.5	0.8925	1667.4	0.9732	1684.0
0.9576	1669.1	0.9431	1666.5		

The ^{1}H and ^{13}C NMR chemical shifts, δ for the mixtures of α,ω-alkanediols in (*β*-CD + PY) shows that there is an appreciable change in

Δ values for –OH protons of diols, –NH proton of PY and >CO carbon of PY as a function of mole fraction of diol. However, not much change in δ values is seen for $–CH_n$ proton and carbon of PY and diols. The NMR chemical shift, δdata of ^{1}H and ^{13}C NMR are tabulated in Table 10 and 11 respectively.

Excess NMR chemical shift, δ^E has also been estimated from the following equation:

$$\delta^E = \delta - X_1\delta_1 - X_2\delta_2^{\infty} \qquad (8)$$

values were fitted to the equation (1). The values of coefficient A_i and the standard deviation are tabulated in Table 6.

Table 10: ^{1}H NMR chemical shift δ (10^{-6}) values for *X* α,ω-alkanediols + (*1-X*) (*β*-CD + PY).

X	δ (10^{-6})		*X*	δ (10^{-6})		*X*	δ (10^{-6})	
1,2-ED			1,3-PPD			1,5-PTD		
	-NH	-OH		-NH	-OH		-NH	-OH
0.0293	8.057	5.246	0.0249	8.058	5.011	0.0551	8.059	5.032
0.0529	8.052	5.254	0.0620	8.056	5.025	0.1259	8.057	5.037
0.1171	8.035	5.272	0.1059	8.054	5.040	0.2136	8.054	5.051
0.2149	8.003	5.296	0.2004	8.041	5.075	0.3048	8.044	5.073
0.3220	7.964	5.320	0.3152	8.020	5.119	0.4162	8.028	5.113
0.4040	7.937	5.336	0.4165	7.998	5.160	0.5006	8.001	5.152
0.4986	7.904	5.352	0.5076	7.974	5.198	0.6154	7.959	5.223
0.5965	7.876	5.368	0.5988	7.948	5.237	0.6998	7.920	5.271
0.6943	7.853	5.377	0.7203	7.911	5.288	0.8078	7.871	5.337
0.8024	7.827	5.378	0.8115	7.887	5.330	0.9192	7.818	5.397
0.9036	7.813	5.379	0.8925	7.859	5.368	0.9732	7.789	5.421
0.9576	7.801	5.379	0.9431	7.842	5.390			

Table 11: ^{13}C NMR chemical shift δ (10^{-6}) values for α,ω-alkanediols + (*1-X*) (*β*-CD + PY).

X	δ (10^{-6})	*X*	δ (10^{-6})	*X*	δ (10^{-6})
1,2-ED		1,3-PPD		1,5-PTD	
0.0293	179.117	0.0249	179.097	0.0551	179.196
0.0529	179.209	0.0620	179.205	0.1259	179.342
0.1171	179.362	0.1059	179.281	0.2136	179.447
0.2149	179.581	0.2004	179.445	0.3048	179.546
0.3220	179.816	0.3152	179.635	0.4162	179.655
0.4040	179.991	0.4165	179.779	0.5006	179.702
0.4986	180.185	0.5076	179.897	0.6154	179.768
0.5965	180.383	0.5988	180.002	0.6998	179.821
0.6943	180.562	0.7203	180.101	0.8078	179.892
0.8024	180.738	0.8115	180.205	0.9192	179.968
0.9036	180.875	0.8925	180.277	0.9732	180.001
0.9576	180.947	0.9431	180.303		

Chemical Shift of –OH groups

The δ values of hydroxyl protons are shown graphically as a function of mole fraction of diol in Figure 11. The δ values of hydroxyl protons show up field shift with the addition of 1,2-ED in *β*-CD + PY. This can be due to the dissociation of the self-associated 1,2-ED in the mixture of 1,2-ED in (*β*-CD + PY). The downfield shift in δ values for 1,3-PPD and 1,5-PTD indicate the formation of hydrogen bonding by OH group (C=O···H-O) of 1,5-PTD in (*β*-CD + PY) mixtures. The δ_i^{∞} values for hydroxyl protons are listed in Table 12. Excess values δ^E are graphically presented in Figure 12. It varies in order 1,5-PTD < 1,3-PTD < 1,2-ED.

The variation of ^{1}H NMR chemical shifts δ of –NH proton against mole fraction is presented in Figure 13. Δ values show the up field shift with the addition of diol in *β*-CD + PY. This shielding of -NH proton over whole composition range indicates the dissociation of self-associated PY dimmer. The δ_i^{∞} values for –NH proton are tabulated in Table 12a. The δ^E values are graphically depicted in Figure 14. The change in chemical shift, δ^E, vary as 1,2-ED < 1,3-PPD < 1,5-PTD.

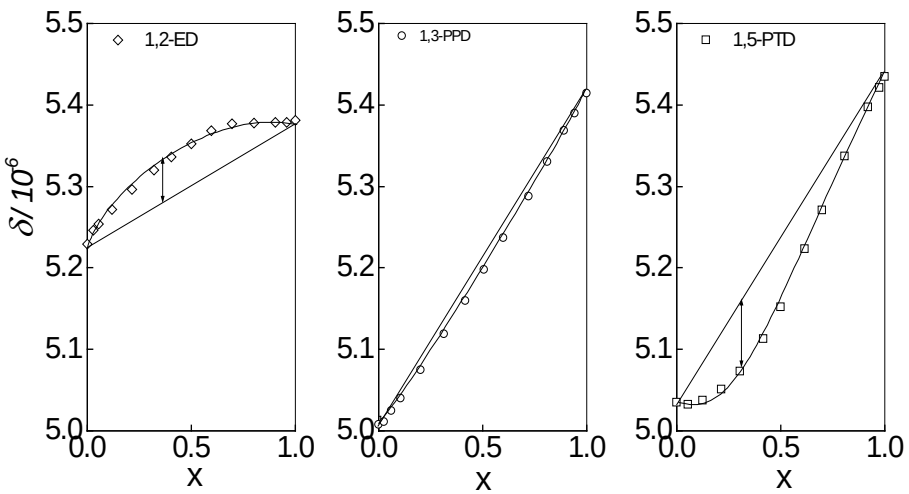

Figure 11: ^{1}H NMR shifts δ for hydroxyl protons *for X* α,ω-alkanediols + (*1- X*) (*β*-CD + PY).

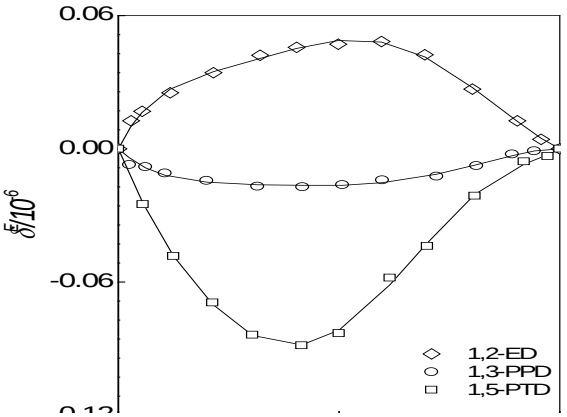

Figure 12: [1]H NMR excess chemical shifts δ^E for hydroxyl protons *for X* α,ω-alkanediols + (*1- X*)(*β*-CD + PY)

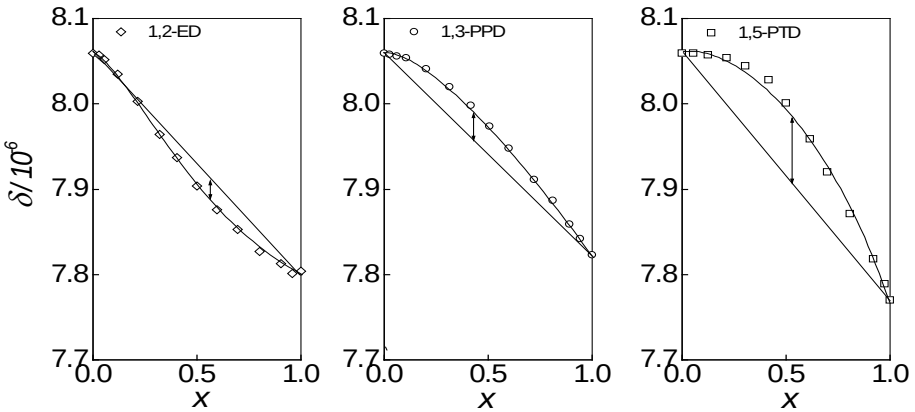

Figure 13: [1]H NMR shifts δ for hydroxyl protons for *X* α,ω-alkanediols + (*1- X*) (*β*-CD + PY)

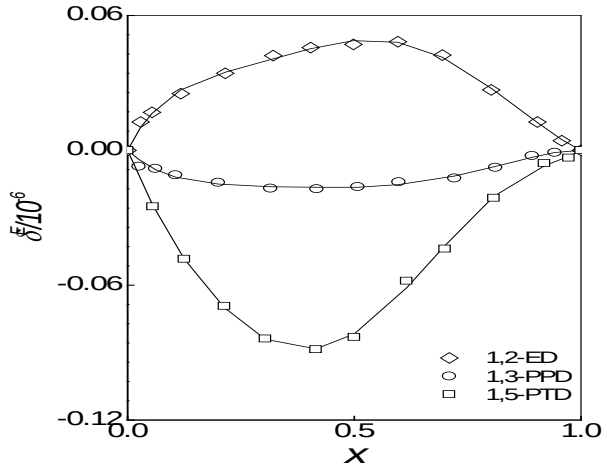

Figure 14: [1]H NMR excess chemical shifts δ^E for -NH protons for *X* α,ω-alkanediols + (*1- X*) (*β*-CD + PY)

Table 12: NMR chemical shift values δ_i^∞ for pure components.

Component	$\delta_i^\infty/10^{-6}$ -OH ^{1}H NMR	$\delta_i^\infty/10^{-6}$ -NH ^{1}H NMR	$\delta_i^\infty/10^{-6}$ >CO ^{13}C NMR
β-CD + PY	-	8.059	179.013
1,2-ED	5.381	-	-
1,3-PPD	5.414	-	-
1,5-PTD	5.481	-	-

Table 12a: NMR chemical shift δ_i^∞ values for α,ω-alkanediols + (*β*-CD + PY at infinite dilution.

Mixture	$\delta_i^\infty/10^{-6}$ -OH ^{1}H NMR	$\delta_i^\infty/10^{-6}$ -NH ^{1}H NMR	$\delta_i^\infty/10^{-6}$ >CO ^{13}C NMR
1,2-ED + (*β*-CD + PY)	5.229	7.804	181.003
1,3-PPD + (*β*-CD + PY)	5.008	7.823	180.356
1,5-PTD + (*β*-CD + PY)	5.035	7.770	180.001

Chemical shifts of –CO group

The experimentally measured ^{13}C NMR chemical shifts values for mixtures of α,ω-alkanediols and *β*-CD + PY are graphically presented in Figure 15. With addition of diol, ^{13}C NMR chemical shifts of >CO group shifts downfield over the whole composition range, which again infer the formation of strong hydrogen bonding by >CO group of PY in the mixtures of α,ω-alkanediols in (*β*-CD + PY). The δ_i^∞ values for the >CO group are also given in Table 12a. δ^E values of ^{13}C NMR of carbonyl group are graphically depicted in Figure 16. The δ^E values increase as 1,2-ED < 1,3-PPD < 1,5-PTD.

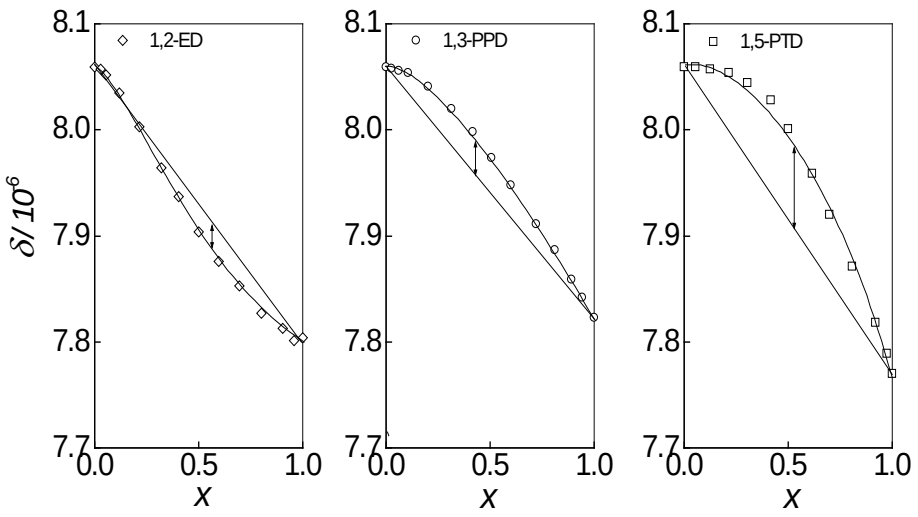

Figure 15: ^{13}C NMR shifts δ of carbonyl group for *X* α,ω-alkanediols + (*1- X*) (*β*-CD + PY)

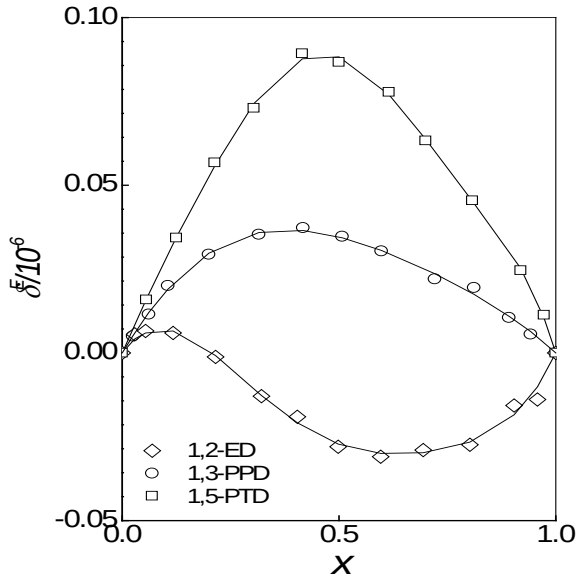

Figure 16: ^{13}C NMR excess chemical shifts δ^E of carbonyl group for α,ω-alkanediols + (*1- X*) (*β*-CD + PY)

Comparison of NMR measurements with excess molar volume data again shows a correlation (Table 13). The maximum/minimum values of ^{1}H and ^{13}C NMR excess chemical shift δ^E and excess molar volume V^E are positioned at about same mole fraction for all the mixtures. It has been found that interactions are taking place through carbonyl group of PY and hydroxyl groups of α,ω-alkanediols in mixtures of α,ω-alkanediols + (*β*-CD + PY). From thermophysical studies, we may conclude that the addition of *β* -CD in 1,5-PTD + PY caused significant changes, which are due to the fitting of 1,5-PTD in the hydrophobic cavity of *β* -CD. The effect of addition of *β* -CD in 1,2-PPD + PY and 1,3-PPD + PY systems are not much significant in comparison to 1,5-PTD + PY, as the hydrophobicity in the 1,2-ED and 1,3-PPD is less than that of 1,5-PTD

Table 13: The values of mole fractions corresponding to the maxima/minima of excess molar volume V^E and excess chemical shifts δ^E.

β-CD + PY	V^E /cm^3.mol^{-1}	δ^E /10^{-6} -OH ^{1}H NMR	δ^E /10^{-6} -NH ^{1}H NMR	δ^E /10^{-6} >CO ^{13}C NMR
1,2-ED	0.5519	0.5557	0.5980	0.5903
1,3-PPD	0.3942	0.3615	0.4153	0.4192
1,5-PTD	0.3846	0.4153	0.4153	0.3538

CONCLUSION

The thermophysical studies reveal that the position of two hydroxyl group caused significant effect in (β-CD + PY). Spectroscopic measurements demonstrate that the carbonyl group of PY and hydroxyl groups of 1,5PTD are the two active sites of interactions. Furthermore, it is observed that the thermophysical properties of {1,5-PTD + (*β*-CD + PY)} system considerably differ from the other isomers. Excellent agreement between thermodynamic and spectroscopic measurements is observed. The maximum/minimum values of ^{1}H and ^{13}C NMR excess chemical shift δ^E and excess molar volume V^E are positioned at about same mole fraction for all the mixtures. The results obtained from viscosity measurements are in good agreement with the thermodynamic studies. From spectroscopic measurements, it may be concluded that hydroxyl groups of α,ω-alkanediols are the active sites of interactions in PY + 1,4-BTD mixtures. Due to larger size of 1, 5 PTD, hydroxyl groups in {1,5-PTD + (*β*-CD + PY)} mixture has more affinity for *β*-CD. However, for remaining binary mixtures, interactions are taking place through both hydroxyl groups of diols and >CO group of amides.

ACKNOWLEDGEMENT

GRC would like to acknowledge the support of UGC, India under INDO-US 21st Century Knowledge Initiative project [F. No. 194-2/2016 (IC)] and the financial support of the SERB-DST India. Authors are thankful to DST for PURSE grant II.

REFERENCES:

Ali.A, S. Khan and S. Hyder.., (2007). Volumetric and Refractive Index Behaviour of α-Amino Acids in Aqueous CTAB at Different Temperatures, J. Chin. Chem.Soc. 1007–1012.doi:10.1016/S1872-1508(07)60055-2.

Bansal.S, N. Kaur, G.R. Chaudhary, S.K. Mehta and A.S. Ahluwalia., (2014) Physiochemical properties of new formulations of 1-ethyl-3-methylimidazoliumbis(trifluoromethylsulfonyl) imide with Tritons, J. Chem. Eng. Data. 59,3988–3999. doi:10.1021/je500502a.

Chaudhary.G.R, S. Bansal, A. Kumar and S.K. Mehta,(2013) Effect of β-cyclodextrin on the behaviour of thermophysical and spectroscopic properties of binary mixtures of (isomeric butanediol + pyrrolidin-2-one), J. Chem. Thermodyn.57, 266-275.doi:10.1016/j.jct.2012.08.026.

Das. D, B. Das and D.K. Hazra, (2004). Ultrasonic velocities and isentropic compressibilities of some symmetrical tetraalkylammonium salts in N,N-dimethylacetamide at 298.15 K, J. Mol. Liq.111,15–18. doi:10.1016/j.molliq.2003.09.017.

George. J and N.V.Sastry, (2003). Densities, Dynamic Viscosities, Speeds of Sound, and Relative Permittivities for Water + Alkanediols (Propane-1,2- and -1,3-diol and Butane-1,2-, -1,3-, -1,4-, and -2,3-Diol) at Different Temperatures, J. Chem. Eng. Data. 48, 1529–1539. doi:10.1021/je0340755

Grzybkowski.W and D. Warmińska, (2016). Apparent Molar Volumes and Isentropic Compressibilities of Tetraalkylammonium Bromides in Aqueous Propane-1,2-diol. An Attempt to Design Hydraulic Liquids, J. Chem. Eng.Data.61,2933–2945. doi:10.1021/acs.jced.5b00964.

Han.S, S. Chen, L. Li, J. Li, A. An, H. Tao, Y. Jia, S. Lu , R. Wang and J. Zhang, (2018). Multiscale and Multifunctional Emulsions by Host-Guest Interaction-Mediated Self-Assembly, ACS Cent. Sci. 4, 600–605. doi:10.1021/acscentsci.8b00084.

He.P, S. Sarkar, E. Gallicchio, T. Kurtzman and L. Wickstrom, (2019). Role of Displacing Confined Solvent in the Conformational Equilibrium of β-Cyclodextrin. *The Journal of Physical Chemistry B. 123* , 8378-8386. doi: 10.1021/acs.jpcb.9b07028

Hoyuelos. F.J, B. Garcı´a, R. Alcalde, S. Ibeas, J.M. Leal, and J.M.Matos, (1996). Shear viscosities of binary mixtures of pyrrolidin-2-one with C6-C n-alkan-1-01s J. Chem. Soc., Faraday Trans. 92, 219–225,

Jerie. K, A. Banowski, J. Przybylski and J. Glinski, (2004). Ultrasonic and positron annihilation studies of liquid solutions of n-hexanol in 1,2 ethanediol. J.mol liq.111,25-31. doi.org/10.1016/j.molliq.2003.08.023

Katrin□ák, T.; L. Hne□dkovský and I. Cibulka. (2012). Partial molar volumesand partial molar isentropic compressions of three polyhydric alcohols derived from propane at infinite dilution in water at temperatures T =(278 to 318) K and atmospheric pressure. J. Chem. Eng. Data. 57,1152−1159.

Kaur. A, S. Bansal, D. Chauhan, K.K. Bhasin, and G.R. Chaudhary, (2019). The study of molecular interactions of aqueous solutions of Choline Acetate at different temperatures, J. Mol.Liq.286,doi:10.1016/j.molliq.2019.110878.

Kaur. A, S. Bansal, C. Prakash and G. Ram, (2019). Probing molecular interactions between Choline Acetate Ionic Liquid and Alcohols □: A comparable thermophysical study of Choline Acetate Ionic Liquid with change in solvent polarities, doi:10.1016/j.molliq.2019.112061.

Li. S and W.C.Purdy, (1992). Cyclodextrins and Their Applications in Analytical Chemistry, Chem. Rev.92, 1457-1470. doi:10.1021/cr00014a009.

Luster. M.L, B.A. Patterson and E.L. Woolley, *(2002).*Apparent molar volumes and apparent molar heat capacities of aqueous ethane-1,2-diol, propane-1,2-diol, and propane-1,3-diol at

temperatures from 278.15 K to 393.15 K and at the pressure 0.35 MPa *J. Chem. Thermodynamics.*34,511-526 doi:10.1006/jcht.2001.0883.

Malandain, H.; Cano and Y. *Europ. (1996). J. Clin. Chem. and Clin. Biochem. 34,* 651

Mehta. S. K, G. Ram, C. Mani and K.K Bhasin, (2006). A comparative study of thermophysical and spectroscopic properties in mixtures of isomeric butanediol and N,N-dimethylformamide, J. Chem. Thermodyn. 38, 836-848. doi:10.1016/j.jct.2005.09.001.

Mehta. S.K, G. Ram, K.K. Bhasin, (2008). Molecular interactions of α,ω-alkanediols in pyrrolidin-2-one: Thermophysical and spectroscopic measurements, J. Chem. Thermodyn. 40, 498-508. doi:10.1016/j.jct.2007.08.005.

Panda. S, V. Singh, N. Islam and R.L. Gardas, (2017). Understanding ion-ion and ion-solvent interactions in aqueous solutions of NMP based protic ionic liquids through partial molar properties and DFT calculations, Fluid Phase Equilib.445,35-44.doi:10.1016/j.fluid. 2017.05.005.

Piekarski. H and A. Pietrzak. (2005). Molecular interactions of alkanediols in methanol and in water: density and heat capacity measurements. J. Mol. Liq. 121, 46-52. doi.org/10.1016/j.molliq.2004.08.025

Quan. D and W. Shin, (2004).Modification of electrode surface for covalent immobilization of laccase. Materials and Science and Engineering:C.24,113-115 doi.org/10.1016/j.msec.2003.09.036

Riddick. J.A, W.A. Bunger and T.K. Sakano, (1986). fourth ed. Organics Solvents: Physical Properties and Methods of Purification, vol. 1, Wiley-Interscience, New York.

Ruiz. C.C, J.A. Bolıvar, J. Aguiar, G. MacIsaac, S. Moroze and R. Palepu, (2001) Langmuir. 17 6831- 6840

Santos. A. F, M.C. Moita, J.F. Silva and I.M. Lampreia, (2017). Volumetric and sound speed study of ammonium-based ionic liquid mixtures with ethanol. 104, 118-127. doi:10.1016/j.jct.2016.09.024.

Schönbeck. C.,(2019). Complexation Kinetics of Cyclodextrins with Bile Salt Anions: Energy Barriers for the Threading of Ionic Groups, J. Phys. Chem. B. doi:10.1021/acs.jpcb.9b09415.

Tsierkezos. N.G and I.E. Molinou, (1998). Thermodynamic properties of Water +Ethylene Glycol at 283.15, 293.15, 303.15 and 313.15 K. J. Chem. Eng. Data 43 989-993.

Verevkin. S.K, (2007). Vapour Pressures and enthalpies of vapourization of a series of the 1,3 alkane diols.J. Chem. Eng. Data 52 301-308.

Walmsley. J.A., (1978). Self-association of pyrrolidinone. 2. Spectral and dielectric polarization studies of benzene solutions. J. Phys. Chem., 82, 2031-2035.

Pb. Univ. Res. J (Sci.) Vol. 69, 2019, pp 63-72

ISOSPIN EFFECTS IN NUCLEAR FRAGMENTATION OF ASYMMETRIC REACTIONS

Preeti Bansal*, Niveksha, and Sakshi Gautam
Department of Physics, Panjab University, Chandigarh -160 014, India
Department of Physics, Chandigarh University, Gharuan, Mohali-140413, Punjab, India.

Abstract

A study on fragmentation of the asymmetric reaction pairs is presented using the isospin dependent quantum molecular dynamics (IQMD) model. The partitioning of the fragmenting system into gas (low density) and liquid (high density) phases in semi-central collisions ($\hat{b}$ = 0.2 - 0.3) is investigated at various beam energies ranging from 80 to 500 AMeV. The findings revealed a cross-over of gas/liquid content. The influence of isospin degree of freedom (via nuclear symmetry energy and nucleon-nucleon scattering cross-section) on the cross-over energy (where gas and liquid content become equal) is investigated in detail. The study revealed dominance of the nucleon-nucleon scattering cross-section over the nuclear symmetry energy. The study concludes that cross-over energy can act as a sensitive probe of isospin-dependent nucleon-nucleon scattering cross-section.

Keywords: Multifragmentation, Nuclear symmetry energy, Molecular dynamics approach.

INTRODUCTION

Nuclear physics deals with the interactions among nucleons and in order to understand such interactions, numerous studies on nuclear structure as well as reactions have been carried out. The studies of nuclear reactions at significant energies (above nuclear binding energy) led to formation of hot/dense nuclear matter and thus, one can get an idea about nuclear interactions at such extreme conditions of temperature and pressure. Earlier, nuclear reactions were restricted in understanding conventional fusion/fission phenomenon. However, with the advancement in accelerator technologies, one can now collide beams of energies ~TeVs. At such energies, various new phenomena such as nuclear multifragmentation, collective flow, particle production, nuclear stopping, have been observed.

Nuclear interactions deal with interactions among neutrons and protons and collisions of isospin symmetric nuclei (one having equal number of neutrons and protons) were performed at various terrestrial laboratories in order to have deeper insight about these interactions. But the present times have witnessed a shift in the interest of community to exotic nuclei as these nuclei could now be accelerated because of rapid advancement in radioactive ion beam (RIB) facilities. This shift has led to the emergence of a new branch of physics named as isospin physics. The present day nuclear physics community is greatly involved in understanding various properties of such isospin asymmetric nuclei (n-p imbalance) ranging from their structure to interactions among the nucleons. The isospin dependence of nucleon-nucleon interactions is one of the major aims in order to have an idea of equation of state of isospin symmetric matter. It is worth mentioning that such studies will have astrophysical implications too as they will determine the properties of neutron stars and supernova explosions.

The isospin dependence of nuclear equation of state (EOS) is poorly known property of exotic nuclei and this uncertainty comes via both nuclear symmetry energy and isospin dependence of scattering cross-section. From the analysis of observations gathered from terrestrial laboratory experimental and astrophysical data, the value of nuclear symmetry energy at normal nuclear matter density (ρ_0) comes close to 30 MeV. However, its behavior at densities other than (ρ_0) is under exploration. Interpretation of experimental data by various transport models has led to constrained behavior of nuclear symmetry energy at subsaturation densities ($\rho < \rho_0$). On the other hand, at supra-saturation densities ($\rho > \rho_0$) comparison of transport model predictions with available experimental data yields divergent behavior of density-dependent symmetry energy. One has to continue probing the nuclear symmetry energy at densities far from saturation by exploring new observables sensitive to it.

Nuclear multifragmentation, an intermediate mechanism between low energy decay modes (such as evaporation, nuclear fission) and high energy decay channels (such as complete vaporization of system), offers a unique possibility to explore the behavior of nuclear equation of state of isospin asymmetric matter and in particular, the nuclear symmetry energy. Various observables from nuclear fragmentation sensitive to nuclear symmetry energy have been put forward in recent past such as isospin fractionation (Xu *et al*. 2000, Baran *et al*., 2002) and isospin diffusion (Tsang *et al*., 2009). The isospin fractionation is an unequal partitioning of neutron and

*Corresponding Author: preetibansal1111@gmail.com
MS Received: November 21, 2019, Accepted: December 24, 2019

proton of isospin asymmetric system between low and high density phases and extensive studies have been carried out in this direction. Such studies have predicted that it is energetically favorable for an asymmetric system to separate into neutron-rich gas phase as compared to liquid phase which is less neutron-rich.

In the present work, we will study the partitioning of system into a liquid (high density) and a gas (low density) phase over a wide range of energies for various mass asymmetric reaction pairs. The mass asymmetry is varied by varying the projectile and keeping the target fixed. It is worth mentioning that the collision dynamics of mass asymmetric reactions differ from symmetric reactions as lot of compressional energy is involved in the latter. The mass asymmetric reactions lack compression and energy might get stored in some other forms. Therefore, it would be interesting to study the dynamics of such asymmetric collisions.

In earlier studies, multiple ways are reported to define this liquid-gas phase. For example, Liu *et al.* (2003, 2004) have defined the gas phase as the free particles emitted during simulations and liquid covers all the fragments with a charge number within 2 to (Z_P + Z_T)/2 at freeze out. Here, Z_P and Z_T are charges of projectile and target. In another study of Liu *et al.* (2005), all fragments with Z ≥ 2 are considered as liquid. Li (2000) quantified the definition of free phase (gas) and bound phase (liquid) as nucleons with local density lesser and greater than ρ_0/8, respectively, where ρ_0 is normal nuclear matter density. Similar definitions of gas and liquid phases on the basis of local densities have been proposed by other authors also. Guo *et al*. (2014) defined the nucleons with local density lesser (greater) than ρ_0/10 as gas (liquid) by using the IBUU04 transport model and took more realistic definition of nuclear gas as A = 1, whereas A > 1 bound nucleons (or fragments) were treated as nuclear liquid. Since the present study is carried out using the isospin-dependent quantum molecular dynamics (IQMD) model, we will use above definition for defining the nuclear gas and liquid phases. It is worth mentioning that the present version of the IQMD model has been reported to correctly predict the fragmentation pattern, *e.g.*, measured fragment yields, charge distribution and related observables such as entropy, at the freeze-out stage over wide energy ranges (Bansal *et al*., 2015, Kaur and Puri, 2013).

THE FORMALISM

Isospin-dependent Quantum Molecular dynamics (IQMD) model: The proposed study has been carried out within the framework of isospin-dependent quantum molecular dynamics model (IQMD), which can be termed as primary model (Hartnack et al., 1998).

In IQMD model, each nucleon is represented by a coherent state that is characterized by 6 time-dependent parameters, $\mathbf{r}_i$ and $\mathbf{p}_i$, respectively.

$$\psi_i(\boldsymbol{r}, \boldsymbol{p}_i(t), \boldsymbol{r}_i(t)) = \frac{1}{(2\pi K)^{3/4}} exp\left[\frac{i}{\hbar}\boldsymbol{p}_i(t).\boldsymbol{r} - \frac{(\boldsymbol{r}-\boldsymbol{r}_i(t))^2}{4K}\right] \quad (1)$$

The parameter, ***K***, which is related to extension of the wave packet in phase-space is system dependent. The total n-body wave function is assumed to be the direct product of coherent states

$$\phi = \prod_i \psi_i(\boldsymbol{r}, \boldsymbol{p}_i(t), \boldsymbol{r}_i(t)) \quad (2)$$

Slater determinant has not been used and thus antisymmetrization is neglected. The initial values of the parameters are chosen in a way that the ensemble of A_T and A_P nucleons gives a proper density distribution as well as a proper momentum distribution of the projectile and target nuclei.

The equations of motion of the many-body system are calculated by the means of a generalized variational principle. We start from the action

$$S = \int_{t_1}^{t_2} L[\phi, \phi^*]dt \quad (3)$$

With the Langrange *L*

$$L = \left(\phi\left|i\hbar\frac{d}{dt} - H\right|\phi\right) \quad (4)$$

Where the total time derivative includes the **variation** with respect to the parameters. The Hamiltonian H contains a kinetic term and mutual interactions, V_{ij}, which can be interpreted as the real part of the Bruckner G-matrix supplemented by the Coulomb interaction.

In IQMD model, baryons are represented by Gaussian-shaped density distributions. Nucleons are initialized in a sphere with radius, R = 1.12 $A^{1/3}$ fm, in accordance with liquid-drop model. Each nucleon occupies a volume of h^3, so that the phase space is uniformly filled. The initial momenta are randomly chosen between 0 and Fermi momentum, therefore, it may happen that the nucleons close to the surface, where the local potential energy is low, are unbound initially. The full Fermi pressure yields a stronger stability of the density profile against vibration modes. The Fermi momentum depends on the ground state density. For ρ_0 = 0.17 fm^{-3}, it has a value of 268 MeV/c. The nucleons of the target and projectile interact by two- and three-body Skyrme forces, Yukawa potential, Coulomb interactions and momentum-dependent interactions. In addition to the use of explicit charge states of all baryons and

mesons, a symmetry potential between protons and neutrons corresponding to the Bethe - Weizsacker mass formula has been included. The hadrons propagate using Hamilton equations of motion:

$$\dot{\boldsymbol{p}}_i = -\frac{\partial\langle H\rangle}{\partial \boldsymbol{r}_i};\ \dot{\boldsymbol{r}}_i = \frac{\partial\langle H\rangle}{\partial \boldsymbol{p}_i}; \tag{5}$$

with

$$\langle H\rangle = \langle T\rangle + \langle V\rangle$$

$$= \sum_i \frac{\boldsymbol{p}_i^2}{2m_i} + V^{Sky} + V^{Yuk} + V^{Cou} + V^{MDI} + V^{sym} \tag{6}$$

The total baryon-baryon potential V_{ij} can be given as:

$$V_{ij} = V_{ij}^{Sky} + V_{ij}^{Yuk} + V_{ij}^{Cou} + V_{ij}^{MDI} + V_{ij}^{sym}$$

$$= \left[t_1\delta(\boldsymbol{r}_i - \boldsymbol{r}_j) + t_2\delta(\boldsymbol{r}_i - \boldsymbol{r}_j)\rho\ \ ((\boldsymbol{r}_i - \boldsymbol{r}_j)/2)\right]$$

$$+t_3\frac{exp\{|\boldsymbol{r}_i - \boldsymbol{r}_j|/\omega\}}{|\boldsymbol{r}_i - \boldsymbol{r}_j|/\omega} + \frac{Z_iZ_je^2}{|\boldsymbol{r}_i - \boldsymbol{r}_j|}$$

$$+ t_4ln^2\left(t_5(\boldsymbol{p}_i - \boldsymbol{p}_j)^2 + 1\right)\delta(\boldsymbol{r}_i - \boldsymbol{r}_j)$$

$$+t_6(1/\rho_0)T_{3i}T_{3j}\delta(\boldsymbol{r}_i - \boldsymbol{r}_j) \tag{7}$$

Where Z_i and Z_j denote the charges of i^{th} and j^{th} baryon, and T_{3i} and T_{3j} are their respective T_3 components, *i.e.*, 1/2 for protons and -1/2 for neutrons. It should be noted that the width K of the distribution function determines the interaction range of the particle and influences the density distribution of finite systems. Therefore, its value has to be adopted to reasonable interactions ranges of the strong interaction.

The momentum dependence, VMDI of the n-n interaction, which may optionally be used in IQMD, is fitted to experimental data on the real part of the nucleon optical potential, which yields

$$VMDI = \delta\ ln^2(\epsilon(\Delta p)^2 + 1)\left(\frac{\rho_{int}}{\rho_0}\right) \tag{8}$$

Hard n-n collisions are included by employing the collision term of the well-known VUU-BUU equation. The collisions are done stochastically, in a similar way as in the cascade models. Two particles collide if their minimum distance d fulfils

$$d \le d_0 = \sqrt{\frac{\sigma_{tot}}{\pi}},\ \ \sigma_{tot} = \sigma(\sqrt{s}, type) \tag{9}$$

Where 'type' denotes the ingoing collision partners. In addition, the Pauli blocking (of the final state) of baryons is taken into account by checking the phase space densities in the final state of a two-body collision. It is assumed that each nucleon occupies a sphere in coordinate and momentum space. We calculate the fractions P_1 and P_2 of final phase space for each of the two scattering partners that are already occupied by other nucleons with the same isospin as that of the scattered ones. The collision is blocked with the probability

$$P_{block} = 1 - [1 - P_1][1 - P_2] \tag{10}$$

and the corresponding collision is allowed with the probability 1- P_{block}. Whenever an attempted collision is blocked, the scattering partners maintain the original momenta prior to scattering.

The variational approach employed in QMD model reduces the complication of time evolution of an n-body wave function by resolving to 6n coupled differential equations for the centroids of the coherent wave functions in configuration and momentum space. This approach allows us to define clusters in a very convenient manner. At the end of the reaction, phase space occupancy is quite low, so nucleons forming a cluster will be closer in coordinate space. This simplest approach of identifying clusters is well known as minimum spanning tree (MST) method. In this method, two nucleons share the same cluster if their centroids in coordinate space are closer than a given clusterization radius R_{clus} that is,

$$|r_i - r_j| \le R_{clus} \tag{11}$$

where r_i and r_j are the spatial coordinates of the two nucleons. The clusterization radius, R_{clus}, is used as a free parameter which may lie between 2-4 fm. The variation in clusterization radius is found to have negligible influence on the final state fragment structure (the end of reaction), since nucleons belonging to different clusters are far away in spatial coordinates.

RESULTS AND DISCUSSION

For the present study, we simulated thousands of events of ^{197}Au+^{197}Au, ^{131}Xe+^{197}Au, ^{85}Rb+^{197}Au, ^{51}Va+^{197}Au and ^{23}Na+^{197}Au having mass asymmetry ranging from 0 to 0.8. The mass asymmetry η is defined as $(A_T - A_P)/(A_T + A_P)$, where A_T and A_P are the masses of target and projectile nuclei, respectively, and asymmetry is varied by using different projectile and fixed target. The simulations are done for soft-momentum-dependent (SMD) equation of state with isospin/energy dependent nucleon-nucleon cross-section.

Further to understand the behavior of gas and liquid content, we display the snapshot of a single event for the reaction of ^{23}Na+^{197}Au at incident energy of 400 AMeV in Figure 1. Blue (red) solid circles represent

the gas (liquid) content. Here, the gas and liquid content is checked from the start (0.1 fm/c) of the reaction till freeze-out stage at 300 fm/c and coordinates of nucleons corresponding to gas and liquid content are plotted in the reaction plane. From the figure, we see that as the reaction proceeds, the well separated projectile and target (initially at 0.1 fm/c) overlap and compressed phase is reached at around 10 fm/c. We also see that the gas content increases initially with a corresponding decrease in liquid content and at final stage (at 300 fm/c), both get saturated.

In Figure 2, we display the gas and liquid content (labelled as G and L, respectively) for the reactions of $^{23}Na+^{197}Au$ (upper panel) and $^{197}Au+^{197}Au$ (bottom panel) at incident energies of 400 and 100 AMeV, respectively. Open (closed) circles represent gas (liquid) content. From the figure, we observe that as

the reaction proceeds, the emission of free nucleons increases with a corresponding decrease in the yield of various mass fragments for both the reactions. The yield of various fragments gets saturated at around 300 fm/c and this stage is known as freeze-out stage. The gas/liquid content gets saturated and thus nucleon nucleon collision happening after 300 fm/c are not hard enough to bring any change in the fragmentation pattern. Therefore, further analysis will be done at 300 fm/c.

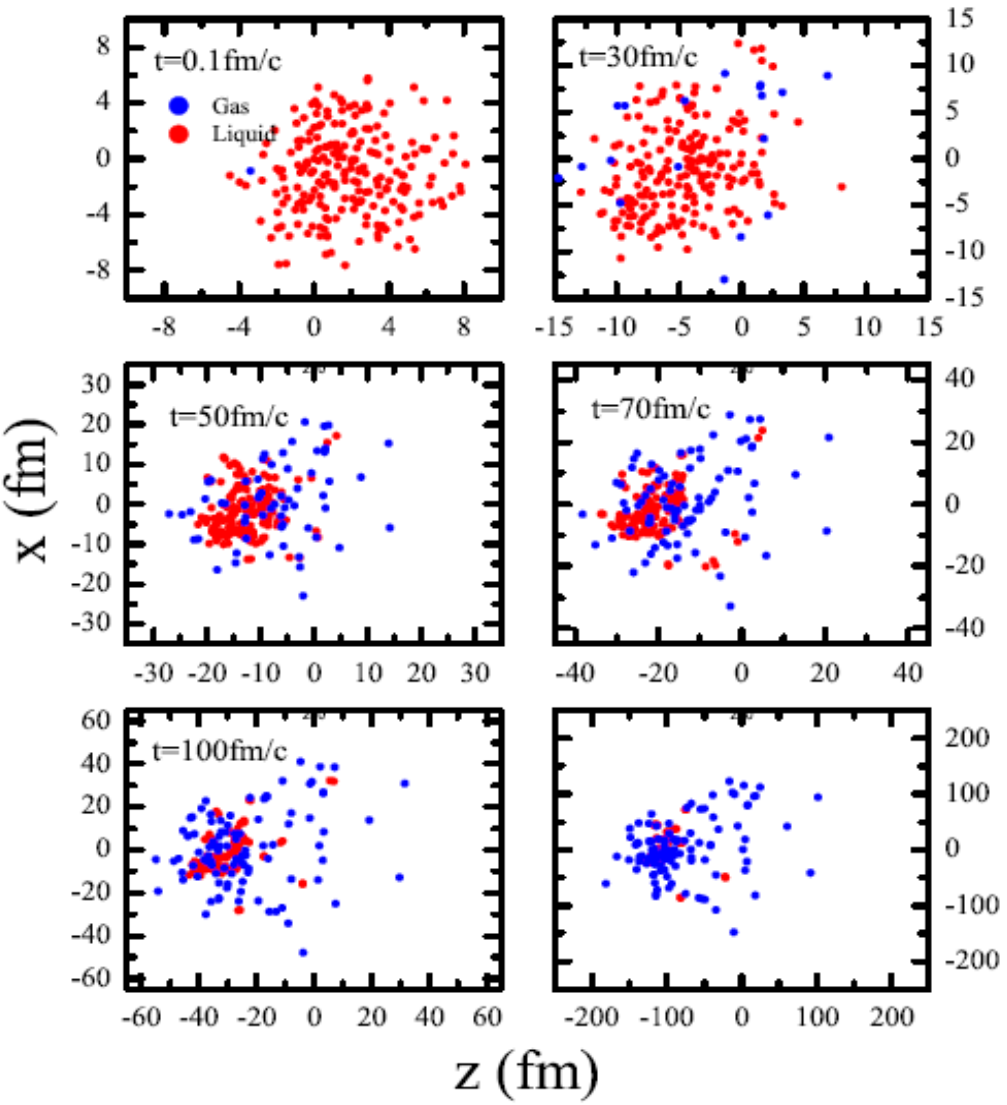

Figure 1: The snapshot of a single event of the reaction of $^{23}Na+^{197}Au$ at energy 400 AMeV in the X-Z plane. Various symbols are explained in the text.

In order to find cross-over energies, the above mentioned mass asymmetric reactions are simulated at different incident energies ranging from 80 AMeV to 500 AMeV. As mentioned earlier, we consider free nucleons (A = 1) at the freeze-out stage as gas and all other fragments (A ≥ 2) as liquid. In Figure 3, we display energy dependence of gas and liquid content (labelled as G and L, respectively) of different reactions. Symbols have same meaning as in Figure 2.

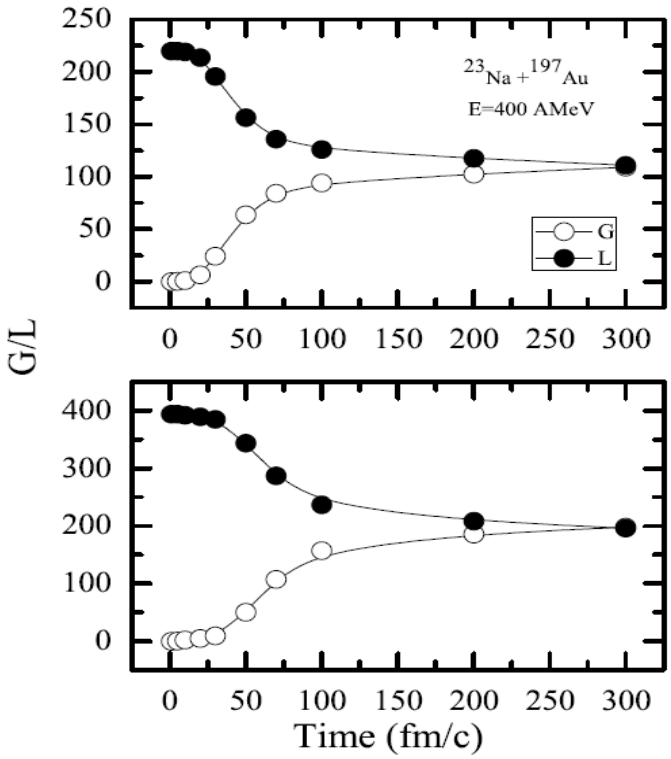

Figure 2: The time evolution of gas and liquid content for the reaction of ^{23}Na+^{197}Au (top panel) and ^{197}Au+^{197}Au (bottom panel) at incident energy of 400 and 100 AMeV, respectively. Symbols are explained in the text.

We observe that gas content for all the colliding pairs is continuously increasing with an increase in energy, while opposite behavior is observed for liquid content. One also notices a higher liquid content at lower energies, whereas gas content dominates at higher beam energies. This is because at lower beam energies, the attractive mean field dominates the dynamics over nucleon-nucleon scattering. Because of lesser number of nucleon-nucleon collisions, there is formation of heavy clusters and the yield of free particles is significantly small and thus resulting in lower gas content over liquid.

On the other hand, at higher energies, nucleon-nucleon collisions dominate the dynamics and this scattering is responsible for emission of free nucleons. Also, the fragments further break into free nucleons at higher energy due to violent nature of the reaction and this results in the dominance of gas over liquid. It is clear from the figure that with the increase in incident energy, emission of free nucleons gets enhanced leading to increase in gas content (open symbols) and corresponding decrease in liquid content (closed symbols) and thus a cross-over is obtained. The energy corresponding to an equal gas and liquid content is labelled as cross-over energy and is designated by an arrow. From the figure, we observed that the cross-over energy decreases as system (projectile + target) mass increases. The cross-over energy is larger for the reaction of ^{23}Na+^{197}Au, while its value is smaller for ^{197}Au+^{197}Au. This is due to the fact that for mass symmetric reactions, a good compressional effect leads to breakage of the system resulting in higher gas content and the cross-over can be obtained at lower beam energy. On the other hand, for mass asymmetric collisions, the compressional energy is very less and thus one requires significantly higher energies for good breakage, pushing the cross-over to occur at higher energies. Note that cross over energy dynamics for mass symmetric reactions has been already studied by authors and collaborators and reported in (Bansal *et al.*, 2018).

As the colliding pairs have neutron-proton imbalance, so it would be interesting to see how isospin degree of freedom affects the cross-over dynamics? The isospin effects enter the dynamical calculations via mean field (symmetry potential) and scattering cross-section (isospin-dependent). Firstly, we simulated the reactions by neglecting the symmetry potential (labelled as 'E_{sym}^{off}') as shown in Figure 4. From the figure, we observed that although individual gas or liquid content shows little sensitivity towards symmetry potential, the cross-over energy is greatly influenced and increased for all reaction pairs. This is because of repulsive nature of symmetry potential and in the absence of these repulsions, the system requires more energy to break into free nucleons. However, the behavior of cross-over energy with mass asymmetry remains intact, *i.e.*, ^{23}Na+^{197}Au has lowest cross-over energy while ^{197}Au+^{197}Au has the highest.

Next, isospin dependence of cross-section will also play a major role in governing the isospin dynamics, so the reactions are also simulated with isospin-independent cross-section, *i.e.*, $\sigma_{np} = \sigma_{nn}$ (or σ_{pp}). It is worth mentioning that earlier the cross-section of neutron-proton collisions is three times of neutron-neutron or proton-proton collisions. The results are displayed in Figure 5 and labelled as '$\sigma_{non\text{-}iso}$'. We again observed an increase in the cross-over energy for all reactions. This is because the net cross-section gets reduced in the case of isospin-independent one as compared to isospin-dependent cross-section. Therefore, the system requires more energy to break due to reduced scattering cross-section and thus cross-over energy will be shifted to higher values.

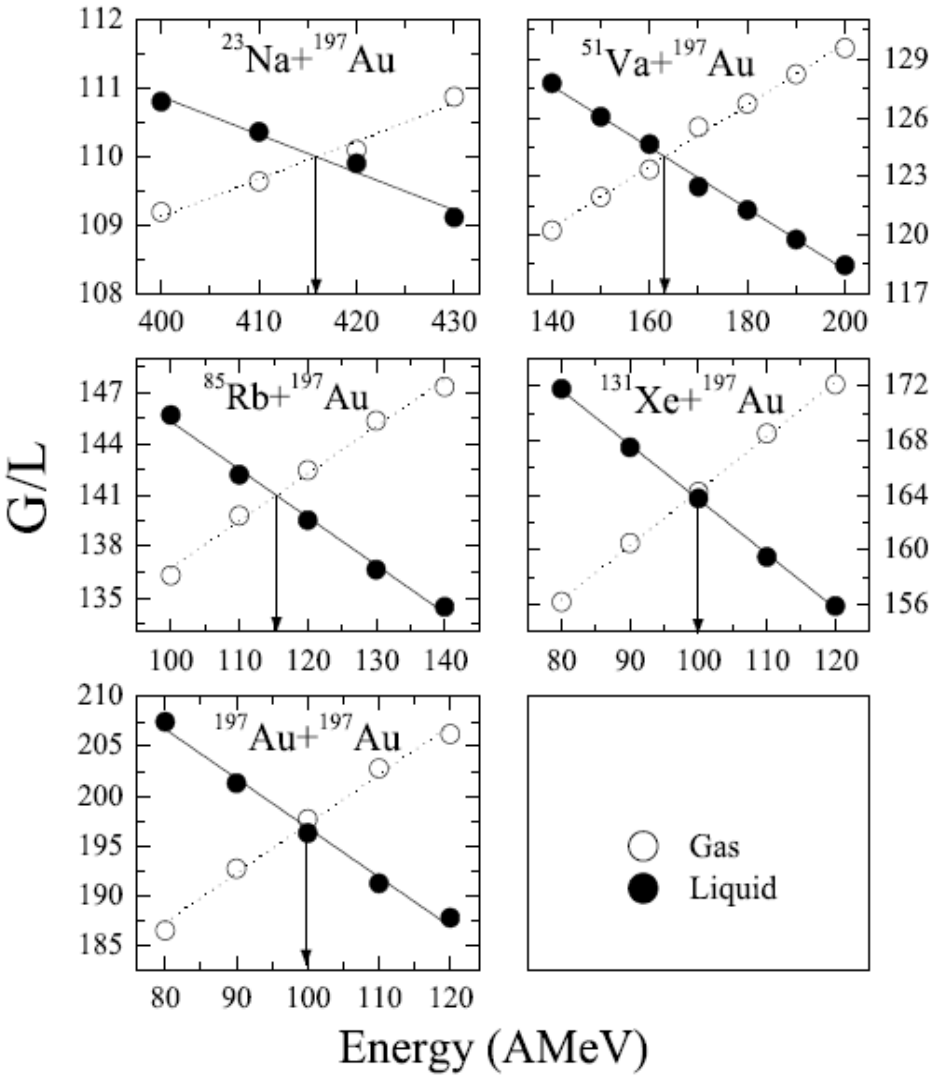

Figure 3: The energy dependence of the gas and liquid content for the reaction pairs having mass asymmetry η = 0, 0.2, 0.4, 0.6 and 0.8. Various symbols are explained in the text.

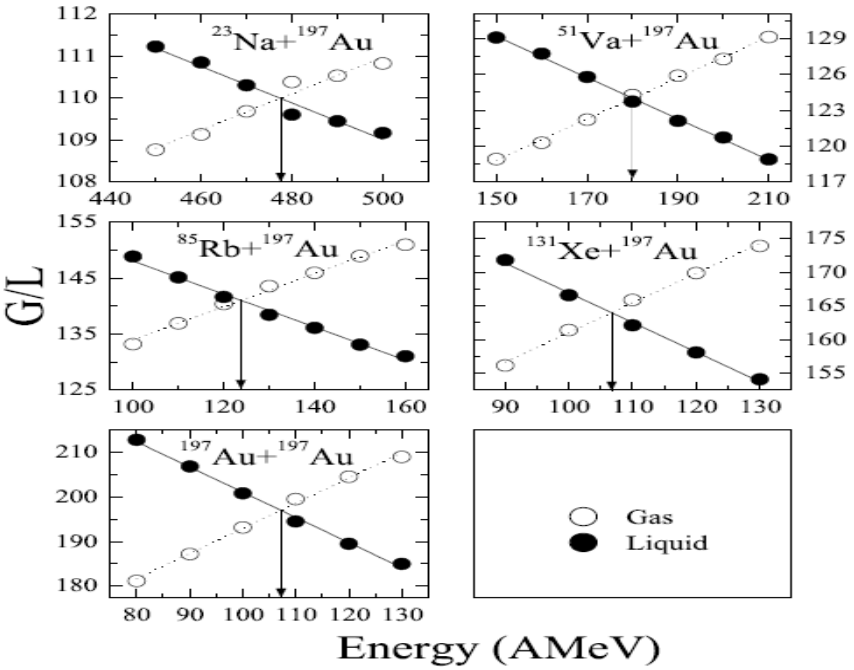

Figure 4: Same as Figure 3, the reactions are simulated by switching off the symmetry potential.

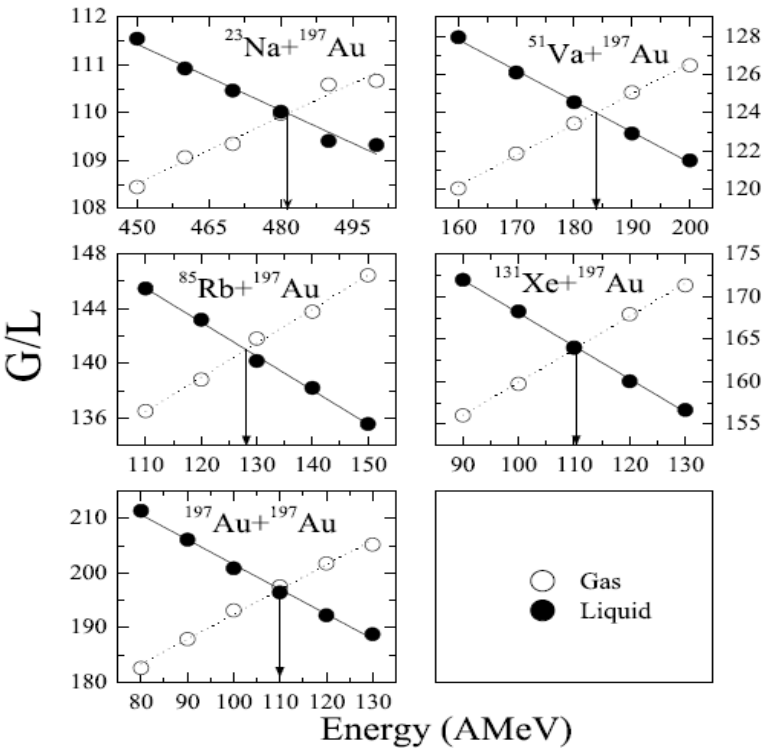

Figure 5: Same as Figure 3, the reactions are simulated by considering isospin-independent cross-section.

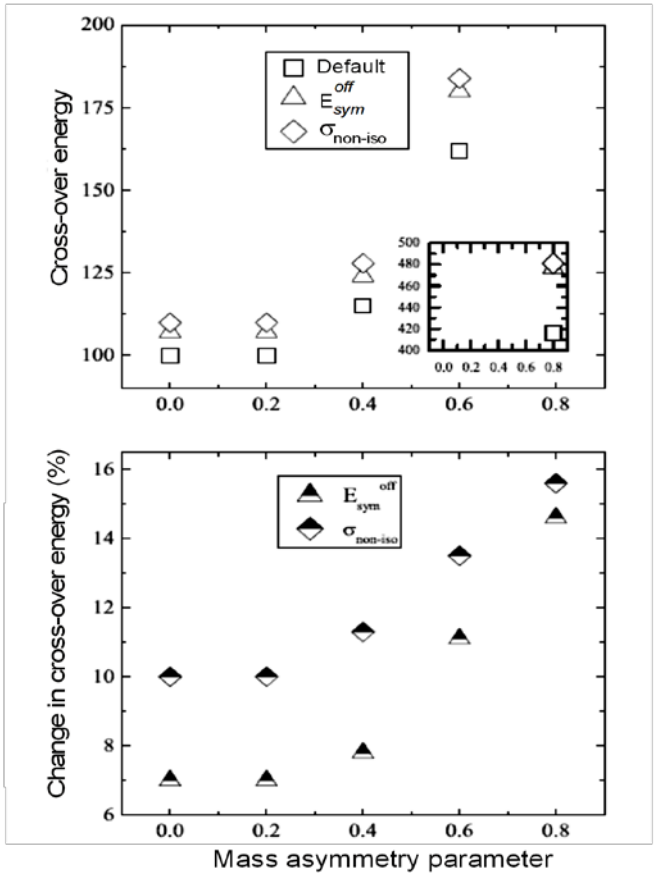

Figure 6: The values of cross-over energy for the mass asymmetric reactions with mass asymmetry varying from 0 to 0.8 (top panel). Inset displays the results for the reaction of mass asymmetry =0.8. Percentage change in cross-over energy values (bottom panel). Various symbols are explained in the text.

Next, we summarize our results of isospin effects on the cross-over energy for all reaction pairs in Figure 6. Top panel displays the values of cross-over energies as a function of asymmetry parameter (η) for default calculation (results of figure 3), without symmetry potential (results of figure 4) and with isospin-independent cross-section (results of figure 5). Squares, triangles and diamonds display the results of default calculations, E_{sym}^{off} and $\sigma_{non\text{-}iso}$. From the figure (top panel), we observed that cross-over energy increases with mass asymmetry in all cases. Furthermore, the role of isopsin effects gets enhanced with mass asymmetry of the colliding pair. Bottom panel displays the percentage change in cross-over energies for the calculations without symmetry potential and calculations by considering the isospin-independent cross-section. From the figure, we observed that percentage change in the cross-over energies is more when we performed the calculations with isospin-independent cross-section compared to calculations without symmetry potential. This could be due to the fact that asymmetric reactions lack compression and thus collisions are not that effective. Therefore, the change in collision cross-section can play a dominant role and alters the fragmentation pattern.

SUMMARY

We have studied yields of gas and liquid contents as a function of incident energy in the fragmentation of asymmetric reaction pairs by varying projectile and keeping target fixed consisting reactions of ^{197}Au+^{197}Au, ^{131}Xe+^{197}Au, ^{85}Rb+^{197}Au, ^{51}Va+^{197}Au and ^{23}Na+^{197}Au. It is observed that yield of the gas content increases and that of the liquid content decreases with increase in the energy for all colliding pairs. We also studied isospin effects on the cross-over energy (the energy corresponding to an equal amount of gas and liquid) and it was found that the nucleon-nucleon scattering cross-section strongly influences cross - over energy compared to nuclear symmetry

energy. Thus, our study concludes that the cross-over energy is a sensitive probe to study the isospin independence of n-n scattering cross-section.

ACKNOWLEDGEMENT

Authors are thankful to Prof. Rajeev K. Puri, Department of Physics, Panjab University Chandigarh for giving access to various computer codes used in the present work.

REFERENCES

Bansal, P., S. Gautam and R. K. Puri. 2015. On the peak mass production of different fragments in intermediate energy heavy-ion collisions. Eur. Phys. J. A 51, 139 (1- 8).

Bansal, P., S. Gautam and R. K. Puri. 2018. Isospin effects in nulear fragmentation of isotopic, isobaric and isotonic reactions. Phys. Rev C 98, 024614 ,1-7.

Baran, V., M. Colonna, M. Di Toro, V. Greco, M. Z- Pfabe and H. H. Wolter. 2002. Isospin effects in Nuclear Fragmentation. Nucl. Phys. A 703, 603-632.

Guo, W. M., G. C. Yong, Y. Wang, Q. Li, H. Zhang and W. Zuo. 2014. Normal or abnormal isospin fractionation as a qualitative probe of nuclear symmetry energy at supradensities. Phys. Lett. B 738, 397-400.

Hartnack, C., R. K. Puri, J. Aichelin, J. Konopka, S. A. Bass, H. Stoecker and W. Greiner. 1998. Modelling the many-body dynamics of heavy-ion collisions: present status and future perspective. Eur. Phys. J A 1, 151-169.

Kaur, S. and R. K. Puri. 2013. Isospin effects on the energy of peak mass production. Phys. Rev. C 87, 014620 (1-4).

Li, B. A. 2000. Neutron-proton differential flow as a probe of isospin dependence of nuclear equation of state. Phys. Rev. Lett. 85 4221-4224.

Liu, J. Y., W. J. Guo, Y. Z. Xing and H. Liu. 2003. Isospin fractionation in nucleon emissions and fragment emissions in intermediate energy heavy-ion collisions. Nucl. Phys. A 726, 123-133.

Liu, J. Y., W. J. Guo, Y. Z. Xing, X. G. Li and Y.Y. Gao. 2004. Isospin effects of Coulomb interaction on the dissipation and fragmentation in intermediate energy heavy-ion collisions. Phys. Rev. C 70, 034610 (1-8).

Liu, J. Y., W. J. Guo, Y. Z. Xing and X. G. Lee. 2005. Isospin momentum-dependent interaction and its role on isospin fractionation ratio in intermediate energy heavy-ion collisions. Chin. Phys. Lett. 22, 65-69.

Tsang, M. B., Y. Zhang, P. Danielewicz, M. Famiano, Z. Li, W. G. Lynch and A. W. Steiner. 2009. Constraints on the density dependence of symmetry energy. Phys. Rev. Lett. 102, 122701 (1-4).

Xu, H. S. *et al*. 2000. Isospin fractionation in Nuclear Multifragmentation. Phys. Rev. Lett. 85, 716-719.

Pb. Univ. Res. J (Sci.) Vol. 69, 2019, pp 73-78

STUDY OF RESISTIVE PLATE CHAMBERS WITH OPTIMIZED READ-OUT STRIPS

R. Kanishka* and V. Bhatnagar

Department of Physics, Panjab University, Chandigarh 160 014, India

Abstract

The Resistive Plate Chambers (RPCs) are active detectors used in many on-going high energy Physics experiments like Compact Muon Solenoid (CMS) at Large Hadron Collider (LHC), Geneva. These detectors will also be used in up-coming experiments like Iron CALorimeter (ICAL) at India-based Neutrino Observatory (INO). An optimization of strip width of read-out boards of RPC is an important part for the detector which needs to be optimized. In this paper, the effect of the width of the strips on the efficiency and cross-talk of glass RPC has been studied.

Keywords: Detector, Resistive plate chamber, Glass, Strip width, Efficiency, Cross-talk.

INTRODUCTION

The resistive plate chambers (RPCs) (Santonico 1981; Santonico 1988) have been extensively used in various experiments like BELLE [Abe *et al.* 2010], CMS (CMS collaboration 1994) and planned to be used in future ICAL-INO (Athar *et al*. 2006, Indumathi *et al*. 2006, Thakore *et al*. 2013, Ghosh *et al*. 2013) experiment. In INO experiment, around 30,000 RPCs will be installed. As such a huge number of detectors to be made from them, an extensive R & D of the detector is necessary. The RPC can track the muons (Chatterjee *et al*. 2014, Bhattacharya *et al*. 2014) that pass through them. The RPCs are the detectors meant to reconstruct the muon track and further study its properties like momentum, charge and direction. A single RPC (Satyanarayana 2009) consists of two graphite coated parallel plate electrodes either of glass or Bakelite of high bulk resistivity (10^{10} - 10^{12} Ω-cm). These plates are separated by button spacers forming a gap which are glued together with side spacers and nozzles at the four corners. A set of pick-up panels or read-out boards, aligned in orthogonal directions are placed on the electrodes at their outer surface. These pick-up panels are separated from electrodes by Mylar (insulating) sheets. A gas mixture (Kalmani *et al*. 2009) consists of Isobutane which absorbs the photons formed due to recombination process, *Freon* (*R134a*) gas to limit the free charge and a quenching gas SF_6. These gases in an appropriate proportion are used in the RPC. This gas mixture is passed through RPC and a high voltage is applied across RPC. Electric signals are induced on the strips of pick-up panels, which are read-out then by using a set of electronic devices. A schematic of RPC is shown in Figure 1.

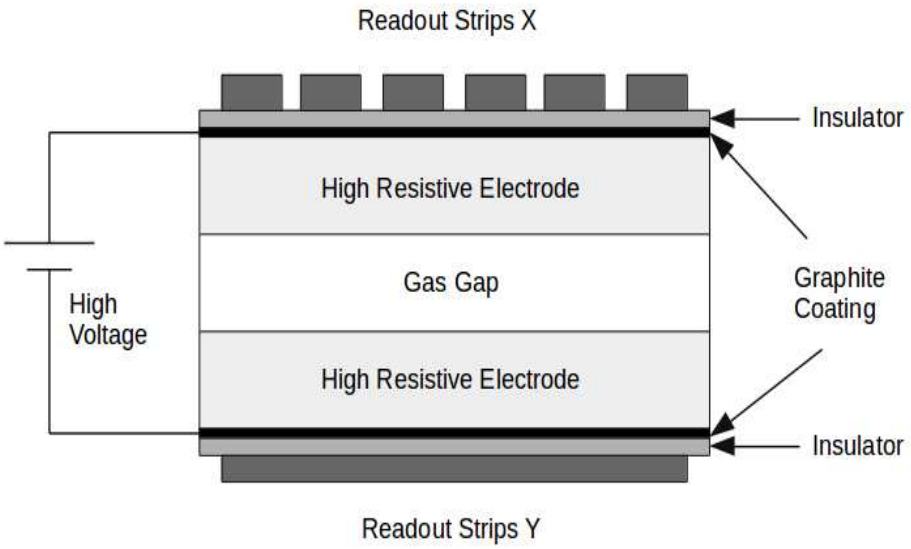

Figure 1: A schematic of RPC detector.

*Corresponding Author: Kanishka.rawat.phy@gmail.com
MS Received: November 6, 2019, Accepted: December 20, 2019

MODES OF OPERATION

The two modes of operation of RPC are, (i) Avalanche Mode (Cardarelli *et al*. 1993, Cardarelli *et al*. 1996) and (ii) Streamer Mode (Fonte 2000, Fonte 2002). Both of these depend on the voltage applied and gas composition used. In the present case, RPC has been operated in avalanche mode for our analysis. The strip width was optimized for the studies, and efficiency and cross-talk measurements were done.

PERFORMANCE OF RPC WITH VARYING STRIP WIDTH

The fabrication and optimization of the strip width of pick-up panels or read-out boards is necessary in order to do the physics analysis precisely. Depending on the various physics goals of the experiment, the strip width of pick-up panels can be optimized. For instance, increasing the strip width gives poor muon momentum resolution but good muon detection efficiency which will be required for neutrino oscillation analysis at ICAL-INO experiment. The fabrication of pick-up panels has been done by two methods as per the availability of the material. The pick-up panel with the strip width size =1.8 cm was fabricated, by taking a 5 mm thick honeycomb core with 50 micron aluminium sheet for grounding. Aluminium sheet was pasted on one side and copper strips of 1.8 cm width with a gap of 0.2 cm pasted on the other side (inner side) of honeycomb core. Each copper strip was terminated with a 50 Ω impedance to match the characteristic impedance of the preamplifier connected for picking up the signals. The other end of strip was soldered to wire having connectors to connect with preamplifiers. The pick-up panels with the strip width size = 2.8 and 3.8 cm was fabricated, by taking a foam interleaved between two 50 micron aluminium sheet. The inner side of aluminium sheet was etched to make 2.8 cm (or 3.8 cm strips for another set of pick-up panels) strips with gap of 0.2 cm. Then, the copper tape with conductive adhesive base was pasted at the end to solder 50 Ω impedance and connectors at other end. Figure 2 shows the pick-up panels fabricated with different strip widths.

Figure 2: Fabricated pick-up panels with the strip width size: 1.8, 2.8, 3.8 cm, respectively.

EFFICIENCY AND CROSS-TALK

The fabrication of 30 cm × 30 cm glass RPC has been done using standardized procedure as explained in the beginning. The measurements were done for the read-out strips (X) (see Figure 1) of RPC detector due to the limited availability of preamplifiers. Figure 3 shows a circuit diagram for testing the RPC in which P_1, P_2, P_3, and P_4 are the scintillator paddles used to make a 4-fold coincidence (a trigger). This trigger along with the main strip of pick-up panel of RPC form a coincidence window required for the efficiency measurements. The dimensions of P_1, P_2, P_3, P_4 has been given in the diagram. Those muons that passed through scintillator paddles and RPC are counted by counters (S_1 - S_7). The scintillator paddles P_1 and P_2 were placed in a manner to create a window of about 14 cm × 1.8 cm (or 2.5 cm or 3.8 cm depending on the scintillator paddles and pick-up panel used). These paddles were aligned with 2nd strip of pick-up panel of RPC which was labelled as "main strip", whereas 1st strip was labelled as "left strip" and 3rd was labelled as "right strip". The RPC was placed after P_2 so that the muon passed through all the four scintillator paddles and also through the RPC. The temperature was maintained at 24-25°C and relative humidity at 40%. But the main source of error was the opening and closing of the door of the lab which caused moisture level sometimes to go up and hence affected the efficiency of the RPCs.

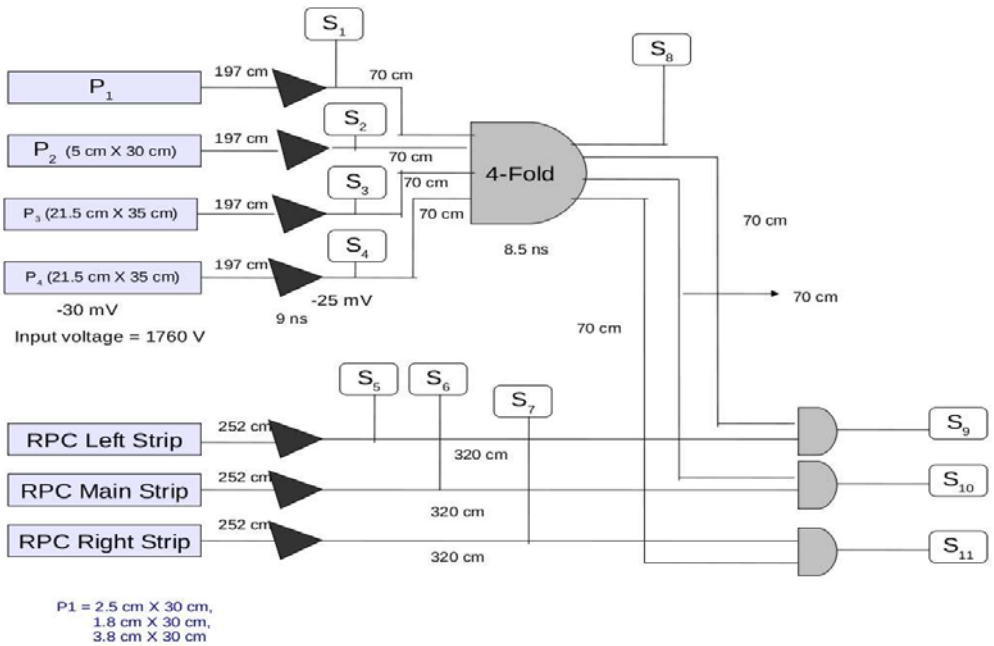

Figure 3: Circuit diagram for testing the RPC.

A threshold voltage of -30 mV (optimized) (Kanishka 2015) was applied to all the discriminators connected with the four scintillator paddles. Signals from all the four paddles were ANDed together to give $P_1.P_2.P_3.P_4$ a 4-fold signal, that acted as a trigger. The trigger and the signal from main strip of pick-up panel of RPC was ANDed and aligned together. Signals from main strip, right and left strips were sent to discriminator and delayed before being ANDed with the trigger signal. When the muon passed through this 4-fold coincidence and RPC, only then the scalar counted it as one count. The number of time this condition was satisfied gave efficiency, as given by the equation:

$$\text{Efficiency} = \frac{\text{Number of strip hits and trigger}}{\text{Total number of trigger}} \qquad (1)$$

The fluctuations in the efficiency were due to the "noise rate", which is the rate at which random noise signal hits the RPC strip. It can be due to dark current in the chamber, cosmic ray particles and stray radioactivity. The RPC strip when not aligned with coincidence window then the signal was picked up by adjacent strips (1st and 3rd), and caused "cross-talk". It can be due to misalignment of the strip of pick-up panel of RPC or due to inadequate amount of quenching gas resulting in the spread of discharge. Using the concept discussed, the results were obtained which are discussed in the next section.

RESULTS

The efficiency and cross-talk have been obtained using the methodology explained above (Kanishka R. *et al*. 2016). Figure 4 shows the efficiency and cross-talk of RPC with the strip width of size: 1.8 cm, 2.8 cm and 3.8 cm in the avalanche mode (three gas mixture). For avalanche mode, the proportion of gases used were *Freon* (*R134a*) : Isobutane : SF_6 :: 95.15 : 4.51 : 0.34. From the figures, it is observed that the efficiency of the RPC increases with voltage and reaches a plateau at higher voltage. The efficiency is greater than 90%. The fluctuations are due to the noise rate. The small width of strips (1.8 cm) also add to the fluctuations as the adjacent strips interfere with each other. A shift in threshold voltage was also observed with the decrease in the strip width size. Table 1 shows the efficiency and cross-talk measurements (approximate values) of RPC operated in avalanche mode with different strip widths of pick-up panels at their operating voltages.

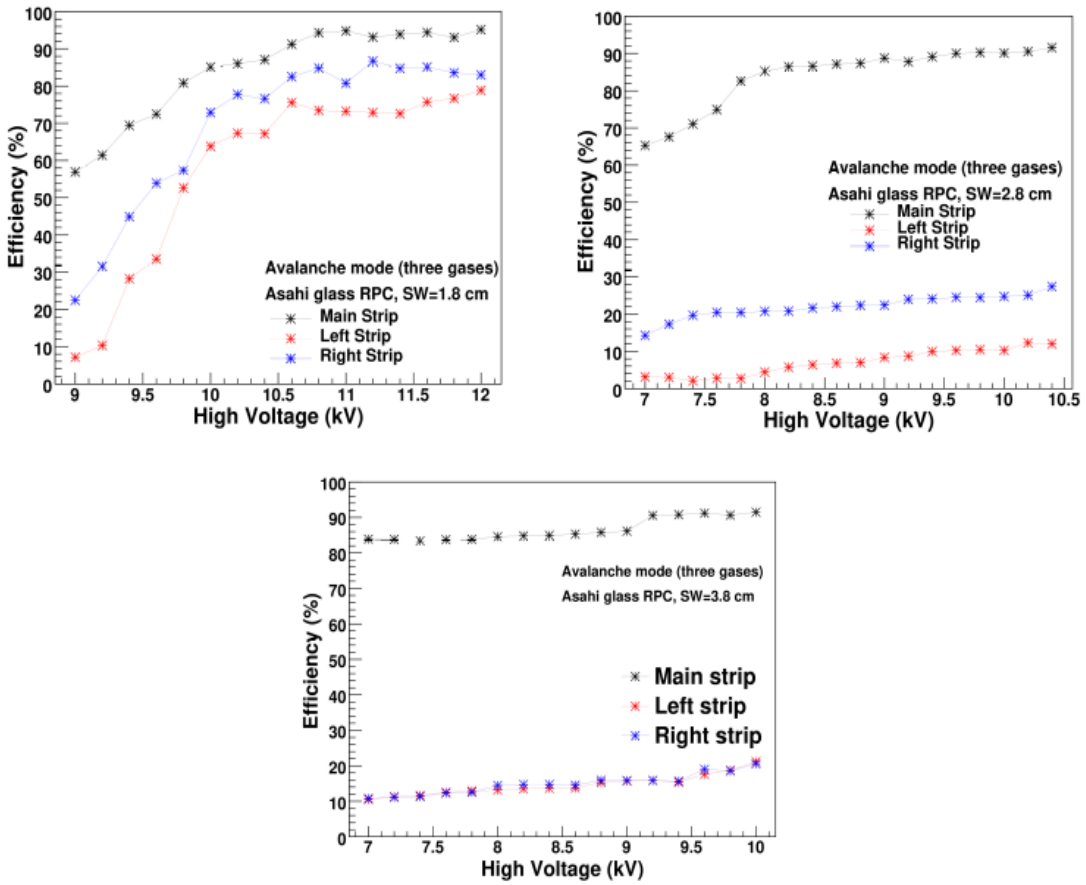

Figure 4: Efficiency and cross-talk of RPC with the strip width size = 1.8 cm, 2.8 cm and 3.8 cm, respectively.

Table 1: Efficiency and cross-talk measurements of the RPC operated in avalanche mode with different strip widths at their operating voltages.

Strip width (cm)	Efficiency (%)	Cross-talk (%)
1.8	95	78
2.8	91	12
3.8	91	20

DISCUSSIONS AND CONCLUSION

A proper R&D of resistive plate chambers is important as these are the active detectors. A glass RPC and pick-up panels were fabricated for the study. The effect of changing strip width of pick-up panels on the performance of RPC has been studied. Strip width optimization is necessary in order to obtain physics results of the users choice with better precision. A shift in threshold voltage was observed for the decrease in strip width size. So the RPC with strip width 2.8 and 3.8 cm gave better results than the strip width of 1.8 cm as the cross-talk in them was reduced. These results will be used for the simulation studies to obtain muon momentum resolution, reconstruction efficiency and charge identification.

ACKNOWLEDGEMENTS

The authors thank engineers and technical staff of PU-EHEP lab. R. Kanishka acknowledges UGC/DAE/ DST (Govt. of India) for funding.

REFERENCES

Abe, T., *et al.* (Belle-II Collaboration). 2010. Belle II Technical Design Report, KEK-REPORT 2010-1, arXiv:physics.ins-det/1011.0352.

Athar, M. S., *et al*., 2006., India-based Neutrino Observatory: Project Report Volume I, http://www.ino.tifr.res.in/ino/OpenReports/INOReport.pdf.

Bhattacharya, K., *et al*.,(INO Collaboration), 2014. Error propagation of the track model and track fitting strategy for the iron calorimeter detector in India-based neutrino observatory, Computer Physics Communications (Elsevier) 185 (12) 3259-3268.

Cardarelli, R., V. Makeev and R. Santonico, 1996. Avalanche and streamer mode operation of resistive plate chambers, Nucl. Instrum. Meth. A 382, 470.

Cardarelli, R., A. Di. Ciaccio and R. Santonico, 1993. Performance of a resistive plate chamber operating with pure CF_3Br. Nucl. Instrum. Meth. A 333, 399.

Chatterjee, A., *et al*., 2014. A Simulations Study of the Muon Response of the Iron Calorimeter detector at the India-based Neutrino Observatory, JINST 9 P07001, [arXiv:1405.7243].

CMS Collaboration, 1994. CMS, the Compact Muon Solenoid: Technical proposal, CERN-LHCC-94-38,CERN-LHCC-P-1(1994).

Fonte, P., 2000. High-resolution timing of MIPs with RPCs-a model, Nucl. Instrum. Meth. A, 456, 6.

Fonte, P., 2002. Applications and new developments in resistive plate chambers IEEE Trans. on Nucl. Sci., 49, 881.

Ghosh, A., T. Thakore and S. Choubey, 2013. Determining the Neutrino Mass Hierarchy with INO, T2K, NOvA and Reactor Experiments, JHEP 1304, 009, arXiv:hep-ph/1212.1305.

Indumathi, D., *et al*., 2006. Neutrino oscillation probabilities: Senstivity to parameters, arXiv:hep-ph/0603264v2.

Kalmani, S. D., *et al*., 2009. On-line gas mixing and multi-channel distribution system, Nucl. Instrum. Meth. A, 602.

Kanishka, A., 2015. Study of upward-going muons in ICAL detector at India-based Neutrino Observatory, Ph.D thesis, Department of Physics, Panjab University, Chandigarh, India.

Kanishka, R., *et al*., Optimisation and Characterisation of Glass RPC for India-based Neutrino Observatory Detectors [arXiv:1605.09361]

Kanishka, R., *et al*., Simulation of strip-width of read-out panels of resistive plate chambers to be communicated for publication.

Santonico, R. and R.Cardarelli, 1981. Development of resistive plate counters. Nucl. Instrum. Meth. A, 187, 377.

Santonico, R. and R.Cardarelli, 1988. Progress in resistive plate counters. Nucl. Instrum. Meth. A, 263, 20.

Satyanarayana, B., 2009. Design and Characterisation Studies of Resistive Plate Chambers, Ph.D thesis, Department of Physics, IIT Bombay, India, PHY-PHD-10-701.

Thakore, T., A. Ghosh, S. Choubey and A. Dighe, 2013. The Reach of INO for Atmospheric Neutrino Oscillation Parameters, JHEP 1305,058, arXiv:hep-ph/1303.2534.

MACHINE LEARNING FOR PARTICLE CLASSFICATION

T. Jyoti*, V. Bhatnagar
Department of Physics, Panjab University, Chandigarh 160 014, India

Abstract

Machine learning plays a great role in many different sectors including healthcare, finance, automobiles (self-driving cars) and social networking sites. It has already extended its applications in the field of sciences including physics for dealing with complex problems. In the context of particle physics, machine learning can be useful for analyzing huge volumes of data collected with the particle detectors. The potential of machine learning as a particle classifier (charged pion, proton, electron, muon, gamma) using the images of the charged particle trajectories simulated with a particle imaging Liquid Argon Time Projection Chamber (LArTPC) detector has been demonstrated in this paper.

Keywords: Neural networks, Convolutional neural network, loss, accuracy.

INTRODUCTION

High energy physics experiments aim for understanding the nature by studying and analyzing the data collected in particle detectors. An important part of understanding particle interactions involve distinguishing different types of interactions and particles produced in the detector. Traditional computer algorithms are designed for analyzing specific set of interactions and based on the prior knowledge of the properties of particles produced in the interaction. Currently, several experiments have started implementing the machine learning (ML) algorithms for analyzing the data. The ML algorithm once designed, learns itself how to separate different interactions. Neutrino experiments at Fermilab including MicroBooNE, NOvA benefit from machine learning (Aurisano 2016; MicroBooNE collaboration 2016). ML techniques have also been employed in many of the data analyses at Compact Muon Solenoid (CMS) experiment including the Higgs discovery (Andrews 2018). The focus of this paper is to leverage machine learning technique to analyze a simulated dataset of charged particle trajectories (pattern of energy deposition) recorded with an LArTPC detector.

MACHINE LEARNING

The machine learning is defined as the field of study that gives computers the ability to learn without being explicitly programmed (Simons 2013). It explores methods that can learn from the observational data and figure out solutions to the problems [Introduction to Machine Learning]. To make the method learn from the examples and test its performance, the data available is split in testing and training groups.

***Training Dataset*:** Initial set of data helps the method to learn how to process the available information. In the field of image processing and computer vision, the training dataset consists of a large number of images and the method is trained on each of those images so that it can recognize the image features like shapes, edges, ridges etc.

***Testing Dataset*:** The ability of the trained method is evaluated using a testing dataset. Any overlap between the training and the testing dataset is completely avoided to have an independent assessment of the performance of the method. The ability to learn the processing of the data and extending it to the cases which were not provided by the training examples is a promising feature of machine learning. The approaches to make a machine learn can be broadly classified into three categories:

***Supervised Learning*:** The computer has to learn and infer the rules of mapping the input to the output using a set of labelled input data. Classification and Regression are a few of the supervised machine learning algorithms.

***Unsupervised Learning*:** No labels are given to the input data and the computer is left on its own to find patterns in the data. It could be complicated than the supervised learning as the problem with no labels becomes less clear, however, this approach is helpful for identifying patterns in the data that were previously unknown. Clustering and anamoly detections are some of the unsupervised learning methods where the features are not understood beforehand.

***Reinforcement Learning*:** This computational approach is based on learning from interactions with the dynamic environment and very similar to how one learns in everyday life where good actions get rewarded and become more common and the bad ones are discouraged. The learning involves mapping situations to actions to maximize a numerical award signal (Sutton 2014, 2015). Reinforcement learning is most commonly used in gaming as games provide rich domain for testing the performance of the reinforcement learning algorithms.

Figure 1 shows the ML algorithms from each of the above categories applied across different fields.

*Corresponding Author: jyoti571@gmail.com
MS Received: November 9, 2019, Accepted: December 30, 2019

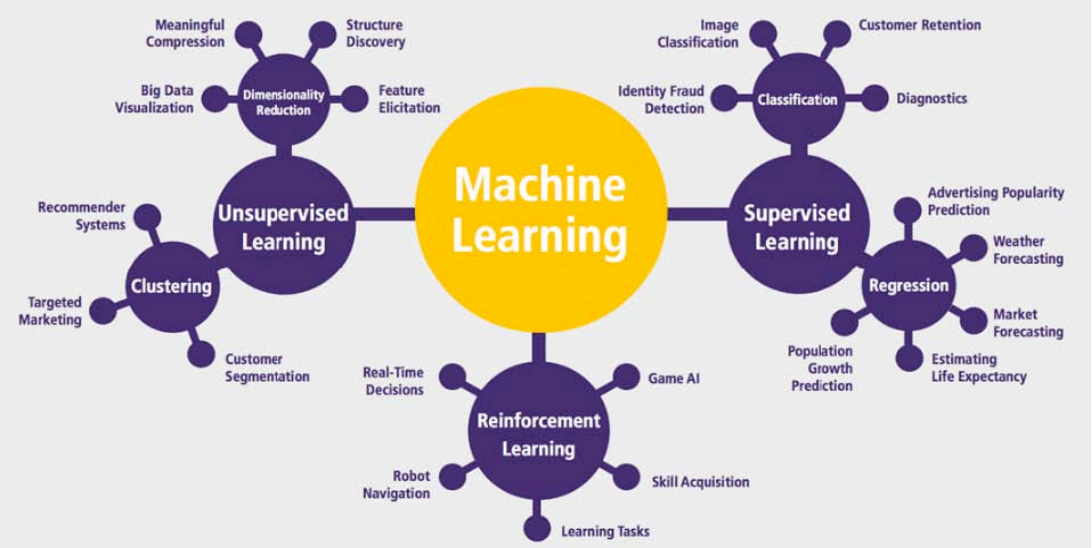

Figure 1: Applications of the machine learning methods in different sectors (EDUCBA 2019).

ARTIFICIAL NEURAL NETWORKS

An artificial neural network is a category of machine learning methods where the learning can be supervised or unsupervised one. The neural network has a *layered* structure based on the neurological functioning of the human brain where each layer consists of a certain number of *neurons*. The neurons are the basic building blocks of a neural network. In training, the neurons process the number of inputs iteratively to adjust the parameters of the network for an optimal prediction of the data (Leopord 2016).

There are several types of artificial neural networks based on their working principals including feed forward neural network, radial basis function neural network, recurrent neural network and convolutional neural network. A convolutional neural network (CNN) consists of an input layer, one or more hidden layers (where the processing of data actually happens) and an output layer as shown in figure 2. The CNNs, in particular, have proven to be quite effective in the field of image recognication and classification.

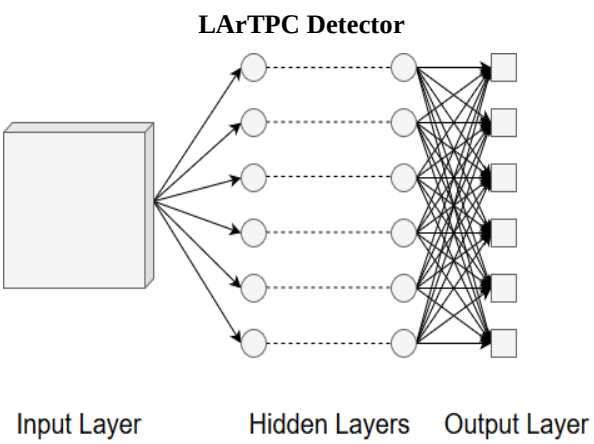

Figure 2: The layers of a CNN (Sherman 2019).

Particle detectors in high energy physics are generally designed to look for new physics phenomenon or compare experimental measurements to theoretical predictions. The aim of a particle detector is to discover the identity of the charged particle alongwith the estimation of its kinematic parameters. The charged particles ionize the material of the detecting medium while traversing the detector's volume, providing tiny signals that are recorded by the detector.

Investigating the details provided by the detector to identify each particle is a technical challenge as different particles exhibit different topology owing to the difference in their masses, charge and the type of interactions they undergo (Wingerter-Seez, 2014). Charged hadrons such as pions and protons leave at rack before depositing their energy in the detector. The muons pass straight through the detector as they have low probability to interact and deposit energy mainly through ionization. The electrons and photons create electromagnetic hower and their paths show many branching trajectories. This distinction between the energy deposition pattern helps the particle-identification (PID) techniques to correctly identify each particle.

LArTPC, a type of particle detector, is being increasingly used in the field of particle detection for its ability to provide efficient differentiation between the particles. It provides a great detail of the particle interactions producing high resolution images of charged particles travelling in the detector. An LArTPC consist of a huge volume of liquid argon bounded by a cathode and an anode plane. When a charged particle passes through the sensitive region of the detector, it produces ionization electrons and scintillation light along its trajectory (Adams 2018). The scintillation light is detected by an array of photomultiplier tubes (PMTs), providing a timing measurement whereas the ionization electrons drift

towards the wire planes under an applied electric field, where there charge is collected and measured as shown in figure 3.

For performing a physics data analysis, an accurate categorization of the ionization trajectory sorted by the particle type is important. The next section studies the application of machine learning algorithm, CNNs as a PID technique, to classify a sample of charged particle trajectories simulated with the LArTPC detector.

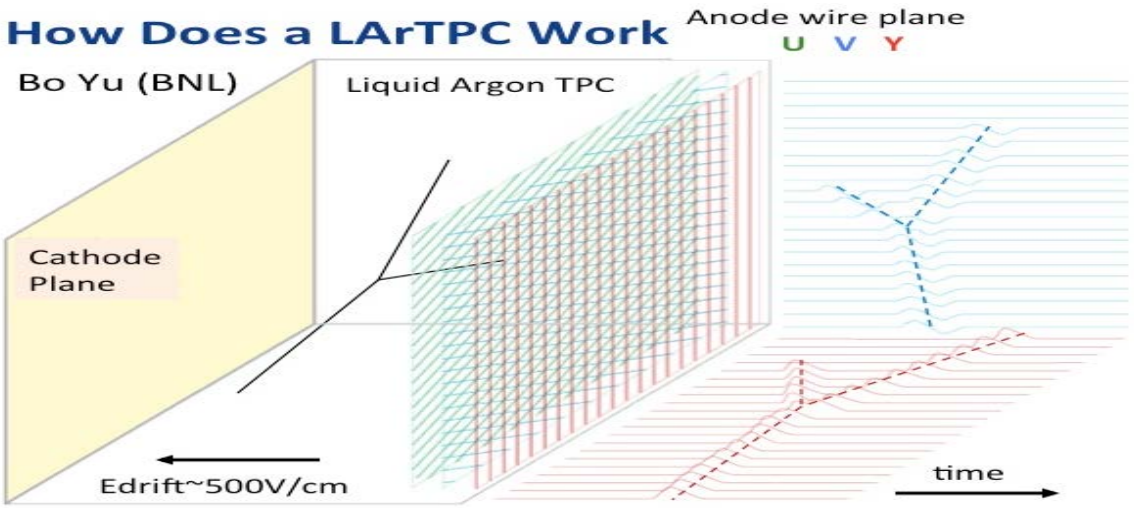

Figure 3: The working principle of an LArTPC. A charged track inside the detector's volume ionizes electrons. The applied electric field causes the ionization to drift toward readout anode wire planes and be collected (Katori 2011).

CHARGED PARTICLE IMAGE CLASSIFICATION USING CNN

The image classification dataset consists of five particles' trajectories (charged pion, proton, electron, muon, gamma) simulated with the LArTPC detector. The generation point of each particles is uniformly distributed within 5.12 m cubic volume and the direction is isotropic. Figure 4 shows the image of the charged particles travelling in the detector. The CNN implemented for the image classification has 10 layers that help extracting the features from the images. The initial layers focus on the low level features such as vertical or horizontal line in the image while the later layers are able to extract more abstract information from the images. The network is fed with half of the available data for training. Since the dataset is a simulated one, the network learns to associate the images with their input labels during the training. Remaining half of the data set is used for testing the network's performance.

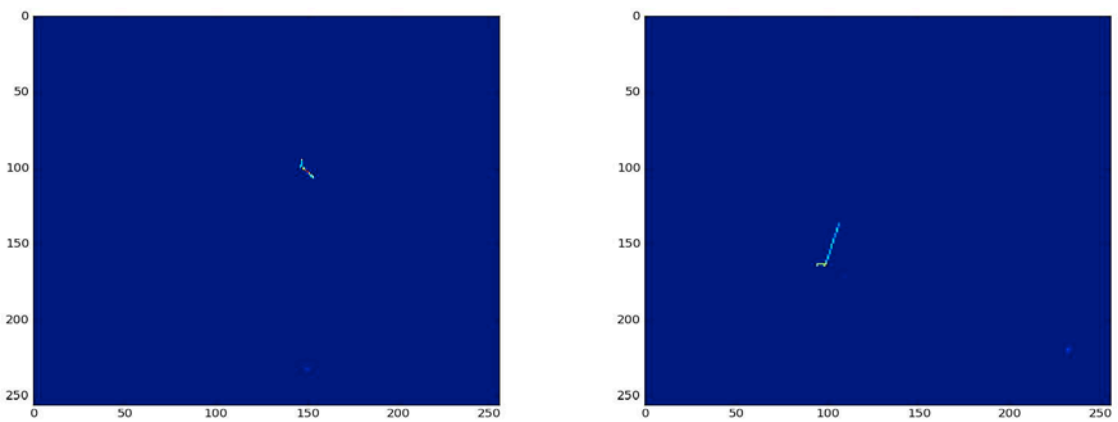

Figure 4 : The trajectory of a simulated proton recorded in the LArTPC detector's volume.

RESULTS

The CNN built to solve the problem is optimized using a loss funtion.The loss function predicts the *loss* which is the difference between the output predicted by the network and the actual output. Different types of loss functions are used depending on the problem in hand including mean-squared error, mean absolute error and cross-entropy (ML Cheatsheet Documentation 2019). This particular study uses cross entropy as the loss function which increases as the predicted value diverges from the actual input label.

Accuracy is a measure of the performance of the method. It is defined as fraction of instances when the method makes correct classification of the input data.

$$\text{Accuracy} = \frac{\text{Number of correct predictions}}{\text{Total number of predictions}} \quad (1)$$

The accuracy and the loss for the network implemented for the image classification with the LArTPC detector is shown in figure 5. This model reaches an accuracy of nearly 80% for the training data and 70% for the testing dataset after 5000 iterations. The loss curve reaches a minimum of 0.4 and 0.6 for the training and testing data, respectively, showing that the loss of the network falls with each iteration.

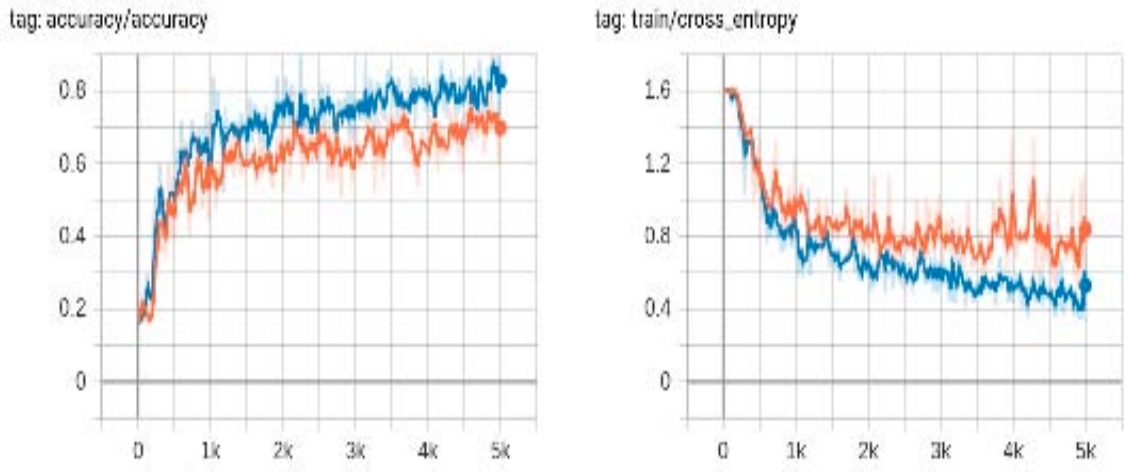

Figure 5 : The accuracy (left) and loss (right) curves for the training and testing samples. The orange line represents the metric measured on a test sample and the blue line represents the same for the training sample.

DISCUSSIONS

This study shows the application of CNN, one of the machine learning algorithms mainly used for computer vision, for the charged particle identification traversing the LArTPC detector. The accuracy of the method increases to 80% on the training dataset after it is trained long enough (5000 iterations). However, the accuracy is comparatively lower on the testing dataset, nearly 70% showing that the method has got slightly over-fitted to the training data. In general, the method is expected to have the generalization ability, i.e., make accurate predictions for the data it was not trained on. The best way to avoid overfitting is using larger dataset covering the entire range of inputs that the method might have to handle. A more learned method will be able to generalize itself better on the testing data.

The ML methods learn to make predictions based on the observations made. Being data driven, these are often much more accurate than the traditional methods of data analysis. However, enough training examples are needed to enhance the performance of the method.

ACKNOWLEDGEMENTS

The authors are thankful to the Deep Learn Physics group as a whole for making the data available and contributing to the development of machine learning algorithms in the field of scientific research. The technique used is fully reproducible and the implementation is available on the website deeplearnphysics.org.

REFERENCES

Adams, C., et al. 2018. *A Deep Neural Network for Pixel-Level Electromagnetic Particle Identification in the MicroBooNE Liquid Argon Time Projection Chamber*, https://arxiv. org/pdf/1808.07269.pdf.

Andrews, M., et al., 2018. *End-to-End Event Classification of High-Energy Physics Data*, inspirehep.net/record/1699884.

Aurisano, A., *et al*., 2016. A Convolutional Neural Network Neutrino Event Classifier, arXiv: 1604.01444.

EDUCBA 2019. Machine Learning Algorithms https://www.educba.com/machine-learning-algorithms/

Introduction to Machine Learning, The Wikipedia Guide.datascienceassn.org/IntroductiontoMachineLearning.pdf

Katori, T. (the MicroBooNE Collaboration), 2011. *MicroBooNE, A Liquid Argon Time Projection Chamber (LArTPC) Neutrino Experiment*, arXiv:1107.5112.

Leopord, H., et al., 2016. *A Survey and Analysis on Classification and Regression Data Mining Techniques for Diseases Outbreak Prediction in Datasets*, http://theijes.com/ papers/v5-i9/A050901011.pdf.

MicroBooNE collaboration, 2016. *Convolutional Neural Networks Applied to Neutrino Events in a Liquid Argon Time Projection Chamber*, arXiv:1611.05531 .

ML Cheatsheet Documentation. 2019. https://readthedocs.org/projects/mlcheatsheet/downloads/pdf/latest/

Sherman, B., J.E. Hopkins, Z. Smith. 2019. *Convolutional Neural Networks*, https://machine-learning-course.readthedocs.io/en/latest/content/deep_learning/cnn.html

Simon, P., 2013. *Too Big to Ignore: The Business Case for Big Data*. Wiley. p.89. ISBN978-1-118-63817-0.

Sutton, R. S., and A.G. Barto, (2014, 2015) *Reinforcement Learning: An Introduction*, SuttonBartoIPRLBook2ndEd.pdf.

Wingerter-Seez, I., 2014 Particle Physics Instrum., arXiv:1804.11246.

Pb. Univ. Res. J (Sci.) Vol. 69, 2019, pp 85-91

STUDY OF PARTICLE PRODUCTION IN HEAVY-ION COLLISIONS USING ULTRA RELATIVISTIC QUANTUM MOLECULAR DYNAMICS MODEL

Lokesh Kumar*, Rajwinder Kaur and Natasha Sharma
Department of Physics, Panjab University, Chandigarh -160014 INDIA

Abstract

The study of particle production in high-energy heavy-ion collisions provides information of the system produced in such collisions. We present the results on particle production of identified particles like pions, kaons, protons, and their anti-particles using the Ultra Relativistic Quantum Molecular Dynamics (UrQMD) Model for gold on gold (Au+Au) collisions at center-of-mass energies $\sqrt{s_{NN}}$ = 2, 7.7, 9.2, 11.5, 19.6, 27, 39, 62.4, 200 GeV and for lead on lead (Pb+Pb) collisions at $\sqrt{s_{NN}}$ = 2.76 TeV in mid-rapidity (|y|<0.1) region. The particle number density or particle yields (dN/dy) and various particle yield ratios are presented as a function of collision energy. The results from the UrQMD model are compared with the corresponding published results from the world experiments. It is observed that the particle yields of pions, kaons, and antiprotons increase with increasing collision energy. However, the proton yields first decrease as a function of energy and then stays constant. The π^-/π^+ ratio is greater than unity at lower energies and becomes unity at higher energies. The K^-/K^+ and $\bar{p}/p$ ratios are less than unity at lower energies but approaches unity at higher energies. The results suggest that particle production mechanism is different at lower energies as compared to that at higher energies. The UrQMD model qualitatively describes the energy dependence trend of particle production observed in experimental data.

Keyword: Particle Production, Heavy-ion, UrQMD, Transverse Momentum Spectra

INTRODUCTION

The ultra-relativistic heavy-ion collisions recreate the conditions similar to that existed in the early universe. These collisions can produce strongly interacting matter under extreme conditions of high temperature and net-baryon density (Adams 2005). This leads to the formation of a deconfined state of matter known as the quark-gluon plasma (QGP). One of the main goals of the heavy-ion collision experiments is to study the properties of QGP and to explore the Quantum Chromodynamics (QCD) phase diagram (Adams 2005). The QCD phase diagram is usually plotted as temperature (T) versus baryon chemical potential (μ_B). Both the axis temperature and baryon chemical potential can be simultaneously controlled by varying the colliding beam energy in heavy-ion collisions. These two axes are obtained experimentally by measuring the transverse momentum (p_T) distribution of the produced identified particles and using the statistical thermal model (Andronic 2018, Stock 2019, Wheaton 2009). Study of yields (dN/dy) of produced particles and their ratios provide information about the particle production mechanism and axes of QCD phase diagram. The various particle ratios are studied as a function of beam energy using the Ultra Relativistic Quantum Molecular Dynamics (UrQMD) model and the results are compared with those from various experiments.

ULTRA RELATIVISTIC QUANTUM MOLECULAR DYNAMICS MODEL

The Ultra-Relativistic Quantum Molecular Dynamics (UrQMD) model is a fully integrated monte carlo simulation package used to generate relativistic heavy-ion collisions (Bass 1998, Bleicher 1999). The model is based on a microscopic transport theory where the phase space description of the reaction is important. UrQMD is designed as a multipurpose tool for studying heavy ion related effects ranging from multi-fragmentation to particle production. It is based on the covariant propagation of color strings, constituent quarks and diquarks accompanied by baryonic and mesonic degrees of freedom. It simulates multiple interactions of in-going and newly produced particles. It has many applications in particle physics, detector design, cosmic ray studies, high energy experimental physics and medical physics. In the present work, the UrQMD model version 2.3 has been used.

The events are generated using the UrQMD model for the Au+Au collisions at $\sqrt{s_{NN}}$ = 2, 7.7, 9.2, 11.5, 19.6, 27, 39, 62.4, 200 GeV energies and for Pb+Pb collisions at $\sqrt{s_{NN}}$ = 2760 GeV energy. These colliding systems and energies are chosen based on the experimental data available from various heavy-ion experiments. This is the first time this model is used to study the particle

*Corresponding Author: lokesh@pu.ac.in
MS Received: October 15, 2019, Accepted: November 27, 2019

production for such a vast range of energies. For this study and to compare the model results with the experimental data, events which have top 5% charged particle multiplicity (representing central collisions with small impact parameter of heavy-ion collisions) are selected for each system and energy. Figure 1 shows the distributions of produced charged particle multiplicity for 0-5% central Au+Au collisions at various center-of-mass energies. It is observed that the average multiplicity of produced particles increases with increase in collision energy.

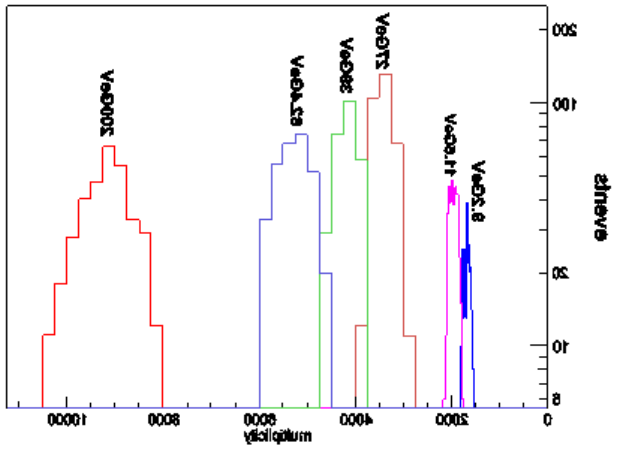

Figure 1: Charged particle multiplicity distribution for 0-5% central Au+Au collisions at various centre of mass energies

The rapidity distributions of pions for Au+Au collisions at $\sqrt{s_{NN}}$ = 2, 7.7, 9.2, 11.5, 19.6, 27, 39, 62.4, 200 GeV and for Pb+Pb collisions at $\sqrt{s_{NN}}$ = 2760 GeV are shown in Figure 2. The rapidity is defined as

$$y = \frac{1}{2} ln \left(\frac{E+p_z}{E-p_z} \right) \quad (1)$$

where, $E = \sqrt{p^2 + m^2}$, represents the energy of the produced particle, $p = \sqrt{p_x^2 + p_y^2 + p_z^2}$ represents the total momentum and *m* represents its mass. It is observed from the rapidity distribution that the rapidity becomes flat with increase in collision energy. This means that collisions become more transparent as the collision energy increases. The experimental results are available for the mid-rapidity region, i.e., |y| < 0.1, the same cut is applied in the analysis of the model results, so that they can be compared to the experimental data.

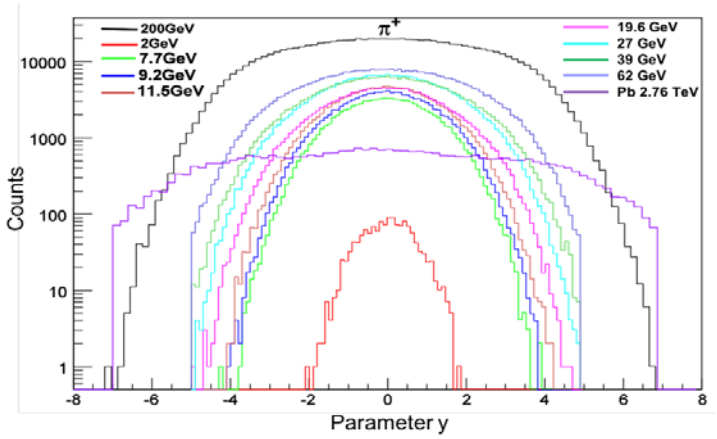

Figure 2: Rapidity distribution of π^+ for heavy-ion collisions at various energies.

RESULTS

Particle Yields

The particle yield, representing the number of particles produced in a given rapidity interval, at mid-rapidity region can be calculated as

(2)

Where $N_{\text{particles}}$ is the number of identified particles, *dy* is the rapidity interval, and N_{events} is the total number of events analyzed. Figures 3a-c show the particle yields of pions, kaons and protons, and their respective anti-particles as a function of center-of-mass energy. The model qualitatively explains the energy dependence behavior observed in experimental data from E866 & E917 collaborations (Ahle 2000a,b), E895 collaboration (Klay 2002), E877 collaboration (Barrette 2000), E802 collaboration(Akiba 1996, Ahle 1998, Ahle 1999a,b), NA49 collaboration (Afanasiev 2002, Anticic 2004, Alt 2006, Alt 2008), STAR collaboration (Abelev 2010, Aggarwal 2010, Kumar 2013a,b, Abelev 2009, Adamczyk 2017) and ALICE collaboration (Abelev 2013). The yields of π^+ and π^- at each energy is of the similar order. The dN/dy of K^+ and K^- increases with increasing energy for both UrQMD model and experimental data. The experimental results for K^- are reasonably explained by the UrQMD model from the AGS energies up to higher BES energies, *viz.*, 39 GeV. The yields of K^+ at lower energies is higher compared to K^- suggesting that K^+ yields are mainly produced by associated production with Λ at lower energies. At higher energies, the $K^+$and K^- yields become similar suggesting that the pair production phenomenon dominates.

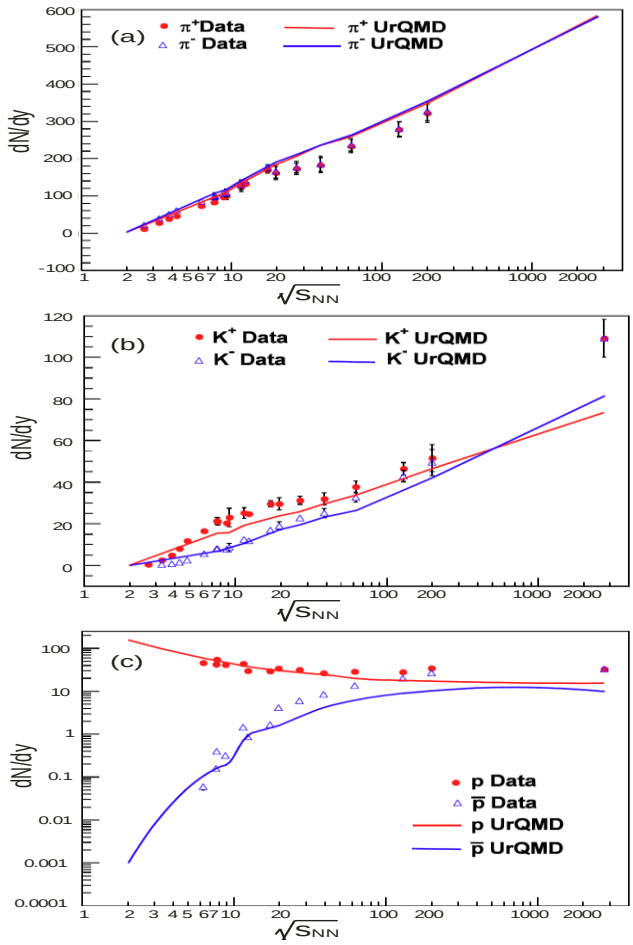

Figure 3: The particle yields of (a) pions (left), (b) kaons (middle), (c) protons (right) and their anti-particles as a function of center-of-mass energy. The lines represent the model results and symbols are used for the experimental data. Red color is used for positively charged particles and blue for negatively charged particles.

The dN/dy of protons (Figure 3 (c)) decreases from lower energies up to around 60 GeV and then remains constant up to 2.76 TeV for both UrQMD model and experimental data. The anti-protons yield increases with increasing energy and becomes constant from 200 to 2760 GeV for both UrQMD model and experimental data. The yield of protons at lower energies is higher compared to anti-protons suggesting that there is large baryon stopping at lower energies. At higher energies, the proton and anti-proton yields become similar suggesting that baryon stopping is negligible at higher energies.

PARTICLE RATIOS

The particle ratios are constructed by taking ratios of the corresponding particle yields dN/dy. Figure 4(a)-(c) show the anti-particle to particle ratios pions, kaons and protons, respectively. Figure 5(a)-(d) show the mix particle ratios for these positively and negatively charged particles separately. The experimental data results from E866 & E917 collaborations (Ahle 2000a,b), E895 collaboration (Klay 2002), E877 collaboration (Barrette 2000), E802 collaboration (Akiba 1996, Ahle 1998, Ahle 1999a,b), NA49 collaboration (Afanasiev 2002, Anticic 2004, Alt 2006, Alt 2008), STAR collaboration (Abelev 2010, Aggarwal 2010, Kumar 2013a,b, Abelev 2009, Adamczyk 2017) and ALICE collaboration (Abelev2013) are shown by red circle symbol and the UrQMD model results are represented by the blue lines.

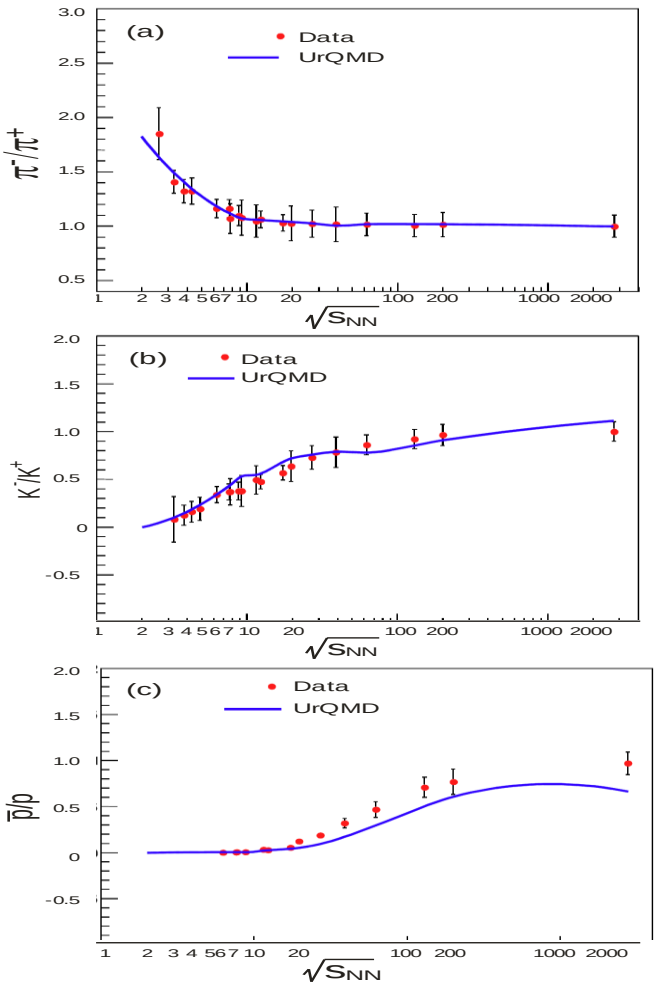

Figure 4: Anti-particle to particle ratios as a function of center-of-mass energy for 0-5% central heavy-ion collisions in mid-rapidity ($|y| < 0.1$).

Figure 4(a) shows the π^-/π^+ ratio as a function of energy. It is observed that the ratio is almost one for energies above ~10 MeV for both the UrQMD model and experimental data. However, at lower energies, the π^-/π^+ ratio is greater than one. This may be due to the significant contribution from resonance decays such as Δ baryons. The UrQMD model seems to explain the data very well. Figure 4(b) shows the K^-/K^+ ratio as a function of energy. The ratio increases with increasing energy and approaches towards unity for higher energies. At lower energies, K^+ yield is higher than K^- suggesting that the K^+ production at lower energies is dominated by the associated production of K^+ with Λ.The UrQMD model explains the K^-/K^+ ratio quite well. Figure 4(c) shows the anti-proton to proton ratio increases with increasing energy, reaching towards value of unity at higher energies for both UrQMD model and experimental data. At lower energies, the anti-proton to proton ratio is much less than one. This may be due to the large baryon stopping at lower energies. The UrQMD model seems to qualitatively explain the data.

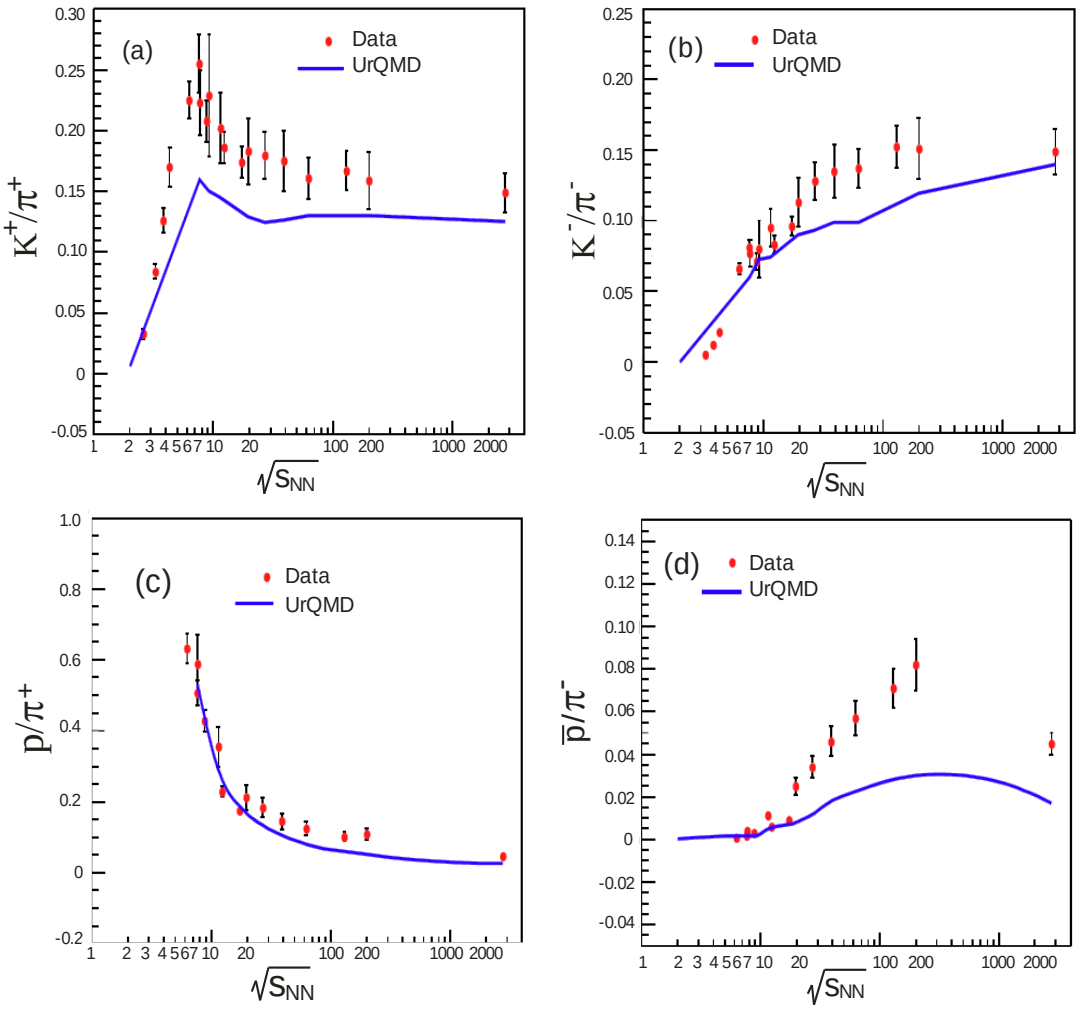

Figure 5: Mixed particle ratios of (a) K^+/π^+, (b) K^-/π^-, (c) p/π^+ and (d) $\bar{p}/\pi^-$ as a function of center-of-mass energy for 0-5% central heavy-ion collisions in mid-rapidity ($|y| < 0.1$).

Figure 5(a) shows the K^+/π^+ ratio as a function of energy. The ratio increases with increasing energy, becomes maximum at collision energy close to 7 GeV, then decreases and become constant from 200 to 2760 GeV, for both the UrQMD model and experimental data from E866 & E917 collaborations (Ahle 2000a,b), E895 collaboration (Klay 2002), E877 collaboration (Barrette 2000), E802 collaboration (Akiba 1996, Ahle 1998, Ahle

1999a,b), NA49 collaboration (Afanasiev 2002, Anticic 2004, Alt 2006, Alt 2008), STAR collaboration (Abelev 2010, Aggarwal 2010, Kumar 2013a,b, Abelev 2009, Adamczyk 2017) and ALICE collaboration (Abelev 2013). The NA49 experiment calls the peak structure as "horn". According to NA49, this horn in the energy dependence of K^+/π^+ ratio suggests the phase transition from hadron gas to quark-gluon plasma. However, the observed peak could be related to the maximum baryon density at 7.7 GeV as predicted by Cleymans (2006). The UrQMD model shows similar trend as data but does not explain the horn structure quite well. Figure 5(b) shows the K^-/π^- ratio as a function of energy. The ratio increases with increasing energy for both the UrQMD model as well as for the experimental data. The UrQMD model shows similar trend as the data. The p/π^+ is shown in Figure 5(c). It is seen than the ratio decreases with increasing energy for both the UrQMD model and experimental data. The higher value of p/π^+ ratio is due to large baryon stopping at mid-rapidity at lower energies. The UrQMD model explains the data quite well. The $\bar{p}/\pi^-$ ratio is shown in Figure 5(d). The ratio increases with increase in energy. It becomes maximum at collision energy close to 200 GeV and then decreases towards 2.76 TeV for both the UrQMD model and experimental data. The UrQMD model qualitatively explains the energy dependence behaviour observed in experimental data.

SUMMARY

The production of identified particles like pions, kaons, protons and their anti-particles are studied using the UrQMD model for Au+Au collisions at $\sqrt{s_{NN}}$ = 2, 7.7, 9.2, 11.5, 19.6, 27, 39, 62.4, 200 GeV and for Pb+Pb collisions at $\sqrt{s_{NN}}$ = 2.76 TeV in mid-rapidity (|y|<0.1) region. The various particle ratios are also studied at these energies. The model results are compared with the available experimental data. It is observed that the pion yields increase with increasing energy. The ratio π^-/π^+ suggests that π^- yields at lower energies are higher compared to π^+ yields. This may be due to the resonance decays such as Δbaryons at lower energies. The K^+ and K^- yield increases with increase in energy. At lower energies the K^+ yield is higher compared to that of K^-. Therefore, K^-/K^+ ratio is less than unity at low energies and becomes close to unity at high energy. In addition, K^+/π^+ first increases towards 7.7 GeV, shows a peak around 7.7 GeV and then decreases towards higher energies. All these results suggest that K^+ production at lower energies is dominated by the associated production of K^+ with Λ. At higher energies, K^+ and K^- pair production dominates. The anti-proton yield increases with increase in energy, whereas proton yield is higher at low energies and then decreases with increase in energy. Both the proton and anti-proton yields saturate from 62.4 to 2760 GeV. The anti-proton to proton ratio is much less than 1 at lower energies and becomes close to 1 at higher energies. In addition, the p/π^+ ratio decreases with increasing energy. All these results suggest that the proton yields at lower energies are higher due to the large baryon stopping at lower energies. The K^-/π^- and $\bar{p}/\pi^-$ ratios increase with increasing energy.

The UrQMD model is able to explain the heavy-ion collisions over a wide energy range, i.e., from 2 GeV upto 2760 GeV. The model has been used successfully at lower energies and this is the first instance that this model is studied in such a vast range of energies. The model reproduces the energy dependence trend of all the experimental yields and ratios qualitatively. We conclude that the pion, kaon, proton and their anti-particle yields are well explained by the UrQMD model especially at lower energies. The experimentally measured anti-particle to particle ratios are also well explained by the UrQMD model. However, the model could not explain the mixed particle ratios except p/π^+ ratio well.

ACKNOWLEDGEMENTS

RK acknowledges the support of resources from the EHEP-HI laboratory and Physics Department Panjab University, Chandigarh for the completion of this project work. NS acknowledges the support of DST-SERB Ramanujan Fellowship (D.O. No. SB/S2/RJN-084/2015). LK acknowledges the support of the SERB grant No. ECR/2016/000109.

REFERENCES:

Abelev, B. I. *et al.* (STAR Collaboration). 2009. Systematic measurements of identified particle spectra in pp, d+Au, and Au + Au collisions at the STAR detector. Phys. Rev. C79, 034909.

Abelev, B. I. *et al.* (STAR Collaboration). 2010. Identified particle production, azimuthal anisotropy, and interferometry measurements in Au+Au collisions at $\sqrt{s_{NN}}$ = 9.2 GeV. Phys. Rev. C81, 024911.

Abelev, B. I. et al. (ALICE Collaboration). 2013. Centrality dependence of π, K, and p production in Pb-Pb collisions at $\sqrt{sNN}$ = 2.76 TeV. Phys. Rev. C88, 044910.

Adamczyk, L. *et al.* (STAR). 2017. Bulk properties of the medium produced in relativistic heavy-ion collisions from the beam energy scan program. Phys. Rev. C96, 044904.

Adams, J. *et al*. (STAR Collaboration). 2005. Experimental and theoretical challenges in the search for the quark–gluon plasma: The STAR Collaboration's critical assessment of the evidence from RHIC collisions. Nucl. Phys. A757, 102-183.

Afanasiev, S. *et al.* (NA49 Collaboration). 2002. Energy dependence of pion and kaon production in central Pb+ Pb collisions. Phys. Rev. C66, 054902.

Aggarwal, M. M. *et al*. (STAR Collaboration). 2010. An experimental exploration of the QCD phase diagram: the search for the critical point and the onset of de-confinement. arXiv:1007.2613;

Ahle, L. *et al.* (E802 Collaboration).1998. Particle production at high baryon density in central Au+Au reactions at 11.6 GeV/. Phys. Rev. C57, 466.

Ahle, L. *et al.* (E-802 Collaboration, E-866 Collaboration).1999a. Centrality dependence of kaon yields in Si + Al amd Au + Au collisions at relativistic energies. Phys. Rev. C60, 044904.

Ahle, L. *et al.* (E802 Collaboration).1999b. Proton and deuteron production in Au+Au reactions at 11.6AGeV/c. Phys. Rev. C60, 064901.

Ahle, L. *et al.* (E866 Collaboration, E917 Collaboration). 2000a. Excitation function of K+ and π+ production in Au + Au reactions at 2–10 AGeV. Phys. Lett. B476, 1-8.

Ahle, L. *et al.* (E866 Collaboration, E917 Collaborations) 2000b. An excitation function of K− and K+ production in Au+ Au reactions at the AGS. Phys. Lett. B490, 53-60.

Akiba, Y. *et al.* (E802 Collaboration). 1996. Particle production in Au + Au collisions from BNL E866. Nucl. Phys. A610, 139C-152C.

Antici, T. et al. (NA49 Collaboration). 2004. Energy and centrality dependence of deuteron and proton production in Pb + Pb collisions at relativistic energies. Phys. Rev. C69, 024902.

Alt, C. *et al.* (NA49 Collaboration). 2006. Energy and centrality dependence of anti-p and p production and the anti-Lambda/anti-p ratio in Pb + Pb collisions between 20/A-GeV and 158/A-Gev. Phys. Rev. C73, 044910.

Alt, C. *et al.* (NA49 Collaboration). 2008. Pion and kaon production in central Pb + Pb collisions at 20A and 30A GeV: Evidence for the onset of deconfinement. Phys. Rev. C77,024903.

Andronic, A., P. Braun-Munzinger, K. Redlich, J. Stachel. 2018. Decoding the phase structure of QCD via particle production at high energy. Nature 561, 321-330 (2018).

Barrette, J. *et al.* (E877 Collaboration). 2000. Proton and pion production in Au+Au collisions at 10.8 A GeV/*c*. Phys. Rev. C62, 024901.

Bass, S. A. *et al*. 1998. Microscopic models for ultrarelativistic heavy ion collisions. Prog. Part. Nucl. Phys. 41, 255-369.

Bleicher, M. *et al*. 1999. Relativistic hadron-hadron collisions in the ultra-relativistic quantum molecular dynamics model. J. Phys. G25, 1859-1896.

Cleymans, J. *et al*. 2006. Statistical model predictions for particle ratios at $\sqrt{s_{NN}}$ = 5.5 TeV, Phys. Rev. C74, 047901.

Klay, J. *et al.* (E895 Collaboration). 2002. Longitudinal Flow of Protons from (2-8)A GeV Central Au + Au Collisions. Phys. Rev. Lett. 88,102301.

Kumar L., 2013. Review of recent results from the RHIC beam energy scan. Mod. Phys. Lett. A 28, 1330033.

Kumar, L. (for STAR Collaboration). 2013. STAR Results from the RHIC Beam Energy Scan-I. Nucl. Phys. A904-905, 256c-263c.

Stock, R., F. Becattini, M. Bleicher and J. Steinheimer. 2019. The QCD Phase Diagram from Statistical Model Analysis. Nucl. Phys. A982, 827-830.

Wheaton, S., J. Cleymans, and M. Hauer. 2009. THERMUS - a thermal model package for ROOT. Comput. Phys. Commun. 180, 84-106.

FORM IV
(See rule 8)

1.	Registration No.	:	ISSN-0555-7631
2.	Place of Publication	:	Old Correspondence Building Panjab University, Chandigarh – 160014 (India)
3.	Periodicity of Publication	:	Annual
4.	**Publisher's & Editors' Name**	:	
	Editor-in-Chief	:	Professor Devinder Mehta
	Nationality	:	Indian
	Editor	:	Professor Jagtar Singh
	Nationality	:	Indian
	Address	:	Research Journal (Science) Room No. 28-29, Old Correspondence Building, Panjab University, Chandigarh- 160014 (India)
5.	Printer's Name	:	Mr. Jatinder Moudgill
	Nationality	:	Indian
	Address	:	Manager Panjab University Printing Press Chandigarh – 160 014.
6.	Name and address of the Individuals who own the newspaper and partners or shareholders holding more than one percent of the total capital.	:	Panjab University, Chandigarh

Professor Devinder Mehta, hereby declare that the particulars given above are true to the best of my knowledge and belief.

Professor Devinder Mehta
Editor-in-Chief

PANJAB UNIVERSITY RESEARCH JOURNAL (SCIENCE)

LIFE MEMBERSHIP FORM

Name _____

Qualification _____

Area of Specialization _____

Present Designation _____

Address: (Tick the address on which you would like to receive the journal.
Local members would receive the journal by hand)

i. Office _____
_____

ii. Residence _____
_____

Telephone (O) _____
(R) _____
(Mobile) _____
Fax _____
Email. _____

Payment Mode:

(Only local cheques are acceptable. Draft to be drawn in favour of
The Registrar, Panjab University, Chandigarh

If by cheque/Draft:
Cheque/D.DNo. _____ Date _____ Amount_____
Name of the Bank: _____

Date _____
Place: _____

SIGNATURES

Subscription fee:

	Inland	**Foreign**
Life Membership:	Rs. 3000/-	US $ 250
Annual Subscription:	Rs. 400/-	US $ 50

Send to: The Editor-in-Chief
Research Journal (Science)
Old Correspondence Building
Panjab University, Chandigarh-160014(India)

INSTRUCTIONS FOR AUTHORS

Panjab University Research Journal of Science (PURJS) is an international peer-reviewed journal covering wide-range of research activities in all disciples of science.

PURJS provides opportunity to scientists, engineers and medical experts to publish original full research articles, rapid communications, state-of-the-art reviews in all disciplines of the science, engineering and medicine.

JOURNAL POLICY: It is PURJS policy to publish only original and unpublished research work, therefore, PURJS does not wish to receive any papers on research work that has already been reported in parts or contains already published text, data, figures, tables or other illustrations or any copyright materials whatsoever that has been submitted or accepted for publication either in a journal or conference proceedings elsewhere in any form, in print or in electronic media. When submitting a manuscript, authors should make a full statement to the Editors that the research work contained in their manuscript is completely original and unpublished. If redundant or duplicate publication is attempted or occurs authors should expect immediate editorial action to be taken including prompt rejection of the submitted manuscript. Submission of any manuscript that contains redundant or duplicate publication of the same or very similar research work violates the policies of this journal

ETHICAL COMPLIANCE: Research papers reporting animal or clinical studies should, where appropriate, contain a statement that they have been carried out with animal or human ethics committee approval. All scientific studies should be carried out in accordance with the relevant national and local guidelines. Each author(s) warrants that his or her research institution has fully approved the protocol for all scientific studies involving animals or humans and that all experiments of any kinds were conducted in compliance with ethical and humane principles of research after ethics committee approval.

SUBMISSION OF MANUSCRIPT: Authors are requested to read PURJS policy before submitting their manuscript to Editors. Authors are encouraged to submit high quality original research work that has not been published or nor under consideration by other journals or conference proceedings elsewhere. Authors should submit manuscript electronically as a Microsoft Word file to the Editor-in-Chief. Authors are highly encouraged to submit manuscript electronically as a MS Word file (preferred) or a PDF file to save time for the reviewing process.

Authors should submit a list of SIX (6) potential referees accompanied with their complete mailing address, telephone, fax and email address, who may be contacted for reviewing the manuscript though refereeing, is done by anonymous reviewers selected by the Editor-in-Chief or Editor. (The selection of the reviewer is the discretion of Editors –in-chief and reviewers may not necessarily be from the list provided).

MANUSCRIPTS - The manuscripts should be typewritten (double spaced) with ample margins.

Page 1 should contain only title of manuscript, author(s) name(s) and affiliation(s), a short running title (abbreviated from the title) not exceeding 40 characters, name & complete mailing address of the person to whom correspondence should be addressed.

Page 2 should contain an abstract not exceeding 150 words. The abstract should contain no illustration or reference to the figures, tables, or authors. The abstract should be followed by 3-4 key words.

Rest of the content also continue from this page and should be described under Headings, Introduction, Results and Discussions. Acknowledgements should be inserted at the end of the text before References.

SHORT COMMUNICATION: A short communication should be a record of completed short investigation giving details of new methods or findings. It should not exceed 4 to 5 typed pages with an Abstract followed by Key words. Body of the text should not have any separate title, like Abstract, Materials and Methods, Results and Discussion except the Acknowledgements and References.

REFERENCES:

While citing references in the text it should conform to the following style:-

Adherence of *E. coli* to intestinal mucosal surface...pathogenesis (Beachey, 1981). According to Arnoldi (1976), these feathers....

The references at the end of article should be in alphabetical order and presented as follows:-

Ahuja, D.B. 1990. Population dynamics of mustard aphid, Lipaphis erysimi (Kalt.) on Indian mustard Brassica juncea. Indian J. Plant Protection, 18 : 233-235.

Bener, A. and F.C. Erk. 1979. The analysis of whorls on specific fingerstips with respect to sex, bilateral asymmetry and genetic relationship. Ann. Hum. Biol., 6 : 349 - 356.

Buskrik, E.R., K.L. Anderson, and J. Brozek. 1956. Unilateral activity and bone and muscle development in the forearm. Res. Quart., 27 : 127-131.

Jain, S.K. 1986. Orchid Wealth of India. In: Biology, Conservation, and Culture of Orchid
s (Ed.S.P.Vij) pp. 319-22. Affiliated East - West Press (New Delhi).

ILLUSTRATIONS: The illustrations, preferably be in the form of text-figures, should also be submitted electronically. All figures whether photographs or drawing, must be numbered in single series (Fig. 1, 2, 3.etc.). The figures should be arranged and numbered in the order in which they are referred to in the text. The figures or photographs (plates) submitted for publication must not be less than 300 DPI. The ratio of length & width of the full figure plate must necessarily be in proportion to the page size of the journal i.e. 23 cm x 18 cm. Figures must carry magnification bars.

Legends to figures should be typed on a separate sheet of paper to be inserted after References. Abbreviations used for the figures should be given in an alphabetical order after the legends.

TABLES: Tables 1, 2, 3 should be single-spaced on separate page and numbered. Each table must bear a short descriptive heading.

PROOFS: Page proof will be sent to corresponding author.

Manuscripts and Correspondence should be addressed:

Editor-in-Chief
Research Journal of Science
Old Correspondence Building
Panjab University,
Chandigarh. 160 014 (India)
Telephone: 0172-2534376
E.mail : resjoursci@pu.ac.in

Published by :
EDITOR-IN-CHIEF
Research Journal (Science)
Panjab University, Chandigarh-160 014
INDIA

www.puchd.ac.in

ISSN-0555-7631

Vol. 65, 2015